5-2018

Opto-Electro-Thermal Approach to Modeling Photovoltaic Performance and Reliability from Cell to Module

Xingshu Sun
Purdue University

OPTO-ELECTRO-THERMAL APPROACH TO MODELING PHOTOVOLTAIC PERFORMANCE AND RELIABILITY FROM CELL TO MODULE

A Dissertation

Submitted to the Faculty

of

Purdue University

by

Xingshu Sun

In Partial Fulfillment of the

Requirements for the Degree

of

Doctor of Philosophy

May 2018

Purdue University

West Lafayette, Indiana

THE PURDUE UNIVERSITY GRADUATE SCHOOL
STATEMENT OF DISSERTATION APPROVAL

Dr. Muhammad A. Alam

School of Electrical and Computer Engineering

Dr. Mark S. Lundstrom

School of Electrical and Computer Engineering

Dr. Peide P. Ye

School of Electrical and Computer Engineering

Dr. Zhihong Chen

School of Electrical and Computer Engineering

Approved by:

Dr. Venkataramanan R. Balakrishnan

Head of the Graduate Program

To my family

ACKNOWLEDGMENTS

First of all, I would like to send my sincere gratefulness to my thesis advisor, Prof. Muhammad A. Alam, for his caring support and inspiring mentorship throughout every stage of my graduate study. His endless curiosity for acquiring knowledge and relentless pursuit for solving grand problems set an excellent paragon for me on how to be a devoted and impactful researcher. His philosophy on "complexity does not have to be complicated" teaches me how to understand tough problems but solve them in a simple yet elegant fashion. I also want to thank him for offering me the best advice on my post-graduation career, which helps me recognize my ultimate career goals and find the best route to achieve them. Indeed, his influence on me is way beyond just research, but profoundly beneficial for my lifetime.

I also wish to convey my heartfelt appreciation to my co-advisor and my very first research advisor, Prof. Mark S. Lundstrom, whom I have been working with since undergraduate. I would like to thank him for opening the door of scientific research for me and introducing me the rigor and passion one must share to become a successful researcher. I always admire his grand vision and leadership in building scientific communities and bringing great minds together to tackle the hardest research problems collaboratively, which otherwise cannot be solved.

Moreover, I thank Prof. Peter P. Ye and Prof. Zhihong Chen for joining my committee and providing constructive and insightful suggestions to improve my research. Though my thesis is on photovoltaics, I am certainly fortunate enough to learn a lot about the design and fabrication of post Moore's Law electronics from their work and classes.

I also acknowledge my research collaborators, Prof. Peter Bermel and Prof. Rakesh Agrawal from Purdue University, Dr. Chris Deline, Dr. Dirk Jordan, Dr. Rebekah Garris and Dr. Tim Silverman from the National Renewable Energy Lab-

oratory, Dr. Wanyi Nie and Dr. Aditya D. Mohite from the Los Alamos National Laboratory for their constant support and fruitful discussion. This thesis cannot be accomplished without their help.

I wish to convey my great thanks to my past groupmates: Sourabh Dongaonkar, Biswajit Ray, Md. Masuduzzaman, Md. Ryyan Khan, Md. Abdul Wahab, Raghu V. K. Chavali, Piyush Dak, Aida Ebrahimi, SangHoon Shin, Jiang Hai, Amir Hanna, Chunsheng Jiang, James Moore, Dionisis Berdebes, Kyle Conrad, and Jesse Maassen, present groupmates: Kamal Karda, Woojin Ahn, Xin Jin, Reza Asadpour, Md. Tahir Patel, Yen-Pu Chen, Bikram K. Mahajan, Xufeng Wang, and Evan Witkoske, my colleagues and friends from other groups: Haejun Chung, Enas Sakr, Zhiguang Zhou, Yubo Sun, Pengyu Long, Junzhe Geng, Mohit Singh, and everyone else who has made my graduate school life, supposedly strenuous, very enjoyable and treasurable. It is my honor to share this experience with you. I am also grateful to Vicki Johnson, Christine Ramsey, Matt Golden, Lynn Zentner, Tanya Faltens, and many other administrative staffs for helping me take care of things outside research.

Last and most importantly, I would like to say a big thank you to my grandparents, parents, wife, and everyone else in my family for their constant support, encouragement, and impetus, not just through my graduate school, but my entire life. My parents are the best illustration of lifelong learners, which has been motivating me to pursue knowledge and education ever since my childhood. Also, I must thank my wife for putting up with me when I immerse myself in research thinking all day long, and "force" me to go outside to enjoy the beautiful nature together with our cutest dog, Butterball.

TABLE OF CONTENTS

Page

Page

Page

Page

LIST OF TABLES

LIST OF FIGURES

Figure Page

Figure Page

Figure Page

Figure Page

Figure Page

Figure Page

Figure Page

ABSTRACT

Sun, Xingshu Ph.D., Purdue University, May 2018. Opto-Electro-Thermal Approach to Modeling Photovoltaic Performance and Reliability from Cell to Module. Major Professors: Muhammad Ashraful Alam, Mark Lundstrom.

Thanks to technology advancement in recent decades, the levelized cost of electricity (LCOE) of solar photovoltaics (PV) has finally been driven down close to that of traditional fossil fuels. Still, PV only provides approximately 0.5% of the total electricity consumption in the United States. To make PV more competitive with other energy resources, we must continuously reduce the LCOE of PV through improving their performance and reliability. As PV efficiencies approach the theoretical limit, however, further improvements are difficult. Meanwhile, solar modules in the field regularly fail prematurely before the manufacturers 25-year warranty. Therefore, future PV research needs innovative approaches and inventive solutions to continuously drive LCOE down.

In this work, we present a novel approach to PV system design and analysis. The approach, comprised of three components: ***multiscale, multiphysics, and time***, aims at systemically and collaboratively improving the performance and reliability of PV. First, we establish a simulation framework for translating the cell-level characteristics to the module level (***multiscale***). This framework has been demonstrated to reduce the cell-to-module efficiency gap. The framework also enables the investigation of module-level reliability. Physics-based compact models - the building blocks for this multiscale framework are, however, still missing or underdeveloped for promising materials such as perovskites and CIGS. Hence, we have developed compact models for these two technologies, which analytically describe salient features of their opera-

tion as a function of illumination and temperature. The models are also suitable for integration into a large-scale circuit network to simulate a solar module.

In the second aspect of the approach, we study the fundamental physics underlying the notorious self-heating effects for PV and examine their detrimental influence on the electrical performance (***multiphysics***). After ascertaining the sources of self-heating, we propose novel optics-based self-cooling methodologies to reduce the operating temperature. The cooling technique developed in this work has been predicted to substantially enhance the efficiency and durability of commercial Si solar modules.

In the third and last aspect of the approach, we have established a simulation framework that can forward predict the future energy yield for PV systems for financial scrutiny and inversely mine the historical field data to diagnose the pathology of degraded solar modules (***time***). The framework, which physically accounts for environmental factors (e.g., irradiance, temperature), can generate accurate projection and insightful analysis of the geographic- and technology-specific performance and reliability of solar modules. For the forward modeling, we simulate the optimization and predict the performance of bifacial solar modules to rigorously evaluate this emerging technology in a global context. For the inverse modeling, we apply this framework to physically mine the 20-year field data for a nearly worn-out silicon PV system and successfully pin down the primary degradation pathways, something that is beyond the capability of conventional methods. This framework can be applied to solar farms installed globally (an abundant yet unexploited testbed) to establish a rich database of these geographic- and technology-dependent degradation processes, a knowledge prerequisite for the next-generation reliability-aware design of PV systems.

Finally, we note that the research paradigm for PV developed in this work can also be applied to other applications, e.g., battery and electronics, which share similar technical challenges for performance and reliability.

1. INTRODUCTION

1.1 Background

To combat climate change and meet the exploding energy demand of a rapidly growing world population, the production of renewable energy must increase significantly. The ability to harvest sufficient renewable energy sustainably will be one of the greatest global challenges of this century [1, 2]. Solar photovoltaics (PV) is one of the fastest growing categories of renewable energy resources [3], due to the availability of abundant solar resources on Earth ($\sim 10^{17}$ kW.h every year) [4–6], the improved "bankability" of PV [7] (i.e., economic viability for institutional lenders to offer financing), and the rapid expansion of manufacture capabilities [8], etc. Remarkably, the total installation of PV worldwide has ramped up from ∼0.17 GW in 2000 to ∼300 GW in 2016, a total ∼180,000% increase in only 16 years [9, 10]! In 2014, almost 7% of the electricity demand was met through PV in Germany [11]. Meanwhile, PV share of total electricity production rose from 2.7% in 2015 to 4.3% in 2016 in Japan [12]. Photovoltaics have also helped to solve electricity poverty in part of Asia and Africa where electricity for household, education, healthcare, and agriculture strongly depends on distributed PV systems [13].

Notwithstanding the significant achievement in PV development, one of the primary obstacles to making PV more prevalent as an energy source is the economic competition with the ultra-low levelized cost of electricity (LCOE) of conventional energy sources, such as oil, natural gas, coal, etc. One can calculate LCOE of PV by dividing the total life-cycle cost ($) by the total energy yield produced (kW.h) over the entire lifetime as

$$\text{LCOE} = \frac{\text{Total Cost}}{\text{Total Energy Yield}} = \frac{Cost_{Fix} + \int_0^{t_{Life}} Cost_{Var}(t)dt}{\int_0^{t_{Life}} P_{Module}(IL, T, t)dt}, \tag{1.1}$$

where $Cost_{Fix}$ and $Cost_{Var}$ denote fixed and variable costs, respectively; $P_{Module}(IL, T, t)$ is the module output power as a function of illumination (IL), temperature (T), and time(t); and t_{Life} is the lifespan of the solar module which is contingent on environmental factors (e.g., temperature (T), relative humidity (RH), ultraviolet light concentration (UV)). *This thesis is dedicated to improve $P_{Module}(IL, T, t)$ and extend t_{Life} in order to drive down LCOE.*

This metric, LCOE, accounts for capital costs, ongoing system-related costs, and discounting of the net value, all of which are normalized by the amount of electricity produced. It provides a number to objectively compare various energy sources. Over the past decades, the PV industry has been striving to reduce the LCOE of solar energy. For instance, many countries have been offering incentive policies in favor of PV, which reduces the numerator in Eqn. 1.1. In the US, individuals and entities are rewarded a Federal tax credit of 30% for installing residential and commercial PV systems [14]. Meanwhile, continuous technical breakthroughs, along with the enlarged manufacturing capacity, in the PV industry have also driven the LCOE down substantially.

Most of the research progress aimed to lower the LCOE of PV can be roughly divided by the following parameters in Eqn. 1.1:

1. ***Lowering the manufacturing cost ($Cost_{Fix}$)***: Optimizing the manufacture lines has helped reduce the CAPEX ($Cost_{Fix}$ of new factories and equipment) for mass production of solar modules [15,16]. For instance, the factory gate price of silicon modules in the US has plunged from \$1.7/W in 2010 to \$0.35/W in 2017. Meanwhile, many groups have been exploring more cost-effective direct-bandgap materials that are both Earth-abundant and compatible with low-cost fabrication processes than the incumbent silicon in the hope of reducing material cost [17]. For example, thin film materials, such as perovskite, have the potential achieve module cost of 0.26 \$/W, half that of silicon technology [18,19].

2. ***Improving the output power*** ***($P_{Module}(IL, T, t)$)***: The first solar cell was a 1% efficient Si solar cell (i.e., convert 1% of the sunlight of 1000 W/m^2 into electricity), developed at Bell Lab in 1951 [20]. Since then, substantial research efforts have been exerted on further improving the efficiency by material purification, electrical design, light management, etc. For example, the efficiency of multicrystalline solar cells (contain more impurities but much cheaper to manufacture than monocrystalline silicon), which comprise 70% of the present global PV production, has clambered up to 21.9% [21]. Even more remarkably, the record efficiency has been soaring toward the fundamental thermodynamic limit — the highest efficiencies for single-junction (GaAs) and multijunction solar cells are currently ∼28.8% [22] and ∼46% [23], respectively. Despite this astonishing progress, as the record efficiencies start to approach the theoretical limit (known as the ShockleyQueisser limit) [24, 25], it has become increasingly more difficult and challenging to push the record efficiency higher. Hence, the record efficiency has been stagnant recently [26]. Indeed new innovations are essential to overcome this research barrier. Recently, a surging technology — bifacial solar modules — that allows light-collection from both the front and rear sides has demonstrated great potential to improve output power [27]. The performance of bifacial modules strongly depends on the environment (e.g., diffuse light, ground albedo coefficient) and the installation (e.g., tilt angle, elevation). However, a comprehensive understanding of their performance and optimization is still missing in a global context; thereby it still entails a rigorous investigation to fully assess the potential of this technology.

3. ***Prolonging the lifetime of solar modules*** ***(t_{Life})***: Solar modules must survive at least for a few decades in the field to ensure the financial viability. Currently, manufacturers guarantee a 25-year warranty (i.e., guaranteed to retain 80% of the initial power output). Also, before deployment, all the solar modules are required to undergo a set of meticulous qualification tests specified by the International Electro-Technical Commission (IEC) to promise long-term

durability [28]. However, recent field surveys have revealed that many solar modules failed prematurely [29] which could result in undesired financial losses. Hence, the reliability of solar modules must be further improved, a prerequisite to continuing driving down the LCOE of PV.

The LCOE of PV is continuously decreasing; nonetheless, an energy outlook report by the U.S. Energy Information Administration still predicts that the LCOE of PV ($59.8 per MW.h) will be approximately four times higher than conventional energy sources, such as natural gas-fired generation ($14 per MW.h for conventional combined cycle) [30]. Another study conducted by Lazard has shown that the LCOE of large-scale utility solar farms has dropped down to $46 per MW.h (already lower than most conventional energy sources) [31]. Hence, there has been a steady increase in constructing utility solar farms even without incentive policies [32]. Residential rooftop solar modules, however, still cost up to $319 per MW.h due to: 1) limited purchasing power, and 2) sub-optimal output power [33]. Therefore, it urges the PV community to continuously engineer solar modules to eliminate the price gap between different PV applications.

In the following parts of the Introduction, we will discuss a set of novel research approaches and technology opportunities — that can lower the LCOE of PV in the future. We will also discuss the challenges associated with implementing these new technologies in practice.

1.2 An End-to-End Approach based on Compact Models

To reduce LCOE, one effective way is to lower $Cost_{Fix}$. Another way to do so is to increase $P_{Module}(IL, T, t)$ and t_{Life} by an end-to-end approach inspired by electronic research. In the electronics industry, it is a common practice that one starts with the physical design at the nm-scale transistor level and then integrates billions of transistors into a cm-scale chip by logic synthesis, see Fig. 1.1. In principle, this end-to-end framework is transferable to PV research whereby one can connect the cell-level

performance to the design of large-scale PV systems; yet this approach has not been fully explored (most papers only report cell-level efficiencies). In this section, we will introduce some pioneering contributions that have implemented this end-to-end research methodology to improve the module output power, $P_{Module}(IL, T, t)$, in Eqn. 1.1 by 1) optimizing module-level efficiency and 2) investigating module reliability.

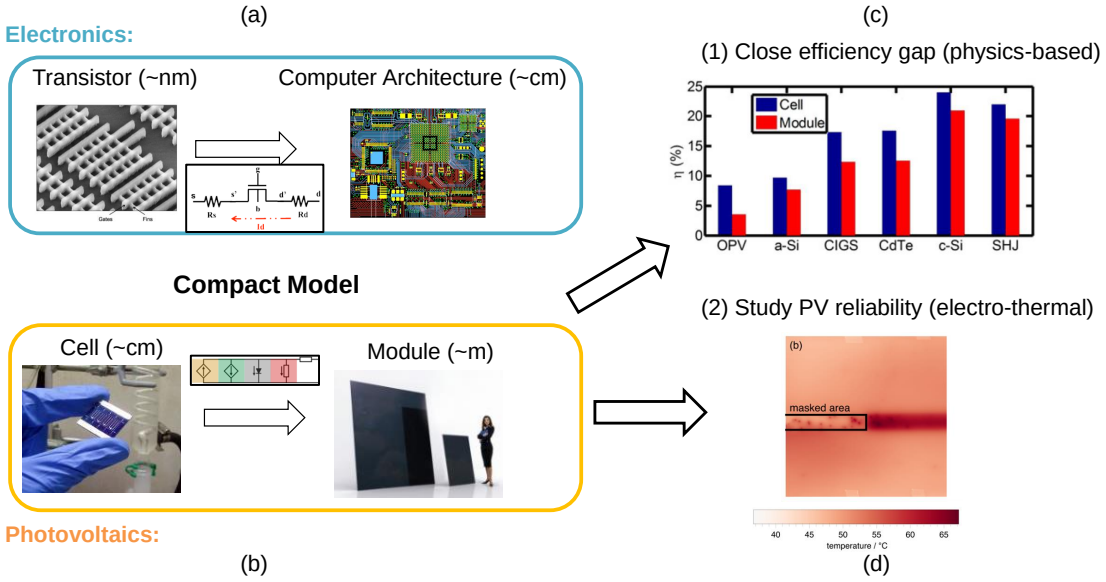

Fig. 1.1. The analogy between (a) the transistor-to-computer approach in IC and (b) the cell-to-module perspective for photovoltaics. This end-to-end approach can facilitate: 1) (c) optimization of the cell-to-module efficiency gap (the plot obtained from [34] ©2016 IEEE) and 2) (d) understanding of PV reliability issues.

1.2.1 Increasing $P_{Module}(IL, T, t = 0)$ by Closing the Cell-to-Module Efficiency Gap

Many commercially available PV technologies demonstrate a remarkable state-of-the-art cell efficiency, e.g., silicon heterojunction technology has just exceeded 26% cell efficiency [35]. However, there still exists a universal gap for cell-to-module efficiencies (e.g., the efficiency gaps are, respectively, ~2.6% and ~3.5% for the 88-cell and 72-

cell solar modules fabricated by Panasonic Inc. [36]). A summary of cell-to-module efficiency gaps for different technologies is shown in Fig. 1.1.

Previous Work on Process-to-Module Modeling. A few studies have pioneered a new process-to-module (end-to-end) modeling framework whereby the contributions of process and cell variations to this efficiency gap have been carefully explored [34, 37, 38]. The simulation flow of this framework generally consists of three hierarchical levels: 1) a compact model that describes deposition process during the fabrication of solar cells and can anticipate material parameters (e.g., bandgap, grain size, thickness) as a function of process parameters such as deposition pressure/temperature, 2) a physics-based compact model that reflects the material properties obtained from the process model to the resulting IV characteristics, and finally 3) individual cell-level IV curves will be concatenated to construct the module-level performance via a circuit network. Based on this framework, it has been observed that the process/cell variations contribute to the cell-to-module efficiency loss, which is as high as those from series resistance and dead area losses. This variation-induced loss persists even in the most advanced technologies. Hence, we must adopt a corresponding bining strategy to minimize this variation-induced loss. Not only can this framework identify the origins of the efficiency gap, but it can also offer novel solutions to surmount this bottleneck at the module level. For example, Dongaonkar *et al.* have proposed in-line scribing techniques after the fabrication of monolithic solar modules [39]. They discovered that such methods can extricate monolithic module from half of the efficiency loss to shunting which corresponds to 1 – 2% absolute improvement in module efficiency.

How About Emerging Technologies? In the aforementioned end-to-end framework, compact models with physically defined parameters are vital to connecting fabrication process occurring on the nm scale to the module level performance on the meter scale, and even predict farm level energy production, far beyond the capability of conventional empirical models [40]. Therefore, physics-based compact models are indispensable. A variety of physics-based compact models have been developed for

commercially available solar cells, such as HIT, CIGS, CdTe [34,41–47]. Similar models, however, are still missing for emerging technologies like perovskites, which has achieved unprecedentedly rapid development (i.e., cell efficiency of 3.8% in 2009 [48] to 22.7% in 2017 [49]). Before the technology of perovskite PV matures for commercial production, it is crucial to establish their efficiency limits and come up with solutions for optimization at the module level. *Thus, it motivates us to develop a set of analytical compact models for different types of perovskite solar cells in the hope of casting some light to improve their module-level performance and enable an accurate prediction of the long-term energy yield for this promising technology.*

1.2.2 Predicting $P_{Module}(IL, T, t)$ by Opto-Electro-Thermal Compact Models

Varying Temperature and Illumination in the Field. Previous end-to-end studies only optimized the module-level performance under the standard test condition (STC), i.e., $IL = 1000$ W/m^2 and $T = 25$ °C in $P_{Module}(IL, T, t)$. However, in the field, illumination intensity and temperature have substantial geographic and seasonal variations, and solar modules rarely operate right at the STC. On the other hand, many of the existing compact models [34,41–47] can only simulate IV characteristics at the STC. Therefore, it is necessary to incorporate illumination and temperature dependencies into the compact models to accurately project the realistic output power $P_{Module}(IL, T, t)$ in the field with varying illumination and temperature.

1.2.3 Extending t_{Life} by Studying Module-Level Reliability.

Besides improving the nascent output power ($P_{Module}(IL, T, t = 0)$), this end-to-end framework has also been applied to study the reliability of large-area solar modules [50–52], such as partial-shading degradation which can reduce t_{Life} significantly after initial installation (will be discussed in detail in Sec. 1.3.2). It must be noted that experiments have shown a pronounced non-uniform temperature distribu-

tion that ensues after partial shading [50], see Fig. 1.1. This thermal effects will then impact the cell-level electrical characteristics and must be solved electro-thermally and self-consistently. As a result, a pure electrical framework may not be able to predict the performance and reliability of the shaded solar modules accurately. However, the temperature dependencies of the existing compact model parameters were not explicitly specified. Consequently, the current framework based on these purely electrical compact models can only perform electrical simulation and is inept to account for the thermal state of the solar modules.

In this thesis, we develop a compact model that can anticipate the illumination- and temperature-dependent IV curves for CIGS, a commercially available technology. This new model can predict the energy yield of large-scale PV farms installed in the field. The model can also be incorporated into an electro-thermal coupled simulation framework to advance our understanding of non-uniform partial shading degradation at the module level.

1.3 Improving $P_{Module}(IL, T, t)$ and t_{Life} through Robust Thermal Management for Photovoltaics

In the previous section, we discussed the importance of connecting cell-level and module-level characteristics by an end-to-end approach, so that we can optimize the process, efficiency, and durability of solar modules. In this section, we wish to talk about thermal properties of PV and their implications on the short- ($P_{Module}(IL, T, t)$) and long- (t_{Life}) term energy yield in Eqn. 1.1.

1.3.1 Eliminate Intrinsic Self-Heating

Why Modules Heat Up. Theoretically, a single-junction solar cell can convert at most ∼33% of the incoming sunlight into electricity [25], whereas the majority of the remaining light is dissipated as heat [24, 53] or directly transmits through the solar cell without being absorbed (the sub-bangap photons). The energy conversion

efficiency of practical solar cells can be even lower due to other non-idealities, such as Shockley-Read-Hall/Auger recombination [54], parasitic series/shunt resistance [55–58], resulting in more heat dissipation and self-heating of solar cells. Depending on the environment, the average temperature of a solar module can be 20^{o}C to 40^{o}C higher than the ambient.

Detriments Caused by Self-Heating. The self-heating of PV modules reduces both short-term and long-term power outputs. In the short term, the efficiencies of different PV technologies decrease with temperature, e.g., the efficiency of crystalline Si modules drops by ∼0.45% for every 1 °C increase in temperature [59]. In the long term, the reliability of modules suffers from thermally activated degradation processes ($\sim e^{-\frac{E_A}{kT}}$), such as contact corrosion and polymer degradation, which accelerate exponentially at higher temperatures. A recent survey in India has shown that solar modules in hot climates degrade at ∼1.5 %/year, eight times faster than the ones installed in cold climates (∼0.2 %/year) [29]. Modules with a 25-year warranty survive less than 15 years in hot environments. As a result, it is important to understand and eliminate PV self-heating to improve both the short-term and the long-term energy yields.

Recently, it also has been recognized that sub-bandgap (sub-BG) photons of the solar spectrum may contribute significantly to self-heating in solar cells. References [60–62] have confirmed experimentally that ∼80% of the sub-BG photons are parasitically absorbed in Si solar cells by the metal reflector and highly doped emitter (free carrier absorption) due to light trapping. Light trapping design is imperative to maintain high short-circuit current in commercial silicon solar modules. Hence, this light trapping induced parasitic absorption is inevitable. Indeed, the substantial amount of sub-BG absorption in Si photovoltaics has explained the higher operating temperature observed during outdoor tests of Si-based modules as compared to GaAs modules, which showed low absorptivity in the sub-BG spectrum [62]. The parasitic sub-BG absorption, however, has not been explored for polycrystalline thin film solar cells (e.g., CIGS, CdTe).

Cooling Techniques. Given the extremely debilitating effects of self-heating on PV performance, it is imperative to develop a set of cooling strategies that can regulate the temperature of PV. There are several active and passive cooling schemes already in use to reduce the operating temperature of PV modules. These include evaporative and fin cooling [63] to enhance convective heat transfer, liquid submerged PV [64, 65] as an alternative heat sink, heat pipe-based systems [66] to improve conductive heat transfer, and so on [67]. These methods cool the solar modules already heated by the sunlight. A scheme designed to prevent or suppress self-heating could be far more effective. Modification of the module configuration based on the fundamental physics of self-heating of PV may create a simpler, yet more effective cooling method for modules. In this context, a recent proposal involving radiative cooling of solar cells has drawn much attention [68–71]. Both experiments and simulations show that radiative cooling can reduce the operating temperature of solar modules by 1 °C to 2 °C. However, references [68–71] have utilized a pure thermal framework [72, 73] to evaluate the temperature reduction of solar modules by radiative cooling, where the role of electricity output of a practical solar module in determining the module temperature was also not accounted for (e.g., a slab of Si wafer instead of a solar cell was assumed in [68–71], and ideal solar cells at the Shockley-Queisser limit were assumed in [71]). As a result, it has still been difficult to ascertain the effectiveness of radiative cooling on commercial PV modules. *Therefore, in this thesis, we will apply an opto-electro-thermal coupled simulation framework to self-consistently investigate the benefit of radiative cooling.*

1.3.2 Eliminate Shading-Induced Heating

Shading-Induced Heating. In addition to intrinsic self-heating, partial shading induced self-heating has also been recognized as one of the reliability concerns for series-connected solar cell technology, especially in thin film photovoltaic technology (TFPV). Unlike crystalline PV technology, monolithic integration (by laser scribing)

for creating a series connection of a single string of 50 — 200 solar cells in TFPV modules makes integration of bypass diodes [74] and rewiring schemes [75] challenging. One of the consequences of partial shading is that the shaded cells are forced into reverse bias to maintain current continuity with the series-connected illuminated cells. Reverse biased solar cells develop a large internal electric field, high current density, and high temperature (due to high power dissipation), all of which can lead to reliability failures of the solar modules. Localized shunts can be formed due to reverse bias and high-temperature stress during the shadow event causing significant permanent damages (mainly losses in fill factor) of the modules. The shunts create worm-like defects caused by delamination between the absorber and buffer layers and material segregation in the absorber [76, 77].

Combat Partial-Shading. Given that shadow-induced heating is a serious reliability concern especially for monolithic solar modules, several novel designs have been proposed to relieve shading stress to mitigate partial shading degradation at the cell, module, and system levels, respectively. At the cell level, one can lower the power dissipation at reverse bias of the shaded cells by reducing the breakdown voltage, which has been demonstrated on c-Si solar modules [78]. Reference [79] shows that similar approach to reduce breakdown voltage can be applied to CIGS by reducing the absorber thickness, such that the required reverse voltage to drive 30 mA/cm2 (photocurrent of unshaded cells) decreases both under dark and light, see Fig. 8 in [79]. At the module-level, improving the geometric design of monolithic modules can also mitigate shadow induced heating. Reference [80] suggests an innovative geometric pattern of solar modules that can break the symmetry in cell shape and orientation to improve shade tolerance as well as total efficiency. Additionally, inducing perpendicular isolation scribe lines to divide a module into several submodules connected in parallel can also diminish the affected area by shadow by constraining shading stress only to the shaded submodules [79]. The design tradeoff of the dead area losses from the addition of the scribe lines needs to be carefully considered. Last but not least, reference [79] also has demonstrated that shading tolerance can be enhanced at the

system level by interconnecting modules into a hybrid configuration both in parallel and series.

To summarize, because solar modules can convert only a fraction of the sunlight into electricity, they self-heat in the field inexorably. The ensuing elevated temperature will substantially accelerate thermally activated degradation pathways (i.e., increase with temperature exponentially) and shorten the lifespan (t_{Life}). *Hence, it urges a deep understanding of self-heating in solar modules to identify the predominant contributing factors, and ultimately contrive cost-effective methods to lower the operating temperature as we will discuss in this thesis.*

1.4 Bifacial Photovoltaics Can Increase $P_{Module}(IL, T, t)$

Bifacial solar photovoltaics are an emerging technology that have demonstrated great potential to improve annual electricity yields and decrease LCOE for photovoltaics. In this section, we will briefly introduce this technology and discuss the prospects and challenges.

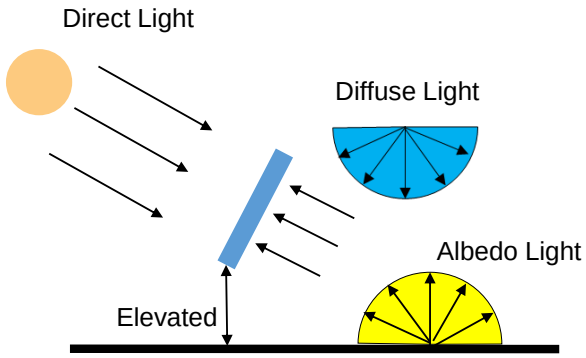

Fig. 1.2. A schematic depicting an elevated bifacial module. The rear side of this bifacial module can absorb diffuse and albedo light in addition to the front-side absorption.

1.4.1 Technical Advantages

Increased Energy Yield. Monofacial solar modules make up 90% of the present PV market [81]. Due to the opaque rear side, however, monofacial solar modules can only collect solar irradiance from the front side; hence, a significant portion of the sunlight that hits on the rear surface is not utilized at all. In contrast to its monofacial counterpart, a bifacial solar module has a transparent rear side, which allows it to recover part of diffuse and albedo light from the rear side, see Fig. 1.2. Therefore, bifacial solar modules can generate more electricity per module area. The first proposal for bifacial solar cells dated back to the 1960s, where Hiroshi filed the first patent on this technology [82]. Since then, Cuevas *et al.* [83] have demonstrated a bifacial gain up to 50% relative to identically oriented and tilted monofacial modules. Here, bifacial gain is defined as

$$\text{Bifacial Gain} = (\text{Y}_{\text{Bi}} - \text{Y}_{\text{Mono}})/\text{Y}_{\text{Mono}}, \tag{1.2}$$

where Y_{Bi} and Y_{Mono} are the electricity yields in kWh for bifacial and monofacial solar modules, respectively.

Longer Lifetime. Bifacial solar modules also have better intrinsic thermal properties than monofacial counterparts; specifically, lower sub-bandgap absorption. Recall that, as discussed in Sec. 1.3.1, the aluminum metal back contact layer in conventional silicon monofacial modules parasitically absorbs a substantial amount of sub-bandgap photons trapped by the textured structure. Instead of the aluminum metal back contact layer, silicon bifacial solar modules adopt interdigitated Al metal grid to let light pass from the rear side. This transparent rear side has been experimentally demonstrated to considerably curtail the absorption of sub-bandgap photons, which potentially renders bifacial modules cooler than monofacial ones [84]. The reduced temperature and lower temperature coefficient (enabled by heterojunction silicon technologies with high open-circuit voltage [85]) can further boost the performance and reliability of bifacial modules. Moreover, the glass-to-glass structure

of bifacial modules improves the long-term durability compared to the traditional glass-to-backsheet monofacial modules. The improved durability will further increase the electricity production of bifacial modules in the long term. It must be noted that the extra rear-side absorption may also heat up bifacial modules. Therefore, though bifacial modules exhibit more desired thermal properties than monofacial ones, which one runs cooler in the field remains an interesting open question.

Compatibility with Existing Manufacturing. Many existing materials (e.g., dye-sensitized [86], CdTe [87], CIGS [88]) are also readily convertible into bifacial solar modules. Due to the high efficiency and the manufacturing compatibility into the bifacial configuration, silicon technologies, e.g., Si heterojunction cells, have received most attention [27]. This process compatibility, the extra energy produced by rear-side collection, and more protracted module lifetime can potentially decrease the installation cost and the LCOE substantially [89, 90]. This overall economic advantages persist in spite of the fact that manufacturing bifacial solar modules can be more expensive than monofacial ones due to additional materials (e.g., dual glasses) and processes (e.g., screen-printing rear contacts). Based on these considerations, the International Technology Roadmap for Photovoltaics (ITRPV) anticipates the global market share of bifacial technology to expand from less than 5% in 2016 to 30% in 2027 [81].

1.4.2 Accurate Forward Modeling to Predict $\int_0^{t_{Life}} P_{Module}(IL, T, t)dt$

The 50% bifacial gain predicted for an idealized standalone bifacial module by Cuevas *et al.* [83], however, is not always achievable in practice; thus, some of the highly optimistic projections regarding technology adoption may not be realistic. For example, intrinsic non-idealities, such as self-shading and mutual-shading (i.e., ground-reflected albedo light reduced by shadows cast by the module itself as well as adjacent modules), can reduce the bifacial gain to less than 10% [91]. Therefore, one can develop rigorous forward modeling method to accurately predict and optimize

the long-term performance potential of bifacial modules, i.e., $\int_0^{t_{Life}} P_{Module}(IL, T, t)dt$, only after accounting for these intrinsic non-idealities rigorously.

The performance of bifacial solar modules depends substantially on the environment (e.g., latitude and longitude) and the deployment (e.g., tilt and azimuth angles). Therefore, they must be optimized specifically for each location. Indeed, the PV community will benefit greatly from a set of empirical equations that can calculate the optimum tilt and azimuth angles of bifacial solar modules given the geographic location, similar to those developed for monofacial ones [92]; however, such design guidelines are not currently available. *In this thesis, we will conduct a thorough study on bifacial solar modules based on our sophisticated forward modeling framework to eliminate these knowledge gaps.*

1.5 Reliability-Aware Design for PV to extend t_{Life}

The ability to extend the lifetime (t_{Life}) of solar modules, another key factor to reduce LCOE for PV, remains an intractable challenge. For example, manufacturers guarantee a 25-year warranty whereas field reports have shown PV lifetimes of less than 15 years [29]. Hence, it is critical to develop degradation-resistance solar modules. The existing empirical approaches, however, fail to capture the essential physics of PV reliability [93]. A lack of fundamental understanding prevents the advance of reliability-aware design for PV systems.

1.5.1 Complexity and Intricacy of PV Reliability

Various Degradation Mechanisms. Degradation of PV systems is not a single process but rather involves a combination of multiple complex physical phenomena (e.g., corrosion, EVA discoloration) that evolve slowly over time and ultimately result in the failure of solar modules. We have summarized a list of common degradation pathways reported in the literature in Table 1.1. Each degradation mechanism also impacts solar modules differently. For example, EVA discoloration/delamination will

decrease short-circuit current by blocking the light transmission optically while solder bond failure primarily affects the series resistance electrically. These degradation pathways are also mutually coupled, i.e., one may trigger/accelerate another. For instance, delaminated EVA or cracked glass can exacerbate moisture ingress into solar modules which in turn causes corrosion of metal contacts. Solder bond failure can generate hot spots in a module, which later will accelerate other thermally activated degradation processes. Thus, PV degradation is in practice often intertwined by these mutual coupling effects, which obfuscates the isolation of degradation mechanisms from field data.

Preventive Strategies. Over the past few years, researchers have developed a set of innovative strategies to curb targeted degradation pathways. Kempe *et al.* have successfully demonstrated that Cerium-doped glass can prevent polymeric encapsulants (e.g., EVA) from UV-induced discoloration [113]. They also have found that silicon, an alternative encapsulant material to EVA, exhibits more robust resistance to UV photons, thereby less susceptible to discoloration. Moreover, potential-induced degradation (PID) - sodium ions migrate under electrical field across module frame to solar cell and eventually create defects in solar cell -- can lower carrier lifetime and cause shunting paths, thereby very pernicious to module performance. Reference [114] has discovered that simply inserting Corning® Willow™ Glass between the aluminum frame and coverglass can impede ion migration and consequentially mitigate PID. At the system level, researchers have also invented a novel PID-preventive transformerless inverter for PV systems by manipulating the voltage polarity [115].

Moreover, Sunpower's high-end interdigitated back contact solar cells (IBC) can achieve a useful lifetime (defined as 99% of modules producing at least 70% of their initial rating power) of more than 40 years and demonstrate much superior reliability in accelerated tests compared to conventional solar modules [116]. This improvement primarily can be attribute to 1) the use of n-type silicon as the solar absorber to eliminate light-induced-degradation, 2) a plated tin coated copper to prevent moisture ingress and oxidation and also strengthen the mechanical properties against stress and

Table 1.1.

A detailed summary of common degradation mechanisms observed in fielded solar modules.

Optical Degradation				**Thermal Degradation**
Mechanism	EVA Discoloration [94, 95]	EVA Delamination [96, 97]	Soiling [98, 99]	Hot Spot [50, 52, 76]
External Factor	UV, Temperature	UV, Humidity, Thermal Cycle	Soil/Dust, Inadequate Cleaning	Partial Shading, Other Degradation
Coupling Effect		Contact Corrosion	Hot Spot	Other Thermally Activated Degradation Processes
Electrical Degradation				
Mechanism	Contact Corrosion [100, 101]	Solder Bond Failure [102–104]	Potential Induced Degradation [93, 105, 106]	Diode/J-box [107, 108]
External Factor	Temperature, Humidity	Thermal Cycle	Temperature, Humidity, Voltage	Temperature, Humidity
Coupling Effect	EVA Delamination	Hot Spot	Corrosion, EVA Delamination	
Mechanical Degradation				
Mechanism	Backsheet Failure [109]	Fractured Cell [110, 111]	Glass Breakage [112]	
External Factor	Thermal Cycling, Humidity, UV	Thermal Cycling, External Stress	Thermal Cycling, External Stress	
Coupling Effect	Contact Corrosion		Contact Corrosion, EVA Delamination	

thermal expansion, 3) the use of UV-quenchers to prevent EVA yellowing [94], and 4) the lower operating temperature that can suppress thermally activated degradation processes (Nominal Operating Condition Temperature are respectively 41.5 °C and 45 °C for Sunpower SPR-X22-360 [117] and GCL-P6/72G [118] solar modules). Indeed, these remedial techniques for PV degradation are compelling, yet they may also make PV manufacturing costlier.

Geographic and Meteorological Factors. On the other hand, the distribution and magnitude of PV degradation vary substantially across geographic locations as revealed by the field surveys [119,120], since each degradation mechanism is sensitive to different environmental factors (e.g., UV radiation causes EVA discoloration), as summarized in Table 1.1. Indeed, it would be most effective to engineer the reliability of solar modules based on geographic locations and meteorological information to ensure maximum longevity. However, there is still a lack of comprehensive understanding of this location- and weather-specific degradation – the foundation for reliability-aware design. *As a result, solar modules are currently manufactured irrespective of location and climate, and are often either overdesigned (at the price of extra cost) or underdesigned (unable to resist localized degradation processes).*

1.5.2 Characterization Method for PV Reliability

A Method to Create Global Degradation Database. Therefore, a characterization method that can diagnose and collect the degradation pathways of fielded solar modules methodically while taking the meteorological information into account can improve our understanding of location- and weather-specific degradation processes and ultimately suggest opportunities for reliability-aware technology improvement. There have been many studies on PV reliability reported in the literature, based on different characterization methodologies. These methodologies can be roughly divided into two groups: off-line and on-line techniques.

Off-line Techniques. Typical off-line techniques examine PV degradation by periodically and temporarily disconnecting solar modules for a detailed characterization. For instance, Jordan *et al.* [121] and Sutterlueti *et al.* [122] inspected the degradation mechanisms of PV systems by interpreting IV curves based on the physically-defined five parameter model and the empirical loss factors model (LFM), respectively. Additional sophisticated characterization techniques (e.g., electroluminescence and infrared imaging) can even yield the spatial-resolved degradation analysis for fielded

solar modules [50, 123]. Indeed, these off-line methods are incredibly powerful for degradation characterization; however, they require interrupting the normal operation of solar modules at the maximum power point, hence not suitable for continuous monitoring.

On-line Techniques. On-line techniques, on the other hand, rely on information routinely collected from solar modules. For example, references [124, 125] have analyzed the on-line temporal evolution of PV degradation by continuously examining three time-series performance metrics: 1) DC/GPOA, the ratio of DC power over the plane-of-array irradiance [126], 2) the performance ratio (PR), a number between 0 and 1 (under standard test condition (STC)) equal to the ratio between actual energy yield and nameplate rating [127], 3) the regression PVUSE method that empirically translates on-site output power to the STC values [128]. These methods have the advantage that the modules are not disconnected/interrupted for characterization. The understanding of the degradation pathways, which is critical to establishing the fundamental physics of degradation and promoting reliability-aware design, is still missing from this analysis.

Machine Learning Techniques. Another on-line characterization approach involves analyzing PV data by statistical machine learning algorithms [129–131]. Machine Learning has been proved to be a potent tool to analyze massive data and generate useful insights for different applications. Nonetheless, the weight functions in these algorithms are not physically defined, and it can be difficult to correlate the weights to specific degradation mechanisms. Moreover, network training necessitates a tremendous amount of field data spanning across different geographic locations and technologies as training sets, which are not easily accessible. Therefore, an on-line methodology that can physically and continuously track the degradation of PV systems in real time by interpreting the available field data (and providing insights obtainable only by off-line techniques) can be a transformative tool for the PV community.

1.6 Outline of The Thesis

The overall research goal of this thesis is to establish an opto-electro-thermal framework that enables simulation and optimization of photovoltaics for improved performance and reliability from cell to module. To do so, our approach embodies three components as delineated in Fig. 1.3.

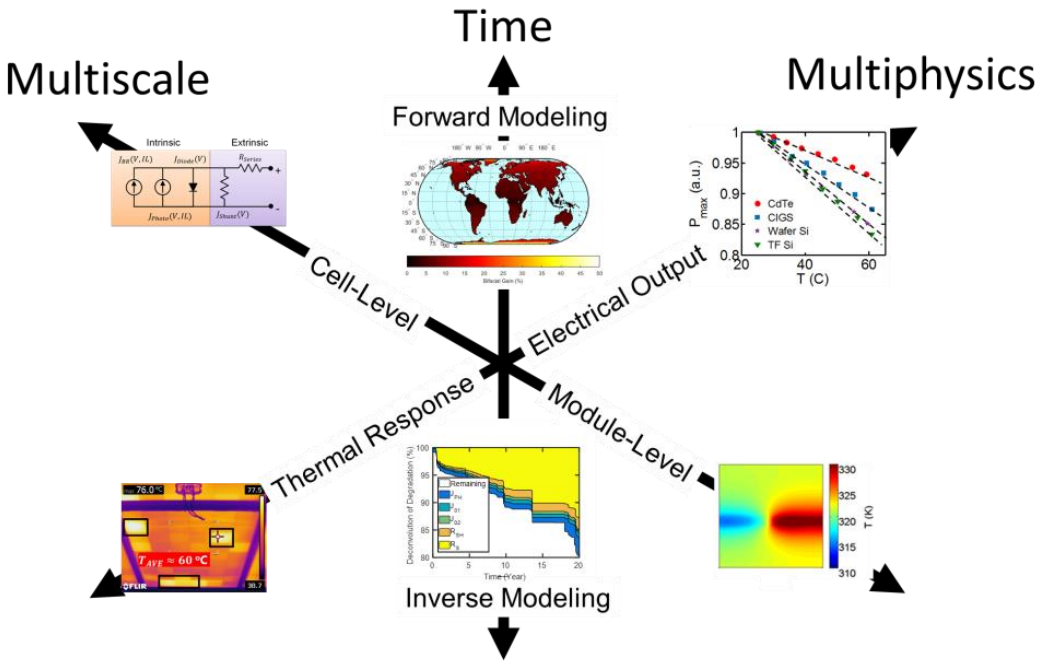

Fig. 1.3. Our approach to studying and enhancing the performance and reliability of solar modules in three domains: 1) connecting individual cell characteristics to module performance (**multiscale**), 2) forward and inverse modeling of electricity yields (**time**), 3) exploring thermal behavior for improving electrical output for photovoltaics (**multiphysics**).

First, we create a **multiscale** simulation framework that is capable of bridging cell-level and module-level characteristics. The framework enables module-level optimization to close the cell-to-module efficiency gap and the study on PV reliability, e.g., partial shading degradation. In this context, our main contribution is to develop a suite of physics-based models (i.e., equivalent circuits) that 1) can describe the

salient features of solar cells as a function of illumination and temperature, and 2) is compatible with circuit simulator so that a network composed of thousands of these equivalent circuits can be used to simulate a solar module.

Second, we investigate the thermal properties (**multiphysics**) of photovoltaics for a variety of technologies to deepen our understanding of PV self-heating as well as its impact on the short- and long-term performance of solar modules and ultimately develop corresponding self-cooling techniques. Specifically, we explore the origins of the intrinsic and extrinsic self-heating observed in solar modules and propose optics-based cooling strategies to reduce the operating temperature spectrally.

Third, we develop a framework to perform forward/inverse modeling of PV systems in the **time** domain. Forward (predictive) modeling of energy yield is critical to scrutinizing the "bankability" of solar farms before installation. Geographical location strongly influences PV performance. Thus, such analysis entails inputting extensive local weather information (sun path, irradiance, temperature, etc.) to our sophisticated system-level simulator. Similarly, performance degradation of solar modules is dictated by local meteorological conditions (e.g., humidity accelerates metal corrosion). Therefore, in the inverse (characterization) direction, we have developed a physics-based algorithm that can monitor and diagnose localized degradation of solar modules by continuously quarrying the field data collected, while accounting for weather information. This algorithm can be applied to analyze solar modules across the globe and yield a comprehensive database of geographic-specific degradation. The resulting database can eventually facilitate the future reliability-aware design for photovoltaics.

The detailed outline of the thesis is below:

- In **chapter 2**, we develop two physics-based analytical models to describe the operation of both perovskite and CIGS solar cells, explicitly accounting non-uniform generation, voltage-dependent carrier collection, and light-enhanced reverse breakdown. The model would allow experimentalists to characterize key

parameters of existing cells, understand performance bottlenecks, and predict performance and reliability of solar modules made of these two materials.

- **In chapter 3**, we discuss the physical origins of self-heating effects in PV: 1) the intrinsic self-heating resulted from sub-bandgap absorption and imperfect thermal radiation and 2) the extrinsic self-heating caused by partial shading. To suppress self-heating, we optically redesign the module structure to reflect the sub-bandgap photons and enhance IR radiation to the surroundings. The self-cooling techniques herein have proven to delay PV module failure due to thermally activated degradation by up to ∼85%.

- **In chapter 4**, we present a global study on the performance and optimization of bifacial solar modules using a rigorous and comprehensive modeling framework. Specifically, our results demonstrate that with a low albedo of 0.25, the bifacial gain of ground-mounted bifacial modules is less than 10% worldwide. However, increasing the albedo to 0.5 and elevating modules 1 m above the ground can boost the bifacial gain to 30%. Moreover, we derive a set of empirical design rules, which optimize bifacial solar modules across the world and provide the groundwork for rapid assessment of the location-specific performance.

- **In chapter 5**, we develop a novel technique capable of continuously monitoring and diagnosing the ongoing degradation in PV systems — the Suns-Vmp method. This method offers a simple and powerful approach to studying time-dependent degradation of solar modules by physically mining the MPP data. We validate the proposed method by analyzing a test facility at the National Renewable Energy Laboratory (NREL).

- **In chapter 6**, we summarize the thesis and discuss a few research directions worth exploring in the future.

1.7 List of Associated Publications

Chapter 2:

- **X. Sun**, R. Asadpour, W. Nie, A. D. Mohite, and M. A. Alam, A Physics-Based Analytical Model for Perovskite Solar Cells, *IEEE J. Photovoltaics*, vol. 5, no. 5, pp. 13891394, Sep. 2015.
- **X. Sun**, T. Silverman, R. Garris, C. Deline, and M. A. Alam, An Illumination- and Temperature-Dependent Analytical Model for Copper Indium Gallium Diselenide (CIGS) Solar Cells, *IEEE J. Photovoltaics*, vol. 1, pp. 110, 2016.
- H. Chung, **X. Sun**, and P. Bermel, Optical approaches to improving perovskite/Si tandem cells, *MRS Adv.*, vol. 1, no. 14, pp. 901910, Jan. 2016.
- H. Chung, **X. Sun**, A. D. Mohite, R. Singh, L. Kumar, M. A. Alam, and P. Bermel, Modeling and designing multilayer 2D perovskite / silicon bifacial tandem photovoltaics for high efficiencies and long-term stability, *Opt. Express*, vol. 25, no. 8, p. A311, Apr. 2017.
- M. A. Alam*, P. Dak*, M. A. Wahab*, and **X. Sun***, Physics-based compact models for insulated-gate field-effect biosensors, landau-transistors, and thin-film solar cells, in *2015 IEEE Custom Integrated Circuits Conference (CICC)*, 2015, pp. 18 (Invited, *Equal Contribution).
- K. A. W. Horowitz, R. Fu, **X. Sun**, T. Silverman, M. Woodhouse, and M. A. Alam, Estimating the Effects of Module Area on Thin-Film Photovoltaic System, in *2017 IEEE 44th Photovoltaic Specialist Conference (PVSC)*, 2017.

Chapter 3:

- **X. Sun**, J. Raguse, R. Garris, C. Deline, T. Silverman, and M. A. Alam, A physics-based compact model for CIGS and CdTe solar cells: From voltage-dependent carrier collection to light-enhanced reverse breakdown, in *2015 IEEE 42nd Photovoltaic Specialist Conference (PVSC)*, 2015, pp. 16.

- T. J. Silverman, M. G. Deceglie, **X. Sun**, R. L. Garris, M. A. Alam, C. Deline, and S. Kurtz, Thermal and Electrical Effects of Partial Shade in Monolithic Thin-Film Photovoltaic Modules, *IEEE J. Photovoltaics*, vol. 5, no. 6, pp. 17421747, Nov. 2015 (Invited).

- Z. Zhou*, **X. Sun***, and P. Bermel, Radiative cooling for thermophotovoltaic systems, *in Infrared Remote Sensing and Instrumentation XXIV*, 2016. (Invited, *Equal Contribution)

- **X. Sun**, R. Dubey, S. Chattopadhyay, M. R. Khan, R. V. Chavali, T. J. Silverman, A. Kottantharayil, J. Vasi, and M. A. Alam, A novel approach to thermal design of solar modules: Selective-spectral and radiative cooling, in *2016 IEEE 43rd Photovoltaic Specialists Conference (PVSC)*, 2016, pp. 35843586.

- **X. Sun**, T. J. Silverman, Z. Zhou, M. R. Khan, P. Bermel, and M. A. Alam, Optics-Based Approach to Thermal Management of Photovoltaics: Selective-Spectral and Radiative Cooling, *IEEE J. Photovoltaics*, vol. 7, no. 2, pp. 566574, Mar. 2017.

- **X. Sun**, Y. Sun, Z. Zhou, M. A. Alam, and P. Bermel, Radiative sky cooling: fundamental physics, materials, structures, and applications, *Nanophotonics*, vol. 6, no. 5, Jan. 2017.

- Z. Zhou, Y. Sun, **X. Sun**, M. A. Alam, P. Bermel, and X. Jin, Radiative cooling for concentrating photovoltaic systems, *in Thermal Radiation Management for Energy Applications*, 2017.

Chapter 4:

- M. R. Khan*, A. Hanna*, **X. Sun***, and M. A. Alam*, Vertical bifacial solar farms: Physics, design, and global optimization, *Appl. Energy*, vol. 206, pp. 240248, Nov. 2017. (*Equal Contribution)

- **X. Sun**, M. R. Khan, A. Hanna, M. M. Hussain, and M. A. Alam, The Potential of Bifacial Photovoltaics: A Global Perspective, in 2017 IEEE 44th Photovoltaic Specialist Conference (PVSC), 2017.

- **X. Sun**, M. R. Khan, C. Deline, and M. A. Alam, Optimization and Performance of Bifacial Solar Modules: A Global Perspective, *Appl. Energy*, 2018 (Accepted).

Chapter 5:

- **X. Sun**, H. Chung, R. V. Chavali, P. Bermel, and M. A. Alam, Real-time Monitoring of Photovoltaic Reliability Only Using Maximum Power Point the Suns-Vmp Method, *in IEEE 44th Photovoltaic Specialist Conference (PVSC)*, 2017.

- D. C. Jordan, C. Deline, S. Johnston, S. R. Rummel, B. Sekulic, P. Hacke, S. R. Kurtz, K. O. Davis, E. J. Schneller, **X. Sun**, M. A. Alam, and R. A. Sinton, Silicon Heterojunction System Field Performance, *IEEE J. Photovoltaics*, pp. 16, 2017.

- **X. Sun**, R. V. K. Chavali, and M. A. Alam, In-Situ Self-Monitoring of Real-Time Photovoltaic Degradation Only Using Maximum Power Point the Sun-Vmp Method, P*rog. Photovoltaics Res. Appl.*, 2018 (Under Review).

Other publications during my Ph.D. program (not included in the thesis):

- **X. Sun**, C. J. Hages, N. J. Carter, J. E. Moore, R. Agrawal, and M. Lundstrom, Characterization of nanocrystal-ink based CZTSSe and CIGSSe solar cells using voltage-dependent admittance spectroscopy, *in 2014 IEEE 40th Photovoltaic Specialist Conference (PVSC)*, 2014, vol. 2, pp. 24162418.

- M. Lundstrom, S. Datta, and **X. Sun**, Emission-Diffusion Theory of the MOSFET, *IEEE Trans. Electron Device*s, vol. 62, no. 12, pp. 41744178, Dec. 2015.

- Y. Sun, **X. Sun**, S. Johnston, C. M. Sutter-Fella, M. Hettick, A. Javey, and P. Bermel, Voc degradation in TF-VLS grown InP solar cells, *in 2016 IEEE 43rd Photovoltaic Specialists Conference (PVSC)*, 2016, pp. 19341937.

- E. Gener, C. Miskin, **X. Sun**, M. R. Khan, P. Bermel, M. A. Alam, and R. Agrawal, Directing solar photons to sustainably meet food, energy, and water needs, Sci. Rep., vol. 7, no. 1, p. 3133, Dec. 2017.

2. PHYSICS-BASED ANALYTICAL MODEL FOR CELL-TO-MODULE MODELING

2.1 Introduction

A cell-to-module modeling framework is crucial to study and optimize the performance and reliability of solar modules [38, 50, 132], which strongly depend on environmental factors (e.g., temperature, irradiance). Therefore, to establish such a framework, analytical models that can describe the temperature- and illumination-dependent IV characteristics are indispensable. However, existing models [40, 133] developed for silicon solar cells fail to accurately model thin film technologies - where the superposition principle does not hold (i.e., the light current equals the sum of the dark current and a constant photocurrent). More importantly, these models use empirical formulations to simulate the temperature- and illumination-dependencies of IV and may not adequately reflect the actual illumination- and temperature- dependencies of cell performance (e.g., light-enhanced breakdown in CIGS [134]). Undoubtedly, physics-based analytical models that can veraciously describe the IV characteristics under different temperatures and illuminations based on physically defined parameters can be very valuable.

Hence, in this chapter [1], we will present two physics-based analytical models developed for two PV technologies at different development stages – 1) the emerging perovskite solar cells [18] and 2) the commercially available copper indium gallium selenide (CIGS) solar cells. This chapter is organized as follows: In Sec. 2.2, we will first discuss the derivation and physics of the analytical model for perovksite solar cells and validate the accuracy thereof by experimental measurements of four

[1]The contents of this chapter are taken from [135] ©2015 IEEE, [136] ©2015 IEEE, [137] ©2016 IEEE

differently configured cells. Next, we will demonstrate the analysis and optimization of cell efficiencies enabled by our analytical model. The results here can shed some light on the potential future improvement of perovksite solar cells, a promising future PV technology. Section 2.3 presents the model for CIGS solar cells, and is divided into two parts — 1) the forward IV with voltage-dependent photocurrent and 2) the light-enhanced reverse breakdown. For both parts, we will discuss the underlying physics and mathematical derivation of the model and systematically validate the model against measurements. Compared to other models that only simulate IV at the standard test condition (IL = 1000 W/m^2 and T = 25 °C), this model explicitly accounts for the temperature and illumination dependencies in the physical parameters; hence, the model is ready to be integrated into an opto-electro-thermal framework that can project energy production ($(P_{Module}(IL, T, t))$) under varying illumination and temperature as well as simulate the degree and spatial distribution the shadow-induced self-heating in CIGS solar cell self-consistently, as discussed in Chapter 3.

2.2 Perovskite Solar Cell

2.2.1 Model Development and Validation

Cell Configuration. A typical cell consists of a perovskite absorber layer (∼300 to 500 nm), a hole transport layer (p-type), an electron transport layer (n-type), and front and back contacts, arranged in various configurations. The traditional structure in Fig. 2.1 (a, b) has PEDOT: PSS and PCBM as the front hole transport layer and the back electron transport layer, respectively; in the inverted structure, however, TiO_2 is the front electron transport layer and Spiro-OMeTAD is the back hole transport layer, as in Fig. 2.1 (c, d). Moreover, for both the traditional and inverted configurations, it has been argued that the absorber layer in high-efficiency cells is essentially intrinsic [138], see Fig. 2.1 (a,c); the mode of operation changes and the efficiency is reduced for cells with significant p-type self-doping [139], see Fig. 2.1

(b,d). Therefore, perovskite solar cells can be grouped into (Type-1) p-i-n, (Type-2) p-p-n, (Type-3) n-i-p, (Type-4) n-p-p cells; the corresponding energy band diagrams are shown in Fig. 2.1.

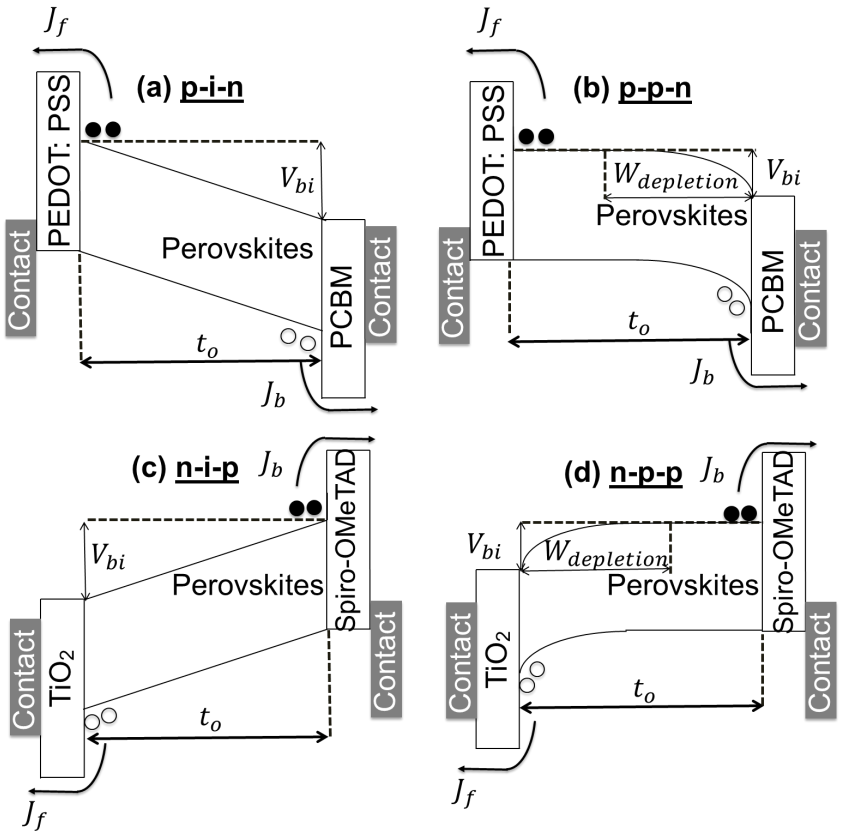

Fig. 2.1. The energy diagram of perovskite solar cells in traditional structure (PEDOT: PSS/ Perovskite/PCBM): (a) Type-1 (p-i-n) and (b) Type-2 (p-p-n) and titania-based inverted cells (TiO_2/Perovskite/Spiro-OMeTAD): (c) Type-3 (n-i-p) and (d) Type-4 (n-p-p).

Continuity Equations. It has been suggested that the high dielectric constant of perovskites allows the photogenerated excitons to dissociate immediately into free carriers [140, 141]. The photo-generated electron and holes then drift and diffuse through the absorber and transport layers before being collected by the contacts. Consequently, an analytical model can be developed by solving the steady state electron and hole continuity equations within the absorber, namely,

$$D\frac{\partial^2 n(x)}{\partial^2 x} + \mu E(x)\frac{\partial n(x)}{\partial x} + G(x) - R(x) = 0, \tag{2.1}$$

$$D\frac{\partial^2 p(x)}{\partial^2 x} - \mu E(x)\frac{\partial p(x)}{\partial x} + G(x) - R(x) = 0. \tag{2.2}$$

Here, $n(p)$ is the electron/hole concentration; D and μ are the diffusion coefficient and mobility, respectively; and $G(x)$ represents the position-dependent photo-generation. The extraordinarily long diffusion length in perovskite [142–144] ensures that one can ignore carrier recombination within the absorber layer, i.e., $R(x) = 0$. Finally, $E(x)$ is the position-resolved electric field within the absorber layer.

Position-resolved electrical field. As shown in Fig. 2.1, $E(x)$ is a constant (linear potential profile) for type-1 (n-i-p) and type-3 (p-i-n) cells, i.e., the absence of doping or trapped charges ensure that $E(x) = (V_{bi} - V)/t_0$, where V_{bi} is the build-in potential and t_0 is the thickness of the intrinsic layer. For type-2 (p-p-n) and type -4 (n-p-p) devices, however, numerical simulation shows that the field essentially linear within the depletion region, i.e., $E(x) = (1 - x/W_d)E_{max}(V)$, where W_d is the depletion width and $|E_{\max}(V)| = 2(V_{bi} - V)/W_d(V)$; $E(x) = 0$ in the neutral region defined by $x > W_d$. The position-dependent $E(x)$ is reflected in the parabolic potential profiles shown in Fig. 2.1 (b) and (d). Our extensive numerical simulation [138] shows that the photogenerated carriers do not perturb the electric field significantly, therefore, the following analysis will presume $E(x)$ is independent of photogeneration at 1-sun illumination.

Position-resolved generation profile. Neglecting any parasitic reflectance from the back surface, we approximate the generated profile in the absorber layer as $G(x) = G_{eff}e^{-x/\lambda_{ave}}$, where G_{eff} and λ_{ave} (∼100 nm) are the material specific constants, averaged over the solar spectrum. Note that the maximum absorption is $G_{max} = \int_0^\infty G_{eff}e^{-x/\lambda_{ave}}dx = G_{eff}\lambda_{ave}$.

Boundary conditions. Finally, electron and hole transport layers are considered perfect conductors for the majority carriers; while they act as imperfect blocking layers for the minority carriers, characterized by the effective surface recombination

velocity $J_{f(b)} = qs_{f(b)}\Delta n(p)$. The $\Delta n(p)$ is the excess minority carrier concentration, and the $s_{f(b)}$ is the effective surface recombination velocity at the front (back) transport layer, accounting for three recombination processes: 1) carrier escaping from the wrong contact; 2) recombination due to the interface defects; 3) recombination within the bulk of the transport layer.

Table 2.1.

Model parameters of Eqs. 2.3 - 2.5 expressed in terms of the physical parameters of the cell. Here, ($V' \equiv q(V - V_{bi})/kT$; $\beta_{f(b)} \equiv D/(t_0 \times s_{f(b)})$); $m \equiv t_0/\lambda_{ave}$; $n \equiv W_d(0\,\mathrm{V})/t_0$; $\Delta \equiv 1 - n\sqrt{(V_{bi} - V)/V_{bi}}$). The physical meaning of the parameters has been discussed in the text.

Variables	**p-i-n / n-i-p**	**p-p-n**	**n-p-p**
$1/\alpha_f$	$\frac{e^{V'}-1}{V'} + \beta_f$	$\Delta + \beta_f\ (V \le V_{bi})$	$\Delta \times e^{V'} + \beta_f (V \le V_{bi})$
		$\frac{e^{V'}-1}{V'} + \beta_f\ (V > V_{bi})$	
$1/\alpha_b$	$\frac{e^{V'}-1}{V'} + \beta_b$	$\Delta \times e^{V'} + \beta_b (V \le V_{bi})$	$\Delta + \beta_b\ (V \le V_{bi})$
		$\frac{e^{V'}-1}{V'} + \beta_b\ (V > V_{bi})$	
A	$\alpha_f \times (\frac{1-e^{V'-m}}{V'-m} - \beta_f)$	$\alpha_f \times (\frac{1}{m}(e^{-m\times\Delta} - 1) - \beta_f)\ (V \le V_{bi})$	$\alpha_f \times (\frac{e^{V'}}{m}(e^{-m} - e^{m\times(\Delta-1)}) - \beta_f)(V \le V_{bi})$
		$\alpha_f \times (\frac{1-e^{V'-m}}{V'-m} - \beta_f)\ (V > V_{bi})$	
B	$\alpha_b \times (\frac{1-e^{V'+m}}{V'+m} - \beta_b)$	$\alpha_b \times (\frac{1}{m}(e^{-m\times(\Delta-1)} - e^{-m}) - \beta_b)\ (V \le V_{bi})$	$\alpha_b \times (\frac{1}{m}(1 - e^{m\times\Delta}) - \beta_b)\ (V \le V_{bi})$
		$\alpha_b \times (\frac{1-e^{V'+m}}{V'+m} - \beta_b)\ (V > V_{bi})$	

Analytical solutions. Remarkably, Eqns. 2.1 and 2.2 can be solved analytically to derive the complete current-voltage characteristics of the four types of perovskite cells, as follows

$$J_{dark} = (\alpha_f \times J_{f0} + \alpha_b \times J_{b0})(e^{\frac{qV}{kT}} - 1), \tag{2.3}$$

$$J_{photo} = qG_{max}(A - Be^{-m}), \tag{2.4}$$

$$J_{light} = J_{dark} + J_{photo}. \tag{2.5}$$

The parameters of the model, namely, $\alpha_{f(b)}$, $\beta_{f(b)}$, $A(B)$, m, n, and Δ are functions of the following physical parameters of the cell (see Table 2.1): t_0 is the thickness of the absorber layer; $J_{f0(b0)}$ is the dark diode current recombining at the front/back transport layer; V_{bi} is the built in potential across the absorber layer; D is the diffusion coefficient; $s_{f(b)}$ is the effective surface recombination velocity at the front/back interface; $W_d(0\,\mathrm{V})$ is the equilibrium depletion width for self-doped devices; and G_{max} is the maximum absorption. The detailed derivation of the model is summarized in Appendix A.

Parameter estimation. Among these parameters, G_{max} is obtained by integrating the position-dependent photon absorption calculated by the transfer matrix method (here $qG_{\max} = 23\,\mathrm{mA/cm^2}$) [145]; $D \approx 0.05\,\mathrm{cm^2 s^{-1}}$ is known for the material system for both electron and hole [143]; V_{bi} can be estimated either by using the capacitance-voltage characteristics [139] or by using the crossover voltage of the dark and light IV [42]. The effective surface recombination velocities can be fitted using the photogenerated current $J_{photo} = J_{light} - J_{dark}$ [146]. Finally, we can obtain the dark diode current $J_{f0(b0)}$ by fitting the dark current.

Experimental validation. In order to validate the model, we fit both dark and light IV characteristics for four different perovskite cells using the model as shown in Fig. 2.2. See Appendix A for the details of the fitting algorithm. Samples #1 (15.7%) and #2 (11.1%) are solution-based PCBM based architecture (Type-1 and Type-2) [138], whereas samples #3 (15.4%) and #4 (8.6%) are titania-based inverted architecture (Type-3 and Type-4) fabricated by vapor deposition and solution process, respectively [147]. The fitting parameters obtained for the four samples are summarized in Table II. Remarkably, the analytical model not only reproduces the key features of the I-V characteristics of very different cell geometries, but also captures

very well the known physical parameters of the cell (e.g. thickness of the absorber). Indeed, the error in the power output due to imperfect fitting is less than 0.1% (absolute) for samples 1-3, and ∼0.5% (absolute) for sample #4.

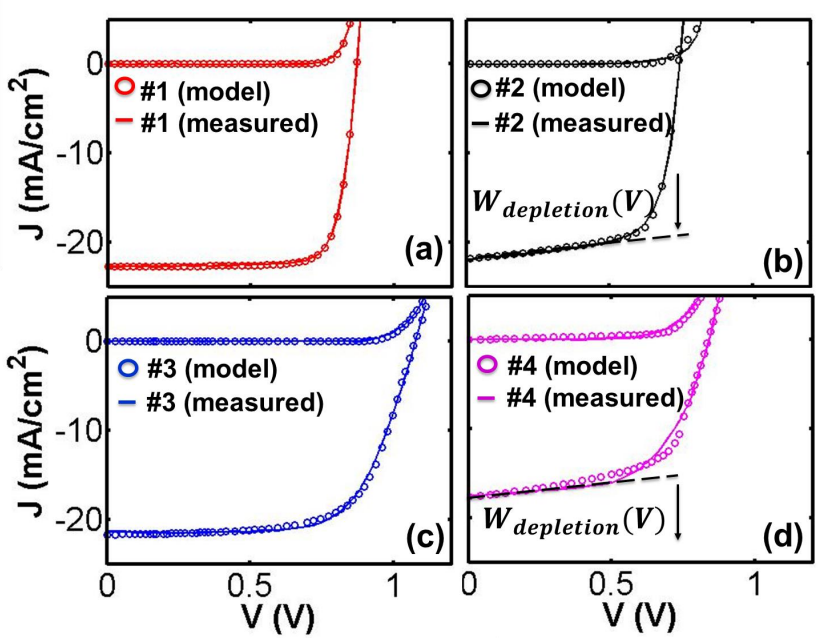

Fig. 2.2. (a) Samples #1 (Type-1 (p-i-n), Efficiency = 15.7%, J_{SC} = 22.7 mA/cm2, V_{OC} = 0.85 V, FF = 81%). (b) Samples #2 (Type-2 (p-p-n), Efficiency = 11.1%, J_{SC} = 21.9 mA/cm2, V_{OC} = 0.75 V, FF = 64%). (c) Samples #3 (Type-3 (n-i-p), Efficiency = 15.4%, J_{SC} = 21.5 mA/cm2, V_{OC} = 1.07 V, FF = 67%). (d) Samples #4 (Type-4 (n-p-p), Efficiency = 8.6%, J_{SC} = 17.6 mA/cm2, V_{OC} = 0.84 V, FF = 58%). Note that i) $qG_{\max} = 23\,\mathrm{mA/cm^2}$ is used. ii) Negligible parasitic resistors (R_{series} and R_{shunt}) except in sample #4.

2.2.2 Efficiency Analysis and Optimization

Limiting factor (self-doped perovksite) Fig. 2.2 (b,d) shows that the light IV of the self-doped devices has a steep decrease (∼0 V to 0.5 V) in photocurrent much before the maximum power point (MPP). Indeed, this characteristic feature can be correlated to self-doping effects arising from the defects or impurities introduced

during the manufacture of the cell. Our model interprets this linear decrease in photocurrent of type-2 and type-4 cells to the well-known voltage-dependent reduction of W_d (V) (also the charge collection region) of a PN junction. Without a physics-based model, this feature can be easily mistaken as a parasitic resistance. The self-doped devices also have an inferior V_{bi} and greater $J_{f0(b0)}$ that leads to a lower V_{OC}, compared to the intrinsic cells with the same configuration, see Table 2.2. Hence, the main factor that limits the performance of samples #2 and #4 is the reduction of charge collection efficiency due to self-doping effect.

Table 2.2.

Extracted physical parameters of samples #1 (Fig 2.2 (a)), #2 (Fig 2.2 (b)), #3 (Fig 2.2 (c)), and #4 (Fig 2.2 (d)).

Sample	**#1**	**#2**	**#3**	**#4**
Type	p-i-n	p-p-n	n-i-p	n-p-p
t_0 (nm)	450	400	310	147
J_{f0} (mA/cm^2)	2.7×10^{-12}	4.0×10^{-12}	1.6×10^{-17}	6×10^{-15}
J_{b0} (mA/cm^2)	4.0×10^{-12}	5.0×10^{-12}	4.8×10^{-17}	4.1×10^{-15}
V_{bi} (V)	0.78	0.67	1	0.75
s_f (cm/s)	2.0×10^2	5.0×10^2	1.0×10^4	13.1
s_b (cm/s)	19.2	8.6×10^2	5.4	∞
W_d(0 V) (nm)	/	300	/	146

Limiting factor (intrinsic perovksite). While examining the intrinsic samples #1 and #3, we note that #1 has the highest fill-factor (FF), but its V_{OC} is 0.3 V smaller than that of #3. The reduction in V_{OC} can be explained by lower V_{bi} and higher $J_{f0(b0)}$ caused by the combination of band misalignment and lower doping con-

centration in the transport layers of the perovskite cells with the traditional structure, which is the major performance limitation of #1. Sample #3, on the other hand, has the lower fill-factor, arising from relatively high effective surface recombination velocities at both contacts, indicating insufficient blocking of charge loss to the wrong contact. Even though #1 and #3 have similar efficiencies, our model demonstrates that the fundamental performance limitations are completely different.

Physically defined parameters. Using the model, we can also extract the thicknesses of the four samples, which are in the expected range (∼350 nm 500 nm for #1 and #3, ∼ 330 nm for #2) [138,147]. Among the samples, there is also a strong correlation between the absorber thickness t_0 and J_{SC} , related to the completeness of the absorption. Moreover, we observe significant shunt resistance ($R_{shunt} = 1$ kΩ.cm^2) in sample #4, which agrees with the reports [147] that thin absorber might lead to shunting pinholes. Further, except for sample #4, all devices have relatively poor (high) s_{front}, which may be caused by insufficient barrier between PEDOT:PSS and perovskites [138] as well as poor carrier collection in TiO_2 [148–150].

Efficiency optimization. Once we extract the physical parameters associated with high-efficiency samples (#1 and #3) with essentially intrinsic absorbers, it is natural to ask if the efficiency can be improved further, and if so, what factors are most important. The physics-based compact model allows us to explore the phase-space of efficiency as a function of various parameters, as follows.

Impact of thickness. For example, while keeping all other parameters equal to the values extracted in Table 2.2, one can explore the importance of absorber thickness on cell efficiency, see Fig. 2.3. Our model shows that both samples are close to their optimal thickness, though there is incomplete absorption ($J_{SC} < qG_{max}$). Thinner absorber cannot absorb light completely, while thicker absorber suppresses charge collection and degrades the fill factor. This is because the competition between the surface recombination and the electric field determines the carrier collection efficiency near the interface, and electric field $E = (V_{bi} - V)/t_0$ decreases with the thickness.

To summarize, for the samples considered, thickness optimization would not improve performance.

Impact of surface recombination velocities. Similarly, we can investigate the effects of the front/back surface recombination velocities on device efficiencies, with all other parameters kept fixed to those in Table 2.2. The deduced surface recombination velocities for samples #1 and #3 are listed in Table 2.2 as well as labeled as black dots in Fig. 2.4. The results suggests that, in principle, improving the front surface recombination velocities by two orders of magnitude can boost the efficiency by ∼3% and even ∼5% for samples #1 and #3, respectively. Any potential improvement in the back selective blocking layer, however, offers very little gain, since most of the photo-generation occurs close to the front contact. Hence, engineering the front transport layer would be essential for further improvement of cell efficiencies.

Design toward thermodynamic limit. But even with the optimal surface recombination velocities, we are still not close to the thermodynamic limit (∼30%), see Fig. 2.4. Towards this goal, one must improve the J_{SC}, FF, and V_{OC} (thermodynamic limit: J_{SC} ∼26 mA/cm2, FF ∼90%, V_{OC} ∼1.3 V [24]). One may reduce the parasitic absorption loss in the transport layers, which can increase G_{max} in Eqn. 2.4, to improve the J_{SC}; one may still improve the FF by increasing the charge diffusion coefficient D, since it is mainly the variable $\beta_{f(b)} = D/(to \times s_{f(b)})$ that determines

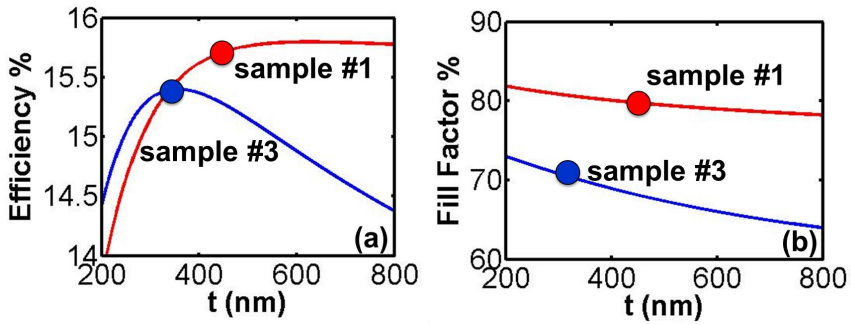

Fig. 2.3. (a) Efficiency vs. absorber thickness for samples #1 and #3. (b) Fill factor vs. absorber thickness for samples #1 and #3.

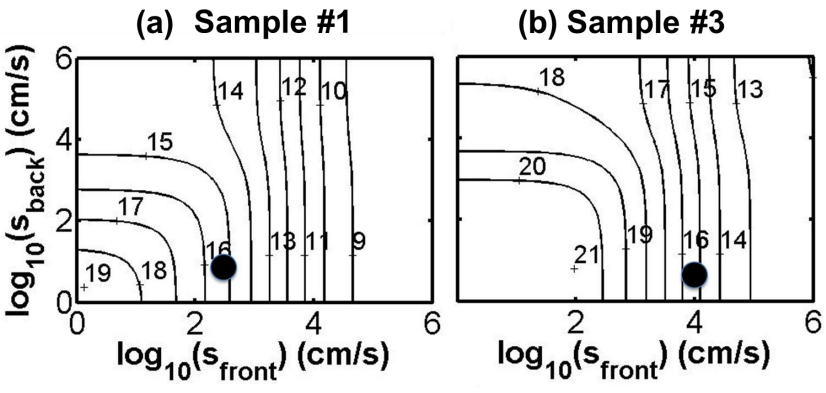

Fig. 2.4. (a) Contour plot of the front/back surface recombination velocities vs. efficiency for sample #1. (b) Contour plot of the front/back surface recombination velocities vs. efficiency for sample #3.

the FF; one may also increase the built-in potential V_{bi}, through adjusting the band alignment at the interface as well as increasing the doping of the transport layers, to improve the V_{OC}.

Hysteresis effect. Finally, it is also important to discuss the hysteresis effect observed in the J-V characteristics, which can be an important concern for the inverted structure shown in Fig. 2.1 (c, d)). The phenomenon arises primarily from by trapping/detrapping of defects within the oxide or at the oxide/perovskite interface [148, 149]. Reassuringly, recent results show that process-improvements, such as Li-treatment of TiO_2, can suppress/eliminate hysteresis, see [151]. Moreover, cells with the traditional structures (oxide-free, as in Fig. 2.1 (a, b)) show very little hysteresis [138, 152]. Given the fact that hysteresis effects will be eventually minimized once perovskites are mature enough for integration in modules, the compact model proposed in this section does not account for the effect of hysteresis explicitly.

2.3 Copper Indium Gallium Selenide (CIGS) Solar Cell

Next, we will discuss the physics-based model developed for CIGS solar cells, a commercially available technology. This section will start with the forward IV model then extend to the reverse breakdown regime. Our model is capable of capturing the salient temperature- and illumination- dependencies of IV characteristics, thereby it can be integrated into an opto-electro-thermal coupled framework to understand PV self-heating. The statistical distribution of shunt current is also included for simulating the variability that contributes the cell-to-module efficiency gap [132].

2.3.1 Forward IV — Voltage-Dependent Carrier Collection

The model describing the forward IV comprises of photocurrent (J_{Photo}), diode current (J_{Diode}), and parasitic components (R_{Series} and J_{Shunt}), see Fig. 2.5(c). We will discuss their physical interpretation and mathematical formulation sequentially as follows.

Photocurrent (J_{Photo})

Cell configuration. A typical CIGS cell consists of a ZnO window layer (∼200 nm), an ultrathin (∼50 nm) but large-bandgap CdS buffer layer, stacked on top of a thick (1 to 3 μm) CIGS absorber layer [153]; see Fig. 2.5(b). J_{Photo} can be obtained analytically by solving the position-dependent continuity equations *only for the photo-generated carriers* [154, 155], namely,

$$D\frac{\partial^2 n_{Gen}\left(p_{gen}\right)}{\partial x^2}+\mu E\left(x\right)\frac{\partial n_{Gen}\left(p_{Gen}\right)}{\partial x}+G\left(x\right)-R_{Gen}(x)=0, \tag{2.6}$$

$$J_{Photo,n(p)}=q\mu E\left(x\right)n_{Gen}\left(p_{Gen}\right)\pm qD\frac{\partial n_{Gen}\left(p_{Gen}\right)}{\partial x}. \tag{2.7}$$

Here, $n_{Gen}\left(p_{Gen}\right)$ is the generated electron (hole) concentration; D and μ are the diffusion coefficient and mobility, respectively; $G(x)$ represents the *position-resolved*

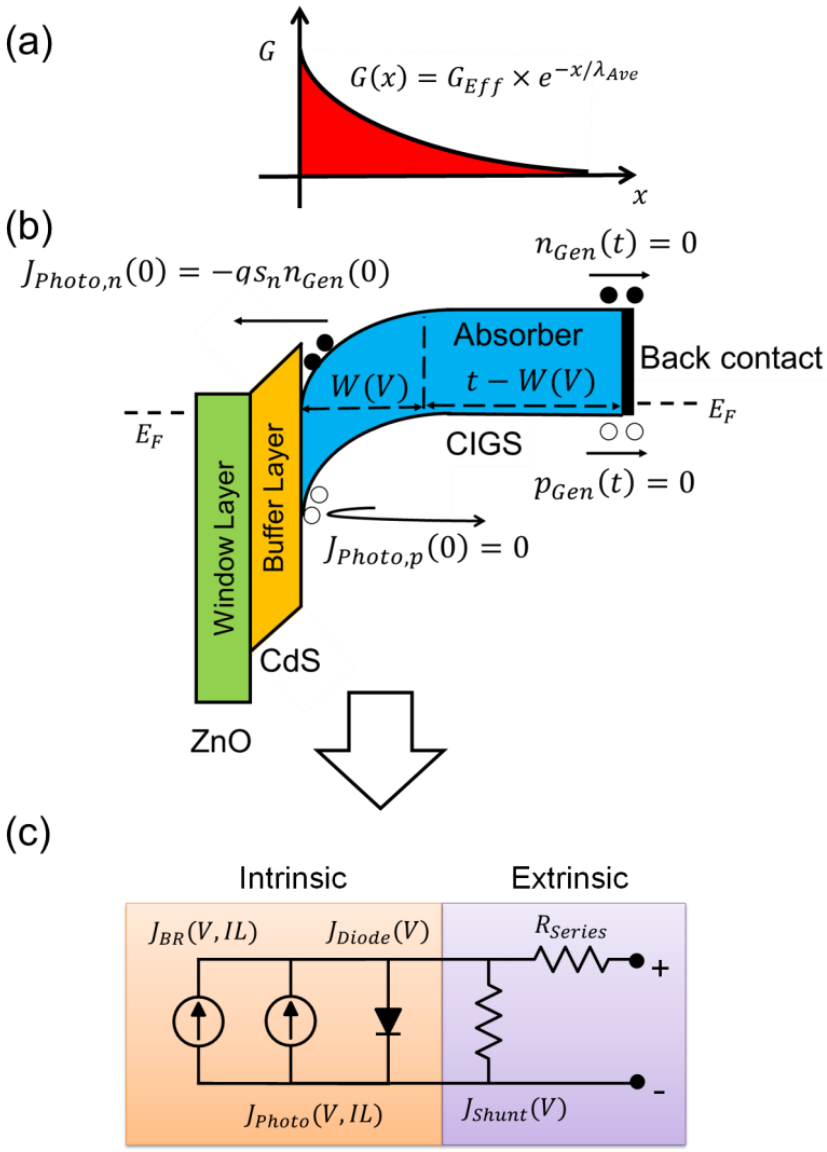

Fig. 2.5. (a) The exponential generation profile in the CIGS absorber layer. (b) The energy band diagram of a typical CIGS cell. The boundary conditions labeled here are only for the generated carriers. (c) The equivalent circuit diagram for CIGS solar cells. The parameters and analytical equations for each element are summarized in Tables 2.4 and 2.5.

generation, as in Fig. 2.5(a); and $R_{Gen}(x)$ is the bulk (radiative, Auger, Shockley-Read-Hall) recombination of the photo-generated carriers before they are collected by

the contacts. Note that $R_{Gen}(x)$ is the difference of bulk recombination rates under light and dark conditions ($R_{Gen}(x) = R_{Light}(x) - R_{Dark}(x)$). Finally, $E(x)$ is the position-dependent electric field within the absorber layer.

Key model assumptions. Equations 2.6 and 2.7 are coupled nonlinear equations, amenable only to numerical solutions, as with ADEPT [156] or Sentaurus [157]. *However, with two simplifications related to $G(x)/R_{gen}(x)$ and the field-dependent carrier collection, we can solve the equation analytically, as follows.*

Approximation 1: Recombination-corrected generation. Neglecting parasitic generation in the window and buffer layers and reflectance from the back metal contact, Beer's law allows us to approximate the generated profile in the absorber layer as $G(x) = G_{Eff}e^{-x/\lambda_{Ave}}$, where G_{Eff} and λ_{Ave} are the material specific constants, averaged over the solar spectrum. Therefore, the total photocurrent in the absence of bulk recombination is $J_{Tot-Photo} = q\int_0^\infty G_{Eff}e^{-x/\lambda_{Ave}}dx = qG_{Eff}\lambda_{Ave}$. The recombination term, $R_{Gen}(x)$, is determined by $n_{Gen}(x)$ and p_{Gen}(x) as well as the carrier lifetime. Using self-consistent optoelectronic numerical simulation, we find that the generation-induced bulk recombination current ($J_{Gen-Rec} = \int_o^t R_{Gen}(x)dx$) is *voltage-independent and remains a small fraction of the total photocurrent up to open-circuit voltage (V_{OC})*, see Fig. A.9(a). This is because, for $V < V_{OC}$, R_{Gen} occurs primarily in the quasi-neutral bulk region, where the bulk recombination is voltage-independent; see Fig. A.8. In addition, *$J_{Gen-Rec}$ scales linearly with $J_{Tot-Photo}$ under different illumination intensities* ($J_{Gen-Rec} = a \times J_{Tot-Photo}$, $a \approx 5\%$) as shown in Fig. A4(b). Therefore, we can account for $R_{Gen}(x)$ in Eqn. 2.6 by normalizing the generation profile to $G'(x) = G_{Eff}{}'e^{-x/\lambda_{Ave}}$ so that the short-circuit current,$J_{SC} = J_{Tot-Photo} - J_{Gen-Rec} = qG'_{Eff}\lambda_{Ave}$. Consequently, Eqn. 2.6 can be rewritten as

$$D\frac{\partial^2 n_{Gen}(p_{Gen})}{\partial x^2} + \mu E(x)\frac{\partial n_{Gen}(p_{Gen})}{\partial x} + G'(x) = 0. \tag{2.8}$$

Approximation 2: Linearity of the electric field We can further simplify Eqn. 2.8 by carefully analyzing the electric field, $E(x)$, from numerical simulation.

Specifically, numerical simulation shows that within the p-type absorber, $E\,(x)$ is linear inside the depletion region (x$\leq W$), *i.e.*, $E\,(x) = [1 - x/W(V)]\ E_{Max}\,(V)$, but vanishes beyond it (x $> W(V)$). Here, W is the depletion width and $|E_{Max}(V)| = 2\beta\,(V_{Bi} - V)\,/W(V)$; V_{Bi} and V are respectively the total built-in potential and the bias voltage across both n and p sides of the junction. Since we only consider $E(x)$ within the p-type absorber, a parameter β is introduced to account for the voltage partition between absorber and window layers, exactly analogous to voltage partition between channel and the oxide in a metal oxide semiconductor (MOS) capacitor [158]. Specifically, with applied voltage V for the entire device, a $\beta \times V$ drops across the absorber layer, while $(1-\beta) \times V$ drops across the window and buffer layers. Our detailed numerical simulation shows that photo-generation up to one-sun illumination does not significantly perturb the electric field; therefore, $E(x)$ in Eqn. 2.8 is assumed to be independent of illumination intensity.

Boundary conditions. Finally, one needs to set the boundary conditions to solve Eqns. 2.7 and 2.8. *For electrons*, the photocurrent at the interface between the buffer and absorber layers (see Fig. 2.5(b)) is given by $J_{Photo,n} = -q \times \mathrm{s}_n \times n_{Gen}$, where $\mathrm{s}_n = v_R e^{-\Delta E_C/kT}$ defines the interface thermionic-emission velocity and ΔE_C is the conduction band offset and v_R is the Richardson velocity [155]; large ΔE_C reduces the thermionic velocity; the reduced carrier-collection efficiency distorts the I-V characteristics [159]. *For holes*, the valence band offset ΔE_V at the buffer/absorber interface is presumed to be large enough so that $J_p = 0$; see Fig. 2.5(b). The back contact at $x = t$ is treated as an ideal ohmic contact (negligible Schottky barrier) for both electrons and holes, so that $n_{Gen} = p_{Gen} = 0$, as shown in Fig. 2.5(b). The assumption of a Schottky-barrier-free back contact is supported by experimental observations [160–162]. If needed, a back-to-back diode circuit can be added to this model to account for the Schottky barrier [163].

Analytical solution. Integrating $G'\,(x)$, $E\,(x)$, two aforementioned assumptions, and the flux boundary conditions into Eqns. 2.7 and 2.8, we obtain the solution of the photocurrent as

$$J_{Photo} = J_{SC} \times f_{Opt} \times f_{Coll}, \tag{2.9}$$

$$f_{Opt} \equiv 1 - \frac{\lambda_{Ave}}{W(V)}\left(\exp\left(-\frac{t - W(V)}{\lambda_{Ave}}\right) - \exp\left(-\frac{t}{\lambda_{Ave}}\right)\right), \tag{2.10}$$

$$f_{Coll} \equiv \left(1 + \frac{v_{Diff}}{s_n \times \exp\left(\frac{q\beta(V_{Bi}-V)}{kT}\right)}\right)^{-1}. \tag{2.11}$$

The parameters in Eqns. 2.9 to 2.11 are physical and can be calibrated using independent measurements. For example, t is the thickness of the CIGS layer, and $W(V)$ and V_{Bi} can be estimated from the Mott-Schottky analysis of capacitance-voltage (C-V) measurements.

Equation interpretation. Notwithstanding their apparent complexity, Eqns. 2.9 to 2.11 can be explained in simple terms. For example, Eqn. 2.10 determines the total optical absorption in the solar cell. So if the cell thickness t is on the order of λ_{Ave} $(t \approx \lambda_{Ave})$, then $f_{Opt} < 1$, indicating incomplete absorption of photons. The formulation of Eqn. 2.10 also ensures that the optical efficiency, f_{Opt}, is bounded between 0 and 1 for any combination of λ_{Ave}, $W(V)$, and t $(> W(V))$. Similarly, Eqn. 2.11 governs the efficiency of carrier collection f_{Coll}. In Eqn. 2.11 , $v_{Diff} \equiv \frac{D}{t - W_{Delp}(V)}$ is the diffusion velocity in the quasi-neutral region and $s_n \equiv v_R e^{-\Delta E_C/kT}$ is the interface thermionic-emission velocity for electrons at the heterojunction. Hence, Eqn. 2.11 balances two competing transport processes of the photogenerated electrons: 1) field-assisted drift toward the heterojunction interface followed by thermionic emission to the front contact, and 2) back-diffusion through the quasi-neutral region followed by recombination at the "wrong" (back) contact. Increasing forward-bias V reduces the depletion field, resulting in the increasing fraction of electrons diffusing to the back contact and recombining there instead of contributing to photocurrent; correspondingly, the collection efficiency, f_{Coll}, decreases. Recall that the carrier loss due to bulk recombination is explicitly accounted for in the normalized generation profile in Eqn. 2.8, which assumes $t \gg W(V)$.

Model simplification. For practical CIGS cells [153], $t \gg \lambda_{Ave}$, $t \gg W(V)$, and $\eta_{Opt} \rightarrow 1$. With these approximations, the photocurrent simplifies to

$$J_{Photo} \simeq J_{SC} \frac{1}{1+\alpha_C \times \exp(\frac{q\beta(V_{Bi}-V)}{kT})}. \tag{2.12}$$

Here, $\alpha_C \approx \frac{D}{t \times s_n} \equiv \frac{v_{Diff}}{s_n}$, which is the ratio between diffusion velocity and thermionic-emission velocity. Equation 2.12 implies that, for high-quality CIGS cells, the hetero-junction (accounted in α_C) is the main cause for voltage-dependent carrier collection, which is in agreement with [42, 164]. Equation 2.12 is a simplified version of Eqns. 2.9 to 2.11 preferred for use in large-scale module simulation for numerical speed and robustness.

Comparison to previous models. It is interesting to compare Eqn. 2.12 to previously published equations (Eqn. 2 in [45] and Eqn. 3 in [165]), *i.e.*, $J_{Photo} \simeq J_{SC}(1 - \frac{\exp(-W_{Delp}(V)/\lambda_{Ave})}{L_{Diff}/\lambda_{Ave}+1})$, where L_{Diff} is the carrier diffusion length. The equation implies that if $L_{Diff} \rightarrow \infty$ (no bulk recombination), then J_{Photo} equals J_{SC}, independent of bias voltage. The detailed simulation in [42], however, shows that even in the absence of bulk recombination, J_{Photo} in heterojunction devices should be zero at V=V_{Bi} due to carrier partition, consistent with Eqn. 2.12 ($J_{Photo} \simeq 0$ at V=V_{Bi} given $\alpha_C \gg 1$). Hence, Eqn. 2.12 is an improvement upon the equation in [45, 165], because the physics of carrier partition between drift and diffusion in the forward bias was captured.

Temperature and illumination dependencies. Let us consider the temperature and intensity dependencies of $J_{Photo}(IL, T)$. Among the four parameters of the photocurrent in Eqn. 2.12, **first**, J_{sc} is proportional to IL, but is essentially independent of T because the bandgap of CIGS is not temperature sensitive [166]. Our measurements support this assertion (see Sec. III): J_{sc} of our CIGS solar samples is measured to be temperature independent within the temperature range of interest (260 K to 360 K), which agrees with [167, 168]. **Second**, the Tdependency of V_{Bi} of a heterojunction can be analytically described in terms of the bandgap, E_G, and the conduction band offset, ΔE_C; see [169]. **Third,** the T dependency of α_c in Eqn.

2.12 can be approximated as $\alpha_c \sim e^{\Delta E_C/kT}$, because α_c is proportional to $1/s_n$ and $s_n \sim e^{-\Delta E_C/kT}$. **Fourth**, the voltage partition factor β is assumed to be temperature independent, because doping density does not change significantly in the temperature range of interest. Note that the temperature and irradiance dependencies of photocurrent in Eqn. 2.12 are handled implicitly through the dependencies of its underlying variables.

Diode Current (J_{Diode})

Equation for diode current. One also has to obtain the analytical description of J_{Diode} in Fig. 2.5(c) to complete the model. The complexity of the diode current depends on the solar cell type. For example, the 5-parameter model shows that diode current in a p-n junction cell can be described by two exponential terms with ideality factors 1 and 2, respectively [40]. The dark currents in p-i-n cells (e.g., perovskite, a-Si) are more complex, but can nonetheless be derived analytically [52, 135, 170]. Although a similar approach can be used to derive the diode current for heterojunction cells (e.g., HIT [164]), two considerations simplify the problem significantly. *First*, numerical simulation shows that the diode current is independent of illumination (up to 1 sun; see Fig. A.6), which has been supported by our experimental results (see Fig. A.7). *Second*, numerical simulation and experimental data for a variety of cells also show that the voltage dependence of the diode current can be expressed as

$$J_{Diode} = J_0(T)(\exp(\frac{qV}{N\,(T)\,kT}) - 1). \tag{2.13}$$

Here, $J_0(T)$ is the temperature-dependent reverse saturation current, which is directly related to the bandgap and carrier diffusion length of the absorber; N is the ideality factor ranging from 1–2, depending on the distribution of defects.

Temperature dependency of diode current. Regarding the two parameters (J_0 and N) of the diode current in Eqn. 2.13, there have been extensive studies regarding their temperature dependencies [171, 172]. It has been argued that J_0 is

linear with $e^{-E_G/N(T)kT}$ and $1/N(T) = 1/2 \times (1 + T/T^*)$ (assuming no tunneling), where E_G is the absorber bandgap, and kT^* (ranging from 30 meV to 150 meV) is the characteristic slope of the exponentially distributed defects in the absorber. Large kT^* indicates that most of the recombination in the depletion region is through the mid-bandgap defects, giving an ideality factor $N = 2$. Small kT^* corresponds to significant density of states of the shallow-level defects close to the valence band; carrier recombination due to such shallow defects gives $N = 1$.

Series and Shunt Resistances (R_{Series} and J_{Shunt})

Series resistance. As shown in Fig. 2.5(c), one must specify shunt and series resistances to complete the model, because they contribute parasitic power loss and increase the cell-to-module efficiency gap. The series resistance depends on the resistivity and thickness of the transparent conductive oxide (TCO) as well as the geometry of the cell [80] and the bulk resistivity of the absorber. It has been shown in [55] that the resistive loss due to 3-D current flow through the TCO layer and the bulk absorber in a solar cell can be modelled by a single resistor, R_{series}. Hence, R_{series} in Fig. 2.5(c) can be easily specified from measurements [173].

Nonlinearity of shunt conduction. Next, let us consider the shunt current. In Si cells, R_{shunt} is modeled as a symmetric linear resistor. For thin-film solar cells, shunt current is also symmetric, but conduction is typically non-ohmic due to space-charge-limited (SCL) transport across the absorber layer [56, 57]. A careful examination of the experimental data [56] of CIGS cells shows that transport transitions from linear to nonlinear shunt current with increasing voltage, namely,

$$J_{Shunt} = G_{Shunt} \times V + I_{OShunt} \times V^{\gamma}. \tag{2.14}$$

where G_{Shunt} and I_{OShunt} are the prefactor of the linear and nonlinear shunt current, respectively, and γ is the power index of SCL transport determined by the defect distribution in the absorber. It has been shown experimentally that J_{shunt} depends

weakly on temperature and illumination [56], so we do not consider it explicitly. Note that Eq. 2.14 has been applied widely to analyze the performance limit of CIGS solar cells [132, 174, 175].

Statistical distribution of shunt conduction. Shunt current is of particular importance for module-level simulation because it is a key source of variability in individual cells. A recent study has shown that log-normal shunt distribution is universal in thin-film technologies (e.g., CIGS, CdTe, a-Si) [56]. Based on careful analysis of 34 commercial CIGS cells, we find that the log-normal distribution is justified here as well (Table Table 2.4 summarizes the key equations). The log-normal distribution exhibits a long 'tail' in its probability density function. In a module, the highly shunted cells at the 'tail' dissipate power generated by their neighboring good cells, degrading overall module efficiency [132].

The forward IV part of the model in Fig. 2.5 (c) is now fully specified, and the temperature/illumination dependencies are summarized in Table 2.4. We will now validate the model against experimental data.

Experimental Validation and Discussion

Sample preparation. The experiments were based on the standard high-efficiency (∼18%) CIGS samples fabricated at NREL. The CIGS absorbers were prepared by a co-evaporation method based on the three-stage process, followed by the deposition of CdS and ZnO layers and Ni/Al grid lines on top of the absorbers [176]. The detailed fabrication process and characterization results of similar devices from NREL have been described in [177, 178].

The model validation involves four steps:

1. *Measurement*: The I-V characteristics of the samples were measured as a function of temperature (282 K to 362 K) and illumination intensities (0 sun to 1 sun).

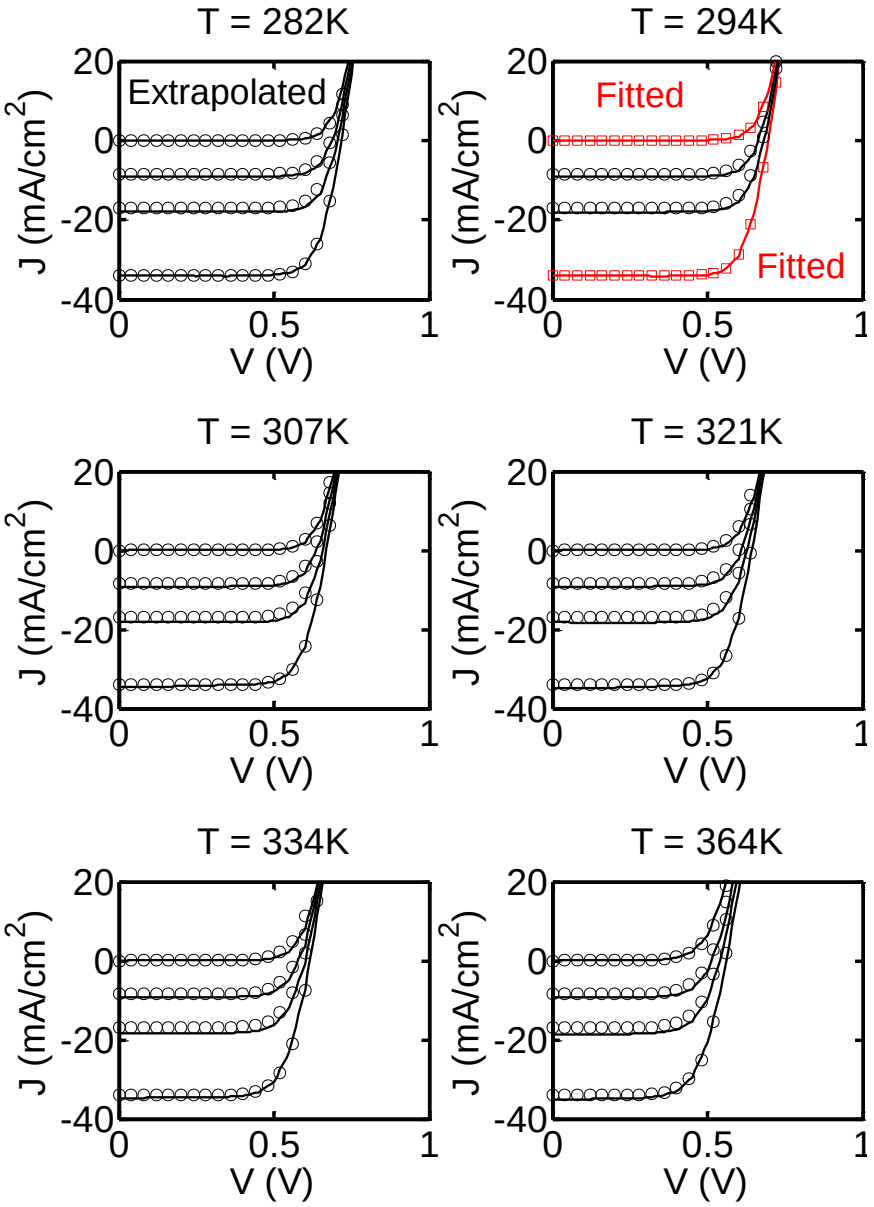

Fig. 2.6. The measured I-V (solid lines) vs. the analytical model (symbols) at different temperatures (282 K 364 K) and illumination intensities (0 sun, 0.25 sun, 0.5 sun, and 1 sun). The square symbols denote the fitted data, whereas the circle symbols are all extrapolated results.

2. *Calibration*: We first fit the dark and light I-V characteristics under 1-sun illumination at a ***single*** temperature (294 K) to Eqns. 2.11 and 2.13 using a nonlinear least-squares fitting algorithm ('lsqcurvefit' function in Matlab ®

[179]). The typical numerical range for the initial guess of each parameter is specified in Table 2.5. The series and shunt resistance were extracted from the dark I-V curve using PVanalyzer [173].

3. *Prediction*: We extrapolated the parameters obtained in step 2 (from I-V at 294 K and 1-sun illumination) to all other temperatures and illumination intensities by the equations in Table 2.4.

Fitting results. As shown in Fig. 2.6, the model predicts the salient features of the experimental I-V characteristics at various T and IL remarkably well. The validation suggests a noteworthy fact that *a single I-V measurement at room temperature and 1-sun intensity may be sufficient to predict cell response at arbitrary combinations of T and IL*, which is necessary to model cell-to-module gap, modules under partial shade, and lifetime energy output. Additionally, final fitting parameters in Eqns. 2.11 and 2.14 are physically relevant, and they provide insight into the construction or pathology of the cells under measurement. Note that the analytical equations and physical parameters are listed in Tables 2.4 and 2.5.

2.3.2 Reverse IV — Light-Enhanced Breakdown

Model Development

The importance of reverse breakdown. Partially shaded solar cells in a module can be stressed into reverse breakdown [52, 180, 181], which results in significant self-heating. Consequently, it is important to include the temperature-dependent breakdown characteristics in the compact model. Interestingly, recent experiments [134, 182] show that the breakdown voltage reduces from -6 V in dark to -2 V under light.

Not avalanche breakdown. Among the various mechanisms, we can exclude avalanche breakdown for the following reasons: given the doping density of 10^{14} to 10^{17} cm^{-3} [155], the avalanche breakdown voltage is expected to be from -10 V to -100 V,

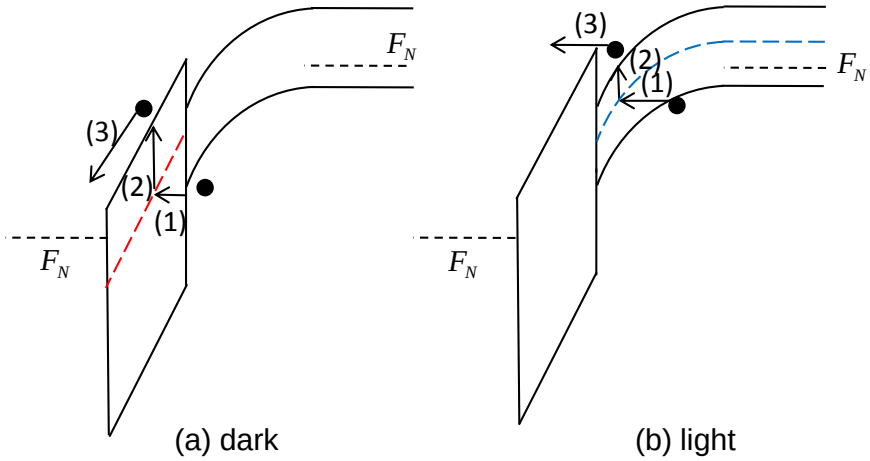

Fig. 2.7. Reverse breakdown current via tunneling-assisted Poole-Frenkel mechanism. (a) In darkness, electrons in the valence band in the absorber tunnel to the defect level (red) in the buffer layer then are emitted to the conduction and collected by the electrode. (b) The empty defect state (blue) under illumination allows Poole-Frenkel conduction directly occurring in the absorber.

which is beyond the magnitudes of both the dark and illuminated breakdown voltages observed in the experimental data. Also, as shown in Fig. 2.8, the dark and light breakdown voltages decrease with increasing temperature (i.e. are characterized by a negative temperature coefficient), inconsistent with avalanche breakdown [155, 183].

Not tunneling breakdown. Similarly, the reverse breakdown cannot be explained by band-to-band tunneling. In general, band-to-band tunneling is described by a negative temperature coefficient because the bandgap shrinks with increasing temperature. The short-circuit current in CIGS, however, is independent of temperature, indicating that the bandgap of neither the buffer nor the absorber layer are temperature dependent. Hence, it is unlikely that the reported light-enhanced breakdown is due to band-to-band tunneling, either.

Poole-Frenkel conduction induced breakdown. Therefore, we propose to model the reverse breakdown using tunneling-assisted Poole-Frenkel conduction [184], characterized by low breakdown voltage and negative temperature coefficient. As

shown in Fig. 2.7, the process of Poole-Frenkel conduction involves the following steps: (1) electrons tunnel toward a defect level elastically; (2) the high electric field lowers the barrier and the temperature assists electrons to emit into the conduction band; and finally, (3) electrons are collected by the contact. The derived equations and physical parameters based on the Pool-Frenkel model are summarized in Tables 2.4 and 2.5.

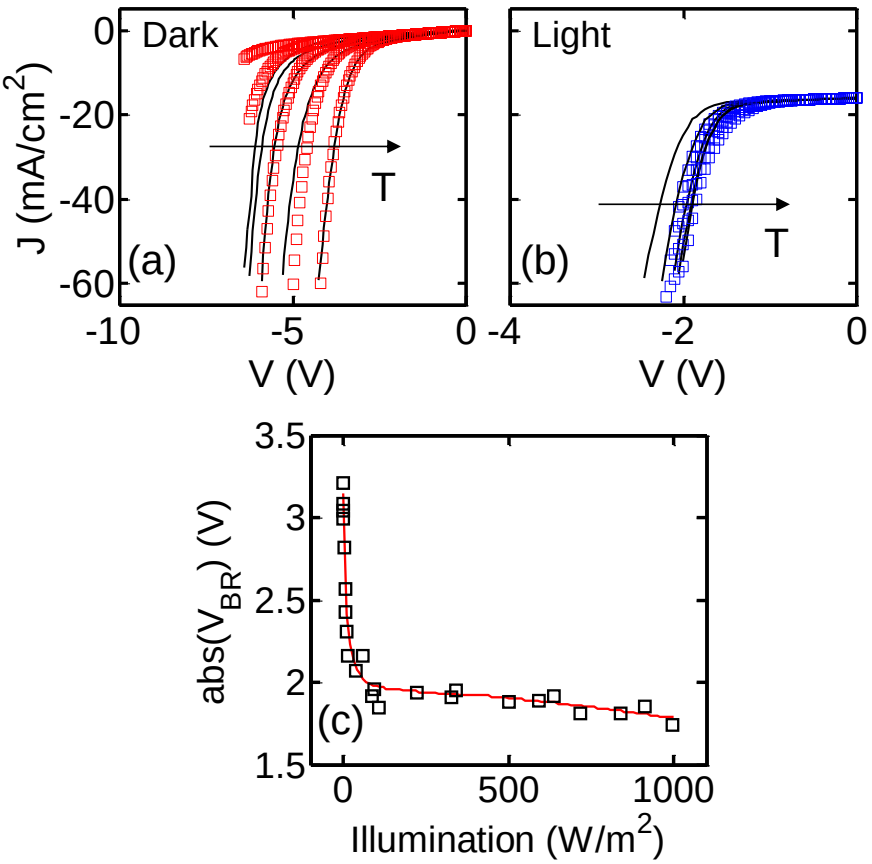

Fig. 2.8. Benchmark results of temperature-dependent CIGS reverse breakdown IV (solid lines) under (a) dark and (b) light against the compact model (squares). Data was measured at Uppsala University [182], and temperature varies from 260 K to 340 K with a 20 K interval. (c) Breakdown voltage of CIGS as a function of illumination intensity. The solid line is the model and squares are measured data from [182].

Experimental Validation

After fitting our model to the experimental data from [134, 182], we find that the model is capable of describing the breakdown characteristics as a function of temperature and voltage under different illumination conditions, see Fig. 2.8. The Poole-Frenkel parameter ($J_{RB0} \sim e^{-E_T/kT}$) depends on the defect level, E_T. The extracted defect level under dark is $E_T = E_C - E_T = 1.2$ eV, whereas the dominant defect level under illumination is 0.4 eV. The hypothesis of Poole-Frenkel conduction to model light-enhanced breakdown must be validated by additional experiments. The transition for breakdown current as a function of illumination intensities is also treated empirically. To our best knowledge, however, it is the first model that provides an intuitive and quantitative interpretation of the light-enhanced breakdown, and is adequate for module-level simulation.

2.3.3 Advantages of Physics-Based Model

A physics-based model is powerful because it makes the following important contributions:

- *First*, the model can be used as a characterization technique. For example, among the parameters obtained by fitting the room-temperature data in Fig. 2.6 and $V_{bi} \approx 0.8$ V (in good agreement with the C-V measurement). In additional, $E_G = 1.1$ eV, consistent with external quantum efficiency (EQE) measurement, and the heterojunction discontinuity for electrons $\Delta E_C = 0.1$ eV were used to extrapolate the I-V data at one sun and 298 K to arbitrary temperatures and illumination intensities. Hence, the model provides a means to calibrate physical parameters without performing C-V or EQE measurements. Indeed, parameters such as ΔE_C are critical, but are difficult to measure by other ways.

- *Second*, the model allows us to predict efficiency at different temperatures and the temperature coefficient of the maximum output power without performing

temperature-dependent light I-V measurement. Excellent agreement is obtained between two sets of experimental data and the analytical model; see Fig. 2.9 and Table 2.3. Note that, unlike [185], there are no empirical fitting parameters to account for the T and IL dependencies in this work and the model does not necessarily need to be calibrated against T-IL data. Therefore, this model can be directly incorporated into a system-level simulation framework to physically predict the performance of CIGS-based solar modules under different ambient temperature and solar irradiance. Together with the model of module lifetime from [54], the simulation framework can also estimate the long-term energy gain of CIGS solar modules for various geographic locations and weather conditions, which provides useful projection and guidance for large-scale PV installations.

- *Third* and finally, the model supports the development of an electro-thermal coupled simulation framework for solar modules. Equivalent circuits based on this model, which can accurately describe the temperature-dependent I-V characteristics at the cell level, can be integrated into a large-scale circuit network to self-consistently simulate the internal electrical and thermal distribution of a module. We will demonstrate such an application by modeling shadow-induced self-heating in CIGS modules in Sec. 3.3.2, and the simulation framework is also transferrable to interpret thermographic imaging for characterizing solar modules [186].

Table 2.3.

Measured and simulated temperature coefficients with uncertainties for P_{max} of the two NREL samples.

P_{max} **Temp. Coeff.** (**% K²**)	**Sample #1**	**Sample #2**
Measurement	-0.38 ± 0.04	-0.40 ± 0.05
Analytical Model	-0.38 ± 0.04	-0.39 ± 0.07

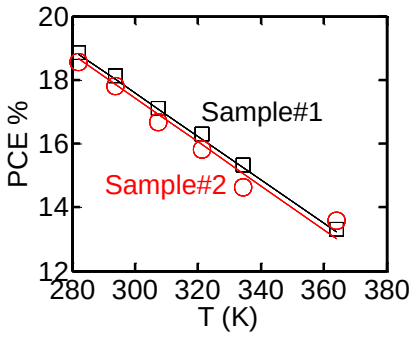

Fig. 2.9. Power conversion efficiency (PCE) of sample # 1 (square) and sample # 2 (circle) vs. the analytical model (solid and dashed lines for #1 and #2, respectively) as a function of temperature.

Model limitations The model, nevertheless, has its limitations. For highly defective CIGS cells, several assumptions in the derivation, e.g., illumination-independent diode (injection) current, may not be valid [44] and the assumption of voltage-independent generation-induced bulk recombination current is not accurate for low-doped absorbers with $W(V) \approx t$. In addition, the bias- and light-induced metastability of defect response is not considered in the process of assessing the temperature and illumination dependencies [187, 188]. Therefore, the model must be used very carefully for very low-efficiency cells, because it is developed based on CIGS cells with moderately high efficiency.

2.4 Conclusions

In this chapter, we provide a comprehensive discussion of two analytical models designated to perovskite and CIGS solar cells, respectively. The key conclusions of this chapter for perovskite and CIGS solar cells are respectively summarized as follows:

2.4.1 Perovskite Solar Cell:

1. We have derived an analytical model that describes both dark and light current-voltage characteristics for four different types [p-i-n/p-p-n and n-i-p/n-p-p] of perovskite solar cells.

2. The model provides a simple and complementary approach to characterize, optimize, and screen fabricated cells. Physical parameters that cannot be directly measured, such as V_{bi} of a p-i-n device, can also be deduced using the model.

3. Apart from determining the parameters of an existing cell and suggesting opportunities for further improvement, this analytical compact model serves another fundamental need, namely, the ability to predict the ultimate performance of the module composed of many individual perovskite cells and closing the cell-to-module efficiency gap unveiled in [189, 190].

2.4.2 CIGS Solar Cell:

1. The model provides a simple recipe to characterize the physical parameters (e.g., V_{bi}) of CIGS solar cell only from I-V data and to estimate the temperature/illumination coefficients of efficiency without performing temperature-and illumination-dependent measurements.

2. The model can be integrated into an electro-thermal coupled module simulation framework to further investigate and reduce the cell-to-module efficiency gap [39], improve module reliability [50], as well as interpret thermal imaging measurements of solar modules [186].

3. At the system level, given the climatic and geographic information, the model can be used to accurately predict the long-term electricity yields for large-scale PV farms, which can provide guidance on solar installation for a given location.

Table 2.4.
The equations of the analytical model

Analytical equations for I-V characteristics	
$J_{Photo} = J_{SC} \frac{1}{1+\alpha_c e^{\frac{q\beta(V-V_{bi})}{kT}}}$	
$J_{Diode} = J_0(e^{\frac{qV}{NkT}} - 1)$	
$J_{Shunt} = G_{Shunt} \times V + I_{OShunt} \times V^{\gamma}$	
$J_{BR} = J_{BR,0} \times V \times \exp(\frac{q}{kT}\sqrt{\frac{-V}{m}})(V < 0)$	
$J_{Light} = J_{Photo} + J_{Diode} + J_{Shunt} + J_{BR}$	
Illumination and temperature dependencies of the parameters	
J_{SC}	$J_{SC,IL} = IL \times J_{SC,one\ sun}$
α_c	$\alpha_{c,T} = \alpha_{c,300\mathrm{K}} \times \exp(\frac{\Delta E_C}{k}\left(\frac{1}{300\mathrm{K}} - \frac{1}{T}\right))$
β	$\beta_T = \beta_{300\mathrm{K}}$
V_{Bi}	$V_{Bi,T} = \frac{\Delta E_C}{q} + \frac{E_G}{q} + \frac{T}{300\mathrm{K}}\left(V_{Bi,300\mathrm{K}} - \frac{\Delta E_C}{q} - \frac{E_G}{q}\right) - \frac{kT}{q} log((\frac{T}{300\mathrm{K}})^3)$
N	$N_T = 2/(1 + \frac{T}{T^*})$
J_0	$J_{0,T} = J_{0,300\ \mathrm{K}} \times \exp(\frac{E_G}{k}\left(\frac{1}{N_{300\ \mathrm{K}} 300\ \mathrm{K}} - \frac{1}{N_T T}\right))$
$J_{BR,0}$	$J_{BR,0} = J_{BR,D} + \tanh(200 \times IL) \times J_{BR,L}$
$J_{BR,D}$	$J_{BR,D,T} = J_{BR,D,300\ \mathrm{K}} \times \exp(\frac{E_{A,D}}{k}\left(\frac{1}{300\ \mathrm{K}} - \frac{1}{T}\right))$
$J_{BR,L}$	$J_{BR,L,T} = J_{BR,L,300\ \mathrm{K}} \times \exp(\frac{E_{A,L}}{k}\left(\frac{1}{300\ \mathrm{K}} - \frac{1}{T}\right))$
m	$m_T = m_{300\ \mathrm{K}}$
Statistical equation for log-normal shunt distribution	
$PDF(I_{OShunt}\|\mu,\sigma)$	$\frac{1}{I_{OShunt}\sigma\sqrt{2\pi}} \times \exp(\frac{-(\log(I_{OShunt})\ -\mu)^2}{2\sigma^2})$

Table 2.5.

Definition and typical values—at room temperature (300 K) and one sun—for the parameters

Fitting parameters for dark I-V		
J_0	Diode saturation Current	$\sim 10^{-6}$ mA/cm^2
N	Ideality factor	1–2
G_{Shunt}	Prefactor of linear shunt current	0–1 mS/cm^2
γ	Power index of log shunt current	2–3
I_{OShunt}	Prefactor of nonlinear shunt current	0–1 mS/(V$^{\gamma-1}$ cm^2)
Fitting parameters for $J_{Photo} = J_{Light} - J_{Diode}$		
J_{sc}	Short-circuit current	35 mA/cm^2
V_{Bi}	Total built-in voltage of the p-n junction	0.6–0.9 V
α_c	Ratio between diffusion velocity and thermionic-emission velocity	50–200
Fitting parameter for J_{BR}		
$J_{BR,D}$	Dark breakdown current density prefactor	6.8×10^{-9} mA/cm^2
$J_{BR,L}$	Light breakdown current density prefactor	2.4×10^{-5} mA/cm^2
m	Breakdown current index	0.24
Parameters used for extrapolation to arbitrary temperatures		
kT^*	Characteristic slope of the bulk defects	60–200 meV
E_G	Bandgap of CIGS	1.0 $\sim$ 1.4 eV
ΔE_C	Conduction band offset between CdS and CIGS layers	0.1 eV
$E_{A,D}$	Dark activation energy of breakdown	1.2 eV
$E_{A,L}$	Light activation energy of breakdown	0.4 eV

3. SELF-HEATING AND COOLING OF SOLAR MODULES

3.1 Introduction

Transition In the last chapter, we develop physics-based analytical models that can describe the temperature- and illumination-dependent IV for solar cells. In this chapter, our objective is to integrate these compact model into a versatile multi-physics simulation framework to 1) understand the self-heating effect in solar modules exposed in the field and 2) develop self-cooling techniques to reduce the operating temperature.

Self-heating A typical solar module converts ∼20% of the incoming sunlight into electricity. Therefore, up to ∼80% of the sunlight may dissipate as heat in the module, causing undesired self-heating as well as performance degradation [29]. Depending on the environment, the average temperature of a solar module can be 20 °C – 40 °C higher than the ambient. Furthermore, self-heating worsens when modules are subject to partial shading (i.e., elevate the temperature up to 80 °C), which has been experimentally confirmed. Such high temperature can abruptly damage the physical and chemical properties of semiconductors and generate shunt defects, which will reduce the fill-factor of solar modules substantially [191].

Performance erosion Self-heating of PV modules reduces both the short-term and long-term power outputs. In the short term, the efficiencies of different PV technologies decrease with temperature, e.g., the efficiency of crystalline Si modules drops by ∼0.45% for every 1°C increase in temperature. In the long term, the reliability of modules suffers from thermally activated degradation processes, such as contact corrosion and polymer degradation, which accelerate at higher temperatures. A recent survey in India has shown that solar modules in hot climates degrade at ∼1.5 %/year,

eight times faster than the ones installed in cold climates (∼0.2 %/year) [29]. The module lifespan was less than 15 years in hot environments, far below the 25-year standard warranty. As a result, it is important to develop effective cooling schemes to improve both the short-term and long-term energy yields as discussed in this chapter.

Chapter flow This chapter [1], as been organized as follows. In Sec. 3.2, we discuss the balance of energy fluxes in solar modules by introducing our opto-electro-thermal coupled framework. Our framework can predict the degree of self-heating as well as the spatial distribution thereof. The underlying physics of PV self-heating is explored in Sec. 3.3. Here, we will explain the intrinsic self-heating (i.e., sub-bandgap absorption and imperfect thermal radiation) and shading-induced self-heating. Next, the corresponding optics-based cooling methods (i.e., selective-spectral and radiative cooling) and their impacts on PV performance ($P_{Module}(IL, T, t)$) and reliability (t_{Life}) are presented in Sec. 3.4.

3.2 Simulation Framework

3.2.1 Energy Balance for Solar Modules

Energy fluxes. A *terrestrial* PV module is subject to the following energy fluxes, see Fig. 3.1: 1) the absorbed solar irradiance, P_{Sun}, determined by the solar spectrum (e.g., AM1.5) as well as the absorptivity of the PV module; 2) the sky cooling, P_{Sky}, through radiative energy exchange with the atmosphere from the side facing the sky; 3) similarly, cooling due to energy transfer to the ground, P_{Ground} from the back-side; 4) convective cooling by air at the top and bottom surfaces and conductive heat transfer through the aluminum frames, $P_{Conv(d),top/bottom}$; 5) most importantly, the output power delivered by PV modules to the external load, P_{Out}.

[1] The contents of this chapter are taken from [136] ©2015 IEEE, [192] ©2017 IEEE

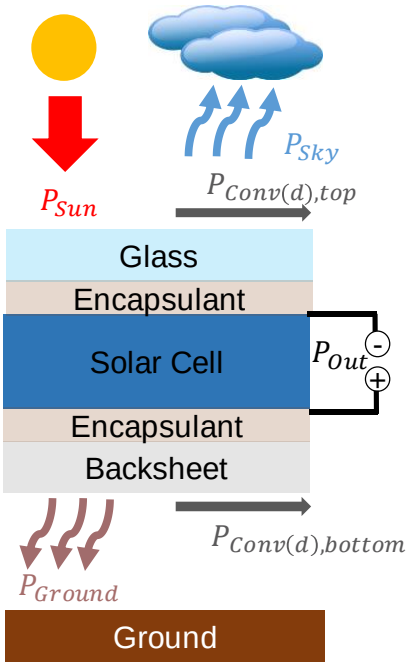

Fig. 3.1. Schematic of a terrestrial PV module, where we have identified the incoming and outgoing energy fluxes. Eqn. 3.1 summarizes the energy-balance equation for the solar module.

Energy-balanced equations. For a thermodynamic system in the steady state, the incoming and outgoing energy fluxes should balance out to reach equilibrium; namely,

$$P_{Sun} = P_{Sky} + P_{Ground} + P_{Conv(d),top} + P_{Conv(d),bottom} + P_{Out}, \tag{3.1}$$

for terrestrial solar modules. Note that each energy flux in (3.1) are determined by the thermal state and optical properties of the PV modules as well as the outside environment. So one must solve (3.1) opto-electro-thermally and self-consistently to calculate the steady-state temperature of PV modules. For instance, o*ptically,* we calculate P_{Sun} by integrating the measured absorptivity and the solar spectrum. *Thermally,* P_{Sky} depends on the temperature of PV modules, T_{PV}, and the ambient temperature, T_A, as well as the emissivity of PV modules and atmospheric transmittance in the

infrared (IR) region. *Electrically*, the output power, P_{Out}, is temperature-dependent and varies among different PV technologies. Finally, the calculated temperature at equilibrium must give energy fluxes that satisfy (3.1).

Solar absorption. Next, we will discuss the physics and formulation to calculate each energy flux in Eqn. 3.1. The absorbed sunlight can be written as

$$P_{Sun} = \int_0^\infty d\lambda I_{Sun}(\lambda) \times \varepsilon(\lambda, \theta_{Sun}) \times \cos(\theta_{Sun}), \tag{3.2}$$

where θ_{sun} is the solar incidence angle ($\theta_{Sun} = 0^o$ in this work), $I_{Sun}(\lambda)$ is spectral flux density of the solar spectrum at different wavelengths λ and $\varepsilon(\lambda, \theta_{Sun})$ is the absorptivity of solar modules at incidence angle θ_{sun}. For conventional solar modules, $I_{Sun}(\lambda)$ is the AM1.5G spectral density, while AM1.5 D and AM0 spectrums should be used for concentrated and extraterrestrial PV, respectively.

Sky cooling power. Sky cooling power in Eqn. 3.1 for terrestrial modules is

$$P_{Sky}(T_{PV}, T_A) = P_{Rad}(T_{PV}) - P_{Atm}(T_A). \tag{3.3}$$

In Eqn. 3.3, $P_{Rad}(T_{PV})$, the thermal emission power radiated from the glass cover for both terrestrial and extraterrestrial modules can be expressed as

$$P_{Rad}(T_{PV}) = \int d\Omega \cos(\theta) \int_0^\infty d\lambda I_{BB}(T_{PV}, \lambda) \times \varepsilon(\lambda, \Omega). \tag{3.4}$$

Here, $\varepsilon(\lambda, \Omega)$ is the angular emissivity of glass; $I_{BB}(T, \lambda) = (2hc^2/\lambda^5)/(\exp(hc/(\lambda k_B T)) - 1)$ where h is the Plank constant, c is the velocity of light, and k_B is the Boltzmann constant; $\int d\Omega = \int_0^{\pi/2} d\theta \sin(\theta) \int_0^{2\pi} d\phi$ is the angular integral over a hemisphere. Similar, $P_{Atm}(T_A)$ which is the thermal radiation from the atmosphere to PV modules can be written as

$$P_{Atm}(T_A) = \int d\Omega \cos(\theta) \int_0^\infty d\lambda I_{BB}(T_A, \lambda) \times \varepsilon(\lambda, \Omega) \times \varepsilon_{Atm}(\lambda, \Omega). \tag{3.5}$$

Using Kirchhoff's law and the Beer-Lambert law [193], the angular emissivity of the atmosphere $\varepsilon_{Atm}(\lambda, \Omega)$ can be written as $\varepsilon_{Atm}(\lambda, \Omega) = 1 - t_{Atm}(\lambda)^{1/\cos(\theta)}$, where

$t_{Atm}(\lambda)$ is the atmospheric transmittance in the zenith direction in Fig. 3.5. As pointed out in [193], the downward atmospheric spectrum can be divided into two sub-spectrums: the first one spanning 8-13 μm, and the second involving the rest of the wavelengths. The 2^{nd} spectrum (outside the 8 -13 μm wavelength range) is emitted by water vapor and carbon dioxide within the lowest few hundred meters of the sky, at the local ambient temperature T_A. In contrast, the 8 - 13 μm spectrum stems from the upper part of the troposphere with $T < T_A$. Hence, the atmosphere has lower spectral emissivity within 8 to 13 μm wavelength, see Fig. 3 in [193]. Because the emissivity depends on wavelength, we calculate the atmospheric radiation (see Eqn. 3.5) by integrating the Planck's equation (at T_A) with the atmospheric emissivity, $\varepsilon_{Atm}(\lambda, \Omega)$, over the entire IR wavelength range.

Ground radiation. Since wavelength-dependent emissivity of backsheet is not available, cooling power of thermal radiation exchange between the bottom surface and the ground (Earth) is calculated using the Stefan–Boltzmann law as

$$P_{Ground}(T_{PV}, T_A) = \sigma \varepsilon F({T_{PV}}^4 - {T_A}^4), \tag{3.6}$$

where ε is the hemispherical emissivity of the back surface, F is the view factor and σ is the Stefan–Boltzmann constant. The ground temperature (could be slightly lower than T_A in practice) is assumed to be the same as the ambient temperature in this work. The view factor is assumed to be unity for terrestrial (i.e., no tilting) solar modules in this chapter.

Convective power. The convective cooling power is calculated by

$$P_{Conv(d)}(T_{PV}, T_A) = h \times (T_{PV} - T_A), \tag{3.7}$$

where h is the effective heat transfer coefficient combing the free and forced convection and conduction. In this chapter, the effective heat transfer coefficient, h, is set to be same for the top and bottom surfaces of solar modules assuming no tilting.

Electricity output. Finally, the electrical output power $P_{Out}(T_{PV})$ of the PV modules is

$$P_{Out}\left(T_{PV}\right) = P_{Out}\left(300\text{ K}\right) \times \left(1 + \beta \times \left(T_{PV} - 300\text{ K}\right)\right). \tag{3.8}$$

Here, for a given PV technology, $P_{Out}\left(300\text{ K}\right)$ is the output power at 300 K and β is the temperature coefficient, which is negative for most solar technologies.

Energy balance. Coupling Eqns. 3.2 to 3.8 into Eqn. 3.1, one can self-consistently solve the temperature of solar modules under different environmental conditions. Note that, unlike the empirical approaches in [194, 195], the opto-electro-thermal simulation framework in this work can physically calculate operating temperature of modules with different solar absorbers (e.g. Si, CIGS) and various environment conditions without any fitting parameters.

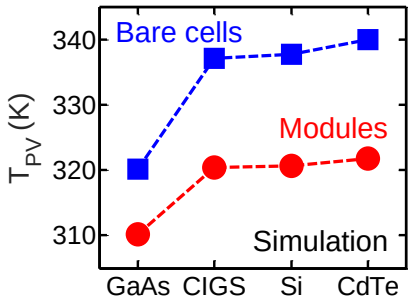

Fig. 3.2. The outdoor operating temperature of bare cells (blue squares) and encapsulated modules (red circles) of GaAs, CIGS, Si, and CdTe.

Benchmark against experiments. Fig. 3.2 shows the temperature calculated by our opto-electro-thermal framework for different PV technologies under the same environment conditions (i.e. the wind speed is ~0.5 m/s giving an effective convective coefficient h=10 W/(K.m^2) [72]; conductive heat transfer only at the module edges through metal frames is neglected; the atmospheric transmittance data is in Fig. 3.5; the ambient temperature T_A and solar irradiance are 300 K and 1000 W/m^2, respectively;). There are also two interesting observations from the simulated data: 1) the operating temperature varies among different PV technologies. Specifically, GaAs modules operate at much lower temperature (~310 K) compared to others.

Remarkably, our simulation anticipates the following two trends observed in the outdoor tests: (a) commercial GaAs modules operates at lower temperature ($\sim$ 10 K) compared to Si-based solar cells [62], and (b) an encapsulated module operates at lower temperature (10-20 K) compared to a bare cell without coverglass [69]. Indeed, these two observations can be attributed to two important self-heating mechanisms in photovoltaics: a) parasitic sub-BG absorption and b) imperfect thermal radiation, which will be discussed in detail in Sec. 3.3.

3.2.2 Electro-Thermal Coupled SPICE Network

Why spatial simulation? So far we have discussed the simulation framework that only solves for the steady-state operation temperature of solar modules. However, because of the uniform-heating assumption, this framework can not spatially resolve the thermal distribution of solar modules caused by partial shading [52] and localized hot spots [39, 132]. These inhomogeneous self-heating effects, on the other hand, are very detrimental to PV performance and reliability, and entail a rigorous modeling approach.

Existing approaches. Commercial multi-physics simulation softwares, e.g., COMSOL [196], have been widely used to simulate spatially-resolved self-heating [197, 198]. Unfortunately, these softwares charge expensive licensing fees and may not be financially affordable to many researchers. Hence, we have developed an open-source electro-thermal coupled simulation framework based on Xyce [199], an open-source parallel SPICE-compatible simulator developed at the Sandia National Lab. This SPICE-based open-access framework can allow us to investigate the degree and spatial distribution of the self-heating effects in solar modules.

Simulation method. This framework can be divided into three parts: 1) the physics-based compact model in Sec. 2.3 that can describe the illumination- and temperature-dependent IV for CIGS solar cells, 2) an electrical circuit network connects the compact model, 3) a thermal circuit network to calculate the temperature

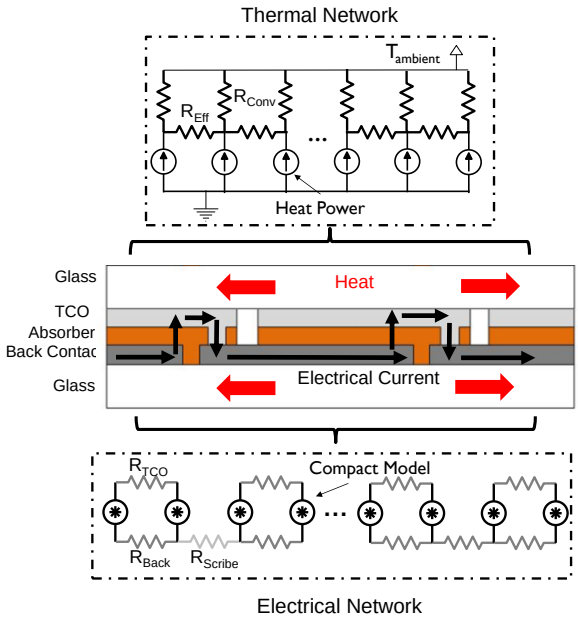

Fig. 3.3. The electrical and thermal circuit network setup for monolithic module simulation. Electrically, one cell is divided into multiple subcells (represented by the compact model) connected by resistors accounting for current flow in the TCO (R_{TCO}) and back contact ((R_{Back}) layers. Moreover, each cell is connected through an interface resistor ((R_{Scribe}) at the scribe area. Thermally, heat power from each cell is accounted by current sources. The heat flow through the glasses, back contacts, absorbers, etc., is represented by an effective thermal resistor (R_{EFF}). Finally, all the current sources are connected to the ambient temperature through the convective thermal resistors (R_{Conv}).

based on the power dissipation (represented as a current source electrically) calculated from the electrical circuit network, see Fig. 3.3. The simulation flow is as follows:

1. The framework will firstly calculate the spatial distribution of voltage and current density based on the compact model and electrical circuit network (i.e., R_{TCO}, R_{Back} and R_{Scribe}) at an initial temperature guess of 300 K across the module.

2. After calculating the electrical profile of the solar module, the framework will calculate the power dissipation of each sub-cell and then estimate the temperature profile thereof using the thermal circuit network.

3. Since our physics-based compact model can electro-thermal dependent, the framework will reiterate the electrical and thermal calculation until it converges. Therefore, we can simulate the spatially resolved self-heating effect in solar module self-consistently.

Transition. In Sec. 3.3.2, we will apply this framework to study the shading-induced self-heating in thin film solar modules extensively and its impacts on the PV durability.

3.3 Physics of Self-Heating

3.3.1 Intrinsic Self-Heating

Sub-BandGap Absorption

Solar spectrum. The solar irradiance consists of photons ranging from the ultraviolet spectrum (∼4 eV) to near-IR region (∼0.5 eV). In general, however, only photons with energy above the bandgap excite electron-hole pairs in a semiconductor to produce electricity. For Si or CIGS solar cells ($E_G \approx 1.1$ eV), the above-bandgap spectrum accounts for ∼84% of the incident solar irradiance. A module with ∼18% efficiency converts part of the above-bandgap solar energy into electricity, the rest is converted to heat through carrier recombination, thermalization, and entropy generation [200]. One way to lower heat generation from above-bandgap photons is to increase the intrinsic solar cell efficiency (by multi-junction design [201], etc.), which is not discussed in this section because we wish to focus on single-junction cells. On the other hand, for Si and CIGS, ∼16% of the sunlight consists of photons with energy below the bandgap. Ideally, the sub-BG photons will not be absorbed by solar cells, rather it should be reflected back by the back metal.

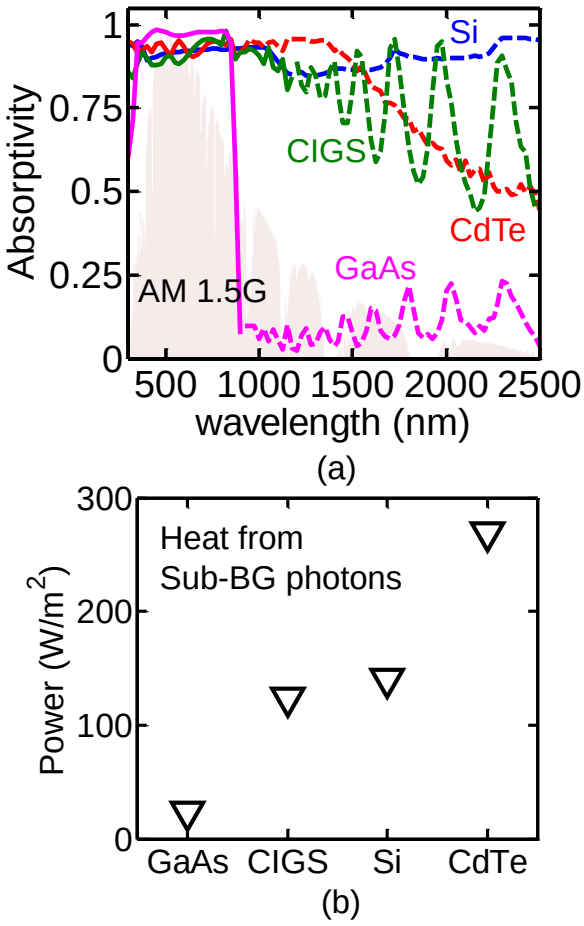

Fig. 3.4. (a) Measured absorptivity for different solar absorber materials vs. photon wavelength (solid lines: above bandgap photons; dashed lines: below bandgap photons). The pink area is AM1.5G spectrum. (b) Heat from sub-BG photons for different technologies.

Absorptivity measurement. We have measured the absorptivity profile of four different samples, with particular emphasis on the sub-BG spectrum. The optical measurements were performed using an Agilent-Cary 5000 spectrophotometer (with an integrating sphere) [202] at NREL. The Si sample was a commercial solar module from Ref. [62], and GaAs [203], CIGS [177] and CdTe [204] samples were fabricated at NREL lab. All the cells (except CIGS) had anti-reflection coating. The cell-level measurement, however, may underestimate the parasitic absorption slightly, because

∼3% of sunlight is absorbed by in the encapsulation layers of a practical module structure [205]. Otherwise, the absorptivity profile of a module is essentially the same as that of ARC-coated bare cell, an assertion validated by our numerical modeling (not shown).

Origins of sub-bandgap absorption. *Our measurements of different PV technologies, however, show various degrees of sub-BG absorption (dashed lines in Fig. 3.4(a)).* Specifically, Si, CIGS, and CdTe show high sub-BG absorption, while most of the below-bandgap photons are reflected in GaAs. The parasitic absorption may be attributed to absorbing back metal reflector, Urbach tail, and free carrier absorption by highly-doped layers (emitter and back surface field in Si or window and buffer layers in CIGS and CdTe) [60,61,206]. Consequently, a large fraction of the sunlight, which consists of the sub-BG photons, now heats the solar module, see Fig. 3.4(b).

Comparison of different technologies. Among these technologies, GaAs is almost immune to sub-BG absorption possibly due to the high-quality metal mirror (gold) and reduced free carrier absorption. The magnitude of sub-BG absorption is similar between CIGS and Si (∼12 % of the solar irradiance). Interestingly, CdTe has the largest parasitic absorption (∼30 %) due to its largest bandgap (∼1.5 eV) and strong absorptivity in the sub-BG spectrum. The consequence of sub-BG absorption among different technologies is reflected in Fig. 3.2, i.e., GaAs and CdTe operate at the lowest and highest temperatures, respectively. Obviously, the sub-BG absorption is not an intrinsic property of a cell technology (it can be reduced by modifying cell design, for example); therefore, the purpose of the discussion above is to highlight the importance of sub-BG absorption in determining the operating temperature of solar modules. Consequently, it is desired to eliminate the sub-BG absorption, which contributes substantially to self-heating, but not to the output power. In Sec. 3.4, we will propose to redesign solar modules optically such that sub-BG photons are not absorbed. Next, however, we will discuss another source of self-heating, namely, imperfect thermal radiation of dissipated heat.

Imperfect Thermal Radiation

Thermal radiation for cooling. Another important factor dictating operating temperature of PV (T_{PV}) is the constant exchange of energy between the module and the surroundings through thermal radiation. Outdoors, solar modules receive thermal radiation from the sky and the ground; meanwhile, the top (glass) and bottom (polymer backsheet) layers of PV modules radiate to the sky and the ground, respectively. Based on the fact that the daytime module temperature is higher than the ambient, the net energy exchange from modules to surroundings is positive. Therefore, the ambient environment cools modules through thermal radiation with a spectrum peaking in the IR wavelengths. Without the cover-glass, however, solar absorbers can display very low emissivity in the IR spectrum, see Fig. 3.5. Hence, the amount of emitted thermal radiation is substantially suppressed for a bare solar cell, resulting in much higher temperature, as shown in Fig. 3.2. As a result, even though cell-level measurements are usually conducted indoors with heat sinks to maintain constant temperature, one must be careful to interpret the results from outdoor cell-level measurements.

Imperfect thermal radiation. Despite the fact that glass and backsheet are already highly emissive in the IR region, they are still not perfect. The emissivity of glass is calculated in Fig. 3.5, which shows a drop of the emissivity in the atmospheric transmission window (blue shaded area). The window corresponds to the wavelength range (8 μm –13 μm) where the atmosphere is transparent (high transmittance) to thermal emission. It is also noteworthy that the wavelengths of peak thermal radiation from many terrestrial objects exactly match the "transparent" window. In other words, objects on Earth can exchange a large amount of energy with the cold troposphere (usually 50 K lower than the ambient temperature at sea level) through these wavelengths. Hence, any dip of the emissivity between 8 μm and 13 μm can lower the cooling power of a thermal emitter. Also, the emissivity of glass at higher angles reduces rapidly beyond 50°, see Fig. 3.5. Since thermal radiation is

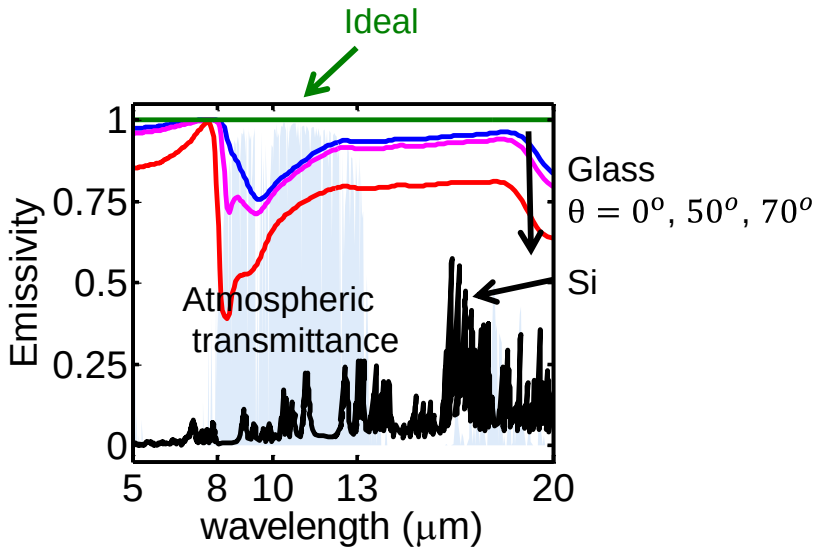

Fig. 3.5. Simulated emissivity profile of glass at different incident angles using S^4 [207]. The (n, k) data was obtained from [208]. The emissivity of Si is obtained from [68]. The ideal emissivity for radiative cooling is also shown here as green line. The blue area is the atmospheric transmittance in the zenith direction calculated by ATRAN [209] for New Delhi in spring with perceptible water vapor (PWV) = 18 mm.

hemispheric (integrated with angles from 0° to 90°), the angle-dependent emissivity of glass reduces the thermal radiation from solar modules compared to an ideal emitter. Overall, the calculated average emissivity (hemispherical emissivity) is 0.82 very close to the commercial solar glass ($\bar{\varepsilon} = 0.84$) [210], while commercial PVF backsheet has $\bar{\varepsilon} = 0.85$ [211], i.e., both have room for improvements. Therefore, it is desirable to re-engineer the top and bottom surfaces of solar modules to enhance thermal radiation for cooling, as we will discuss in Sec. 3.4.

3.3.2 Shading-Induced Self-Heating

What is partial shading? Partial-Shading has long been known as a major degradation [52, 76]. When shadow is cast by surroundings (e.g., building, vegetation) on a solar module and creates non-uniform illumination , it disrupts the electrical

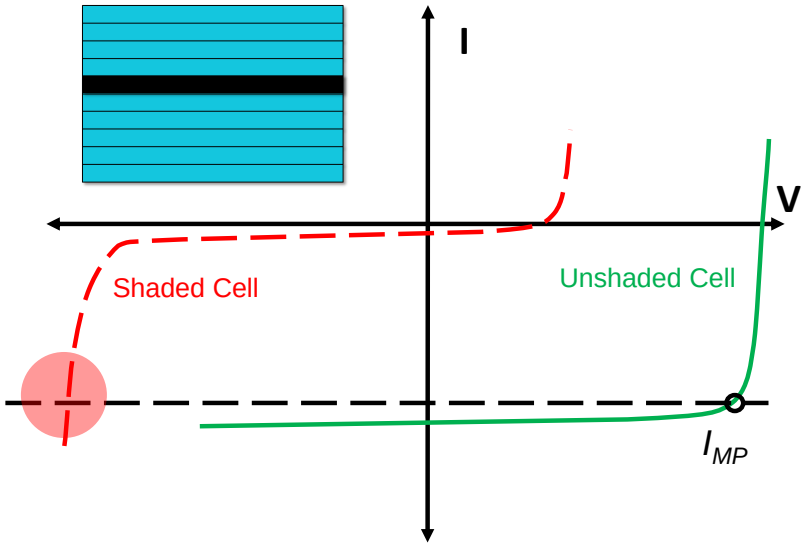

Fig. 3.6. IV characteristics of the shaded cell and unshaded cell in a monolithic solar module. Due to series-connected current matching, the shaded cell is subject to reverse breakdown, thereby significant self-heating.

performance of series-connected solar cells. Namely, the current density of the shaded cell will substantially reduce because of the lost photocurrent, see Fig. 3.6. However, in a series circuit, the current must be continuous. Therefore, the unshaded cell will forces the shaded cell into reverse breakdown in order to maintain current continuity. Consequently, the shaded cell, instead of generating electricity, starts to dissipate heat and local hot spots ensue. In conventionally silicon solar modules, it is common to bypass current using a diode under shading and eschew shading-induced self-heating. The maximum number of silicon cells protected by a single bypass diode protects is determined by the breakdown voltage, which is typically 24 for a breakdown voltage of -12 V [212]. Thin film solar modules, however, can only have one bypass diode per module (typically consist of 100+ cells) due to the monolithic structure. The insufficient bypass diode protection renders thin film solar modules extremely susceptible to shading-induced self-heating [191].

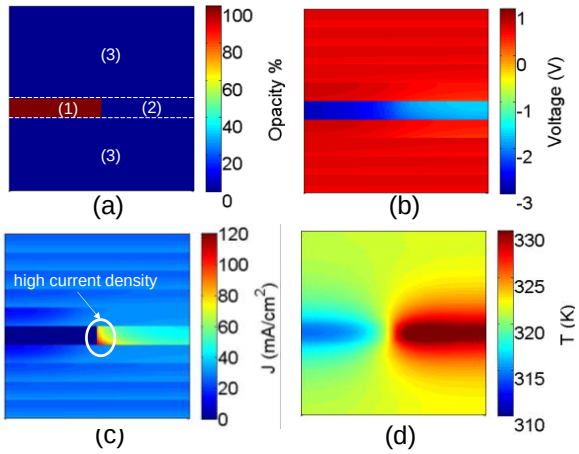

Fig. 3.7. (a) The spatial distribution and opacity of the shadow. Regions 1 and 2 are the shaded and unshaded areas of the fifth shaded cell, respectively. Region 3 represents the unshaded cells. (b) The voltage distribution of the module. (c) The current distribution of the module. (d) The temperature profile of the module.

Shading-induced degradation. The elevated temperature causes severe thermal stress on the solar modules, accelerating thermally activated degradation processes, such as contact corrosion. Furthermore, the high temperature resulted from partial shading can impose detrimental effects on physical and chemical properties of the semiconductor absorbers and cause irreversible efficiency loss. As a result, it is crucial to investigate the degree and distribution of shading-induced self-heating, and properly design qualification test for commercial solar modules, i.e., IEC 61215 [79, 213].

Simulation demonstration. For demonstration, we simulate a partial-shaded solar module using the framework developed in Sec. 3.2.2. Fig. 3.7 shows the simulation response of this partially shaded module, biased at the maximum power point associated with the unshaded module. For this illustrative example, we assume that the left half of 5th cell (region 1) is fully shaded, as in Fig. 3.7(a). Since region 1 can no longer produce photocurrent, the need for current continuity with fully illuminated cells in region 3 require that the shaded cells in regions 1 and 2 be forced

into reverse breakdown, as shown in Fig. 3.7(b). As shown in Fig. 3.7(c), the current density is indeed extremely high near the edge between the shaded and unshaded areas. The reverse voltage at the boundary is high (around -3 V) resulting in large breakdown current at the illuminated side due to light-enhanced breakdown. The reverse voltage decreases toward right in region 2; therefore, the breakdown current reduces away from the interface between regions 1 and 2 as well. Due to light-enhanced breakdown, the current in the unshaded area (region 2) is much higher than that of the shaded area (region 1); so is the generated heat. Counterintuitively, the temperature rise is more pronounced in the unshaded half of the shaded cell, even though the shaded side operates at higher reverse voltage. The spatial redistribution of the temperature due to partial shading in Fig. 3.7(d) is also in agreement with Fig. 5 in [52] and more detailed finite element-based simulation in Ref. [50].

Mitigation methods. Given shading-induced self-heating as this pernicious phenomenon to PV reliability, there have been several proposed techniques to mitigate this issue. For example, Dongaonkar *et al.* [80] redesign the geometry of the module to enhance the symmetry of shading, i.e., reduce the non-uniformity of shading. Their results indicate substantial improvement of shading resistance. Silverman *et al.* [79] also proposed partial shading aware design at threefold levels: 1) at the cell-level, one can reduce the absorber thickness to lower the breakdown voltage, whereby reduce the heat dissipation under shading stress, 2) at the module-level, the module can be further be divided into submodules connected in parallel by laser scribing, which can also improve shading durability, and 3) at the system level, by rewiring the module connection from completely series-connected into partially parallel-connected, one can circumvent shading-induced thermal stress. Hence, Sec. 3.4 will primarily focus on how to reduce the intrinsic self-heating phenomenon, namely, sub-bandgap absorption and imperfect thermal radiation, in solar modules by novel optical designs.

3.4 Optics-Based Self-Cooling

The optical methods. Thermodynamics dictate that modules must self-heat, but our focus is on avoidable temperature rise due to a) strong sub-BG absorption, b) inadequate thermal radiation. To mitigate this parasitic self-heating, we propose two optics-based cooling methods, namely, selective-spectral cooling and radiative cooling. We will briefly discuss the practical implementation or the economic viability of these cooling methods in the 3.4.3; for now, we focus on the effectiveness of the ideal designs in reducing the module temperature.

3.4.1 Selective Spectral Cooling

Filtering undesired photons. Ideally, since the sub-BG photons do not contribute to the electricity output, they should be reflected by the cells or modules. Instead, our measurements in Fig. 3.4 show a large fraction of sub-BG photons are absorbed by the cell (e.g., $\sim$300 W/m^2 for CdTe), which in turn heats up the solar module. Note that the parasitic absorption is related to the intrinsic material properties of PV modules (e.g., free carrier absorption, reflection loss), and it is not trivial to eliminate the parasitic absorption by improving absorber materials. An alternative approach may involve selective reflection the sub-bandgap photons *before* they enter the solar absorber by implementing optical filters or selective mirrors, see Fig. 3.8.

Filter design. Ideally, the optical filter in Fig. 3.8(a) should be a short-pass filter, which only allows photons above E_G to pass and reflect the rest. Such a filter can be realized using quarter-wave stacks [214]. It is important that the filter does not interfere with sky-cooling, therefore, the optical filter should be inserted in between coverglass and polymer encapsulant. The filter can also be engineered to reflect the high-energy ultraviolet photons, which does not contribute efficiently to carrier generation, but cause polymer yellowing and encapsulation delamination [215, 216]. We, however, will not study or optimize for the latter.

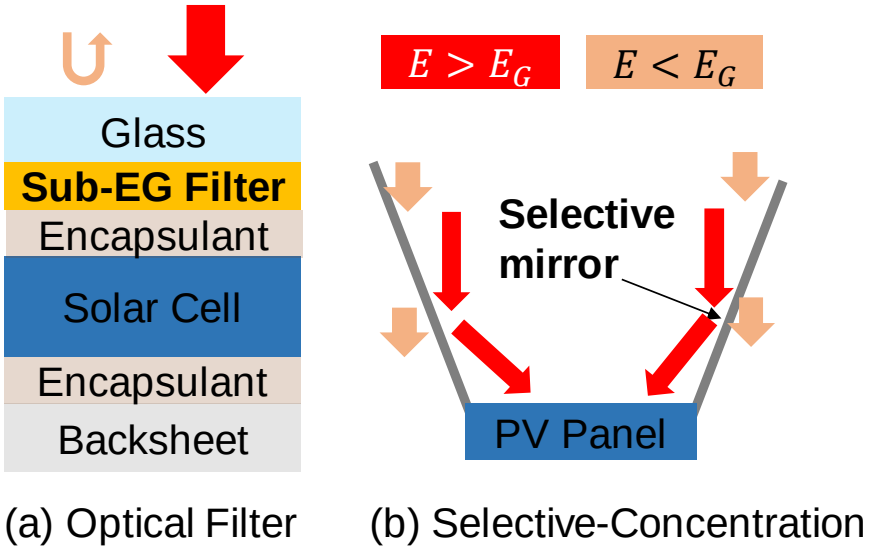

Fig. 3.8. Possible implementations of selective-spectral cooling by using a reflective optical filter or wavelength-selective mirror reflector for LCPV.

Other applications. Selective-spectral cooling can also be particularly interesting for low-concentration PV (LCPV) applications, where the heat from sub-BG photons scales with concentration factor, but without the benefit of active cooling. For LCPV, side mirrors are used to concentrate sunlight onto PV modules. The widely-used metal-coated mirrors, however, have the disadvantage of reflecting the near-IR sunlight, which is dissipated as heat in PV modules. One potential improvement is to adopt wavelength-selective mirror using nanophotonics [69,217] or IR transmissive polymeric films [218,219] such that only the useful photons are directed to solar modules and the rest just pass through the mirror, see Fig. 3.8(b). Self-heating due to sub-BG photons is therefore reduced.

3.4.2 Radiative Cooling

Radiation-enhanced design. As discussed in Sec. 3.3, the top (glass) and bottom (polymer backsheet) layers of PV modules are not ideal in terms of emitting

IR thermal radiation to the atmosphere and the ground. Hence, we propose to add radiative cooler layers to enhance thermal radiation from PV modules to the surroundings, see Fig. 3.9. The radiative cooler on top of the glass should have the ideal emissivity profile in Fig. 4 for maximum thermal emission, but must be transparent below 2.5 μm wavelength for solar irradiance. For objects at temperatures close to 300 K, thermal radiation shorter than 2.5 μm wavelength is negligible ($\sim$ 0.02 W/m^2 at 340 K). Hence, the transparency shorter than 2.5 μm does not sacrifice much radiative cooling power. In principle, such spectral response can be achieved using a nanophotonic crystal [69, 217]. An ideal blackbody can be used on the back surface to maximize thermal radiation exchange with the ground, but one can still use the radiative cooler for the back layer, since its performance is very close to a blackbody for IR radiation near 300 K. Note that those selective emitters which restrain thermal radiation between 8 m and 13 μm in [193, 220] are not suitable for cooling solar modules. The hemispherical emissivity of such emitters ($\bar{\varepsilon} = 0.32$) is far below that of glass ($\bar{\varepsilon} = 0.82$) , and actually would lead to higher temperature of solar modules. Those designs are only of great interest for cooling below the ambient, which solar modules illuminated under sunlight cannot achieve because solar irradiance (1000 W/m^2) is greater than thermal radiation of objects at $\sim$300 K.

3.4.3 Cooling Results and Implications

Ideal conditions. An interesting question is how much temperature reduction can be obtained by the two aforementioned cooling methods. To answer this question, we explored the cooling effects using our opto-electro-thermal coupled modeling framework to simulate the one-sun solar module temperatures with and without cooling. The simulation assumes ideal scenarios of the cooling methods (*i.e., ideal filter with cutoff at E_G for selective-spectral cooling and unity IR emissivity for radiative cooling),* which reveals the theoretical maximum reduction of temperature.

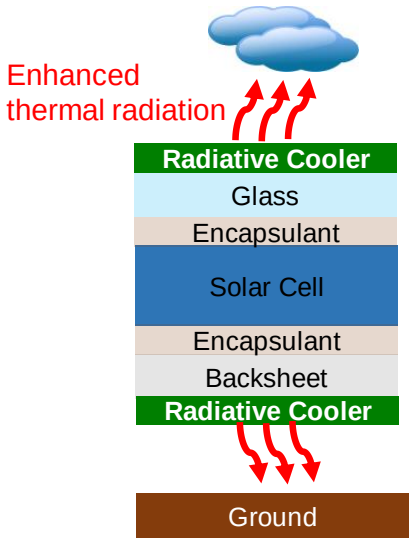

Fig. 3.9. Schematic of a solar module with enhanced radiative cooling.

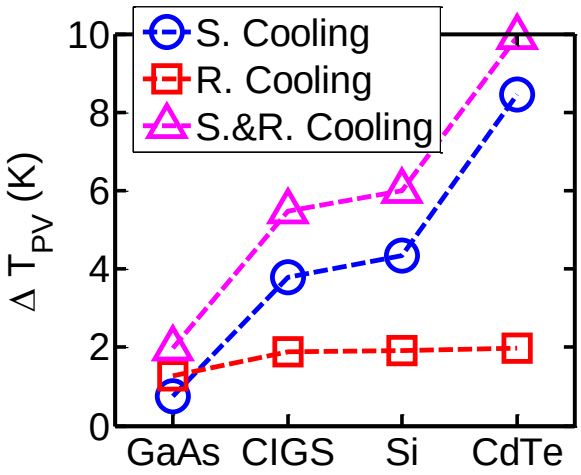

Fig. 3.10. Temperature reduction (with respect to module temperatures in Fig. 3.2) using different cooling methods (S. Cooling: selective-spectral cooling; R. Cooing: radiative cooling; S.& R. Cooling: selective-spectral cooling and radiative cooling combined) for different technologies.

Temperature reduction. Figure 3.10 illustrates the temperature reduction (ΔT_{PV}) using the cooling schemes, compared to the module temperatures in Fig. 3.2. One important observation is that the selective-spectral cooling method can re-

duce module temperatures by ∼4 K for CIGS and Si and ∼8 K for CdTe, but only ∼0.5 K for GaAs. This is because most of the sub-BG photons are already reflected in GaAs and further filtering these photons do not provide efficient cooling. Perfect radiative cooling provides limited cooling benefits (∼1 K to 2 K reduction) compared to glass covered modules for all technologies, which agrees with the calculation in [9]. The results indicate that replacing glass ($\bar{\varepsilon} = 0.82$) and PVF backsheets ($\bar{\varepsilon} = 0.85$) with ideal thermal emitters does not result in a large decrease in the temperatures of conventional terrestrial PV modules. By applying both cooling schemes simultaneously, one can achieve a superposed temperature reduction. The additive cooling is understandable since these two cooling methods address different sources of PV self-heating, namely, parasitic sub-BG absorption and imperfect thermal radiation.

Environmental factors dictate self-cooling. So far, we have calculated T_{PV} by assuming the ambient temperature $T_A = 300$ K, an effective convective coefficient $h = 10$ W/(K.m^2) (∼0.5 m/s wind speed), and the atmospheric transmittance for New Delhi in spring (Fig. 3.5). The remaining question is how environmental factors change the cooling effect. **First**, as h increases in a windier condition, more of the heat is lost through convection. Hence, the effectiveness of spectral and radiative cooling (reflected in absolute $\Delta\ T_{PV}$, see Fig. 3.11(a)) is reduced at higher wind speeds (higher h), because the excess heat is carried away by convection. Since wind speed depends on the season and the geographical location (e.g., average monthly wind-speed in New Delhi is around 4.2 m/s and 0.8 m/s in June and October, respectively [221]), the overall effectiveness of the self-cooling strategies must be evaluated carefully for a solar farm installed in a given geographical location. **Second**, at a fixed wind speed, radiative cooling is more effective in a hotter climate as shown in Fig. 3.11 (b), because thermal radiation power scales with temperature as $P \sim {T_{PV}}^4$. On the other hand, intrinsic power loss (e.g., carrier recombination) increases with temperature, leading to more heat dumped from the above-bandgap irradiance. Hence, reflecting the heat power from sub-BG photons, i.e., selective-spectral cooling, is slightly less effective with increasing T_A, as shown in Fig. 3.11 (b). Even though

selective-spectral and radiative cooling show different trends with the ambient temperature, the cooling gain by integrating these cooling methods is almost independent of T_A. **Third**, the degree of cooling depends on the illumination intensity, see Fig. 3.11 (c). Since the heat dissipated in the module is reduced at lower illumination, the relative efficiency improvement by the proposed cooling techniques is also suppressed at lower illumination. **Finally**, the presence of water vapor and CO_2 reduces the transmittance between 8 m and 13 m of the atmosphere, directly suppressing thermal radiation from the glass encapsulation to the outer space [193]. Consequently, radiative cooling is expected to be less useful in humid and cloudy climates.

Benefits of Cooling. We have demonstrated temperature reduction of the cooling methods on different PV technologies. The next obvious question is: how much energy yield gain can be achieved by cooling PV modules? For Si solar modules in terrestrial environments with an average ambient temperature of 300 K and wind speed of 0.5 m/s, the highest temperature reduction by applying the cooling methods is 6 K for Si commercial modules. Given the typical temperature coefficient $\beta \approx -0.45$ %/K of Si, 6 K can provide 2.7 % improvement to the short-term electricity output, corresponding to 0.5 % absolute increase in the efficiency of Si solar modules. Hence, the proposed cooling methods offer an alternative way to improve the efficiencies without changing the intrinsic material properties of the solar cells.

What about long-term energy gain due to self-cooling? Most degradation processes, such as moisture ingress and potential-induced degradation, are thermally activated; according to an Arrhenius relationship, the time to failure of solar modules is proportional to $\exp(-E_A/k_BT)$, where E_A is the effective activation energy and k_B is the Boltzmann constant. Using the calibrated average activation energy, $E_A = 0.89$ eV, accounting for a variety of degradation mechanisms (e.g., corrosion of interconnect, EVA yellowing, potential-induced degradation) [222] and the empirical equation for lifetime from [93], *6 K reduction in average operating temperature can delay PV module failure due to thermally activated degradation by up to ∼85%.* As a result,

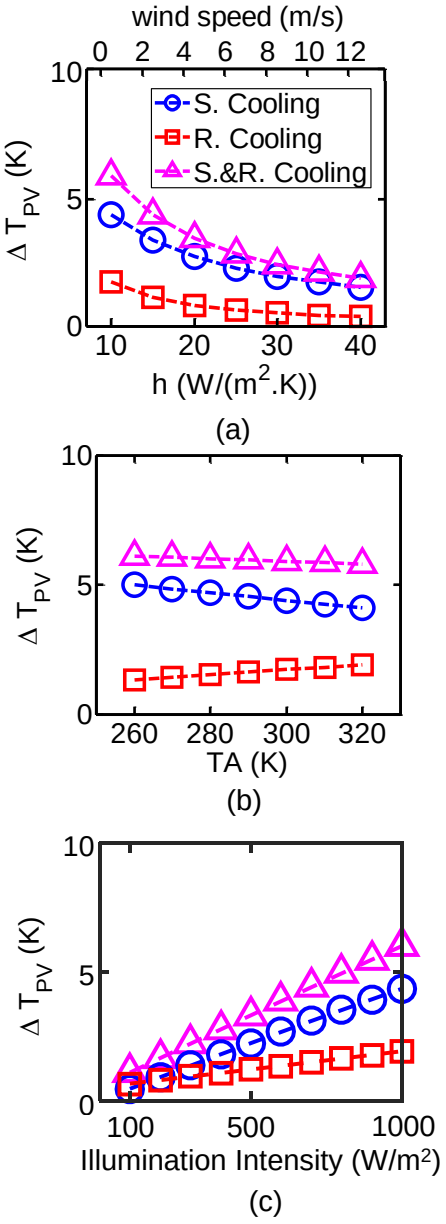

Fig. 3.11. Temperature reduction of conventional Si modules as a function of (a) convective coefficient/wind speed, (b) the ambient temperature, and (c) the illumination intensity. The default environment parameters for this simulation are TA = 300 K, h = 10 (W/(m^2.K)), and illumination = 1000 W/m^2. The atmospheric transmittance is taken from Fig. 3.5.

selective-spectral and radiative cooling can offer significant reliability improvements and greatly reduce the levelised cost of electricity (LCOE).

Environmental Factor. So far, the calculation of short- and long-term energy gains due to cooling has assumed a constant average ambient temperature of 300 K, solar irradiance of 1000 W/m^2, and wind speed of 0.5 m/s (h = 10 W/(K.m^2)). In practice, the increase of energy yields of a PV module over the course of an entire year depends on the local environment (e.g., illumination, wind speed, relative humidity, and ambient temperature). For example, the effectiveness of selective-spectral and radiative cooling is reduced at locations with high wind speed, because the module temperature is already low, and the additional benefits of selective-spectral/radiative cooling is relatively small. In addition, solar modules installed in environments with higher humidity and higher ambient temperature degrade substantially faster; hence, cooling the solar modules will significantly enhance the reliability and boost integrated energy yields. Hence, one must properly account for the geographic and temporal variation of the environmental factors to accurately predict all the incremental electricity yields by adopting the approaches discussed in this section.

Selective-spectral vs. Radiative Cooling. Integrating selective-spectral and radiative cooling provides the most cooling advantages for solar modules, but one also needs to consider the feasibility and cost in practice. Zhu [69] has demonstrated experimentally the use of a photonic crystal (PhC) structure to improve the hemispherical emissivity for radiative cooling but the emissivity still drops substantially at higher incidence angles (Fig. 3.8 (b) in [69]) and the hemispherical emissivity is estimated to be around 0.9, still far from unity. The fabrication cost of a nanophotonic structure also makes it an impractical option for large-scale manufacture. Additionally, though Ref. [68] argues that PhC structure can exhibit hydrophobicity and self-cleaning function, the potential soiling issues from the deep air holes in PhC still need to be carefully considered especially in environments lack of rain water. Other high-emissivity coverglass applications have also been explored especially for extraterrestrial PV modules, such as pseudomorphic glass (PMG) [223]. The economic viability of adopting such a glass-technology, especially for large-scale terrestrial solar farms, remains an interesting open question.

On the other hand, selective-spectral cooling in general is more beneficial than radiative cooling, making selective-spectral cooling much more preferable. Optical filters with customized wavelength selectivity are commercially available and may be suitable for large-scale manufacturing. Including additional UV blocking in the filter can further prevent performance degradation from yellowing and delamination of encapsulants [215,216]. The non-ideal sharpening of the filter which can degrade short circuit current and the tradeoff between cutoff sharpness and pass-band transmissivity must be carefully engineered. It also is important to note that the bandgaps of Si and GaAs decrease with temperature, characterized by the temperature coefficient (-4.73 x 10^{-4} eV/K for Si and -5.41 x 10^{-4} eV/K for GaAs), which may affect the optimal cutoff wavelength of the filter. The variation of bandgaps, however, is very small ($\sim$0.01 eV in the temperature range of interest for one-sun solar modules (300 K to 320 K). For concentrated PV with much higher operating temperature, the cutoff of the filter has to be optimized carefully to account for the temperature-dependence of bandgap. Alternative ways for selective-spectral cooling include de-texturing the front layer or nitridizing the back surface field in Si modules, both of which have been demonstrated experimentally [61, 224]. Hence, selective-spectral cooling can be more advantageous than radiative cooling for conventional solar modules, unless cost-friendly cover materials with high IR emissivity and solar transmittance are discovered. However, radiative cooling could be very effective for extraterrestrial solar modules in the absence of air convective cooling. Therefore, for both space and concentrated PV, radiative cooling remains promising to be further explored.

3.5 Conclusions

In this chapter, we discuss the self-heating effect in solar modules and propose the corresponding remedial self-cooling methods to counteract heating. The main conclusions of this chapter are:

1. We develop an opto-electro-thermal coupled simulation framework to find the stead-state operating temperature of solar modules by solving the energy-balance equation. The results are systemically validated by measurements for a variety of PV technologies.

2. By integrating the physics-based compact model from Chapter 2 into an eletro-thermal coupled circuit network, We create an open-source SPICE-based simulation framework to study the magnitude and spatial profile of non-uniform self-heating effects for monolithic solar modules.

3. we find that the intrinsic self-heating in PV modules has large components due to parasitic sub-BG absorption and inadequate thermal radiation. These results are confirmed by measurements of different solar technologies (i.e., GaAs, CIGS, Si and CdTe) and outdoor tests in literature [62, 69].

4. Besides intrinsic self-heating, shading-induced self-heating is also very deleterious to the reliability of solar modules, especially for monolithic solar module where bypass diode provides limited protection. Our simulation indicates that partial shading can elevate the temperature of the shaded cell up to 330 K, greatly accelerating the thermally activated PV degradation processes.

5. To reduce the operating temperature, we have proposed to optically redesign solar modules by implementing selective-spectral cooling (i.e., eliminate sub-BG parasitic photon absorption) and radiative cooling (i.e., enhance thermal radiation to the surroundings).

6. Substantial temperature reduction has been demonstrated in different PV technologies based on our self-consistently opto-electro-thermal simulation. Potentially, the temperature reduction can provide 0.5% absolute increase in efficiency and extend the lifetime by 80% for one-sun Si terrestrial solar modules.

7. We also predict that selective cooling is likely to be more cost-competitive as well as more effective than radiative cooling for conventional solar modules, while

the prospects of using radiative cooling in concentrated and extraterrestrial PV remain encouraging. The effectiveness of these cooling methods bring new potentials to improve reliability and performance of photovoltaics.

4. FORWARD MODELING OF BIFACIAL SOLAR MODULES

4.1 Introduction

In the last two chapters, we developed a physics-based modeling framework to calculate the temperature of a self-heated solar module, and its temperature- and illumination-dependent performance. In this chapter, we will extend the framework to estimate the annual energy yield ($\int_0^{1\ \mathrm{Year}} P_{Module}(IL, T, t)dt$) of bifacial solar modules with realistic meteorological data (with hourly/daily/seasonal variations of temperature and illumination).

As mentioned in Sec. 1.4, bifacial solar modules have demonstrated great potential to oust monofacial modules and further drive down the LCOE of PV. Several groups have reported on the performance of south-north-facing, optimally tilted, standalone bifacial solar modules, both numerically [91, 225–227] and experimentally [228, 229]. These studies have shown that the deployment parameters (e.g., elevation, orientation) and the environmental conditions (e.g., irradiance intensity, ground albedo) dictate the energy output of bifacial solar modules, and the synergistic effects of these factors ought to be accounted for when evaluating the performance of bifacial technologies. Unfortunately, these analyses are confined to only a few locations, so these studies do not offer any guidance regarding the optimized configuration and the maximum energy output in a global context where irradiance and albedo vary significantly.

Other groups have focused on worldwide studies but confined themselves to specific configurations that are not necessarily optimal. For example, Guo *et al.* [230] and Ito *et al.* [231] have presented worldwide analyses of east-west-facing, vertical bifacial solar modules. These vertical modules reduce soiling/snow losses [232, 233]

and produce more energy output during peak-energy-consumption hours compared to their south-north-facing counterparts. Guo *et al.* concluded that, for an arbitrary geographic location, an albedo threshold always exists above which vertical bifacial solar modules will outperform optimally tilted monofacial counterparts.

All these studies, however, confine themselves only to specific module configurations [230] or few geographic locations [91]. Consequently, there is still a lack of understanding in terms of the energy yield and optimization of bifacial module in a global context. Therefore, a full investigation of this promising technology can be very valuable to the community. Hence, we provide a global analysis and optimization of a variety of module configurations using our comprehensive opto-electro-thermal simulation framework. Our results reveal that the bifacial gain of ground-mounted bifacial modules is no more than $\sim 10\%$ across the globe for an albedo of 0.25, typical for groundcover of vegetation and soil. On the other hand, increasing albedo to 0.5 using artificial reflectors (e.g., white concrete) can double the bifacial gain to ∼20%; further, elevating the module 1 m above the ground can improve the bifacial gain to ∼30%. These results highlight the importance of highly reflective groundcover and module elevation for increasing/optimizing bifacial gain.

We also summarize our numerical results into a set of empirical equations that can analytically and optimally configure bifacial modules as a function of three design parameters—elevation (E), azimuth angle (γ_M), and tilt angle (β)—as schematically illustrated in Fig. 4.1. Our optimization results anticipate that for ground-mounted bifacial modules with an albedo of 0.5, east-west-facing vertically installed bifacial modules (Bi_{EW}) will outperform south-north-facing optimally tilted (Bi_{SN}) ones by up to 15% for latitudes within 30^o, and vice versa for latitudes above 30^o. In summary, our work offers a global perspective on standalone bifacial solar modules to facilitate a more detailed LCOE calculation of this technology [234, 235].

This chapter [1] is organized as follows: Section 4.2 introduces the simulation framework. Section 4.3 presents the global performance of bifacial solar modules for various

[1]The contents of this chapter are taken from [236]

deployment scenarios. Section 4.4 shows the derivation of a set of empirical equations that can analytically optimize bifacial solar modules for any arbitrary geographic location. Finally, Section 4.5 provides some concluding thoughts.

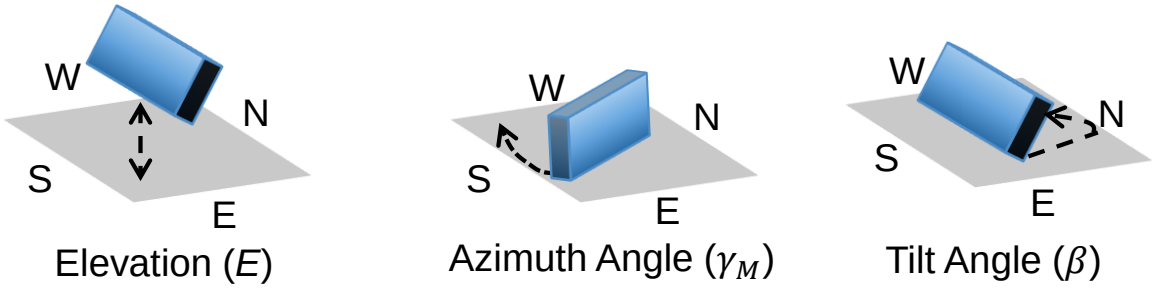

Fig. 4.1. The three parameters discussed in this chapter to optimize bifacial modules.

4.2 Simulation Framework

4.2.1 Irradiance Model

Solar Path. First, we begin by calculating the position of the sun, i.e., the solar path, which is a prerequisite to obtaining the insolation and its collection by solar modules. In this section, we use NREL's solar position algorithm [237] implemented in the Sandia PV modeling library [238] to simulate the solar path—specifically, the solar zenith (θ_Z) and azimuth (γ_S) angles at any arbitrary time and geographic location.

Simulate GHI. Next, we estimate the intensity of solar irradiance as follows. First, we calculate the intensity of global horizontal irradiance (GHI or I_{GHI}) on a minute-by-minute basis by inputting the solar path into the Haurwitz clear-sky model [239–241] implemented in PVLIB [238]. The clear-sky model assumes an idealized atmospheric condition (i.e., high irradiance transmission), which exists only for certain locations and weather conditions. Therefore, directly applying the clear-sky model often results in an overestimation of solar insolation. Fortunately, the

NASA Surface Meteorology and Solar Energy database [242] provides open access to the satellite-derived 22-year *monthly* average insolation on a horizontal surface (kWh/(m^{2}day)), In_{Hor}, with a *spatial resolution* of 1 × 1 degree (latitude and longitude). The challenge here is that the database only provides monthly average irradiance, while accurate simulation of PV output necessitates a higher temporal resolution. Therefore, it is imperative to convert this monthly average into a minute-by-minute basis (given by the clear-sky model). To do so, we first assume constant daily horizontal insolation within a given month, and for each day thereof, we scale the minute-by-minute simulated $I_{GHI,clear-sky}$ to the average insolation In_{Hor} to obtain the final I_{GHI} following $I_{GHI} = I_{GHI,clear-sky} \times (In_{Hor} / \int I_{GHI,clear-sky} dt)$. Consequently, our approach allows us to simulate I_{GHI} while fully accounting for the geographic and climatic factors.

Irradiance Decomposition. The calculated I_{GHI} must be further decomposed into two segaments: a) direct normal irradiance (DNI or I_{DNI}) and b) diffuse horizontal irradiance (DHI or I_{DHI}). The relationshp between these irradiance components can be expressed as follows:

$$I_{GHI} = I_{DNI} \times \cos(\theta_Z) \ + I_{DHI}. \tag{4.1}$$

Next, given the minute-by-minute sky clearness index $k_{T(M)}$, we use the Orgill and Hollands model [243] to empirically estimate I_{DNI} and I_{DHI} from I_{GHI}. Specifically, the clearness index is defined as the ratio between I_{GHI} and extraterrestrial irrdiance (I_0) on a horizontal surface, i.e., $k_{T(M)} = I_{GHI}/(I_0 \times \cos(\theta_Z))$, where I_{GHI} is already known and I_0 can be analytically computed based on the day of year (DOY) [244,245]. Inputting $k_{T(M)}$ into the Orgill and Hollands model, we can decompose I_{GHI} into I_{DNI} and I_{DHI}. An example of the simulated irradiances at Washington DC (38.9^o N and 77.03^o W) on June 10th is shown in Fig. 4.2. Other empirical models have also been proposed for GHI decomposition [246–248], but they produce comparable results [249]. The conclusions therefore are not affected by the model selection herein.

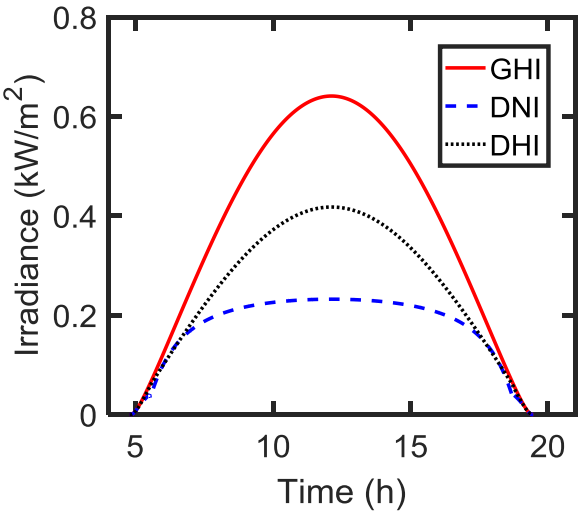

Fig. 4.2. Global horizontal irradiance (GHI), direct normal irradiance (DNI), diffuse horizontal irradiance (DHI) at Washington, DC (38.9^o N and 77.03^o W) on June 10th.

Next, we model the angular contributions of I_{DHI} obtained earlier. Note that the angular distribution of I_{DHI} is strongly correlated to the clearness index [92]. The diffuse irradiance that subtends the angular region adjacent to I_{DNI} is referred as the circumsolar irradiance $I_{Diff(C)}$. $I_{Diff(C)}$ results from light scattering by aerosols particularly prevalent under clear sky. The diffuse irradiance that emerges from the Earth horizon at $\theta_Z = 90^o$ is called horizon brightening $I_{Diff(H)}$ and is caused by the Earth albedo irradiance. Both $I_{Diff(C)}$ and $I_{Diff(H)}$ are then superimposed on an isotropic diffuse irradiance background $I_{Diff(Iso)}$ to form an overall anisotropic diffuse irradiance spectrum [250]. The anisotropicity of the diffuse irradiance has a vital impact on the performance of solar modules due to the angularly dependent self-shading and light collection. Hence, we need to adopt the angle-dependent Perez model [250, 251] obtained from [238] to decompose I_{GHI} to correct for the overoptimistic estimation of PV energy production associated with a simpler isotropic model [92].

4.2.2 Light-Collection Model

After calculating the irradiance, the second step involves calculating the integrated light collection by a solar module arising from each irradiance component, i.e., direct, diffuse, and albedo light, as depicted in Fig. 4.1. *In our view-factor based approach, we consider a single standalone module in two dimensions, which is equivalent to an infinitely long row of modules in three dimensions.*

Direct Irradiance. To evaluate the contribution of the direct irradiance I_{DNI}, we first need to know the angle of incidence (AOI) between I_{DNI} and the front/rear surface of a solar module. Fortunately, AOI can be analytically calculated based on the solar θ_Z and γ_S angles as well as the tilt (β) and azimuth (γ_M) angles of the solar module, expressed as

$$AOI = cos^{-1}\left\{\cos\left(\theta_Z\right) \times \cos\left(\beta\right) + \sin\left(\theta_Z\right) \times \sin\left(\beta\right) \times \cos\left(\gamma_S - \gamma_M\right)\right\}. \quad (4.2)$$

For a bifacial solar module, the tilt β_{Rear} and azimuth $\gamma_{M(Rear)}$ angles of the rear side are $(180^o - \beta_{Front})$ and $(\gamma_{M(Front)} + 180^o)$, respectively. Finally, the illumination by I_{DNI} on both the front and rear sides of solar modules can be estimated as follows:

$$I_{PV:Dir(Front/Rear)} = (1 - R_{Loss}) \times \cos(AOI_{(Front/Rear)}) \times I_{DNI}, \quad (4.3)$$

where R_{Loss} is the angle-dependent reflection loss from the module surface. Here, we use a widely applied empricial equation from [230, 251–253] that has demonstrated great accuracy in analytically approximating the angular reflectivity.

Tracking System. Because the solar module is not always perfectly aligned with the solar position (i.e., $AOI \neq 0$), it can not fully collect the direct irradiance. Solar trackers, which can continuously align the module with the direction of the direct irradiance, can recover this loss. For example, assuming that the Sun only moves from east to west (i.e., on the equator during spring/fall equinox) with a constant intensity I_0, a dual-axis tracking system (that rotates both the tilt and azimuth angles of the solar module) can recover

$$\frac{\int_0^t I_0 dx - \int_0^t I_0 \cos(\theta_Z) dx}{\int_0^t I_0 \cos(\theta_Z) dx} = \frac{\pi}{2} - 1 \approx 57\%$$

of the direct light for a horizontal module relative to a fixed-tilt system (t is the total daytime and θ_Z changes from 0 to $\pi/2$ linearly with time). It should be noted that tracking systems will provide a lower gain for a tilted solar module, and they also can not improve the collection of diffuse light. Therefore, it is hard to achieve this gain of 57% in practice. Still, more than half of the utility solar farms (mostly monofacial modules) in the United States have already implemented either single-axis (only rotate the tilt angle) or dual-axis trackers [254]. Moreover, Dupuis et al. have also shown single-axis tracking can boost the energy yield of a bifacial solar module by up to 23.7% [255]. In spite of the additional cost, integrating bifacial modules with tracking systems can be a very attractive option to achieve ultra-high energy yields, and therefore should be thoroughly investigated in the future.

Diffuse Irradiance. The calculation of diffuse light is more involved than that of direct light due to the anisotropic angular spectrum consisting of circumsolar, horizon brightening, and isotropic diffuse light. Each of the diffuse components requires a distinct approach to estimate its light collection by solar modules. A complete list of equations to calculate the contribution from diffuse light is given below,

$$I_{PV:Diff(Iso)} = (1 - R_{Loss}^{Int}) \times I_{Diff(Iso)} \times VF_{M \to Sky}, \tag{4.4}$$

$$I_{PV:Diff(C)} = (1 - R_{Loss}) \times I_{Diff(C)} \times \cos(AOI_{Cir}), \tag{4.5}$$

$$I_{PV:Diff(H)} = (1 - R_{Loss}) \times I_{Diff(H)} \times \sin(\theta_T), \tag{4.6}$$

$$I_{PV:Diff} = I_{PV:Diff(Iso)} + I_{PV:Diff(C)} + I_{PV:Diff(H)}, \tag{4.7}$$

where $VF_{M \to Sky} = (1 + \cos(\theta_T))/2$ is the module-to-sky view factor and AOI_{Cir} is the angle of incidence for circumsolar diffuse light (equal to that of direct light until

$\theta_Z > 85^0$). Note, that because $I_{Diff(Iso)}$ is isotropic, rather than for one fixed angle, R^{Int}_{Loss} in Eqn. 4.4 is the integral of reflection losses over the solid-angle window of the isotropic diffuse irradiance incident onto the surface (see Eqns. (6a–6c) in [253]). Equations 4.4 to 4.7 enable us to analytically calculate the diffuse illumination on both the front and rear surfaces of solar modules.

Albedo Irradiance. Light-collection calculation of ground-reflected albedo light requires careful examination of self-shading, i.e., the ground shadow cast by solar modules, which substantially reduces illumination onto the ground, and consequently, the ground-reflected albedo irradiance both on the front and rear sides of a solar module [91, 256]. Since bifacial solar modules do not absorb the infrared sub-bandgap photons (which potentially can mitigate self-heating, see Chapter 3) [84], only the visible above-bandgap photons will be self-shaded in the ground shadow. There are two categories of self-shading effects: 1) self-shaded direct and circumsolar diffuse irradiances, and 2) self-shaded isotropic diffuse irradiance, both of which are considered in our calculation as described below.

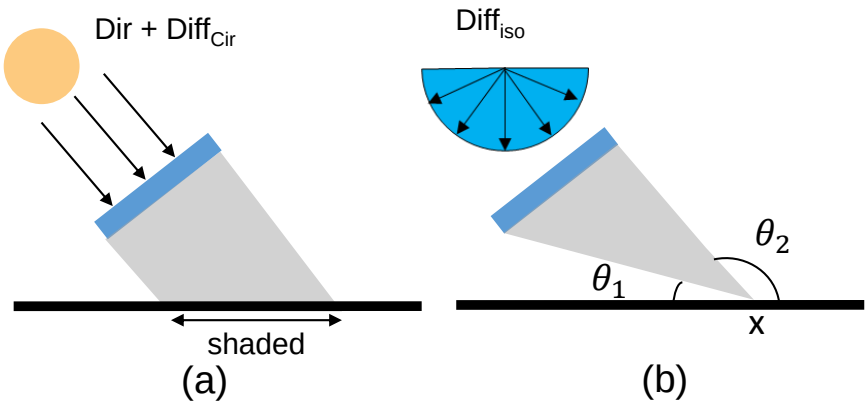

Fig. 4.3. Self-shading of albedo light from (a) direct ($I_{Dir)}$) and circumsolar diffuse light ($I_{Diff(cir)}$), and (b) isotropic diffuse light ($I_{Diff(iso)}$).

Reflected Direct and Circumsolar Diffuse Irradiance. As shown in Fig. 4.3(a), part of the ground does not receive I_{Dir} and $I_{Diff(C)}$ due to self-shading by

solar modules. Thus, only the unshaded portion of the ground can contribute to the reflected I_{Dir} and $I_{Diff(C)}$ albedo light. It can be evaluated by

$$I^{DNI+Diff(C)}_{PV(Front/\mathrm{Rear}):Alb} = (1 - R^{Int}_{Loss}) \times R_A \times [I_{Dir} \times \cos(\theta_Z) + I_{Diff(C)}] \times \cos(\theta_{Z(Cir)}) \times (\frac{1 - \cos(\theta_{T(Front/\mathrm{Rear})})}{2} - VF_{shaded \to Front/\mathrm{Rear}} \times L_{Shadow}/H), \tag{4.8}$$

where R_A is the ground albedo coefficient, $\theta_{Z(Cir)}$ is the zenith angle of the circumsolar diffuse light (equals θ_Z until $\theta_Z > \theta_{Z(Max)} = 85^o$), L_{Shadow} is the length of the shadow cast by a solar module, $H = 1$ m is the module height, and $VF_{shaded \to Front/Rear}$ is the view factor from the shaded region of the ground to the front/rear side. We calculate L_{Shadow} and $VF_{shaded \to Front/Rear}$ analytically following the methodologies in [257–259]. Note that the ground in our framework is assumed to be a Lambertian reflector, i.e., an ideal diffuse reflector with a rough surface that reflects the incident light isotopically. In practice, no surface is purely Lambertian, but instead, they lie between a Lambertian reflector and a specular reflector (like a mirror where the Fresnel law governs reflection). Coakley has presented a set of empirical equations that can model the directional albedo light for a variety of groundcovers [260]. The impact of this anisotropic albedo light on bifacial modules remains an interesting open question for future research.

Reflected Isotropic Diffuse Irradiance. Blocked by solar modules, only a fraction of isotropic diffuse irradiance from the sky can reach to the ground and be reflected, see Fig. 4.3(b). Self-shading due to sky masking of $I_{Diff(Iso)}$ erodes the albedo collection of solar modules, because $I_{Diff(Iso)}$ depends strongly on the location of the ground (x) from which the view factor $VF_{x \to sky}(x)$ is calculated [251], i.e.,

$$VF_{x \to sky}(x) = 1 - [cos(\theta_1) + cos(\theta_2)]/2, \tag{4.9}$$

The masking angles θ_1 and θ_2 at position x are labeled in Fig. 4.3(b). Note that only a portion of the reflected $I_{Diff(Iso)}$ illuminates the rear side of a solar

module, characterized by the view factor from position x to the front/rear side, $VF_{x\rightarrow Front/Rear}(x) = 1 - VF_{x\rightarrow Sky}(x)$. Finally, one must integrate the albedo irradiance collected by the solar module over the ground to estimate the total illumination

$$I^{Diff(Iso)}_{PV(Front/Rear):Alb} = 1/H \times (1 - R^{Int}_{Loss}) \times R_A \times I_{Diff(Iso)} \times \int_{-\infty}^{+\infty} VF_{x\rightarrow sky}(x) \times VF_{x\rightarrow Front/Rear}(x) dx. \tag{4.10}$$

Here, Eqn. 4.10 assumes an infinitely large ground reflector, which yields slightly higher albedo light compared to the finite ground reflector used in [11], [14]. Our framework is general and can account for finite ground correction, if needed.

Eventually, the total contribution of the albedo irradiance on the front/rear side is given by the sum of Eqns. 4.8–4.10:

$$I_{PV(Front/Rear):Alb} = I^{Diff(Iso)}_{PV(Front/Rear):Alb} + I^{DNI+Diff(C)}_{PV(Front/Rear):Alb}. \tag{4.11}$$

The light-collection model enables us to rigorously calculate the total illumination on both the front and rear sides of a bifacial solar module by accounting for self-shaded albedo light. Knowing the total amount of light incident on the module, we next couple this optical illumination to the electro-thermal model of the module to assess the total energy production by a bifacial solar module. This crucial aspect of the calculation has sometimes been omitted in various publications [259, 261].

4.2.3 Electro-Thermal Module Model

Power Conversion Efficiency. In the third and final step of the overall model, we must convert the incident light into electrical output. In our framework, the energy conversion from solar illumination into electricity is estimated as follows:

$$P_{PV} = I_{PV(Front)} \times \eta_{Front} + I_{PV(Rear)} \times \eta_{Rear}, \tag{4.12}$$

whereP_{PV} is total output power by bifacial solar modules, η_{Front} and η_{Rear} are the front- and rear-side efficiencies, respectively, and $I_{PV(Front)}$ and $I_{PV(Rear)}$ denote the

front- and rear-side illumination of solar modules, respectively. Although the model is general and can be used for any technology, for illustration, we use the performance parameters obtained from commercially available bifacial solar module Bi60 manufactured by Prism Solar [262]. Specifically, the standard test condition (STC) efficiency of the front side for the simulated bifacial module $\eta_{Front(STC)} = 17.4\%$.The bifaciality of the module, which is defined as the ratio between the rear-side and front-side efficiencies, is $\eta_{Rear(STC)}/\eta_{Front(STC)} = 90\%$, corresponding to $\eta_{Rear(STC)} = 15.6\%$.

Electro-Thermal Model. The efficiency ($\eta(T_M)$) of bifacial solar modules in the field also depends on the real-time operating temperature described by

$$\eta(T_M) = \eta_{(STC)} \times \{1 + \ \beta \times (T_M - 298 \text{ K})\}. \tag{4.13}$$

Here, $\beta = -0.41\%/K$ is the temperature coefficienct retreived from [262] and T_M is the module temperature. Under solar illumination, self-heating elevates T_M above the ambient temperature T_A [192]. Due to the additional rear-side absorption relative to monofacial, the bifacial module is expected to have greater energy input. However, bifacial modules are more transparent to sub-bandgap photons than monofacial modules, resulting in less self-heating [84]. Indeed one can solve the energy-balance equation self-consistently to obtain T_M, but this approach is only amenable to numerical methods and is not ideal for large-scale simulation. Hence, we use an analytical formula developed by Faiman [194] that empirically calculates T_M based on the illumination and windspeed as follows:

$$T_M \ = T_A + \frac{I_{PV(Front)} + I_{PV(Rear)}}{U_0 + U_1 \times WS}, \tag{4.14}$$

where WS denotes the wind speed that dictates convective cooling; and U_0 and U_1 are empirical fitting parameters contingent on module type and deployment (e.g., open rack and rooftop). Equation 4.14 calculates the module temperature based on both the front and rear solar absorption, thereby has explicitly considered temperature variation due to different ground albedo (e.g. vegetation vs. concrete). Here, we calibrate U_0 and U_1 to the nominal operating cell temperature ($NOCT = 47C^o$) of the

Prism Solar Bi60 bifacial solar modules [262]. Global monthly average windspeed and ambient temperature data sets, also provided by the NASA meteorological database [242], are used in Eqn. 4.14 to calculate T_M, and sequentially, the temperature-corrected efficiency of bifacial solar modules. Note that the windspeed and T_A data in [242] involve monthly averages; in other words, our simulation assumes that the windspeed and T_A are constant within a month. For locations with high intra-day temperature variation, the results may overestimate the energy yield since the highest diurnal temperature (when solar modules generate most power) can be higher than the average (a morning-to-noon temperature difference up to 45 ^{o}C in desert environments [263]) and therefore significantly reduces the efficiency. Accounting for the hourly variation of T_A and windspeed will improve the accuracy of the results, which will be an important aspect of future research on the topic.

Power Loss due to Nonuniform Illumination. As demonstrated by both simulation and experiments, self-shading can cause spatially nonuniform illumination on the rear surface of solar modules [91, 264, 265]. Equation 4.12 neglects this additional power loss from non-uniform illumination distribution. Note that elevating modules above the ground improves the illumination uniformity and reduces the loss associated with nonuniform illumination. Furthermore, the homogeneous front-side illumination can also offset the nonuniformity at the rear side and mitigate the corresponding loss. Nonetheless, if needed, the inclusion of such performance degradation can be easily achieved in our framework by using the analytical method described in [266].

4.2.4 Simulation Demonstration

To validate the aforementioned comprehensive simulation framework, we benchmark our results against the available data from the literature (including simulation [91] and experiments [229, 267]) as well as field data measured by NREL. Among these data sets, Ref. [91] performed sophisticated ray-tracing simulation for optimiz-

ing annual production of bifacial modules in two different locations (i.e., Cairo and Oslo). Sugibuchi *et al.* [267] measured bifacial gain with two different albedo coefficients (grass versus shell grit), and here, only data from May to August is used to eliminate snowing effects. The measured data from Ref. [229] was taken at Albuquerque, New Mexico, by the Sandia National Labororaties from 02/2016 to 02/2017, and it covers variously configured bifacial modules (e.g., 15^o tilted east-west and 30^o tilted south-north facing bifacial modules). Finally, the field data recorded by NREL were taken at Golden, Colorado, dating from 12/2016 to 08/2017. Note that the geographic locations of our benchmark results span across Asia, Africa, Europe, and North America.

Remarkably, our results match the bifacial gain reported in the literature within 6.4%. This excellent match was obtained even though our framework uses the NASA 22-year average meteorological database and assumes idealities such as infinite-size ground reflectors and obstruction-free shading. The benchmark results against field measurement are summarized in Table 4.1. The framework allows us to simulate and optimize the performance of standalone bifacial solar modules with different configurations (e.g., bifaciality, orientation, elevation, albedo) at any arbitrary time and geographic location. For example, Fig. 4.4 summarizes the simulated output power of three unique types of solar modules: 1) south-north-facing monofacial ($Mono_{SN}$), 2) south-north-facing bifacial (Bi_{SN}), and 3) east-west-facing bifacial (Bi_{EW}). These modules are all elevated 0.5 m above the ground with an albedo of 0.5 typical for white concrete. Bi_{EW} is tilted 90^o, i.e., vertical installation, whereas the tilt angles of $Mono_{SN}$ and Bi_{SN} are optimized (for maximum production) at 37^o and 48^o, respectively.

In the following section, we will extend our single-day analysis to the annual performance of differently configured solar modules in a global context, while fully exploring the effects of self-shading on the performance and optimization of bifacial solar modules.

Table 4.1.
Modeling Framework Validation Against Literature

Location (Type)	Elevation / Height	Albedo / Bifaciality	Tilt Angle / Facing	Reported Bi. Gain	Calculated Bi. Gain	Difference
Cairo (Sim.) [91]	1/0.93 (m)	0.2/0.8	26^o/South	11.0 %	11.1 %	-0.1 %
Cairo (Sim.) [91]	1/0.93 (m)	0.5/0.8	22^o/South	24.8 %	25 %	-0.2 %
Oslo (Sim.) [91]	0.5/0.93 (m)	0.2/0.8	51^o/South	10.4 %	13.6 %	-3.2 %
Oslo (Sim.) [91]	0.5/0.93 (m)	0.2/0.8	47^o/South	16.4 %	22.8 %	-6.4 %
Hokkaido * (Exp.) [267]	0.5/1.66 (m)	0.2/0.95	35^o/South	23.3 %	25.7 %	-2.4 %
Hokkaido * (Exp.) [267]	0.5/1.66 (m)	0.5/0.95	35^o/South	8.6 %	13 %	-4.4 %
Albuquerque (Exp.) [229]	1.08/0.984 (m)	0.55/0.9	15^o/South	32.5** %	30.2 %	2.3 %
Albuquerque (Exp.) [229]	1.08/0.984 (m)	0.55/0.9	15^o/West	39** %	36.7 %	2.3 %
Albuquerque (Exp.) [229]	1.03/0.984 (m)	0.25/0.9	30^o/South	19** %	14.6 %	4.4 %
Albuquerque *** (Exp.) [229]	0.89/0.984 (m)	0.25/0.9	90^o/South	30.5** %	32.2 %	-1.6 %
Golden (Exp.) ****	1.02/1.02 (m)	0.2/0.6	30^o/South	8.3 %	8.6 %	-0.3 %

* Only data from May to August were used to eliminate snow effects. ** Average bifacial gain of multiple test modules was used. *** The east-west-facing vertical modules measurement in [229] shows great discrepancy between two modules; therefor, it is not included here. **** Bifacial measurement (12/2016 to 08/2017) performed by NREL.

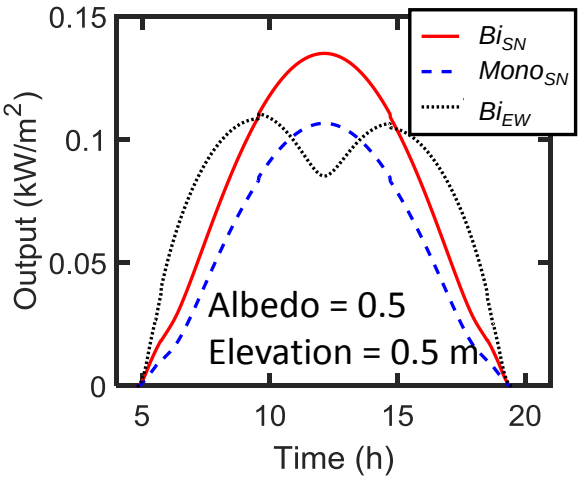

Fig. 4.4. Electricity output of a solar module in three configurations on a minute-by-minute basis at Washington, DC (38.9^o N and 77.03^o W) on June 10th.

4.3 Global Performance of Bifacial Solar Modules

Global maps of location- and configuration-specific performance of optimized bifacial solar modules have not been reported in the literature. Hence, we apply the rigorous framework presented in Sec. 4.2 to investigate bifacial gain of bifacial modules relative to their monofacial counterpart worldwide. For concreteness, we will focus on the worldwide results for three cases: (a) ground mounting with a ground albedo of 0.25 (natural ground reflector such as vegetation and soil), (b) ground mounting with a ground albedo of 0.5 (white concrete), and (c) 1 m elevation with a ground albedo of 0.5. *Here, we will illustrate that only limited bifacial gain is achievable across the entire world due to the low albedo of natural groundcover and self-shading of albedo light; however, one can substantially improve the bifacial gain by deploying highly reflective groundcovers and elevating the modules above the ground to reduce self-shading.* For a comprehensive comparison of bifacial performance, Appendix B includes an extensive table of global maps of optimal deployment, bifacial gain, and annual electricity production for a broad range of elevation and ground albedo.

Bifacial Gain. Bifacial gain is defined by Eqn. 1.2, which measures the improvement of bifacial module over monofacial ones. Figure 4.5(a.2) shows that an albedo of 0.25 (typical for natural groundcover) results in a bifacial gain of less than 10% globally, even when the *ground-mounted* bifacial solar modules have been optimized for azimuth and tilt angles to maximize annual energy production. The limited bifacial gain herein is attributable to 1) the low ground albedo coefficient as well as 2) performance erosion due to self-shading. To further improve the bifacial gain, one must either increase the ground albedo coefficient, elevate modules above ground to reduce self-shading, or apply both simultaneously. Indeed, our results elucidate that increasing the ground albedo to 0.5 can boost the bifacial gain of ground-mounted modules to ∼20% globally, as shown in Fig. 4.5(b.2). The substantial improvement of bifacial gain encourages the development of cost-effective artificial ground reflectors to supersede natural groundcovers. In addition, our simulation also predicts that elevating the module 1 m above the ground can further increase the bifacial gain to ∼30% by recovering self-shading induced losses, see Fig. 4.5(c.2). However, elevating modules can result in additional installation cost; so, careful optimization of module elevation is required to maximize the bifacial gain while restraining installation cost. In the next section, we will derive a set of empirical rules to calculate the optimum elevation analytically.

Clearness Index. The performance of bifacial solar modules also depends on the local climatic condition, i.e., the annual sky clearness index $k_{T(A)}$, which indicates the amount of extraterrestrial irradiance transmitting through the atmosphere and reaching to the ground. Interestingly, bifacial gain decreases with clearness index, i.e., the absolute bifacial gain is ∼5% higher in Shanghai than Cairo as shown in Fig. 4.5(c.2). This increase in the bifacial gain is due to the higher concentration of diffuse light in the lower-transmitting atmosphere in Shanghai ($k_{T(A)}$≈0.35 in Shanghai compared to $k_{T(A)}$≈0.7 in Cairo). *Therefore, despite the lower total solar insolation, bifacial solar modules benefit more in Shanghai than Cairo due to the additional rear-side absorption of diffuse light.* This finding, i.e., bifacial modules are more advantageous in

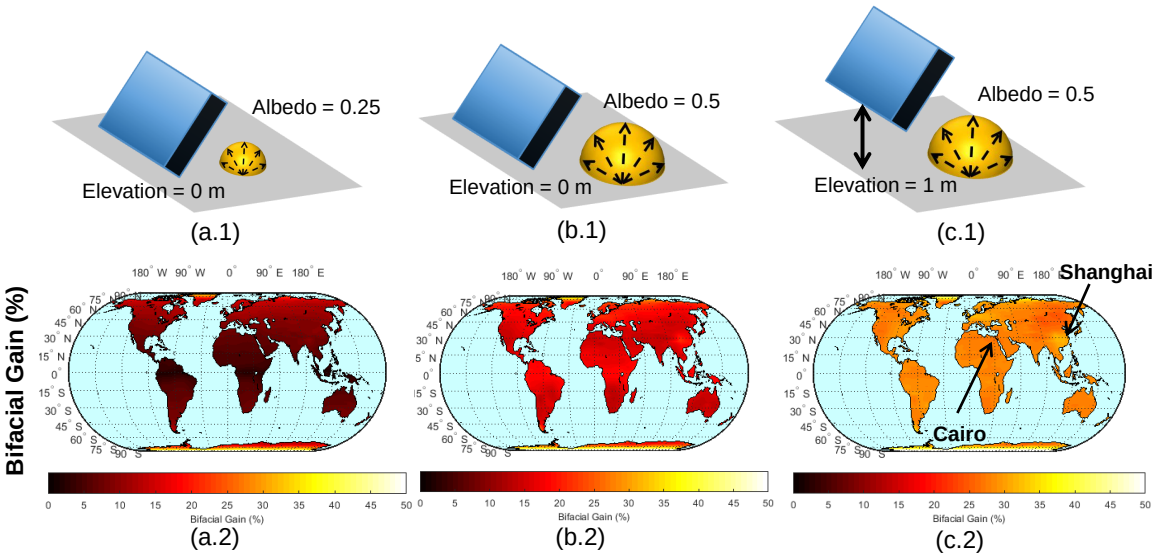

Fig. 4.5. Three different deployment scenarios of bifacial solar modules are simulated (depicted in the first row), i.e., (a) ground mounted with a ground albedo of 0.25, (b) ground mounted with a ground albedo of 0.5, and (c) 1m elevated with a ground albedo of 0.5. Global maps of these scenarios showing optimal bifacial gain (the second row)

cloudier locations, has a profound yet practical implication on the adoption of bifacial modules globally. Note that the analytical equations developed to estimate bifacial gain in [268–270] do not always account for the clearness index, so the results may not be accurate. Hence, great caution should be taken when applying these equations to evaluate the location-specific performance of bifacial solar modules.

In this section, we have summarized our key results for ground-mounted modules with an albedo of 0.25, the bifacial gain of fully optimized bifacial modules is less than 10% worldwide. Increasing the albedo to 0.5 and elevating modules 1 m above the ground, one can increase the bifacial gain up to ∼30% globally. In the following section, we will explain how these optimizations were achieved and present a set of empirical guidelines for deploying bifacial modules.

4.4 Worldwide Optimization of Bifacial Modules

As already highlighted, there are three design parameters to optimize the electricity yield of bifacial modules—elevation (E), azimuth angle (γ_M), and tilt angle (β). These parameters are mutually dependent; specifically, optimal azimuth and tilt angles are a function of elevation. To isolate correlation among the parameters, we optimize the energy yield of bifacial modules by changing a single parameter, while keeping the other two parameters constrained. In this section, we specifically discuss the 1) minimum elevation E_{95} to achieve 95% of maximum energy production; 2) optimum azimuth angle at fixed elevation, 3) finally, optimum tilt angle for given E and γ_M. More importantly, for each parameter, we have derived a set of empirical equations that can analytically estimate the optimal value for any arbitrary location.

4.4.1 Elevation

Effect of Elevation. An important factor affecting the performance of bifacial modules is their elevation above the ground. Highly elevated modules suffer considerably less from self-shading as shown in [91,227,256], which accords with our results in Sec. 4.3. Therefore, elevation is a crucial design parameter to optimize the performance of bifacial solar modules. However, as the elevation continues to increase, the loss due to self-shading diminishes gradually until its effect is completely negligible. Hence, for infinitely large ground reflectors, the energy production of bifacial modules plateaus at high elevation above the ground [91,256] and elevating the module further does not improve the energy yield, see Fig. 4.6(a).

The elevation cutoff where production of bifacial solar modules starts to saturate is valuable to installers for minimizing the installation cost while preserving sufficient electricity yields. So, we estimate the average minimum elevation (E_{95}) to achieve 95% of the maximum energy production (i.e., self-shading free) as a function of latitude at a fixed ground albedo, see Fig. 4.6(b). It is noteworthy that E_{95} decreases almost linearly with latitude, which is attributable to the suppressed self-shading by higher

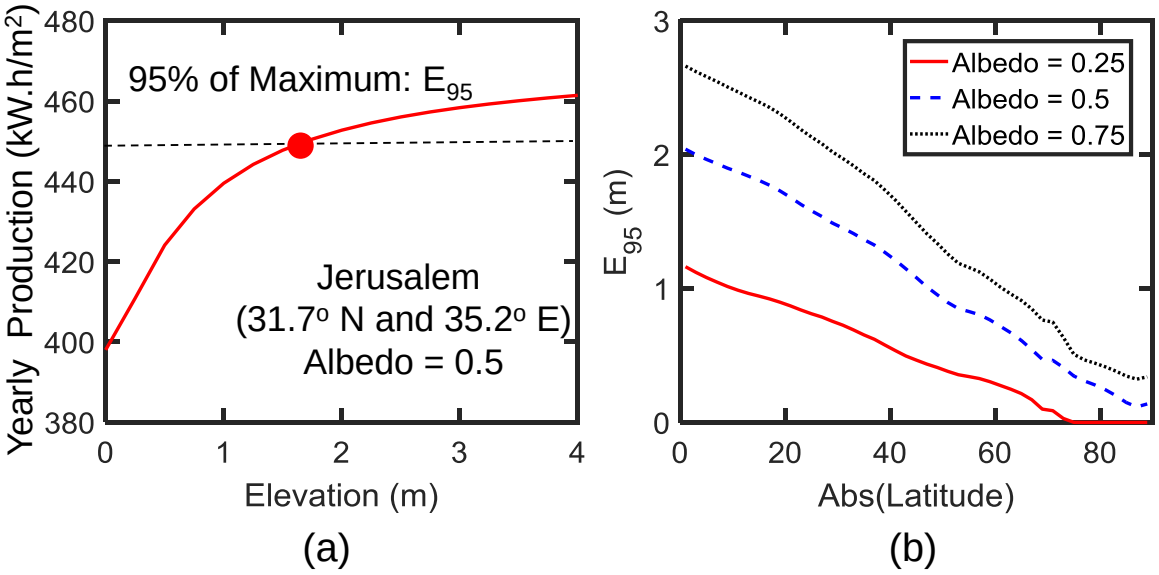

Fig. 4.6. (a) Yearly electricity production of optimally oriented and tilted bifacial solar modules with a height of 1 m as a function of elevation at Jerusalem (31.7^o N and 35.2^o E). The ground albedo is 0.5. The dashed line is the cutoff for 95% of the self-shading-absent maximum energy yield and red circle is the minimum elevation E_{95} to achieve this threshold. (b) E_{95} of bifacial solar as a function of absolute latitude for ground albedos of 0.25, 0.5, and 0.75. Note that the minimum elevation for each latitude in this plot is the average over longitudes with different clearness indexes

optimal tilt angle at higher latitude. In addition, E_{95} rises with higher ground albedo up to almost 3 m near the Equator. Higher ground albedo increases the contribution of albedo light, making bifacial modules more susceptible to self-shading. Thus, E_{95} has to increase to compensate the added self-shading loss.

Empirical Equations. By applying linear regression to the results in Fig. 4.6, we derive a set of empirical equations to estimate E_{95} as a function of module height, latitude, and ground albedo, see Table 4.2. The relative error of the empirical equations compared to our numerical results is less than 1% for realistic albedo coefficients (from 0.25 to 0.75). Hence, these equations can assist installers to minimize the installation cost associated with elevating modules without sacrificing energy production. Note that our equations assume a large ground reflector area (> 100 times the mod-

ule area [91]); otherwise, E_{95} is expected to drop because of the reduced view factor between the small ground area and the bifacial modules at high elevation.

Note that elevating solar modules can also enhance convective cooling power (wind speed increases with elevation [271]), thereby reduce the operating temperature. This cooling gain can boost the efficiency as well as improve the long-term durability of solar modules [192]. On the hand other, it must be pointed out that elevating modules above the ground can impose additional installation expenditure (contingent on labor and material cost), but the empirical rules derived here does not account for these additional costs. Thus, a full optimization of elevation will balance the installation cost versus the energy yield for minimizing the LCOE.

4.4.2 Optimal Azimuth Angle (East-West vs. South-North)

Once the elevation is determined, one must also optimize the orientation of bifacial modules to maximize energy production. Here, we optimize the azimuth angle of bifacial modules at a given elevation. Our simulation reveals that the optimal azimuth angle of bifacial solar modules is essentially either east-west- or south-north-facing, except for the Arctic and Antarctic regions where the bifacial gain is essentially independent of azimuth angle due to the polar day. Therefore, we confine our optimization to two orientations: 1) east-west-facing bifacial modules (Bi_{EW}) and 2) south-north-facing bifacial modules (Bi_{SN}).

Figure 4.7 summarizes the performance comparison between Bi_{EW} and Bi_{SN} for the deployment scenarios as presented in Sec. III, i.e., (a) ground mounting with a ground albedo of 0.25, (b) ground mounting with a ground albedo of 0.5, and (c) 1 m elevation with a ground albedo of 0.5. Note that the tilt angles of Bi_{EW} and Bi_{SN} in Fig. 4.7 are also optimized, which will be discussed in detail later. We point out that across the entire globe, the optimal tilt angle of Bi_{EW} is found to be 90^o, i.e., vertical installation, which accords with [230].

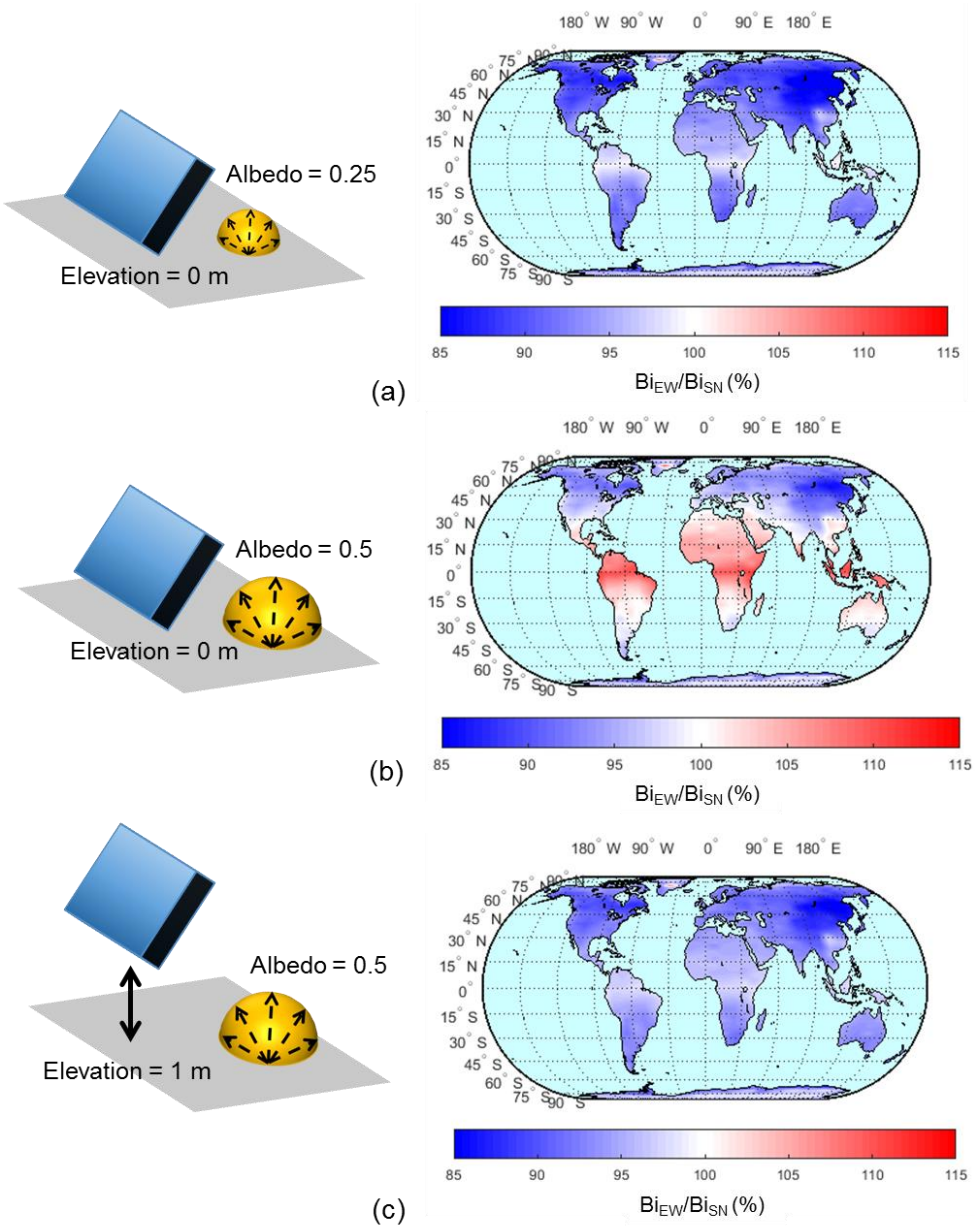

Fig. 4.7. Global maps showing energy yield ratio of Bi_{EW} over Bi_{SN} for three different scenarios: (a) ground mounted with a ground albedo of 0.25, (b) ground mounted with a ground albedo of 0.5, and (c) 1 m elevated with a ground albedo of 0.5.

Low Albedo. Interestingly, our simulation anticipates that Bi_{SN} can outperform vertical Bi_{EW} by up to 15% worldwide for ground mounting with an albedo of 0.25,

see Fig. 4.7(a). With a limited albedo of 0.25, the collection of direct light dictates the total production; vertical Bi_{EW}, however, does not absorb any direct light at noon, when direct light peaks. Consequently, Bi_{SN} is more favorable than Bi_{EW} with a low albedo.

High Albedo. If the albedo increases to 0.5 at zero elevation, surprisingly, Bi_{EW} can produce more electricity than Bi_{SN} up to 15% within 30^o latitude from the Equator, see Fig. 4.7(b). With albedo equal to 0.5, the contribution of albedo light is comparable to direct and diffuse light. Self-shading of albedo light, however, diminishes the production of Bi_{SN}; thus, Bi_{EW} (vertical installation is less susceptible to self-shading) is the preferred configuration. Note that the superior performance of vertical Bi_{EW} shown here has an important implication for bifacial technologies, especially for desert environments (e.g., Saudi Arabia), where Bi_{EW} has the additional advantage of reduced soiling arising from higher tilt angle. Reduced soiling has two advantages, namely, increased energy output and reduced cleaning cost. At higher latitude, the optimal tilt angle Bi_{SN} increases rapidly, which, in turn, diminishes the loss from self-shading. Consequently, Bi_{SN} outperforms Bi_{EW} in regions of high latitude, see Fig. 4.7(b).

Elevation. Remarkably, our simulation indicates that once the modules are mounted more than 1 m above the ground, the optimal orientation of bifacial modules again becomes Bi_{SN} globally, see Fig. 4.7(c). This change of optimal azimuth angle reflects the fact that elevation reduces self-shading of bifacial modules. Thus, Bi_{SN}suffers less from self-shading and can produce more power than Bi_{EW}. As a result, at an elevation of E_{95} with minimal self-shading, the optimum orientation is always south-north facing across the entire world.

Critical Latitude. We have shown that Bi_{EW} can outperform Bi_{SN} if self-shading is severe, and vice versa. The magnitude of self-shading at a given location varies as a function of elevation and ground albedo. Specifically, for a given elevation and ground albedo, there exists a critical latitude (Lat_{Cri}) below which Bi_{EW} is more productive than Bi_{SN} and vice versa. For example, in Fig. 4.7(b), Lat_{Cri} is about

30^o, with a slight variation along longitude due to the clearness index. Enabled by our simulation framework, we have calculated the average Lat_{Cri} as a function of ground albedo and elevation for different clearness indexes, see Fig. 4.8. Next, we perform linear regression to our results to develop the empirical equations that calculate Lat_{Cri} based on elevation E, module height H, and ground albedo R_A, see in Table 4.2. These equations will help installers to choose between Bi_{EW} and Bi_{SN} for maximizing electricity yields for a given location and elevation.

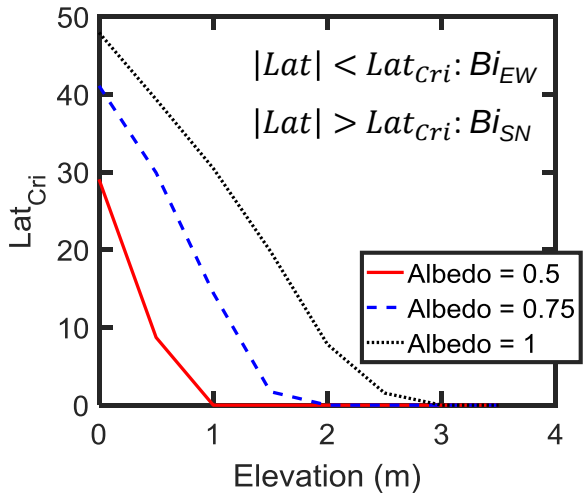

Fig. 4.8. Critical latitude (Lat_{Cri}), below which Bi_{EW} is more favorable than Bi_{SN} and vice versa, as a function elevation for albedo of 0.5, 0.75, and 1.

4.4.3 Optimal Tilt Angle

After optimizing azimuth angle, it is important to determine the optimal tilt angle of bifacial modules. As mentioned, for Bi_{EW}, vertical installation ($\beta = 90^o$) produces the most electricity. Tilting Bi_{SN} optimally, on the other hand, depends on geographic location and module deployment. Consequently, we have performed a comprehensive study on the optimal tilt angle of Bi_{SN} as a function of latitude, elevation, and albedo, see Fig. 4.9.

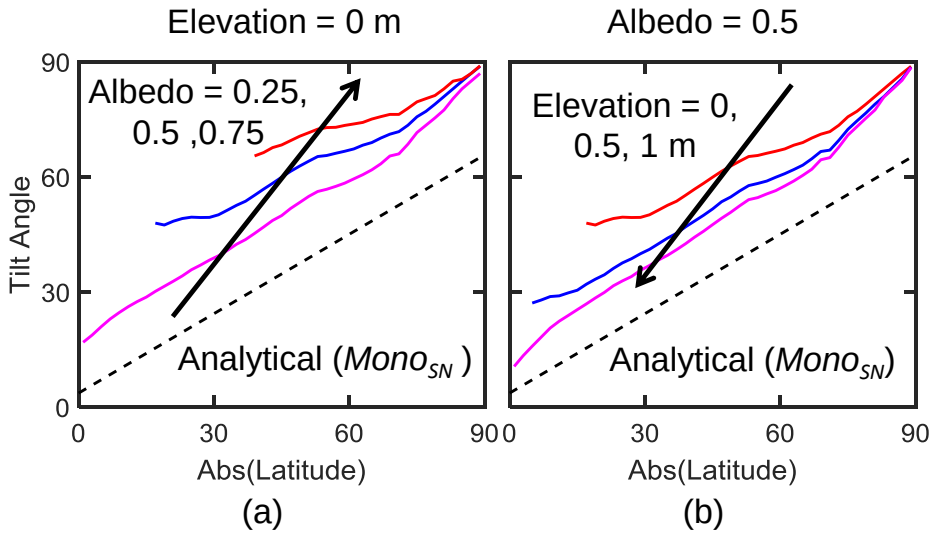

Fig. 4.9. The optimal tilt angle of Bi_{SN} above Bi_{cri} for (a) albedo of 0.25, 0.5, and 0.75 with ground-mounting and (b) elevations of 0 m, 0.5 m, and 1 m at fixed albedo of 0.5. The optimal tilt angle here is the average over longitudes with different clearness indexes. The arrow indicates the increment of albedo and elevation in (a) and (b), respectively. The black dashed line is the optimal tilt angle for MonoSN obtained analytically from [92].

Our simulation results show that the optimal tilt of Bi_{SN} follows the same trend as $Mono_{SN}$ as shown in Fig. 9 (i.e., tilt angle increases with latitude) although the tilt angle of Bi_{SN} is always slightly higher from that of the monofacial counterpart (black dashed lines). This increased tilt enhances the rear-side albedo light collection, consistent with previous studies [91, 227]. The higher tilt angle of Bi_{SN} make them more resistant to soiling compared to monofacial ones, since the soiling loss reduces with increasing tilt angle [272]. Reduced soiling loss will further enhance the bifacial gain of Bi_{SN} relative to $Mono_{SN}$ in the field. Because the optimal tilt angle may differ between $Mono_{SN}$ *and* Bi_{SN}, *the analytical equation previously developed to access optimal tilt angle of monofacial modules is not applicable to bifacial ones.* Therefore, we developed a new set of equations formulated to tilt Bi_{SN} optimally as a function of elevation (E), module height (H), and ground albedo (R_A), whereby we implicitly

take the effect of self-shading into account. Equations for this calculation are listed in Table 4.2 of the appendix. The influence of clearness index on optimal tilt is found to be minimal; thus, it has been neglected in these empirical relationships.

Overall, we find that the energy production of bifacial modules optimized by our equations in Table 4.2 is within 5% relative difference compared to those optimized numerically, which ensures the fidelity of the empirical guidance developed here.

Note that the empirical rules herein are developed for a single standalone bifacial module. At the farm level, in addition to self-shading, a shading effect caused by adjacent rows (i.e., mutual shading) will further diminish the performance, thereby affecting the optimization [256]. For instance, E_{95} is higher for a farm than for a standalone module in order to mitigate mutual shading between each row. We also wish to emphasize the location-specific optimum configuration (Table 4.2) obtained in this work assumes an idealized condition (e.g. the absence of shading from nearby objects such as a tree or a chimney, etc.). With these local objects present, a module may have to be tilted/elevated differently from the empirical rule herein. Software tools such as PVsyst [273] that account for non-ideal factors (e.g., obstruction shading) should be used in practical designs. Obviously, these non-ideal conditions will reduce the energy output on a case-by-case basis.

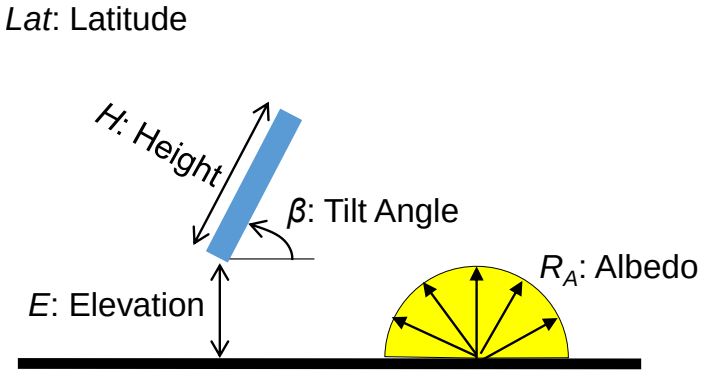

Fig. 4.10. Physical definitions of the parameters in Table 4.2

Table 4.2.

A set of analytical equations to optimize the elevation and orientation of bifacial solar modules

E_{95} **in meter for a module height of** H	
$E_o = H \times (-Lat \times (0.028 \times R_A + 0.009) + 3.3 \times R_A + 0.4)$	E_{95} is the minimum elevation to achieve at least 95% of the self-shading absent maximum energy yield, i.e., further elevation only provides limited energy boost.
if $E_o \leq 0$, $E_{95} = 0$ and if $E_o > 0$, $E_{95} = E_o$	
Lat_{cri} **of bifacial solar module for a given elevation** (E)**, module height** (H)**, and albedo** (R_A)	
$Lat_o = E/H \times (44 \times R_A - 62) + 37 \times R_A + 12$	Lat_{cri} is the critical latitude below which Bi_{EW} produces more electricity than Bi_{SN} and vice versa.
if $Lat_o \leq 0$, $Lat_{cri} = 0^o$ and if $Lat_o > 0$, $Lat_{cri} = Lat_o$	
Optimal tilt angle β_{Opt} **for** Bi_{SN} **for a given elevation** (E)**, module height** (H)**, and albedo** (R_A)	
$\beta_o = a \times Lat + b$	β_{Opt} is the optimal tilt angle for Bi_{SN} for the maximum electricity yield
$a = 0.86 - 0.57 \times R_A \times \exp(-E/H)$	
$b = 4.5 + 62 \times R_A \times \exp(-E/H)$	
if $\beta_o \geq 90^o$, $\beta_{Opt} = 90^o$ and if $\beta_o < 90^o$, $\beta_{Opt} = \beta_o$	

4.5 Conclusion

In summary, we have developed a comprehensive opto-electro-thermal framework to study and optimize bifacial solar modules in a global context. The key conclusions of the chapter are:

1. Our framework calculates the minute-by-minute solar irradiance data by combining the NASA 22-year average meteorological database [242] with our sophisticated irradiance model for arbitrary location and time. The calculated irradiance is used as inputs into our light-collection model, where the contributions from direct, diffuse, and albedo light are physically and geometrically estimated on both the front and rear surfaces of a bifacial solar module. Here, the effect of self-shading is fully accounted for. Last but not least, we use an

opto-electro-thermal coupled framework to self-consistently convert light absorption into annual electricity yield.

2. Our calculation predicts that for a low ground albedo of 0.25 corresponding to vegetation/soil, ground-mounted bifacial solar modules can only achieve bifacial gain up to 10% relative to their monofacial counterpart across the entire world (except for the Arctic and Antarctic regions). However, by boosting the albedo to 0.5 via artificial ground reflectors as well as lifting modules 1 m above the ground surface to reduce self-shading, one can potentially enhance the bifacial gain up to 30%. Hence, our finding encourages the future development of cost-effective ground reflectors and module-elevating schemes to make bifacial modules more financially viable.

3. We demonstrate the enormous impact of self-shading on the optimization of bifacial solar modules. Our analysis reveals that under severe self-shading, i.e., high albedo and low elevation, the vertical Bi_{EW} configuration is superior because Bi_{SN} is more prone to self-shaded albedo loss. For instance, for an albedo of 0.5 and zero elevation, vertical Bi_{EW} can outperform Bi_{SN} up to 15% below the latitude of 30^o, and vice versa beyond the latitude of 30^o. In contrast, with a reduced albedo to 0.25, i.e., less self-shading, Bi_{SN} is more beneficial than Bi_{EW} across the globe.

4. Enabled by our rigorous simulation framework, we have developed a set of empirical design rules to analytically and optimally configure bifacial solar modules in arbitrary geographic locations. Specifically, they can 1) determine the minimum elevation to achieve 95% of the maximum self-shading free energy production, above which further elevating modules offers insufficient benefits, 2) locate the critical latitude Lat_{Cri} below which the east-west orientation is more favorable than the south-north orientation, and 3) calculate the optimal tilt angle of bifacial modules. These empirical equations (within 5% relative

difference compared to numercial simulation) enable rapid design of bifacial modules globally without performing sophisticated local optimization.

5. INVERSE MODELING OF PV RELIABILITY — THE SUNS-VMP METHOD

5.1 Introduction

In the previous chapter, the *annual* energy yield of bifacial solar module is calculated *assuming no degradation*; namely, $P_{Module}(IL, T, t)$ does not degrade and $t_{Life} = 1$ Year in $\int_0^{t_{Life}} P_{Module}(IL, T, t)dt$. In reality, however, $P_{Module}(IL, T, t)$ often monotonically decreases with time because of various degradation mechanisms (e.g., corrosion, EVA yellowing), and consequently modules fail at t_{Life}. Therefore, without properly taking degradation into account, the projected energy output will be over-optimistic. In this chapter, we have developed a simple and powerful strategy to mine the time-series field data to yield a deep understanding of the temporal evolution of $P_{Module}(IL, T, t)$ and identify various degradation pathways, inspired by the well-known Suns-Voc method,. The Suns-Voc method [274], where one monitors the open-circuit voltage by manually varying illumination intensity of a solar simulator (see. Fig. 5.1), has been demonstrated to be a useful characterization tool during module development. Obviously, it cannot apply directly to field data composed exclusively of maximum power point (MPP) current (I_{mp}) and voltage (V_{mp}) information. Hence, we propose *the Suns-Vmp method* that, by taking advantage of the natural daily variation of sunlight, can deduce circuit parameters as a function time by fitting the reconstructed MPP IV throughout the day, see Fig. 5.1. By systematically and physically mining the streaming MPP data, the method can monitor the reliability of solar modules in real time.

In this chapter [1], we begin by introducing the detailed methodology of the Suns-Vmp method in Sec. 5.2. In Sec. 5.3, the Suns-Vmp method is applied to an NREL test facility to extract the degradation rate and identify the dominant degradation modes. Sec. 5.4 discusses the implication of the Suns-Vmp method on the prediction and design of PV reliability and the limitation herein. Finally, we summarize the chapter in Sec. 5.5.

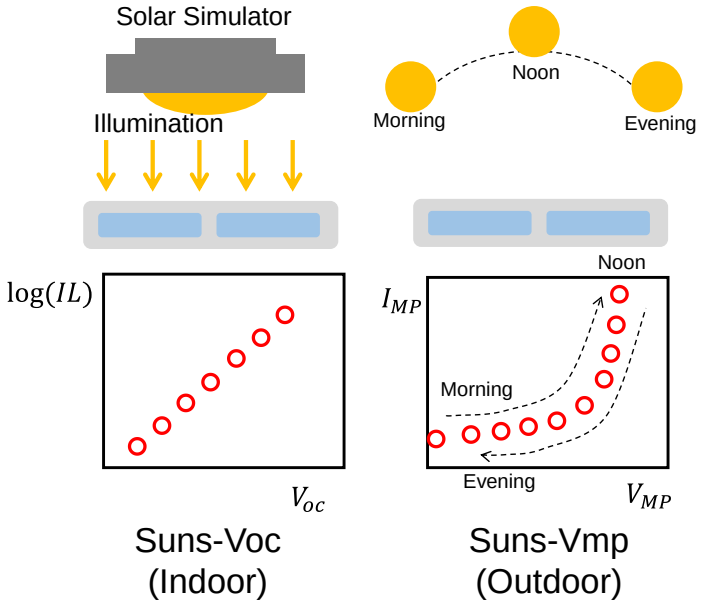

Fig. 5.1. A schematic illustration to explain the working principles of the Suns-Voc and Suns-Vmp method.

5.2 Algorithm Overview of the Suns-Vmp Method

In this section, we will discuss the Suns-Vmp algorithm, as summarized in Fig. 5.2. The algorithm has the following four steps: 1) develop the physics-based equivalent circuit model for a specific technology; 2) extract pristine (time-zero) circuit parameters based on datasheet/pre-installation IV characteristics; 3) preprocess MPP

[1]The contents of this chapter are taken from [275] Copyright ©1999-2018 John Wiley & Sons, Inc (still under review)

data to reconstruct IV characteristics synthetically, and 4) finally, analyze the time-degradation of circuit parameters for insights regarding the dominant degradation modes.

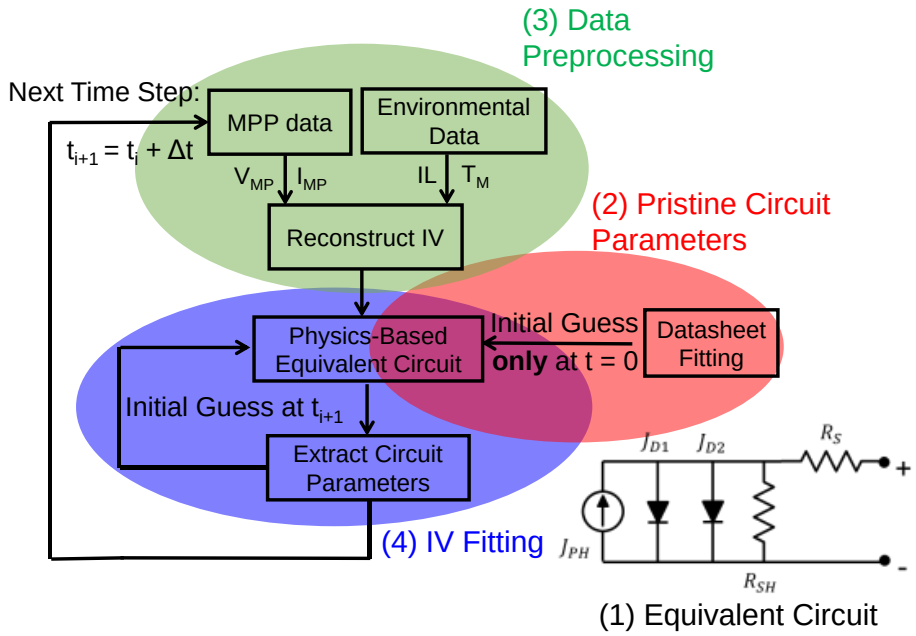

Fig. 5.2. The flowchart of the Suns-Vmp method. The analytical formulation of the five-parameter model is from [40, 133] and summarized in Appendix C.

5.2.1 Step 1: Development and Choice of the Equivalent Circuit (Compact Model)

Mainstream PV technologies can be categorized into three groups: 1) p-n homojunction (e.g., c-Si and GaAs), 2) p-i-n junction (e.g., a-Si and perovskites), and 3) p-n heterojunction (e.g., CIGS and CdTe). Depending on a particular technology, we select the corresponding equivalent circuit in the Suns-Vmp method, see for example, [137] for CIGS, [135] for perovskites, [34] for silicon heterojunction. *Since a solar cell is exposed to varying illumination intensity and temperature, the equivalent*

circuit must be capable of describing the illumination- and temperature-dependent IV curves.

In this chapter, we will demonstrate the Suns-Vmp method on a c-Si PV system, therefore we make use of the well-known five parameter model for Si solar modules [40], which explicitly accounts for the illumination- and temperature-dependencies of circuit parameters, namely, J_{PH}, J_{01}, J_{02}, R_{SH}, and R_S, see Fig. 5.2. The complete set of equations and parameter descriptions for the five parameters is summarized in Appendix C. If needed, the five parameter model can be generalized to include nonlinear shunt resistance [56] and temperature- and illumination-dependent series resistance [146, 276].

5.2.2 Step 2: Extracting Pristine Module Parameters

Next, we extract the pristine (time-zero) module parameters (before the module is fielded) as robust initial guesses for the Suns-Vmp method. We do so by fitting the complete illumination- and temperature-dependent IV measurements available from the datasheet or pre-installation measurements. With the robust initial guesses, we can eliminate multiple solutions in the sequential IV fitting process, see Fig. 5.3. Typical datasheet usually provides a set of full IV measurement under various illumination and temperature conditions which guarantee the uniqueness of the extracted circuit parameters and consequently the robustness of the initial guess.

5.2.3 Step 3: Preprocessing MPP Data

After obtaining the time-zero circuit parameters, we construct – at any time during the onsite operation – a synthetic IV curve by sampling MPP data over a given period (typically 2-3 days, referred as measurement window hereafter). Recall that in the Suns-Voc measurement [278, 279], one traces the open circuit voltage of solar cells, through deliberately varying the intensity of the solar simulator, to construct the IV curve in the absence of series resistance. In the Suns-Vmp method, however, we

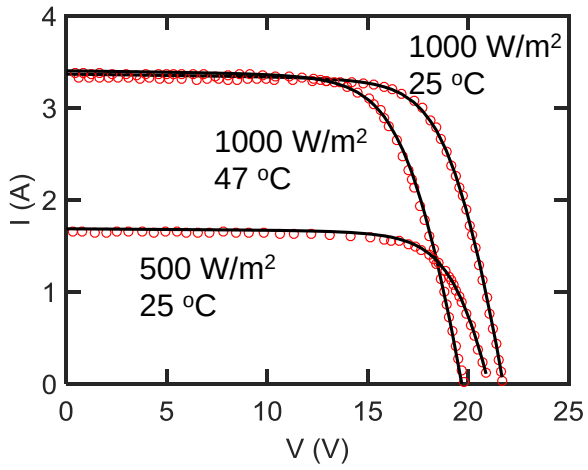

Fig. 5.3. Initial fitting to the datasheet (Siemens M55 [277]) for time-zero circuit parameters. The extracted circuit parameters are summarized in Appendix C.

take advantage of the natural temporal variation of the sunlight (the plane-of-array irradiance: G_{POA}) and the cell temperature (T_C) to track the maximum power point. Hence, due to the changing G_{POA} and T_C, the module output I_{mp} and V_{mp} (operating current and voltage at the maximum power point, respectively) increase from morning to noon then decrease from noon to evening, see Fig. 5.4(a). For example, if the data is recorded every 10 minutes of 8 diurnal hours over a 3-day measurement window, then 144 data points of four variables (i.e. G_{POA}, T_C, I_{mp}, V_{mp}) are available to calculate the circuit parameters of the compact model, namely, calibrating the circuit parameters until the MPP IV is reproduced as shown in Fig. 5.4(b). *Note that Suns-Vmp method does not interrupt the normal module operation by disconnecting solar modules for IV sweeps or deviating them from the MPP bias* [274, 280]*; thus the technique empowers characterization of solar modules in real-time operation.*

In the Suns-Vmp methodology, to reduce uncertainties in the extraction, we also explicitly preprocess the data to account for 1) cell-to-module temperature difference, 2) spectral mismatch between pyranometer and solar modules, and 3) reflection loss as a function of time. The specific steps are summarized in Appendix C. Also,

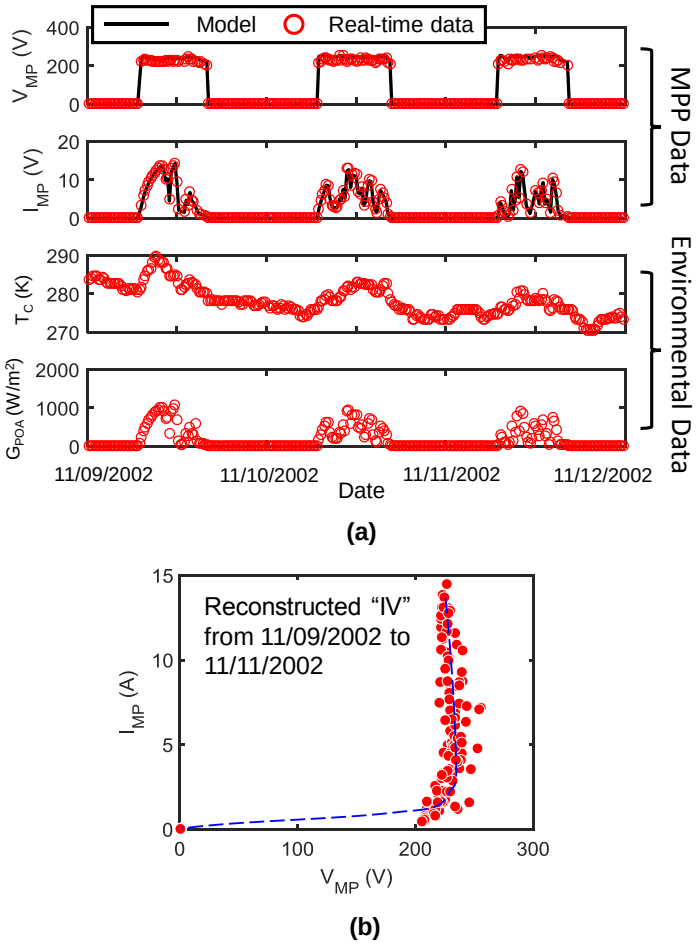

Fig. 5.4. (a) Three-day MPP and environmental data (circles) from 11/09/2002 to 11/11/2002 of the test facility in Sec. 5.3. The fitting results of the MPP data (solid lines) using the Suns-Vmp method is also present. (b) An illustration of reconstructing IV from the MPP data in (a).

while the basic algorithm is easy to understand, it is important to realize that the (G_{POA}, T_C, I_{mp}, V_{mp}) may involve noisy or corrupted data. In this case, the window duration must be choosen judiciaously and the corrupted data must be rejected, for a robust parameter extraction of the compact model. Hence, we have developed a physics-based self-filtering algorithm to preprocess the data as follows before fitting (see Appendix C for additional details).

The *measurement window* of MPP data must be chosen such that it is long enough to contain sufficient illumination/temperature variations, but short enough such that the module does not degrade significantly within the window. The time-scale of degradation processes is slow [129], thereby the circuit parameters can be assumed to be constant over the course of a few days. Hence, the recommended measurement window of MPP data can be up several days (e.g., three days in Fig. 5.4), as long as there exists sufficient variation in illumination and temperature to reconstruct the MPP IV. In the case of catastrophic degradation (such as partial shading degradation in thin-film solar modules [50]), the extracted circuit parameters become the average value of pre- and post-degradation values over time.

5.2.4 Step 4: MPP IV Fitting Algorithm

After reconstructing MPP IV and preprocessing environmental data, we proceed with using rigorous fitting algorithms to model the measured MPP data and extract circuit parameters. In this chapter, we have used the nonlinear least-squares fitting algorithm and bio-inspired particle swarm optimization (PSO) ("lsqcurvefit" and "particleswarm" functions in Matlab® [179], respectively), both of which have been found to give identical results. Note that both fitting algorithms require a lower and upper bound of each circuit parameter at each time step. In our analysis, circuit parameters are assumed to degrade monotonically as a function of time (i.e., no recovery) with a *maximum* degradation rate of 1%/day, except for the short-circuit current J_{Ph}. Hence, given the used length of measurement window, the upper and lower bound can be determined. Since the short-circuit current may fluctuate abruptly due to soiling and precipitation, the upper and lower bound thereof are set to be the datasheet short-circuit current and zero, respectively. Even though recovery of certain degradation pathways is possible (e.g., output power recovers after removing voltage stress for potential induced degradation [93, 281]), such recovery is expected

to be negligible due to constant environmental stress (e.g., thermal cycling, moisture exposure) applied on the operating solar modules.

For any inverse algorithm such as the Suns-Vmp method, one must ensure that the uniqueness of the degradation analysis. Hence, we present a sensitivity analysis of these two algorithm parameters, i.e., measurement window and maximum degradation rate of circuit parameters, on the final extraction of degradation rates, see Fig. 5.5. Our results show that moderate change in the algorithm parameters in the Suns-Vmp method does not interfere with the final results — the deduced degradation rates of performance metric remain unique.

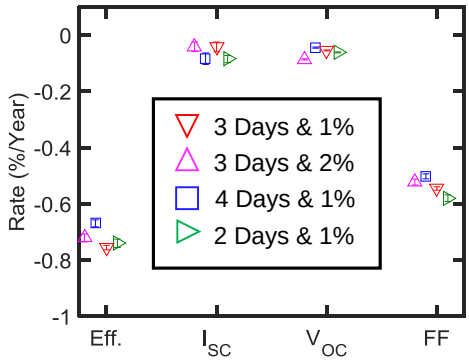

Fig. 5.5. Degradation rate of performance metrics of the negative array as a function of different settings (i.e., measurement window and maximum degradation rate of circuit parameters) in the Suns-Vmp method.

In the next section, we will demonstrate the Suns-Vmp method on an NREL test facility with recorded field data to analyze the degradation of solar modules in real time. The analysis will reveal the possible root causes of power losses by physically interoperating the time-dependent circuit parameters.

5.3 Application to Field data

5.3.1 Introduction to the Field Data

The studied PV system (No: NREL x-Si #7) perches at the west side of the Solar Energy Research Facility (SERF) building at NREL, Golden, CO, USA. It comprises two arrays with negative and positive monopole, each of which consists of five strings with 14 x-Si Siemens M55 solar modules [277] totaling to around 7.42 kW capacity. In 2007, a negatively grounded inverter replaced the previous bipolar inverter, but we maintain the bipolar naming convention (negative versus positive) in this chapter. The modules are 45^o tilted and oriented 22^o east of south. All the onsite MPP and environmental data (illumination and module temperature) including the metadata were retrieved from the publicly accessible NREL PV Data Acquisition (PVDAQ) database [282] with time resolution spanning from 1 min to 15 min. The analyzed field data is from 05/13/1994 to 12/31/2014. Three measurements of module temperature were initially recorded by thermocouples attached to the backsheets but significant inconsistency was found after the eighth year. Therefore, we applied the calibrated Faiman model [194] to obtain module temperature. In addition to continuous MPP data, outdoor IV measurements were also carried out at the array level using a portable Daystar I–V tracer. These IV data sets help us validate the analysis obtained from the Suns-Vmp method. More details on this PV systems can be found in Appendix C.

Figure 5.6 displays the example data while highlighting the two major challenges of analyzing this field data – 1) several gaps even up to 5 years of absent field data and 2) corrupted data with outliers possibly due to instrumentation error, inverter clipping, weather condition, etc. First, to mitigate the uncertainty in deducing the circuit parameters induced by missing data, the Suns-Vmp method makes use of the results from the previous time step as initial guesses and establishes the upper/lower bounds with a preset maximum change rate when fitting the MPP IV. Second, we need a self-consistent scheme to detect and remove these outliers. Toward this goal,

we have created a continuous self-filtering algorithm as summarized in Appendix C. Enabled by these techniques, the Suns-Vmp method can retain excellent error control, *i.e., the mean absolute percentage error (MAPE) is less than 5% for both Vmp and Imp throughout the entire 20-year analysis.*

5.3.2 Results and Validation

Figure 5.7 summarizes the extracted circuit parameters of the negative array by fitting the five-parameter model (see Fig. 5.2) in [40, 133] to the MPP data with a three-day measurement window over a span of 20 years (from 1994 to 2014). The positive array also shows a very similar result, therefore not included here. The maximum photocurrent (J_{PH}) fluctuates possibly due to the accumulation of dust/snow [98] or recalibration of the pyranometer during 20 years. However, it is expected that this fluctuation in J_{PH} does not disturb the extraction of other parameters, since the five-parameter model assumes voltage-independent J_{PH} and therefore the fluctuation will just shift the IV in Fig. 5.4 but not change the underlying IV characteristics (shape). Remarkably, it appears that all the circuit parameters in Fig. 5.7 were degrading (e.g., shunt resistance (R_{SH}) reduces, and series resistance (R_S) increases). To quantify the degradation rate, we calculate the efficiency at standard test condition (STC) at each time step, see Fig. 5.8.

Validation 1: Comparison to DC/G_{POA}

Remarkably, the extracted STC efficiency by the Suns-Vmp method compares well with that of the conventional DC/G_{POA} method [283], showing both the negative and positive arrays near their warranty lifetime (80% of initial efficiency). However, the result obtained from the DC/G_{POA} method shows greater fluctuation than the Suns-Vmp method due to 1) the empirical approaches to filtering outliers and 2) linear temperature-correction of real-time output power to STC by a constant temperature coefficient (which changes over time). Because the Suns-Vmp method uses a

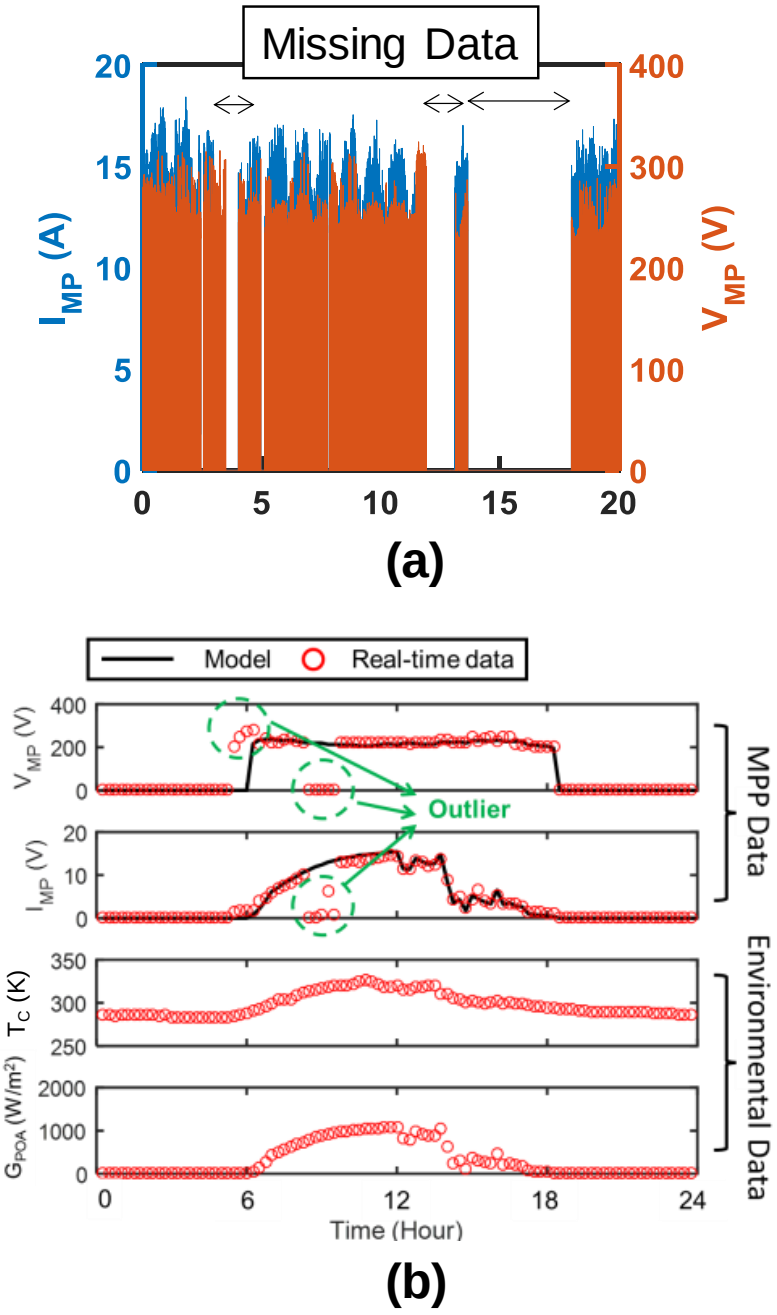

Fig. 5.6. (a) 20-year data of IMP and VMP of the negative monopole. (b) One-day data exhibits the existence of corrupted outlier points.

physics-based equivalent circuit for outlier filtering and temperature correction, the fluctuation is substantially reduced. Note that, for the Suns-Vmp method, we correct

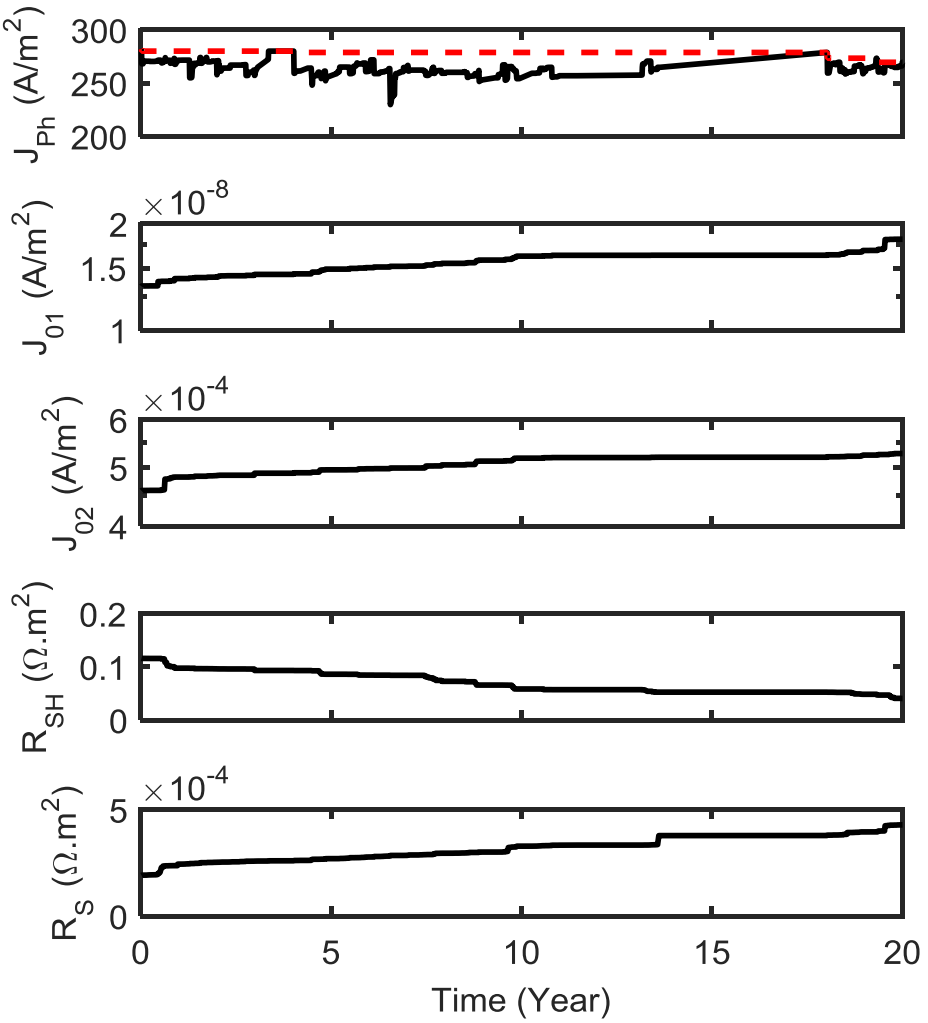

Fig. 5.7. The extracted circuit parameters under standard test condition of the five-parameter model for the negative array as a function of time. Notations: J_{PH} is the maximum photocurrent density; J_{01} is the reverse saturation current density with ideality factor of 1; J_{02} is the reverse saturation current density with ideality factor of 2; R_{SH} is the shunt resistance; R_S is the series resistance. J_{PH} is corrected so that it monotonically decreases with time (red dashed line).

J_{PH} so that it monotonically decreases with time (i.e., soiling loss is recoverable) when calculating the STC efficiency, see Fig. 5.7.

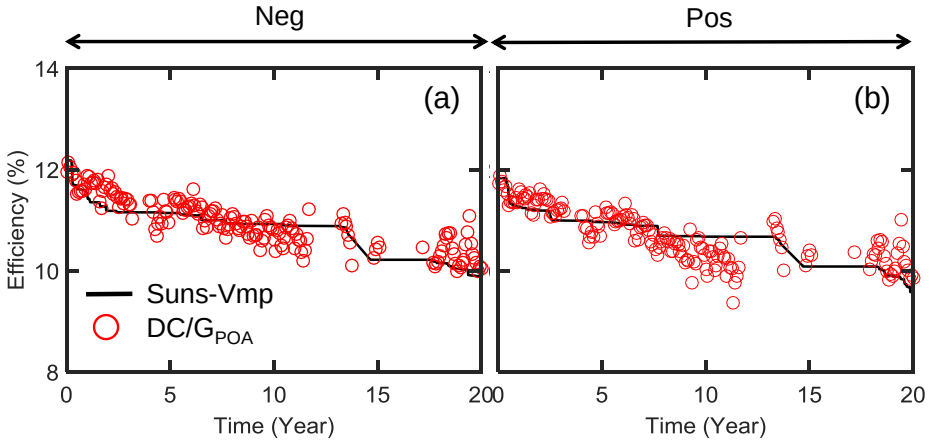

Fig. 5.8. Temporal STC efficiencies calculated by the Suns-Vmp and DC/GPOA methods for the arrays with a negative (a) and positive monopole (b), respectively.

Validation 2: Outdoor IV Measurement

To further validate the Suns-Vmp method, we benchmark the obtained results against those characterized by the periodic outdoor IV measurement through 20 years. Figure 5.9 shows the comparison between real-time (not STC) PV performance metrics calculated by circuit parameters deduced by the Suns-Vmp and direct outdoor IV measurements. Indeed, we find great consistencies (less than 4% MAPE) between these two methods, which corroborates the accuracy of the extraction by the Suns-Vmp method.

Validation 3: Parameter Degradation Rates

Besides the performance metric, we also benchmark the rate of change of the performance metrics estimated from the Suns-Vmp method against outdoor IV from [99] in Fig. 10 (top), which again are in good agreement. The error bars are calculated within 95% confidence interval. We note that, given that the Sun-Vmp method is a real-time analysis, it can substantially reduce the uncertainty associated with

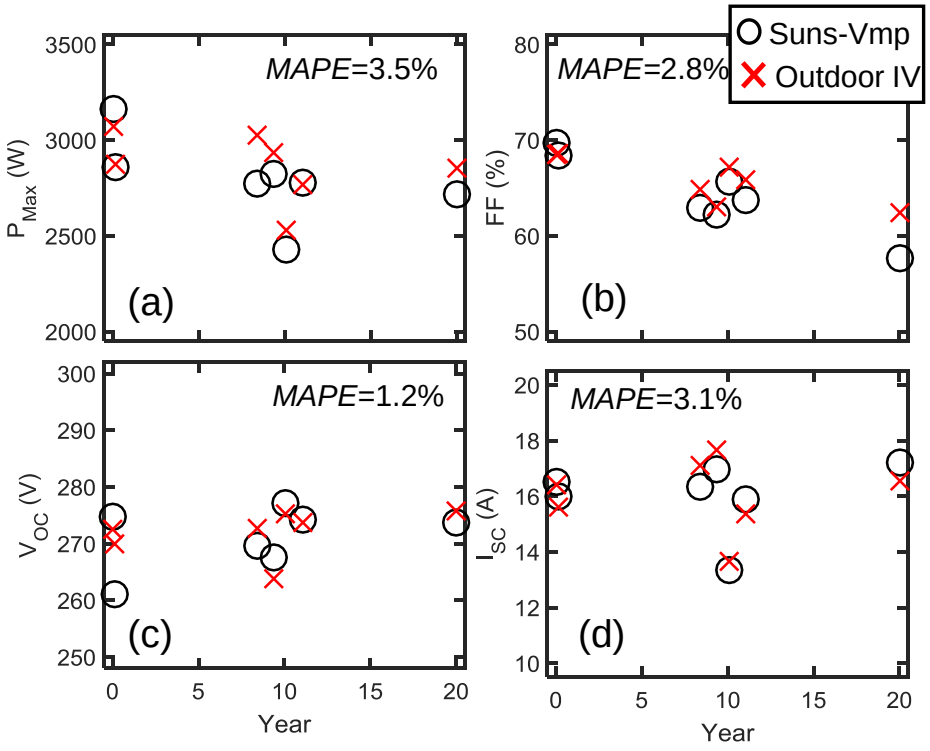

Fig. 5.9. Comparison of performance metric generated by the Suns-Vmp method and outdoor array IV measurement for the negative array. The mean absolute percentage errors (MAPE) are also labeled in each plot.

calculating the degradation rate (the uncertainties of the efficiency degradation rate of the negative pole are around 0.02 %/Year and 0.2 %/Year extracted by the Suns-Vmp method and outdoor IV, respectively), compared to the intermittent IV measurements which only contains a limited number of data points. The degradation rate of the efficiencies for both the negative and positive arrays are around 0.7%/Year. It is noteworthy that the efficiency degradation may be primarily attributed to the reduction in fill factor (-0.6 to -0.4 %/Year), while Voc and Isc only worsen slightly.

We attribute this degradation to the increased series resistance, which erodes fill factor without substantially affecting Voc and Isc. Both the Suns-Vmp and outdoor IV measurement reveal the rapid increment of series resistance at the rate of 5 –

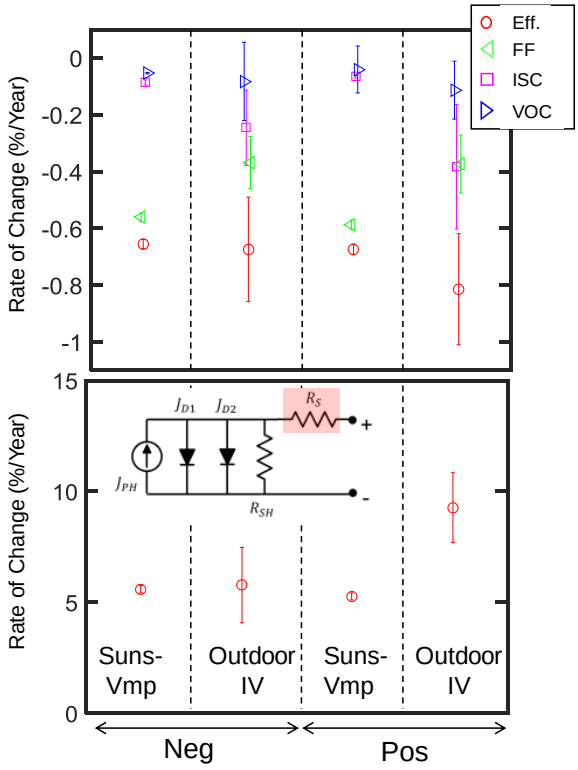

Fig. 5.10. Rate of change of the performance metrics (top) and series resistance R_S (bottom) of the analyzed PV systems via the Suns-Vmp method and outdoor IV measurement.

10%/year as shown in Fig. 5.10 (bottom), which confirms our conjecture of series-resistance induced efficiency degradation.

Validation 4: Onsite inspection

Next, we will deconvolve and quantify the power losses ascribed to each circuit parameter to identify the predominant physical degradation pathways. As shown in Fig. 5.11 (a), we deconvolve the power losses associated with each parameter for the negative array. The key observations are threefold:

1. At the end of 20 years, Fig. 5.11(a) elucidates that the increased series resistance is the dominant contributor to efficiency reduction for both the negative and

positive polarities. Remarkably, the on-site infrared image in Fig. 5.11(a)(b) exhibits localized hot spots caused by solder bond failure, in accord with our deconvolution analysis of increasing series resistance. It is generally known that the failure of solder bonds is because of thermal stress induced by the different thermal expansion coefficients of solder joints and components during repeated thermal cycles [102, 104]. Therefore, solder bonds fail (crack) at the cycle of failure in a stepwise fashion [284]. Indeed, the incremental time signature of the series resistance is stepwise in the Suns-Vmp analysis, see Fig. 5.11(a).

2. Discoloration of the encapsulants can be expected because of the relatively high ultraviolet light concentration at Denver (altitude of ∼1800 m) [285]. Indeed, a photograph of the solar modules in the field shows that the majority of the solar cells suffer from discoloration, see Fig. 5.11(c). Meanwhile, notwithstanding the J_{PH} fluctuation shown in Fig. 7, our deconvolution results also manifests a symmetric decrease of J_{PH} and ascribes a significant amount of power loss (∼4%) to J_{PH} reduction, an indicator of discoloration. This agreement again confirms the PV degradation diagnosed by the Suns-Vmp method. It is noteworthy that the photocurrent reduction due to discoloration has occurred within the first year of installation. Another study has also found early advent of discoloration, i.e., discoloration has been seen in 50% of the solar module less than five years old [97].

3. The operating voltage of the modules is only around 200 V; therefore, the efficiency degradation by potential-induced degradation (PID) is expected to be insignificant [106]. Indeed, our result confirms this conjecture by showing that only ∼3% power loss is due to shunting (R_{SH}) and increased recombination currents (J_{01} and J_{02}), both of which are effective indicators for PID [286, 287].

As demonstrated here, the Suns-Vmp allows us to quantitatively and qualitatively diagnose the pathology of degraded solar modules exposed in the field by analyzing

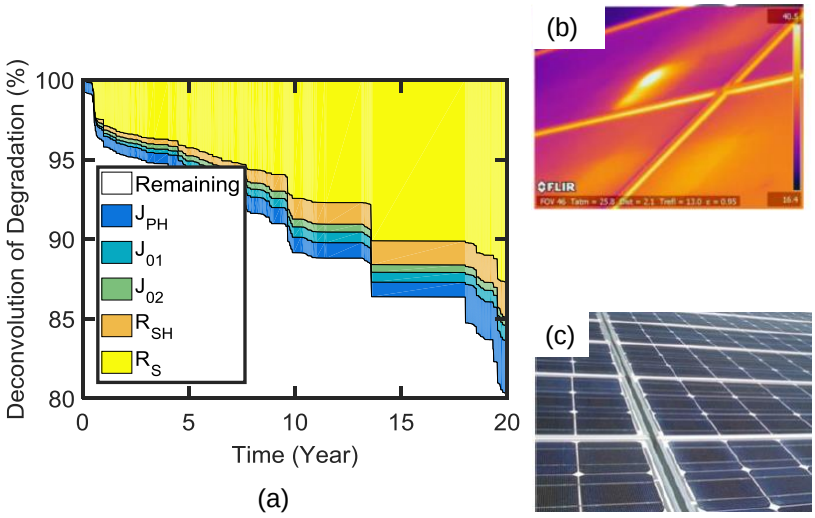

Fig. 5.11. (a) Temporal degradation deconvolution with respect to circuit parameters for the negative polarity. (b) IR image shows a hot spot caused by solder bond failure. (c) Picture shows that most cells suffer from discoloration in the center. *(b) and (c) are obtained from [99] ©2015 IEEE.

and interpreting the time signature of individual circuit parameters. All the results have been validated by both outdoor IV measurement and on-site characterization.

5.4 Implications of the Suns-Vmp Method

In the previous section, we have applied the Suns-Vmp method to an NREL test facility and demonstrated its capability of analyzing the degradation of solar modules in real time. Next, we discuss the potential use of the time-dependent parameters obtained through the analysis and limitations of the approach.

5.4.1 Geography and Technology-Specific Reliability-Aware Design

The underlying physical degradation mechanisms of PV are strongly contingent on local meteorological factors and different technologies, e.g., solar modules exposed in

humid regions are more susceptible to contact corrosion [29], and monolithic thin-film solar modules are vulnerable to partial shading degradation [50]. Similarly, modules more likely to suffer from PID should adopt Corning® Willow™ Glass to impede ion migration [114]. Therefore, ideally, module design ought to be geography- and technology-dependent. However, solar modules are often overdesigned for reliability (perhaps at a considerable cost) so that they can survive a broad range of weather conditions. This is due to the lack of comprehensive understanding of local degradation. The Suns-Vmp method offers an opportunity to efficiently diagnose the degradation pathways of fielded solar modules of different technologies across the entire world. The results can be ultimately collected in a global database, allowing the manufacturers to design and produce the next generation reliable-aware PV with maximized durability.

5.4.2 More Accurate Long-Term Reliability Prediction

Accurate prediction of long-term energy production by PV systems is crucial to evaluating the bankability thereof. Various degradation pathways depend nonlinearly on stress time and local stress factors (irradiance, voltage, moisture, temperature). Therefore, it is difficult to predict future energy yields based on empirical linear degradation models [119]. In this regard, the Suns-Vmp method can facilitate accurate reliability prediction. Recently, several physics-based degradation models have been developed that can directly map various PV degradation modes (e.g., corrosion, PID, yellowing) to the temporal behavior of circuit parameters [288, 289]. We have discussed these degradation models in details in Appendix D. The extracted circuit parameters by the Suns-Vmp method can be used to calibrate these degradation models (e.g., moisture diffusion coefficient for corrosion). Integrated with the weather forecast, the calibrated degradation models will predict the lifespan of solar modules. Alternatively, the time-dependent circuit parameters can train machine learning algorithms; the trained machine learning algorithms [129] can predict PV lifetime. The

validity of these predictive approaches, however, remains an interesting open question and requires more rigorous research efforts.

5.4.3 Guidance for Collecting Field Data

The Suns-Vmp methodology highlights the importance of physics-based modeling in creating databases. For example, we have seen fitting of the pristine module characteristics requires temperature- and illumination-dependent IV measurement to ensure a robust and unique initial guess. Second, we have noted that weather data may be corrupted or missing. Thus it is important for PV databases to contain complementary information from multiple sources [290]. Finally, compact model parameters offer an important recipe for improving data compression and computational efficiency; the model parameters can diagnose the module by only deciphering the stored Vmp-Imp information (a byproduct data of normal operation at maximum power point) for the entire duration.This eliminates the need for deliberate measurement of massive IV data [131] and time-consuming collection of field data [97].

5.4.4 Intra-Cell Variability

Process-induced variability can lead to performance variation in the cell, module, or array levels [34, 38, 132], especially for the thin-film PV where binning is not possible. Similarly, various degradation modes introduce local variability as well. For example, non-uniform degradation (e.g., cells adjacent to module edges are more prone to contact corrosion than those located away from the edges [101]; solar modules close to the negative array are more susceptible to PID [291]), etc. As implemented, the Suns-Vmp method uses a single equivalent circuit to analyze a string consisting of multiple modules and thus accounts for "average" variability/degradation. As a result, it is critical to investigate how performance variability can potentially affect the accuracy of the Suns-Vmp method. Therefore, we have tested Suns-Vmp under various scenarios of performance variability, and the results are listed in Appendix

C. Remarkably, our findings highlight that the circuit parameters extracted by the Suns-Vmp method are still valid to interpret PV degradation with *moderate* non-uniformity. Affected by severe non-uniformity, however, the Suns-Vmp method may not be able to identify the primary circuit parameters contributing to power losses. For instance, the Suns-Vmp method could attribute the predominant degradation to the increased recombination current (J_{01} and J_{02}), and series resistance R_S , whereas the actual degradation is due to reduced shunt resistance R_{SH}. For these cases, it will be important to represent the string by a few equivalent circuit models. Despite the increase in the parameter number, the following considerations are expected to simplify the calibration process: 1) availability of time-zero information of each module, 2) the large amount of data available within the measurement window, and 3) several degradation modes (e.g., yellowing) are expected to affect all the modules uniformly, while others (e.g., PID) are dominated by a few modules. Ability to account for non-uniform degradation will be an important direction of future research on this topic.

5.5 Conclusion

To summarize, we have presented a novel method, i.e., the Suns-Vmp method, for analyzing the PV degradation:

1. The Suns-Vmp method enables in-situ monitoring and diagnosis of PV reliability in real time by systemically and physically mining the time-series MPP data. The method can extract physically defined circuit parameters by fitting IV consisting of the varying MPP data over a characterization window. The extracted circuit parameters can be used to estimate the STC efficiency, quantitively deconvolute PV degradation, and identify the dominant degradation pathways.

2. We have demonstrated the Suns-Vmp method by analyzing MPP data from an NREL test facility, where physics-based circuit parameters and efficiency

of the solar modules have been extracted as a function of time. Independent outdoor IV measurements have systemically validated our results. Our analysis suggests that the PV system degrades at a rate of 0.7%/Year, primarily due to reduced short-circuit current and increased series resistance most likely caused by discoloration and weakened solder bond, respectively. The on-site optical photograph and IR image indeed substantiate our interpretation of the physical degradation pathways, i.e., discoloration and solder bond failure.

3. The analysis of deconvoluting the underlying degradation pathways by the Suns-Vmp method can deepen the current understanding of technology- and geographic-dependent degradation, and inspire more robust environment-specific designs for the next-generation reliability-aware solar modules. The Suns-Vmp method can be used to calibrate physics-based degradation models as well as train machine learning algorithms, both of which can then predict power degradation of PV and improve the evaluation of bankability.

6. SUMMARY AND FUTURE WORK

6.1 The Summary of This Thesis

Through decades of research and development, solar modules have finally achieved a LCOE comparable to that of conventional fossil fuels. To meet the surging demand for renewable energy, however, we must continue making solar modules more efficient and reliable to drive down the LCOE, which is described by Eqn. 1.1. As the PV performance is getting close to its fundamental limit, it has become much harder to keep the improvement momentum forward. In this regard, new innovations and novel research approaches are needed. Therefore, in this thesis, we have established a novel framework encompassing three components (***multiscale, multiphysics, and time***) of solar modules to exploit new potentials for enhancing the performance and extending the lifespan thereof, as shown in Fig. 1.3. The essential contributions of this thesis are summarized below:

6.1.1 Chapter 2: *Modeling* $P_{Module}(IL, T, t)$

In this chapter, we have developed the foundational compact models, indispensable for end-to-end modeling of solar modules for both perovskite and CIGS technologies:

1. By analytically solving the coupling drift-diffusion and Poisson equations, we have derived a set of compact models that describe the salient characteristics of variously configured perovskite (i.e., p-i-n/p-p-n and n-i-p/n-p-p junctions) and CIGS solar cells.

2. Enabled by our physically defined parameters, we extend the model of CIGS solar cells to describe the illumination- and temperature-dependent IV ranging

from forward bias to reverse breakdown. This ability is crucial to study partial-shading degradation in which non-uniform temperature distribution prevails.

3. The models developed here enables rapid characterization of cell performance merely by IV measurement, even can extract physical parameters (e.g., the built-in potential for a p-i-n junction) which cannot be directly measured by conventional techniques, such as capacitance spectroscopy.

4. The extracted parameters from the models can provide useful insights into the construction and pathology of cell performance, and suggests new opportunities for further improvements.

5. The models are compatible to be integrated into a large-scale module-level simulator that serves to diminish the cell-to-module efficiency gap, investigate electro-thermal reliability issues, interpret module-level characterization (e.g., electroluminescence imaging), and predict/optimize the system-level performance of solar farms.

6.1.2 Chapter 3: *Improving* $P_{Module}(IL, T, t)$ *and* t_{Life}

Here we investigate the self-heating effects of solar modules including their erosion to electrical performance and develop self-cooling methodologies. The compact model developed in the prior chapter has been applied here to simulate shading-induced self-heating. The findings in this chapter highlight the importance of thermal properties in PV and have profound implications on the short- and long-term electricity yields of PV systems:

1. By numerically solving the energy-balance equation, we have developed an opto-electro-thermal coupled simulation framework to simulate the temperature of modules exposed outside accurately. Incorporating this framework into the SPICE-based module simulation, we are also able to anticipate the thermal distribution of partially shaded modules adequately.

2. We have identified two classes of phenomena contributing significantly to PV self-heating: intrinsic self-heating and shading-induced self-heating. The first phenomenon originates from the sub-bandgap absorption observed experimentally in four different widely-used technologies as well as the imperfect thermal radiation of coverglass within the atmospheric transmission window (8 -13 m wavelength). The latter type of self-heating is due to the fact that shaded cells in series-connected monolithic modules are coerced to reverse breakdown in order to maintain current continuity with the unshaded neighbors. Revealed by our simulation, the light-enhanced reverse breakdown discussed in Chapter 2 will exacerbate shading-induced heating substantially and must be considered in the IEC 61215 qualification test for shading.

3. Last but not least, we have correspondingly developed techniques targeted at the fundamental sources of self-heating selective spectral (reject sub-bandgap photons by optical filters) and radiative cooling (increase thermal radiation upwards to the sky) to cool down solar modules in the field spectrally. Our calculation anticipates a temperature reduction of 6 degrees for commercial solar modules attainable by our methods. This cooling gain can provide a 0.5% absolute increase in efficiency and prolong lifetime by 85%.

6.1.3 Chapter 4: Predicting $\int_0^{t_{Life}} P_{Module}(IL, T, t)dt$

Long-term projections of electricity yields of PV systems determine the financial viability and thereby must be carefully evaluated. The resurgence of bifacial solar modules (the first one dates back to the 1960s) have received much attention due to their higher output power, more reliable structure, and compatibility with current fabrication processes. The performance and optimization of bifacial modules in a global context, however, is still missing in the literature. Hence, we study the worldwide prospects of this technology in this chapter.

1. We have developed a rigorous modeling framework for bifacial modules, comprising three parts: 1) the temporal- and geographic-specific irradiance model based on the NASA 22-year meteorological database; 2) an analytical and geometric light collection model, whereby contributions of direct, diffuse, and albedo irradiance onto both the front and rear sides are evaluated, and more importantly, self-shading of albedo irradiance, which dictates the performance and optimization of bifacial modules, are explicitly accounted for; 3) an electro-thermal coupled model that calculates the operating temperature of bifacial solar modules, and consequently the temperature corrected electricity output from the total illumination.

2. We have performed a global investigation and optimization of bifacial solar modules using our modeling framework. Remarkably, our simulation anticipates the bifacial gain of ground-mounted modules to be less than 10% worldwide for an albedo of 0.25 (typical for natural groundcover). However, elevating modules to 1 m and adopting highly reflective groundcover (albedo = 0.5) can enhance bifacial gain to 30% globally. These findings encourage the future development of cost-effective artificial ground reflector as well as module elevation techniques to ensure sufficient energy production improvements of bifacial technologies.

3. By applying regression analysis, we have derived a set of practical guidelines for installers to maximize energy output while retrenching installation cost. Specifically, for a given location, our design rules can analytically calculate: 1) the minimum elevation E_{95} of bifacial modules to achieve at least 95% of the self-shading absent maximum energy production, 2) the preference between east-west versus south-north orientation, and 3) the optimal tilt angle.

4. The results in this chapter provide insights into the potential performance of bifacial solar modules in a global context and lay out the groundwork to a more detailed LCOE study for scrutinizing the financial viability of this promising technology. Furthermore, the empirical design rules developed here can fas-

ten the total design cycle of bifacial solar modules by providing a preliminary optimization scheme.

6.1.4 Chapter 5: Extending t_{Life}

To further reduce the LCOE of PV, the module lifetime must be increased, without increasing the cost, if possible. A module optimized for a specific geographic condition can achieve these conflicting objectives; unfortunately, the geographic- and technology-dependent degradation mechanisms (e.g., corrosion is more pronounced in hot and humid environments) have been difficult to quantify based on traditional on-line and off-line measurements. The lack of understanding, in turn, makes it challenging to create reliability-aware designs for durable PV. Hence, in this chapter, we have developed a novel technique, i.e., the Suns-Vmp method, that can interpret the routinely collected maximum power point (MPP) data of installed solar modules to produce a significant amount of information regarding the geography-specific PV degradation. The resulting databased will eventually facilitate the geographic- and technology-specific design to improve module lifetime.

1. The Suns-Vmp method is an in-situ monitoring and diagnostic method for PV degradation of in-field modules. The method tracks the time-varying MPP data over a measurement window of a few days to create a synthetic MPP IV. The evolution of these synthetic IV over the years translated to a set of physics-based circuit parameters allows one to deconvolute PV degradation quantitatively, and ascertain the predominant degradation pathways.

2. We have validated the proposed method on a silicon module system, which has been running over 20 years, operated by NREL. Separate outdoor IV measurement has systemically validated our results. We find that the system degrades at a rate of 0.7 %/Year and we attribute the major degradation to solder bond failure and EVA discoloration, consistent with on-site optical characterizations.

3. The method developed here can extend the current understanding of geographic- and technology-contingent degradation, and facilitate more durable environment-specific design. Moreover, integrated with time-dependent degradation models or Machine Learning algorithms, the Suns-Vmp method can also serve to predict the long-term reliability of solar farms and in turn help scrutinize the bankability of solar installation at any arbitrary location in the world.

6.2 Future Work

This thesis is intended to lay out the groundwork for a universal framework to tackle the current research challenges of continuously improving the performance and reliability of PV systems, and ultimately reducing the LCOE. In this section, we would like to propose a few prospective research directions that can be built on the framework developed in this thesis.

6.2.1 Farm-Level Study of Solar Farm

Mutual Row Shading. In this thesis, we study the performance and optimization of a single standalone bifacial module. In this isolated circumstance, self-shading of albedo light by the module itself is the detrimental factor to the total energy output. Once extended to the farm-level study (composed of multiple rows of modules installed in proximity), calculation of system performance ought to also include the effect emerging from mutual shading as depicted in Fig. 6.1. There are four types mutual shading concurrent in a bifacial solar farm:

1. Shadow of direct light directly cast by neighboring row can occur in the case of extremely close row spacing, as illustrated in Fig. 6.1(a). This shading effect can impose undesired non-uniform illumination on the module and lead to serious power loss even under the protection by bypass diodes. However, this effect will vanish when modules are placed far apart.

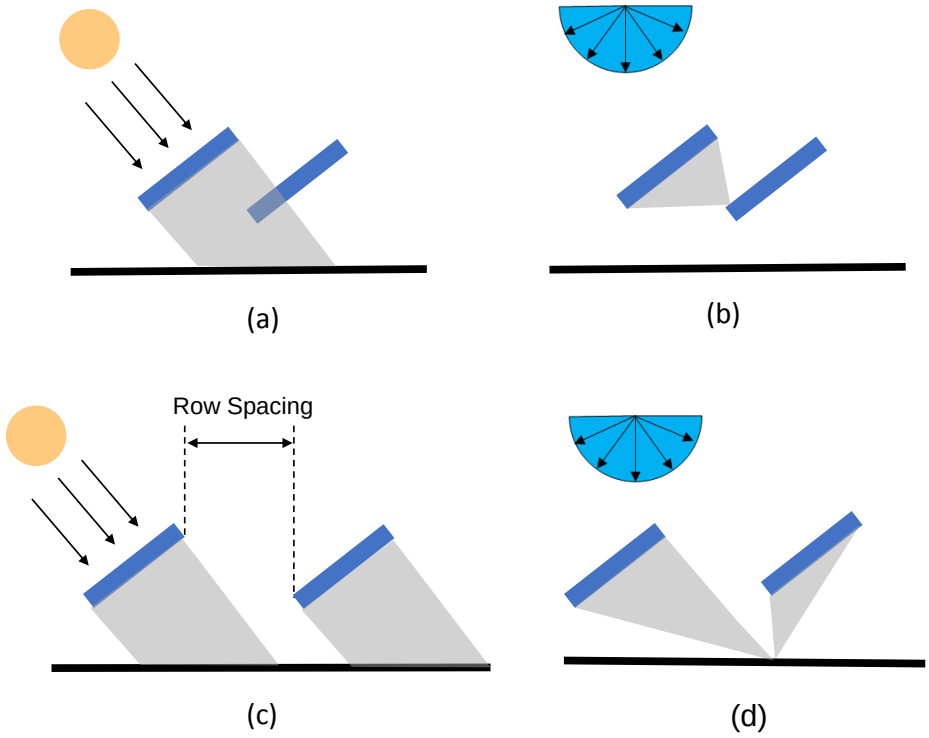

Fig. 6.1. Different types of mutual shading between adjacent rows in a bifacial solar farm. Mutual shading due to (a) blocking of direct and (b) partial masking of diffuse light onto the module by neighboring rows, which could lead to severe non-uniform shading. Mutual shading of albedo light from (c) blocking of direct light and (d) partial masking of diffuse light onto the ground.

2. Partial masking of isotropic diffuse varies as a function of position on the module. It is because the part near the bottom of a module encounters a wider masking angle by the adjacent module compared to the region near the top, see Fig. 6.1(b). Masking of diffuse light creates non-uniform illumination, particularly in cloudy and overcast climates.

3. Additional to self-shading, neighboring rows can also block direct light reaching onto the group, thereby decreasing albedo light, see Fig. 6.1(c). In a bifacial farm, where the contribution from albedo light is much pronounced than monofacial ones, such an effect should be carefully evaluated.

4. Also similar to self-shading, adjacent rows can also mask diffuse light onto the ground, see Fig. 6.1(d). This effect strongly depends on the positions of the group as well as the module because of highly position-resolved view factors involved in this calculation.

It shall be noted that the analytical and geometric simulation framework present in Chapter 4 can be easily extended to capture all these four shading effects, and the same equations are applicable with adjusted parameters. Moreover, we can also input the calculated illumination profile to the module simulator present in Chapter 3 to accurately quantify power lost to partial illumination because of mutual shading.

More Complicated Optimization. For the optimization of a single bifacial module, we only considered three critical parameters, i.e., elevation (E), azimuth angle (γ_M), and tilt angle (β). Once expanding into farm design, row spacing (R) should be fully accounted for. The essential challenge of farm-level optimization is that the dependencies of mutual-shading on all four parameters (E, γ_M, β, R) and the coupling effect among them. For example, a module with a flatter tilt angle are less prone to partial shading of blocking direct light by neighbors; hence, it has higher tolerance to very close row spacing. The bottom line here is that a simple "trial-and-error" approach obviously cannot yield meaningful results for such an intricate optimization problem and one must search the optimum solution in this four-dimensional design space.

6.2.2 Comprehensive Economic Evaluation:

Module Cost versus Land Cost. Regarding the design of solar farms, a key metric for comparison is the LCOE in the unit of \$/kW.h, namely, the amount of financial cost to generate a certain quantity of electricity. The initial investment for large-scale solar farms is very capital intensive, primarily coming from the cost of purchasing modules and land area; but the cost of these two elements can be conflicting as a function of row spacing in a farm. For instance, setting the module

far apart can mitigate loss from mutual shading (particularly prevalent in bifacial solar farms), thereby improving the energy yield per module cost. Obviously, a farm does not fully utilize the land area for widely separated row spacing, which in turn reduce energy output per land cost. The unit price for modules and especially land strongly vary from region to region and country to country. Hence, each farm entails a unique design to optimum balancing the cost tradeoff between module and land.

New Rule Must Be Developed. The historical rule-of-thumb of optimizing monifacial farms starts with finding the optimal tilt angle for the modules using an empirical equation (derived for a single standby module), and then determine the row spacing to guarantee no blocking of direct light by adjacent rows on Dec. 21 at 9 am (i.e., it is on winter solstice when the Sun has the lowest elevation angle and modules are most likely to suffer from mutual shading of direct light through the year). The rule is well-suited when land cost is not a constraint (e.g., in suburb areas). *If land (e.g., urban areas) is expensive, this rule does not apply.* The emerging floating solar farms provides an illustrative example [292]. Since land area is a constraint in the floating solar farms, the row spacing ought to be more compact (modules are placed in vicinity to each other), and module will be tilted less oblique (modules are tilted nearly flat in this case) to prevent blocking of direct light by close-by modules. There is no comprehensive study on optimizing bifacial solar farms in full consideration of land versus module cost. Therefore, we encourage future research to focus on the optimization of bifacial PV at the farm scale accounting for these economic factors.

Reliability Factors. Besides energy output, long-term in-field reliability of solar modules must be considered to calculate LCOE of bifacial solar farms — a topic not fully explored in the literature. For example, it has been demonstrated experimentally that compared to conventional tilting, east-west facing vertical installations is immune to soiling degradation; so cleaning costs and water usage are significantly reduced. Moreover, south-north facing bifacial solar modules are also more tilted than monofacial counterparts to avert shading losses. Therefore, of great interest to the community is to map a critical latitude across the globe where the tilt angle of bifacial

modules are higher than the avalanche angle of soil or snow such that it can recover soiling/snowing loss. In the future, along with energy output, these aforementioned factors pertinent to reliability ought to be thoroughly analyzed for LCOE calculation.

6.2.3 Holistic Inverse Modeling Framework: Inclusion of Degradation Models

In this thesis, we present the Suns-Vmp method to inversely characterize degraded solar modules by merely examining the MPP data. However, this method only identifies major degradation pathways based on the extracted circuit parameters (e.g., series resistance increase is an indicator of solder bond failure); yet it can neither distinguish between degradation pathways that have the same effects on circuit parameters, nor can it predict future behavior of these degradation processes. In this section, we would like to introduce a broader perspective on inverse modeling, specifically with the inclusion of time-dependent degradation models.

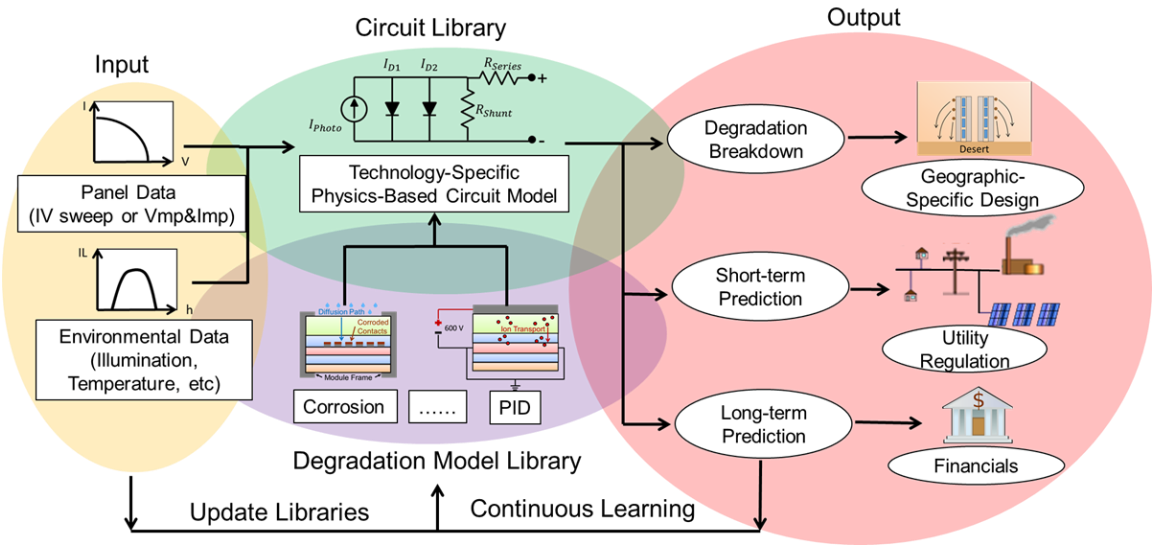

Fig. 6.2. The illustration of the holistic inverse modeling framework.

Overview of the Framework

The holistic inverse modeling framework embodies four major foundational blocks, i.e., Input, Circuit Library, Degradation Model Library, and Output, as depicted in the diagram of Fig. 6.2. Each block is interconnected in the calculation to yield insightful information on module degradation as well as accurate short- and long-term projections of future energy yields. Next, we will illustrate the calculation flow of this framework in depth as followings:

Step 1: The input into this framework encompasses two elements: 1) the electrical data which can either be intermittent IV sweep or time-series MPP data; and 2) the other is a comprehensive set of environmental data which dictates the system performance. By integrating these two data sets into our technology-specific circuit models (see Chapter 2), we can extract the temporal evolution of circuit parameters. It must be noted that the Suns-Vmp method developed in Chapter 5 plays a vital role in this process in terms of physically deciphering input data, especially if full IV sweep is absent or recorded in inadequate time resolution (e.g., only one IV measurement per year).

Step 2: After acquiring the time-resolved circuit parameters, we input them into our library of degradation models (e.g., potential-induced degradation, corrosion) coupled with a complete list of environmental data (e.g., irradiance, temperature, humidity). In Appendix D, we have listed a set of analytical models to simulate PV degradation. The degradation models here must be physics-based, namely, they appropriately model the physical processes underlying a specific degradation mechanism as well as the corresponding effect on the relevant circuit parameters (e.g., solder bond failure to series resistance). Moreover, these models must incorporate environmental data into the calculation which dictates the rate and distribution thereof. One example will be modeling how ultraviolet light gradually depletes the protective photobleacher inside EVA and eventually cause encapsulant discoloration [94]. Note that the physical parameters used by

the degradation model will be technology- and manufacturer-specific, such as the content of photobleacher inside EVA in the discoloration model differs from manufacturer to manufacturer. Hence, in the same location, there can exist a broad distribution of degradation rates of solar modules made by different manufacturers [119]. Since the framework calibrates the physical parameters specific to the analyzed technology, we can physically account for a variety of these location- and technology-specific degradation processes. It must be pointed out that previous work where degradation models were also applied calibrate the parameters through a set of accelerated tests pertinent to a specific degradation model, e.g., UV test for EVA discoloration, see Fig. 6.3. Here, one must design the accelerated tests to cover all the degradation modes, while each test must be executed multiple times at different conditions (e.g., temperature, humidity) for parameter calibration (e.g., activation energy). This procedure can be cumbersome, and still one may overlook specific degradation when designing the experiments. Moreover, this technique may not apply to existing aged PV systems, which have already suffered from degradation significantly and does not permit accelerated tests. One of the breakthroughs in our framework is to physically extract these parameters of degradation models by mining the past field data (dashed line in Fig. 6.3). This new approach fully takes advantage of the natural test chamber — the outside environment — and can eliminate the need for accelerated tests.

Step 3: The calibrated degradation models from Step 2 enables a set of useful outputs, as illustrated in Fig. 6.2. First, the deconvolution analysis of degradation mechanism can inspire technology- and location-specific reliability design for manufacturers. For instance, if the framework indicates that contact corrosion dominates, for the next fleet of modules to be installed in the same location, manufacturers may increase the width of mental fingers and implement better sealing encapsulants such that they are more resistant to corrosion. The corrosion degradation model can even project the amount of degradation as a

function of finger width increment, if necessary. Second, input with short-term weather forecast, the framework can predict the short-term energy production , which is crucial for utility companies to regulate electrical grid in advance. Hour-by-hour, day-by-day, and season-by-season variability of solar energy are one of the obstacles to complete energy reliance on PV for humanity. Obviously, energy storage can potentially solve this issue of variability, but recent technology development in battery still cannot suffice to meet the required capacity. As a result, to prevent electricity shortage or overloaded grid, utility companies need the short-term projection of photovoltaic energy yields to optimally regulate other sources (e.g., coal plants) as well as distribute electricity in the grid accordingly. In this context, once calibrated and input with weather forecast, this framework can serve this important mission by providing projected short-term energy yields to utility companies. Third, our framework can perform more accurate long-term projection of energy yields than conventional methods (e.g., simple linear regression) that fail to model the inherent nonlinearity of PV degradation. The calculated energy yield is crucial to estimate the LCOE and assess the bankability of a solar farm for investors. Inaccuracy or error in the long-term projection can cause undesired financial losses, particularly when amortization is involved. Therefore, our framework — that can comprehensively and physically model PV degradation — will shed some light on the future development of software used for predictive calculation of solar farms [293].

Step 4: Last but not least, the framework is not one-time calculation. Rather, it continuously mines the field data to circumvent the possibility of missing certain degradation pathways which may appear invisible initially but arise later to inflict damages on the module performance. It is also of equal importance to continually update our degradation library, which may not be complete in the first place. If pronounced discrepancies are detected between the model and the field data, we need to immediately develop new models as well as refine

the physics and formulation of the existing degradation models, with the help from sophisticated off-line characterization techniques (e.g., electroluminescence imaging) to fully understand the physics behind certain degradation.

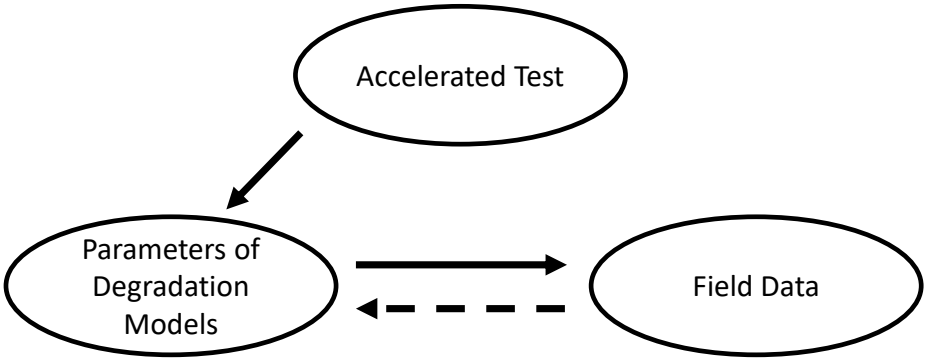

Fig. 6.3. The flow of modeling approach of traditional approaches such as [94]; meanwhile, this holistic framework enables extracting physical parameters of degradation directly from field data.

Technical Challenges of This Framework

Once successfully implemented, this holistic inverse framework will become an omnipotent tool for improving the reliability of solar modules. Yet, there still exist a few technical challenges that need to be overcome as we will discuss below.

1. Modeling Degradation Processes:

Incomplete Understanding of Physics. Since calibrating degradation models entails processing massive environmental data (may up to decades with a minute-by-minute resolution), conventional and computationally intensive modeling approaches based on Finite Element Method (FEM) are not suited here. Instead, one must simplify the model into an analytical (compact) form. However, degradation mechanisms inside solar modules involve slow and complex physical processes, which may be difficult to model analytically. Therefore, the veracity of the model assumptions must be validated with great caution. Since the rates of degradation pathways gen-

erally follow the Arrhenius relationship (i.e., processes accelerate exponentially with temperature as $exp(-E_A/kT)$), time windows with high temperature (e.g., summer) contribute prominently to the development of degradation processes, and render other time periods irrelevant in the calculation. Therefore, the degradation models may be able to selectively simulate degradation processes only for the high-temperature time windows which can substantially simplify the calculation. Indeed, the fidelity of this approach in practice remains as an open question for future research.

Coupling Effect of Degradation Processes. As shown in Table 1.1, besides deteriorating module performance, a degradation process can also be activated or accelerated by others. For example, glass cracking creates extra paths for moisture ingress and ultimately accelerates contact corrosion. This coupling effect – that considerably intertwines the modeling of these degradation processes – ought to be adequately modeled in this framework. To make physical parameters of the degradation model as a function of other processes could be one solution to this problem.

2. Mapping Degradation to Circuit Model:

Degradation Processes Are Not Orthogonal. Even with fully specified degradation models, it still requires mapping their impacts to the parameters in the circuit model for inverse modeling. Ideally, the impact of degradation processes should be orthogonal. Namely, one degradation only affects one specific circuit parameter without overlapping each other. In reality, however, multiple degradation pathways can change the same circuit parameter concurrently, thereby making them indistinguishable, e.g., both EVA delamination and EVA discoloration reduce photocurrent. In this case, one may have to rely on acceleration tests to calibrate degradation models beforehand in order to decompose them in the field data.

Non-Uniform Degradation. The Suns-Vmp method discussed in Chapter 5 applies a single circuit to represent a string of solar modules which can further break down into multiple cells. Many of the common PV degradation pathways, nonetheless, are highly position-resolved (PID varies from cell to cell with a module, see Fig. 13 in [294]) and a single circuit may be insufficient in the case of severe non-uniformity,

as discussed in Sec. 5.4.4. One obvious solution is, instead of merely one circuit, to adopt multiple sub-circuits to account for this non-uniformity. The ensuing issues here is that the increased number of circuit parameters can cause non-uniqueness of the solution when fitting to either MPP or full IV sweep.

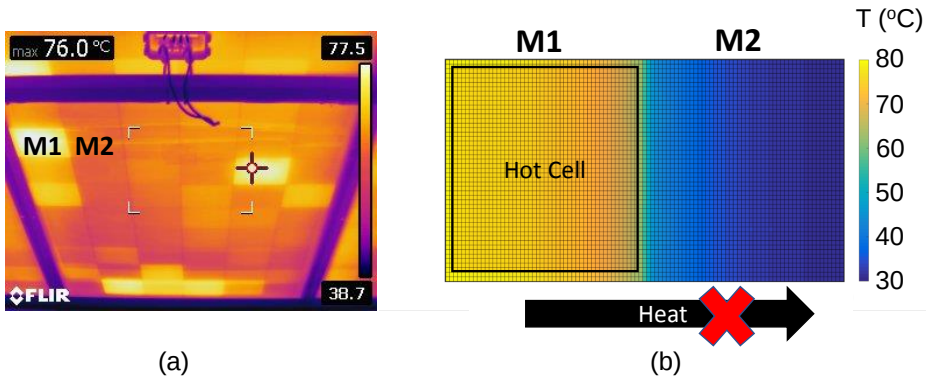

Fig. 6.4. (a) IR image (facing the backsheet) of a two years old solar module installed in India showing the distribution of hot cells. (b) Electro-thermal coupled simulation results of the temperature profile for cells M1 and M2 in (a). This plot is taken from [295] ©2016 IEEE.

To overcome this numerical difficulty, one may add another thermal probe in addition to the existing electrical probe (current and voltage), see Fig. 6.4 (a). Specifically, thermal imaging can easily translate the non-uniform characteristics present in a degraded module to temperature distribution. Applying the electro-thermal framework developed in Chapter 2, one spatially determines the variation between each cell from the thermal image and ultimately extract the circuit parameters for each cell from the electrical measurement self-consistently, as demonstrated in see Fig. 6.4 (b). Of course, the feasibility of this approach shall be explored as a future research problem.

6.3 Final Remarks

Energy demand is increasing with the exploding world population; also, global warming is endangering the environment for us and our posterity, a result of con-

sumption of fossil fuels for decades. Therefore, it is the author's deepest belief that clean energy, such like solar PV, will sooner or later supersede traditional fossil fuels to become the dominant energy source for humanity. However, the only path toward this Utopia is to continuously reduce the LCOE of PV to make them more financially competitive. As the performance of PV is approaching the fundamental physical limit, new research angles and ingenious engineering must be invented and carried out to keep pushing the boundary of improvements.

This thesis has brought new perspectives to PV research. Part of the framework discussed in the thesis is inspired by other fields, such as the cell-to-module approach discussed here is in analogous to the transistor-to-computer route in electronics. However, this quasi-orthogonal approach is versatile and ubiquitous, and utterly transferable to other research areas. For instance, like PV, self-heating is becoming a pressing issue for deeply scaled transistors with increasing power density. Radiative cooling, already demonstrated for PV, could also serve as a means to alleviate self-heating, particularly for portable electronics where active cooling is difficult. Moreover, one can also apply the inverse modeling framework to applications where reliability is a serious concern, such as biosensors and internet-of-things (IoT) devices. The author hopes that the thesis can also enlighten readers outside the PV community, and facilitate the future confluence of multidisciplinary research.

REFERENCES

REFERENCES

[1] "Renewable Energy Sources and Climate Change Mitigation," 2012. [Online]. Available: https://www.ipcc.ch/pdf/special-reports/srren/SRREN_FD_SPM_final.pdf

[2] IRENA, "REthinking Energy," p. 96, 2014. [Online]. Available: http://www.irena.org/-/media/Files/IRENA/Agency/Publication/2014/IRENA_REthinking_fullreport_2014.pdf

[3] "Technology Roadmap: Solar Photovoltaic Energy - 2014 edition," 2014. [Online]. Available: http://www.iea.org/publications/freepublications/publication/technology-roadmap-solar-photovoltaic-energy---2014-edition.html

[4] O. Morton, "Solar energy: Silicon Valley sunrise," *Nature*, vol. 443, no. 7107, pp. 19–22, 9 2006. [Online]. Available: http://www.nature.com/doifinder/10.1038/443019a

[5] K. Solangi, M. Islam, R. Saidur, N. Rahim, and H. Fayaz, "A review on global solar energy policy," *Renewable and Sustainable Energy Reviews*, vol. 15, no. 4, pp. 2149–2163, 5 2011. [Online]. Available: http://linkinghub.elsevier.com/retrieve/pii/S1364032111000220

[6] S. Mekhilef, R. Saidur, and A. Safari, "A review on solar energy use in industries," *Renewable and Sustainable Energy Reviews*, vol. 15, no. 4, pp. 1777–1790, 5 2011. [Online]. Available: http://linkinghub.elsevier.com/retrieve/pii/S1364032110004533

[7] W. Hoffmann, "PV solar electricity industry: Market growth and perspective," *Solar Energy Materials and Solar Cells*, vol. 90, no. 18-19, pp. 3285–3311, 11 2006. [Online]. Available: http://linkinghub.elsevier.com/retrieve/pii/S0927024806002509

[8] "Annual Energy Outlook 2015." [Online]. Available: https://www.eia.gov/pressroom/presentations/sieminski_05042015.pdf

[9] "2016 Snapshot of Global PV Markets," International Energy Agency, Tech. Rep. [Online]. Available: http://www.iea-pvps.org/fileadmin/dam/public/report/statistics/IEA-PVPS_-_A_Snapshot_of_Global_PV_-_1992-2016__1_.pdf

[10] E. WESOFF, "IEA: Global Installed PV Capacity Leaps to 303 Gigawatts." [Online]. Available: https://www.greentechmedia.com/articles/read/iea-global-installed-pv-capacity-leaps-to-303-gw#gs.ije6DbE

[11] "Electricity production from solar and wind in Germany in 2014 (German version)," Germany: Fraunhofer Institute for Solar Energy Systems ISE, Tech. Rep., 2015. [Online]. Available: http://www.ise.fraunhofer.de/de/downloads/pdf-files/data-nivc-/stromproduktion-aus-solar-und-windenergie-2014.pdf

[12] W. Pentland, "Japan's Solar Boom Is Accelerating." [Online]. Available: https://www.forbes.com/sites/williampentland/2017/01/23/japans-solar-boom-is-accelerating/#6bfc5b4232c9

[13] A. Yee, "In Rural Bangladesh, Solar Power Dents Poverty." [Online]. Available: https://www.nytimes.com/2016/10/04/opinion/in-rural-bangladesh-solar-power-dents-poverty.html

[14] "Residential Renewable Energy Tax Credit." [Online]. Available: https://energy.gov/savings/residential-renewable-energy-tax-credit

[15] D. B. Needleman, J. R. Poindexter, R. C. Kurchin, I. Marius Peters, G. Wilson, and T. Buonassisi, "Economically sustainable scaling of photovoltaics to meet climate targets," *Energy Environ. Sci.*, vol. 9, no. 6, pp. 2122–2129, 2016. [Online]. Available: http://dx.doi.org/10.1039/C6EE00484Ahttp://xlink.rsc.org/?DOI=C6EE00484A

[16] K. A. Horowitz, R. Fu, and M. Woodhouse, "An analysis of glassglass CIGS manufacturing costs," *Solar Energy Materials and Solar Cells*, vol. 154, pp. 1–10, 9 2016. [Online]. Available: http://linkinghub.elsevier.com/retrieve/pii/S0927024816300435

[17] S. M. McLeod, C. J. Hages, N. J. Carter, and R. Agrawal, "Synthesis and characterization of 15% efficient CIGSSe solar cells from nanoparticle inks," *Progress in Photovoltaics: Research and Applications*, vol. 23, no. 11, pp. 1550–1556, 11 2015. [Online]. Available: http://doi.wiley.com/10.1002/pip.2588

[18] S. Kazim, M. K. Nazeeruddin, M. Grätzel, and S. Ahmad, "Perovskite as light harvester: a game changer in photovoltaics." *Angewandte Chemie (International ed. in English)*, vol. 53, no. 11, pp. 2812–24, 3 2014. [Online]. Available: http://www.ncbi.nlm.nih.gov/pubmed/24519832

[19] M. Cai, Y. Wu, H. Chen, X. Yang, Y. Qiang, and L. Han, "Cost-Performance Analysis of Perovskite Solar Modules," *Advanced Science*, vol. 4, no. 1, p. 1600269, 1 2017. [Online]. Available: http://doi.wiley.com/10.1002/advs.201600269

[20] M. A. Green, "The path to 25% silicon solar cell efficiency: History of silicon cell evolution," *Progress in Photovoltaics: Research and Applications*, vol. 17, no. 3, pp. 183–189, 5 2009. [Online]. Available: http://doi.wiley.com/10.1002/pip.892

[21] J. Benick, A. Richter, R. Muller, H. Hauser, F. Feldmann, P. Krenckel, S. Riepe, F. Schindler, M. C. Schubert, M. Hermle, A. W. Bett, and S. W. Glunz, "High-Efficiency n-Type HP mc Silicon Solar Cells," *IEEE Journal of Photovoltaics*, vol. 7, no. 5, pp. 1171–1175, 9 2017. [Online]. Available: http://ieeexplore.ieee.org/document/7984794/

[22] M. A. Green, Y. Hishikawa, W. Warta, E. D. Dunlop, D. H. Levi, J. Hohl-Ebinger, and A. W. Ho-Baillie, "Solar cell efficiency tables (version 50)," *Progress in Photovoltaics: Research and Applications*, vol. 25, no. 7, pp. 668–676, 7 2017. [Online]. Available: http://doi.wiley.com/10.1002/pip.2909

[23] "New world record for solar cell efficiency at 46% French-German cooperation confirms competitive advantage of European photovoltaic industry." [Online]. Available: https://www.ise.fraunhofer.de/en/press-media/press-releases/2014/new-world-record-for-solar-cell-efficiency-at-46-percent.html

[24] M. A. Alam and M. Ryyan Khan, "Fundamentals of PV efficiency interpreted by a two-level model," *American Journal of Physics*, vol. 81, no. 9, pp. 655–662, 9 2013. [Online]. Available: http://aapt.scitation.org/doi/10.1119/1.4812594

[25] W. Shockley and H. J. Queisser, "Detailed Balance Limit of Efficiency of p-n Junction Solar Cells," *Journal of Applied Physics*, vol. 32, no. 3, p. 510, 1961. [Online]. Available: http://link.aip.org/link/JAPIAU/v32/i3/p510/s1&Agg=doi

[26] "NREL efficiency chart." [Online]. Available: https://www.nrel.gov/pv/assets/images/efficiency-chart.png

[27] R. Guerrero-Lemus, R. Vega, T. Kim, A. Kimm, and L. E. Shephard, "Bifacial solar photovoltaics - A technology review," *Renewable and Sustainable Energy Reviews*, vol. 60, pp. 1533–1549, 2016. [Online]. Available: http://dx.doi.org/10.1016/j.rser.2016.03.041

[28] R. Arndt and R. Puto, "Basic understanding of IEC standard testing for photovoltaic panels," *... [2012]. Http://Tuvamerica. Com/Services/Photovoltaics/...*, no. 978, pp. 1–15, 2010. [Online]. Available: http://www.tuv-sud.us/services/photovoltaics/ArticleBasicUnderstandingPV.pdf

[29] "All-India India Survey of Photovoltaic Module Degradation : 2013," Tech. Rep. [Online]. Available: http://www.ncpre.iitb.ac.in/uploads/ChendamangalamFinalReporte-copy_upload.pdf

[30] "Levelized Cost and Levelized Avoided Cost of New Generation Resources in the Annual Energy Outlook 2017." [Online]. Available: https://www.eia.gov/outlooks/aeo/pdf/electricity_generation.pdf

[31] "Lazards Levelized Cost of Storage Analysis V11.0." [Online]. Available: https://www.lazard.com/perspective/levelized-cost-of-energy-2017/

[32] N. Groom, "Big solar is leaving rooftop systems in the dust." [Online]. Available: https://www.reuters.com/article/us-solar-costs/big-solar-is-leaving-rooftop-systems-in-the-dust-idUSKCN0ZL0DA

[33] J. Conca, "Which Is Cheaper – Rooftop Solar Or Utility-Scale Solar?" [Online]. Available: https://www.forbes.com/sites/jamesconca/2015/07/30/which-is-cheaper-rooftop-solar-or-utility-scale-solar/#f90ab411e5da

[34] R. V. K. Chavali, E. C. Johlin, J. L. Gray, T. Buonassisi, and M. A. Alam, "A Framework for Process-to-Module Modeling of a-Si/c-Si (HIT) Heterojunction Solar Cells to Investigate the Cell-to-Module Efficiency Gap," *IEEE Journal of Photovoltaics*, vol. 6, no. 4, pp. 1–13, 7 2016. [Online]. Available: http://ieeexplore.ieee.org/lpdocs/epic03/wrapper.htm?arnumber=7475492

[35] K. Yoshikawa, H. Kawasaki, W. Yoshida, T. Irie, K. Konishi, K. Nakano, T. Uto, D. Adachi, M. Kanematsu, H. Uzu, and K. Yamamoto, "Silicon heterojunction solar cell with interdigitated back contacts for a photoconversion efficiency over 26%," *Nature Energy*, vol. 2, no. 5, p. 17032, 3 2017. [Online]. Available: http://www.nature.com/articles/nenergy201732

[36] "Panasonic Photovoltaic Module HIT-N245 and HIT-N240," 2015. [Online]. Available: https://eu-solar.panasonic.net/cps/rde/xbcr/solar_en/VBHN240_245SJ25_EN.pdf

[37] M. A. Alam, B. Ray, M. R. Khan, and S. Dongaonkar, "The essence and efficiency limits of bulk-heterostructure organic solar cells: A polymer-to-panel perspective," *Journal of Materials Research*, vol. 28, no. 04, pp. 541–557, 2 2013. [Online]. Available: http://www.journals.cambridge.org/abstract_S0884291412004256

[38] E. S. Mungan, Y. Wang, S. Dongaonkar, D. R. Ely, R. E. Garcia, and M. A. Alam, "From Process to Modules: End-to-End Modeling of CSS-Deposited CdTe Solar Cells," *IEEE Journal of Photovoltaics*, vol. 4, no. 3, pp. 954–961, 5 2014. [Online]. Available: http://ieeexplore.ieee.org/document/6781016/

[39] S. Dongaonkar and M. A. Alam, "In-Line Post-Process Scribing for Reducing Cell to Module Efficiency Gap in Monolithic Thin-Film Photovoltaics," *IEEE Journal of Photovoltaics*, vol. 4, no. 1, pp. 324–332, 1 2014. [Online]. Available: http://ieeexplore.ieee.org/lpdocs/epic03/wrapper.htm?arnumber=6646237

[40] M. Hejri, H. Mokhtari, M. R. Azizian, M. Ghandhari, and L. Soder, "On the Parameter Extraction of a Five-Parameter Double-Diode Model of Photovoltaic Cells and Modules," *IEEE Journal of Photovoltaics*, vol. 4, no. 3, pp. 915–923, 5 2014. [Online]. Available: http://ieeexplore.ieee.org/lpdocs/epic03/wrapper.htm?arnumber=6756936

[41] M. Eron and A. Rothwarf, "Effects of a voltage-dependent light-generated current on solar cell measurements: CuInSe2/Cd(Zn)S," *Applied Physics Letters*, vol. 44, no. 1, p. 131, 1984. [Online]. Available: http://scitation.aip.org/content/aip/journal/apl/44/1/10.1063/1.94577

[42] J. E. Moore, S. Dongaonkar, R. V. K. Chavali, M. A. Alam, and M. S. Lundstrom, "Correlation of Built-In Potential and IV Crossover in Thin-Film Solar Cells," *IEEE Journal of Photovoltaics*, vol. 4, no. 4, pp. 1138–1148, 7 2014. [Online]. Available: http://ieeexplore.ieee.org/document/6810770/

[43] S. Hegedus, D. Desai, and C. Thompson, "Voltage dependent photocurrent collection in CdTe/CdS solar cells," *Progress in Photovoltaics: Research and Applications*, vol. 15, no. 7, pp. 587–602, 11 2007. [Online]. Available: http://doi.wiley.com/10.1002/pip.767

[44] M. Gloeckler, C. R. Jenkins, and J. R. Sites, "Explanation of Light/Dark Superposition Failure in CIGS Solar Cells," *MRS Proceedings*, vol. 763, p. B5.20, 1 2003. [Online]. Available: http://journals.cambridge.org/abstract_S194642740013338X

[45] X. X. Liu and J. R. Sites, "Solar-cell collection efficiency and its variation with voltage," *Journal of Applied Physics*, vol. 75, no. 1, pp. 577–581, 1 1994.

[Online]. Available: http://scitation.aip.org/content/aip/journal/jap/75/1/10.1063/1.355842

[46] K. W. Mitchell, A. L. Fahrenbruch, and R. H. Bube, "Evaluation of the CdS/CdTe heterojunction solar cell," *Journal of Applied Physics*, vol. 48, no. 10, pp. 4365–4371, 10 1977. [Online]. Available: http://aip.scitation.org/doi/10.1063/1.323429

[47] W. W. Gärtner, "Depletion-Layer Photoeffects in Semiconductors," *Physical Review*, vol. 116, no. 1, pp. 84–87, 10 1959. [Online]. Available: https://link.aps.org/doi/10.1103/PhysRev.116.84

[48] A. Kojima, K. Teshima, Y. Shirai, and T. Miyasaka, "Organometal Halide Perovskites as Visible-Light Sensitizers for Photovoltaic Cells," *Journal of the American Chemical Society*, vol. 131, no. 17, pp. 6050–6051, 5 2009. [Online]. Available: http://pubs.acs.org/doi/abs/10.1021/ja809598r

[49] W. S. Yang, B.-W. Park, E. H. Jung, N. J. Jeon, Y. C. Kim, D. U. Lee, S. S. Shin, J. Seo, E. K. Kim, J. H. Noh, and S. I. Seok, "Iodide management in formamidinium-lead-halidebased perovskite layers for efficient solar cells," *Science*, vol. 356, no. 6345, pp. 1376–1379, 6 2017. [Online]. Available: http://www.sciencemag.org/lookup/doi/10.1126/science.aan2301

[50] T. J. Silverman, M. G. Deceglie, X. Sun, R. L. Garris, M. A. Alam, C. Deline, and S. Kurtz, "Thermal and electrical effects of partial shade in monolithic thin-film photovoltaic modules," in *2015 IEEE 42nd Photovoltaic Specialist Conference (PVSC)*. IEEE, 6 2015, pp. 1–6. [Online]. Available: http://ieeexplore.ieee.org/document/7355668/

[51] B. E. Pieters, "Spatial Modeling of Thin-Film Solar Modules Using the Network Simulation Method and SPICE," *IEEE Journal of Photovoltaics*, vol. 1, no. 1, pp. 93–98, 7 2011. [Online]. Available: http://ieeexplore.ieee.org/document/5999681/

[52] S. Dongaonkar, C. Deline, and M. A. Alam, "Performance and Reliability Implications of Two-Dimensional Shading in Monolithic Thin-Film Photovoltaic Modules," *IEEE Journal of Photovoltaics*, vol. 3, no. 4, pp. 1367–1375, 10 2013. [Online]. Available: http://ieeexplore.ieee.org/document/6558752/

[53] M. R. Khan, X. Wang, and M. A. Alam, "Fundamentals of PV Efficiency: Limits for Light Absorption," pp. 1–8, 12 2012. [Online]. Available: http://arxiv.org/abs/1212.2897

[54] X. Wang, M. R. Khan, J. L. Gray, M. A. Alam, and M. S. Lundstrom, "Design of GaAs Solar Cells Operating Close to the Shockley-Queisser Limit," *IEEE Journal of Photovoltaics*, vol. 3, no. 2, pp. 737–744, 4 2013. [Online]. Available: http://ieeexplore.ieee.org/lpdocs/epic03/wrapper.htm?arnumber=6458975

[55] G. T. Koishiyev and J. R. Sites, "Impact of sheet resistance on 2-D modeling of thin-film solar cells," *Solar Energy Materials and Solar Cells*, vol. 93, no. 3, pp. 350–354, 3 2009. [Online]. Available: http://linkinghub.elsevier.com/retrieve/pii/S0927024808004121

[56] S. Dongaonkar, J. D. Servaites, G. M. Ford, S. Loser, J. Moore, R. M. Gelfand, H. Mohseni, H. W. Hillhouse, R. Agrawal, M. A. Ratner, T. J. Marks, M. S. Lundstrom, and M. A. Alam, "Universality of non-Ohmic shunt leakage in thin-film solar cells," *Journal of Applied Physics*, vol. 108, no. 12, p. 124509, 12 2010. [Online]. Available: http://aip.scitation.org/doi/10.1063/1.3518509

[57] S. Dongaonkar, K. Y., S. Mahapatra, and M. A. Alam, "Physics and Statistics of Non-Ohmic Shunt Conduction and Metastability in Amorphous Silicon pin Solar Cells," *IEEE Journal of Photovoltaics*, vol. 1, no. 2, pp. 111–117, 10 2011. [Online]. Available: http://ieeexplore.ieee.org/document/6095307/

[58] S. Dongaonkar, K. Y, D. Wang, M. Frei, S. Mahapatra, and M. A. Alam, "On the Nature of Shunt Leakage in Amorphous Silicon p-i-n Solar Cells," *IEEE Electron Device Letters*, vol. 31, no. 11, pp. 1266–1268, 11 2010. [Online]. Available: http://ieeexplore.ieee.org/document/5565387/

[59] A. Virtuani, D. Pavanello, and G. Friesen, "Overview of Temperature Coefficients of Different Thin Film Photovoltaic Technologies," in *25th European Photovoltaic Solar Energy Conference and Exhibition*, 2010, pp. 4125–4128.

[60] Z. C. Holman, M. Filipič, B. Lipovšek, S. De Wolf, F. Smole, M. Topič, and C. Ballif, "Parasitic absorption in the rear reflector of a silicon solar cell: Simulation and measurement of the sub-bandgap reflectance for common dielectric/metal reflectors," *Solar Energy Materials and Solar Cells*, vol. 120, no. PART A, pp. 426–430, 1 2014. [Online]. Available: http://linkinghub.elsevier.com/retrieve/pii/S0927024813003097

[61] R. Santbergen and R. van Zolingen, "The absorption factor of crystalline silicon PV cells: A numerical and experimental study," *Solar Energy Materials and Solar Cells*, vol. 92, no. 4, pp. 432–444, 4 2008. [Online]. Available: http://linkinghub.elsevier.com/retrieve/pii/S0927024807004023

[62] T. J. Silverman, M. G. Deceglie, B. Marion, S. Cowley, B. Kayes, and S. Kurtz, "Outdoor performance of a thin-film gallium-arsenide photovoltaic module," *2013 IEEE 39th Photovoltaic Specialists Conference (PVSC)*, pp. 0103–0108, 6 2013. [Online]. Available: http://ieeexplore.ieee.org/lpdocs/epic03/wrapper.htm?arnumber=6744109

[63] M. Chandrasekar and T. Senthilkumar, "Passive thermal regulation of flat PV modules by coupling the mechanisms of evaporative and fin cooling," *Heat and Mass Transfer*, 2015. [Online]. Available: http://link.springer.com/10.1007/s00231-015-1661-9

[64] H. Koehler, "Cooling photovoltaic (PV) cells during concentrated solar radiation in specified arrangement in coolant with as low electric conductivity as possible," 2000.

[65] L. Zhu, R. F. Boehm, Y. Wang, C. Halford, and Y. Sun, "Water immersion cooling of PV cells in a high concentration system," *Solar Energy Materials and Solar Cells*, vol. 95, no. 2, pp. 538–545, 2 2011. [Online]. Available: http://linkinghub.elsevier.com/retrieve/pii/S0927024810005374

[66] A. Akbarzadeh and T. Wadowski, "Heat pipe-based cooling systems for photovoltaic cells under concentrated solar radiation," *Applied Thermal*

Engineering, vol. 16, no. 1, pp. 81–87, 1 1996. [Online]. Available: http://linkinghub.elsevier.com/retrieve/pii/1359431195000123

[67] A. Royne, C. Dey, and D. Mills, "Cooling of photovoltaic cells under concentrated illumination: a critical review," *Solar Energy Materials and Solar Cells*, vol. 86, no. 4, pp. 451–483, 4 2005. [Online]. Available: http://linkinghub.elsevier.com/retrieve/pii/S0927024804003071

[68] L. Zhu, A. Raman, K. X. Wang, M. A. Anoma, and S. Fan, "Radiative cooling of solar cells," *Optica*, vol. 1, no. 1, pp. 32–38, 2014. [Online]. Available: http://www.opticsinfobase.org/optica/abstract.cfm?URI=optica-1-1-32

[69] L. Zhu, A. P. Raman, and S. Fan, "Radiative cooling of solar absorbers using a visibly transparent photonic crystal thermal blackbody," *Proceedings of the National Academy of Sciences*, p. 201509453, 9 2015. [Online]. Available: http://www.pnas.org/lookup/doi/10.1073/pnas.1509453112

[70] A. Gentle and G. Smith, "Is enhanced radiative cooling of solar cell modules worth pursuing?" *Solar Energy Materials and Solar Cells*, vol. 150, pp. 39–42, 2016. [Online]. Available: http://linkinghub.elsevier.com/retrieve/pii/S0927024816000520

[71] T. S. Safi and J. N. Munday, "Improving photovoltaic performance through radiative cooling in both terrestrial and extraterrestrial environments," *Optics Express*, vol. 23, no. 19, p. A1120, 9 2015. [Online]. Available: http://www.osapublishing.org/viewmedia.cfm?uri=oe-23-19-A1120&seq=0&html=true

[72] S. Armstrong and W. Hurley, "A thermal model for photovoltaic panels under varying atmospheric conditions," *Applied Thermal Engineering*, vol. 30, no. 11-12, pp. 1488–1495, 8 2010. [Online]. Available: http://dx.doi.org/10.1016/j.applthermaleng.2010.03.012http://linkinghub.elsevier.com/retrieve/pii/S1359431110001225

[73] A. Jones and C. Underwood, "A thermal model for photovoltaic systems," *Solar Energy*, vol. 70, no. 4, pp. 349–359, 2001. [Online]. Available: http://linkinghub.elsevier.com/retrieve/pii/S0038092X00001493

[74] S. Silvestre, a. Boronat, and a. Chouder, "Study of bypass diodes configuration on PV modules," *Applied Energy*, vol. 86, no. 9, pp. 1632–1640, 2009. [Online]. Available: http://dx.doi.org/10.1016/j.apenergy.2009.01.020

[75] Dzung Nguyen and B. Lehman, "A reconfigurable solar photovoltaic array under shadow conditions," in *2008 Twenty-Third Annual IEEE Applied Power Electronics Conference and Exposition*. IEEE, 2 2008, pp. 980–986. [Online]. Available: http://ieeexplore.ieee.org/document/4522840/

[76] J. E. Lee, S. Bae, W. Oh, H. Park, S. M. Kim, D. Lee, J. Nam, C. B. Mo, D. D. Kim, J. Yang, Y. Kang, H. Lee, and D. D. Kim, "Investigation of damage caused by partial shading of CuInxGa (1-x) Se 2 photovoltaic modules with bypass diodes," *Progress in Photovoltaics: Research and Applications*, vol. 24, no. 8, pp. 1035–1043, 8 2016. [Online]. Available: http://doi.wiley.com/10.1002/pip.2738http://dx.doi.org/10.1002/pip.1160

[77] P.-O. Westin, M. Edoff, U. Zimmermann, and L. Stolt, "Reverse bias damage in CIGS modules," in *24th European Photovoltaic Solar Energy Conference and Exhibition*, no. September, 2009, pp. 2967–2970. [Online]. Available: http://urn.kb.se/resolve?urn=urn:nbn:se:uu:diva-109181

[78] A. E. Brooks, D. Cormode, A. D. Cronin, and E. Kam-Lum, "PV system power loss and module damage due to partial shade and bypass diode failure depend on cell behavior in reverse bias," in *2015 IEEE 42nd Photovoltaic Specialist Conference (PVSC)*. IEEE, 6 2015, pp. 1–6. [Online]. Available: http://ieeexplore.ieee.org/lpdocs/epic03/wrapper.htm?arnumber=7356290

[79] T. J. Silverman, L. Mansfield, I. Repins, and S. Kurtz, "Damage in Monolithic Thin-Film Photovoltaic Modules Due to Partial Shade," *IEEE Journal of Photovoltaics*, pp. 1–6, 2016. [Online]. Available: http://ieeexplore.ieee.org/lpdocs/epic03/wrapper.htm?arnumber=7523923

[80] S. Dongaonkar and M. A. Alam, "Geometrical design of thin film photovoltaic modules for improved shade tolerance and performance," pp. 6–11, 2 2013. [Online]. Available: http://doi.wiley.com/10.1002/pip.2410

[81] "2017 International Technology Roadmap for Photovoltaic (ITRPV)," 2017.

[82] M. Hiroshi, "Radiation energy transducing device," 1966.

[83] A. Cuevas, A. Luque, J. Eguren, and J. del Alamo, "50% more output power from an albedo-collecting flat panel using bifacial solar cells," *Solar Energy*, vol. 29, no. 5, pp. 419–420, 1982. [Online]. Available: http://linkinghub.elsevier.com/retrieve/pii/0038092X82900780

[84] A. Hubner, A. Aberle, and R. Hezel, "Temperature behavior of monofacial and bifacial silicon solar cells," in *Conference Record of the Twenty Sixth IEEE Photovoltaic Specialists Conference - 1997*. IEEE, 1997, pp. 223–226. [Online]. Available: http://ieeexplore.ieee.org/document/654069/

[85] S. Grover and J. V. Li, "Theory and analysis of temperature coefficient of open-circuit voltage (dVOC/dT) in heterojunction solar cells," in *2015 IEEE 42nd Photovoltaic Specialist Conference (PVSC)*. IEEE, 6 2015, pp. 1–3. [Online]. Available: http://ieeexplore.ieee.org/document/7356039/

[86] J. Liang, J. Yang, G. Zhang, and W. Sun, "Flexible fiber-type dye-sensitized solar cells based on highly ordered TiO2 nanotube arrays," *Electrochemistry Communications*, vol. 37, pp. 80–83, 12 2013. [Online]. Available: http://linkinghub.elsevier.com/retrieve/pii/S1388248113004025

[87] A. Romeo, G. Khrypunov, S. Galassini, H. Zogg, and A. Tiwari, "Bifacial configurations for CdTe solar cells," *Solar Energy Materials and Solar Cells*, vol. 91, no. 15-16, pp. 1388–1391, 9 2007. [Online]. Available: http://linkinghub.elsevier.com/retrieve/pii/S0927024807001031

[88] T. Nakada, "Microstructural and diffusion properties of CIGS thin film solar cells fabricated using transparent conducting oxide back contacts," *Thin Solid Films*, vol. 480-481, pp. 419–425, 6 2005. [Online]. Available: http://linkinghub.elsevier.com/retrieve/pii/S0040609004015834

[89] D. Brearley, "Bifacial PV Systems," *SolarPro*, no. 10.2, 2017. [Online]. Available: http://solarprofessional.com/articles/design-installation/bifacial-pv-systems#.Wm6zGq6nGiM

[90] F. Toor, E. Cahill, C. Liu, M. Feinstein, J. Melnick, and K. See, "Continuing education: going back to school for photovoltaic innovation," *State of the Market Report, Lux Research*. [Online]. Available: https://members.luxresearchinc.com/research/report/11903

[91] U. A. Yusufoglu, T. M. Pletzer, L. J. Koduvelikulathu, C. Comparotto, R. Kopecek, and H. Kurz, "Analysis of the Annual Performance of Bifacial Modules and Optimization Methods," *IEEE Journal of Photovoltaics*, vol. 5, no. 1, pp. 320–328, 1 2015. [Online]. Available: http://ieeexplore.ieee.org/lpdocs/epic03/wrapper.htm?arnumber=6960821

[92] A. Luque and S. Hegedus, *Handbook of Photovoltaic Science and Engineering*, 2nd ed. Wiley, 2010.

[93] P. Hacke, S. Spataru, K. Terwilliger, G. Perrin, S. Glick, S. Kurtz, and J. Wohlgemuth, "Accelerated Testing and Modeling of Potential-Induced Degradation as a Function of Temperature and Relative Humidity," *IEEE Journal of Photovoltaics*, vol. 5, no. 6, pp. 1549–1553, 11 2015. [Online]. Available: http://ieeexplore.ieee.org/lpdocs/epic03/wrapper.htm?arnumber=7229241

[94] M. A. Mikofski, D. F. J. Kavulak, D. Okawa, Y.-c. Shen, A. Terao, M. Anderson, S. Caldwell, D. Kim, N. Boitnott, J. Castro, L. A. L. Smith, R. Lacerda, D. Benjamin, and E. F. Hasselbrink, "PVLife: An integrated model for predicting PV performance degradation over 25+ years," in *2012 38th IEEE Photovoltaic Specialists Conference*, no. 2. IEEE, 6 2012, pp. 001 744–001 749. [Online]. Available: http://ieeexplore.ieee.org/document/6317932/

[95] D. Berman, S. Biryukov, and D. Faiman, "EVA laminate browning after 5 years in a grid-connected, mirror-assisted, photovoltaic system in the Negev desert: effect on module efficiency," *Solar Energy Materials and Solar Cells*, vol. 36, no. 4, pp. 421–432, 4 1995. [Online]. Available: http://linkinghub.elsevier.com/retrieve/pii/0927024894001987

[96] D. Wu, J. Zhu, T. R. Betts, and R. Gottschalg, "Degradation of interfacial adhesion strength within photovoltaic mini-modules during damp-heat exposure," *Progress in Photovoltaics: Research and Applications*, vol. 22, no. 7, pp. 796–809, 7 2014. [Online]. Available: http://doi.wiley.com/10.1002/pip.2460

[97] S. Chattopadhyay, R. Dubey, V. Kuthanazhi, J. J. John, C. S. Solanki, A. Kottantharayil, B. M. Arora, K. L. Narasimhan, V. Kuber, J. Vasi, A. Kumar, and O. S. Sastry, "Visual Degradation in Field-Aged Crystalline Silicon PV Modules in India and Correlation With Electrical Degradation," *IEEE Journal of Photovoltaics*, vol. 4, no. 6, pp. 1470–1476, 11 2014. [Online]. Available: http://ieeexplore.ieee.org/lpdocs/epic03/wrapper.htm?arnumber=6919266

[98] M. G. Deceglie, M. Muller, Z. Defreitas, and S. Kurtz, "A scalable method for extracting soiling rates from PV production data," in *2016 IEEE 43rd*

Photovoltaic Specialists Conference (PVSC), no. June. IEEE, 6 2016, pp. 2061–2065. [Online]. Available: http://ieeexplore.ieee.org/document/7749992/

[99] D. C. Jordan, B. Sekulic, B. Marion, and S. R. Kurtz, "Performance and Aging of a 20-Year-Old Silicon PV System," *IEEE Journal of Photovoltaics*, vol. 5, no. 3, pp. 744–751, 5 2015. [Online]. Available: http://ieeexplore.ieee.org/document/7042258/

[100] M. D. Kempe, A. A. Dameron, and M. O. Reese, "Evaluation of moisture ingress from the perimeter of photovoltaic modules," *Progress in Photovoltaics: Research and Applications*, vol. 22, no. 11, pp. 1159–1171, 11 2014. [Online]. Available: http://doi.wiley.com/10.1002/pip.2374

[101] M. Kempe, "Modeling of rates of moisture ingress into photovoltaic modules," *Solar Energy Materials and Solar Cells*, vol. 90, no. 16, pp. 2720–2738, 10 2006. [Online]. Available: http://linkinghub.elsevier.com/retrieve/pii/S0927024806001632

[102] U. Itoh, M. Yoshida, H. Tokuhisa, K. Takeuchi, and Y. Takemura, "Solder joint failure modes in the conventional crystalline si module," *Energy Procedia*, vol. 55, no. 3, pp. 464–468, 2014. [Online]. Available: http://dx.doi.org/10.1016/j.egypro.2014.08.010

[103] M. T. Zarmai, N. Ekere, C. Oduoza, and E. H. Amalu, "A review of interconnection technologies for improved crystalline silicon solar cell photovoltaic module assembly," *Applied Energy*, vol. 154, pp. 173–182, 9 2015. [Online]. Available: http://linkinghub.elsevier.com/retrieve/pii/S0306261915005838

[104] Y.-L. Shen, "Numerical Study of Solder Bond Failure in Photovoltaic Modules," *Procedia Engineering*, vol. 139, pp. 93–100, 2016. [Online]. Available: http://linkinghub.elsevier.com/retrieve/pii/S1877705815030568

[105] S. Hoffmann and M. Koehl, "Effect of humidity and temperature on the potential-induced degradation," *Progress in Photovoltaics: Research and Applications*, vol. 22, no. 2, pp. 173–179, 2 2014. [Online]. Available: http://dx.doi.org/10.1002/pip.1160http://doi.wiley.com/10.1002/pip.2238

[106] J. Hattendorf., R. Löw, W.-M. Gnehr, L. Wulff, M. Koekten, D. Koshnicharov, A. Blauaermel, and J. Esquivel, "Potential Induced Degradation in Mono-Crystalline Silicon Based Modules: An Acceleration Model," in *27th EU PVSEC*, 2012, pp. 3405 – 3410.

[107] Maoyi Chang, Chienyu Chen, C. H. Hsueh, W. J. Hsieh, E. Yen, K. L. Ho, H. P. Chuang, C. Y. Lee, and Haomin Chen, "The reliability investigation of PV junction box based on 1GW worldwide field database," in *2015 IEEE 42nd Photovoltaic Specialist Conference (PVSC)*. IEEE, 6 2015, pp. 1–4. [Online]. Available: http://ieeexplore.ieee.org/document/7356130/

[108] D. C. Jordan, T. J. Silverman, J. H. Wohlgemuth, S. R. Kurtz, and K. T. VanSant, "Photovoltaic failure and degradation modes," *Progress in Photovoltaics: Research and Applications*, vol. 25, no. February 2013, pp. 659–676, 4 2017. [Online]. Available: http://dx.doi.org/10.1002/pip.1160http://doi.wiley.com/10.1002/pip.2866

[109] E. Wang, H. E. Yang, J. Yen, S. Chi, and C. Wang, "Failure Modes Evaluation of PV Module via Materials Degradation Approach," *Energy Procedia*, vol. 33, pp. 256–264, 2013. [Online]. Available: http://linkinghub.elsevier.com/retrieve/pii/S1876610213000763

[110] A. Morlier, F. Haase, and M. Kontges, "Impact of Cracks in Multicrystalline Silicon Solar Cells on PV Module PowerA Simulation Study Based on Field Data," *IEEE Journal of Photovoltaics*, vol. 5, no. 6, pp. 1735–1741, 11 2015. [Online]. Available: http://ieeexplore.ieee.org/document/7244349/

[111] M. Dhimish, V. Holmes, B. Mehrdadi, and M. Dales, "The impact of cracks on photovoltaic power performance," *Journal of Science: Advanced Materials and Devices*, vol. 2, no. 2, pp. 199–209, 6 2017. [Online]. Available: http://linkinghub.elsevier.com/retrieve/pii/S2468217917300540

[112] C. Barry, "Why Glass Sometimes Breaks," 2010. [Online]. Available: https://www1.eere.energy.gov/solar/pdfs/pvrw2010_barry.pdf

[113] M. D. Kempe, T. Moricone, and M. Kilkenny, "Effects of cerium removal from glass on photovoltaic module performance and stability," N. G. Dhere, J. H. Wohlgemuth, and D. T. Ton, Eds., 8 2009, p. 74120Q. [Online]. Available: http://proceedings.spiedigitallibrary.org/proceeding.aspx?doi=10.1117/12.825699

[114] J. Oh, G. TamizhMani, S. Bowden, and S. Garner, "Surface Disruption Method With Flexible Glass to Prevent Potential-Induced Degradation of the Shunting Type in PV Modules," *IEEE Journal of Photovoltaics*, no. 2156, pp. 1–6, 2016. [Online]. Available: http://ieeexplore.ieee.org/document/7725518/

[115] "PID-preventive transformerless PV inverter," 2013. [Online]. Available: https://assets.omron.eu/downloads/publication/en/v1/pid-prevention_white_paper_en.pdf

[116] "SunPower® Module 40-year Useful Life." [Online]. Available: https://us.sunpower.com/sites/sunpower/files/media-library/white-papers/wp-sunpower-module-40-year-useful-life.pdf

[117] "X-Series Residential Solar Panels - SunPower." [Online]. Available: https://us.sunpower.com/sites/sunpower/files/media-library/data-sheets/ds-x22-series-360-residential-solar-panels.pdf

[118] "GCL-P6/72G - GCL System Integration Technology Co. Ltd." [Online]. Available: http://en.gclsi.com/wp-content/uploads/2016/12/P6-72G-EN.pdf

[119] D. C. Jordan, S. R. Kurtz, K. VanSant, and J. Newmiller, "Compendium of photovoltaic degradation rates," *Progress in Photovoltaics: Research and Applications*, vol. 24, no. 7, pp. 978–989, 7 2016. [Online]. Available: http://dx.doi.org/10.1002/pip.1160http://doi.wiley.com/10.1002/pip.2744

[120] A. Ndiaye, A. Charki, A. Kobi, C. M. Kébé, P. A. Ndiaye, and V. Sambou, "Degradations of silicon photovoltaic modules: A literature review," *Solar Energy*, vol. 96, pp. 140–151, 10 2013. [Online]. Available: http://linkinghub.elsevier.com/retrieve/pii/S0038092X13002703

[121] D. C. Jordan, C. Deline, S. Johnston, S. R. Rummel, B. Sekulic, P. Hacke, S. R. Kurtz, K. O. Davis, E. J. Schneller, X. Sun, M. A. Alam, and R. A. Sinton, "Silicon Heterojunction System Field Performance," *IEEE Journal of Photovoltaics*, pp. 1–6, 2017. [Online]. Available: http://ieeexplore.ieee.org/document/8114171/

[122] J. Sutterlueti, S. Ransome, J. Stein, and J. Scholz, "Improved PV performance modelling by combining the PV_LIB toolbox with the Loss Factors Model (LFM)," in *2015 IEEE 42nd Photovoltaic Specialist Conference (PVSC)*. IEEE, 6 2015, pp. 1–6. [Online]. Available: http://ieeexplore.ieee.org/document/7355996/

[123] T. Potthoff, K. Bothe, U. Eitner, D. Hinken, and M. Köntges, "Detection of the voltage distribution in photovoltaic modules by electroluminescence imaging," *Progress in Photovoltaics: Research and Applications*, vol. 18, no. 2, pp. 100–106, 3 2010. [Online]. Available: http://doi.wiley.com/10.1002/pip.941

[124] G. Belluardo, P. Ingenhoven, W. Sparber, J. Wagner, P. Weihs, and D. Moser, "Novel method for the improvement in the evaluation of outdoor performance loss rate in different PV technologies and comparison with two other methods," *Solar Energy*, vol. 117, pp. 139–152, 7 2015. [Online]. Available: http://linkinghub.elsevier.com/retrieve/pii/S0038092X15002182

[125] D. C. Jordan and S. R. Kurtz, "The Dark Horse of Evaluating Long-Term Field PerformanceData Filtering," *IEEE Journal of Photovoltaics*, vol. 4, no. 1, pp. 317–323, 1 2014. [Online]. Available: http://ieeexplore.ieee.org/document/6619436/

[126] D. C. Jordan and S. Kurtz, "PV degradation risk," in *the World Renewable Energy Forum*, Denver, 2012.

[127] H. Haeberlin and C. Beutler, "Normalized Representation of Energy and Power for Analysis of Performance and On-line Error Detection in PV-Systems," in *European Photovoltaic Solar Energy Conference and Exhibition, 17th*, Nice, France, 1995.

[128] C. Jennings, "PV module performance at PG&E," in *Conference Record of the Twentieth IEEE Photovoltaic Specialists Conference*. IEEE, 1988, pp. 1225–1229. [Online]. Available: http://ieeexplore.ieee.org/document/105900/

[129] R. H. French, R. Podgornik, T. J. Peshek, L. S. Bruckman, Y. Xu, N. R. Wheeler, A. Gok, Y. Hu, M. A. Hossain, D. A. Gordon, P. Zhao, J. Sun, and G.-Q. Zhang, "Degradation science: Mesoscopic evolution and temporal analytics of photovoltaic energy materials," *Current Opinion in Solid State and Materials Science*, vol. 19, no. 4, pp. 212–226, 8 2015. [Online]. Available: http://linkinghub.elsevier.com/retrieve/pii/S1359028614000989

[130] T. J. Peshek, J. S. Fada, Y. Hu, Y. Xu, M. A. Elsaeiti, E. Schnabel, M. Köhl, and R. H. French, "Insights into metastability of photovoltaic materials at the mesoscale through massive IV analytics," *Journal of Vacuum Science & Technology B, Nanotechnology and Microelectronics: Materials, Processing, Measurement, and Phenomena*, vol. 34, no. 5, p. 050801, 9 2016. [Online]. Available: http://avs.scitation.org/doi/10.1116/1.4960628

[131] Y. Hu, V. Y. Gunapati, P. Zhao, D. Gordon, N. R. Wheeler, M. A. Hossain, T. J. Peshek, L. S. Bruckman, G.-Q. Zhang, and R. H. French, "A Nonrelational Data Warehouse for the Analysis of Field and Laboratory Data From Multiple Heterogeneous Photovoltaic Test Sites," *IEEE Journal of Photovoltaics*, vol. 7, no. 1, pp. 230–236, 1 2017. [Online]. Available: http://ieeexplore.ieee.org/document/7763779/

[132] S. Dongaonkar, S. Loser, E. J. Sheets, K. Zaunbrecher, R. Agrawal, T. J. Marks, and M. A. Alam, "Universal statistics of parasitic shunt formation in solar cells, and its implications for cell to module efficiency gap," *Energy & Environmental Science*, vol. 6, no. 3, p. 782, 2013. [Online]. Available: http://xlink.rsc.org/?DOI=c3ee24167j

[133] M. T. Boyd, S. a. Klein, D. T. Reindl, and B. P. Dougherty, "Evaluation and Validation of Equivalent Circuit Photovoltaic Solar Cell Performance Models," *Journal of Solar Energy Engineering*, vol. 133, no. 2, p. 021005, 2011. [Online]. Available: http://solarenergyengineering.asmedigitalcollection.asme.org/article.aspx?articleid=1458040

[134] P. Szaniawski, J. Lindahl, T. Törndahl, U. Zimmermann, and M. Edoff, "Light-enhanced reverse breakdown in Cu(In,Ga)Se2 solar cells," *Thin Solid Films*, vol. 535, pp. 326–330, 5 2013. [Online]. Available: http://linkinghub.elsevier.com/retrieve/pii/S0040609012011364

[135] X. Sun, R. Asadpour, W. Nie, A. D. Mohite, and M. A. Alam, "A Physics-Based Analytical Model for Perovskite Solar Cells," *IEEE Journal of Photovoltaics*, vol. 5, no. 5, pp. 1389–1394, 9 2015. [Online]. Available: http://ieeexplore.ieee.org/document/7160671/

[136] X. Sun, J. Raguse, R. Garris, C. Deline, T. Silverman, and M. A. Alam, "A physics-based compact model for CIGS and CdTe solar cells: From voltage-dependent carrier collection to light-enhanced reverse breakdown," in *2015 IEEE 42nd Photovoltaic Specialist Conference (PVSC)*. IEEE, 6 2015, pp. 1–6. [Online]. Available: http://ieeexplore.ieee.org/document/7355778/

[137] X. Sun, T. Silverman, R. Garris, C. Deline, and M. A. Alam, "An Illumination- and Temperature-Dependent Analytical Model for Copper Indium Gallium Diselenide (CIGS) Solar Cells," *IEEE Journal of Photovoltaics*, vol. 1, pp. 1–10, 2016. [Online]. Available: http://ieeexplore.ieee.org/lpdocs/epic03/wrapper.htm?arnumber=7515167

[138] W. Nie, H. Tsai, R. Asadpour, J.-C. Blancon, A. J. Neukirch, G. Gupta, J. J. Crochet, M. Chhowalla, S. Tretiak, M. A. Alam, H.-L. Wang, and A. D. Mohite, "High-efficiency solution-processed perovskite solar cells with millimeter-scale grains," *Science*, vol. 347, no. 6221, pp. 522–525, 1 2015. [Online]. Available: http://www.sciencemag.org/content/347/6221/522

[139] A. Guerrero, E. J. Juarez-Perez, J. Bisquert, I. Mora-Sero, and G. Garcia-Belmonte, "Electrical field profile and doping in planar lead halide perovskite solar cells," *Applied Physics Letters*, vol. 105, no. 13, p. 133902, 9 2014. [Online]. Available: http://scitation.aip.org/content/aip/journal/apl/105/13/10.1063/1.4896779

[140] V. D'Innocenzo, G. Grancini, M. J. P. Alcocer, A. R. S. Kandada, S. D. Stranks, M. M. Lee, G. Lanzani, H. J. Snaith, and A. Petrozza, "Excitons versus free charges in organo-lead tri-halide perovskites." *Nature communications*, vol. 5, p. 3586, 2014. [Online]. Available: http://www.ncbi.nlm.nih.gov/pubmed/24710005

[141] M. M. Lee, J. Teuscher, T. Miyasaka, T. N. Murakami, and H. J. Snaith, "Efficient hybrid solar cells based on meso-superstructured organometal halide perovskites." *Science (New York, N.Y.)*, vol. 338, no. 6107, pp. 643–7, 11 2012. [Online]. Available: http://www.ncbi.nlm.nih.gov/pubmed/23042296

[142] Q. Dong, Y. Fang, Y. Shao, P. Mulligan, J. Qiu, L. Cao, and J. Huang, "Electron-hole diffusion lengths ¿175 m in solution grown CH3NH3PbI3 single crystals," *Science*, 2015. [Online]. Available: http://www.sciencemag.org/cgi/doi/10.1126/science.aaa5760

[143] S. D. Stranks, G. E. Eperon, G. Grancini, C. Menelaou, M. J. P. Alcocer, T. Leijtens, L. M. Herz, A. Petrozza, and H. J. Snaith, "Electron-hole diffusion lengths exceeding 1 micrometer in an organometal trihalide perovskite absorber." *Science (New York, N.Y.)*, vol. 342, no. 6156, pp. 341–4, 10 2013. [Online]. Available: http://www.ncbi.nlm.nih.gov/pubmed/24136964

[144] V. Gonzalez-Pedro, E. J. Juarez-Perez, W.-S. Arsyad, E. M. Barea, F. Fabregat-Santiago, I. Mora-Sero, and J. Bisquert, "General Working Principles of CH3NH3PbX3 Perovskite Solar Cells." *Nano letters*, vol. 14, no. 2, pp. 888–93, 3 2014. [Online]. Available: http://www.ncbi.nlm.nih.gov/pubmed/24397375

[145] L. A. a. Pettersson, L. S. Roman, O. Inganäs, and O. Inganas, "Modeling photocurrent action spectra of photovoltaic devices based on organic thin films," *Journal of Applied Physics*, vol. 86, no. 1, p. 487, 1999. [Online]. Available: http://scitation.aip.org/content/aip/journal/jap/86/1/10.1063/1.370757

[146] R. V. K. Chavali, J. E. Moore, X. Wang, M. A. Alam, M. S. Lundstrom, and J. L. Gray, "The Frozen Potential Approach to Separate the Photocurrent and Diode Injection Current in Solar Cells," *IEEE Journal of Photovoltaics*, vol. 5, no. 3, pp. 865–873, 5 2015. [Online]. Available: http://ieeexplore.ieee.org/document/7072502/

[147] M. Liu, M. B. Johnston, and H. J. Snaith, "Efficient planar heterojunction perovskite solar cells by vapour deposition." *Nature*, vol. 501, no. 7467, pp. 395–8, 9 2013. [Online]. Available: http://www.ncbi.nlm.nih.gov/pubmed/24025775

[148] E. L. Unger, E. T. Hoke, C. D. Bailie, W. H. Nguyen, A. R. Bowring, T. Heumuller, M. G. Christoforo, and M. D. McGehee, "Hysteresis and transient behavior in current-voltage measurements of hybrid-perovskite absorber solar cells," *Energy & Environmental Science*, pp. 3690–3698, 2014. [Online]. Available: http://pubs.rsc.org/en/content/articlehtml/2014/ee/c4ee02465f

[149] H. J. Snaith, A. Abate, J. M. Ball, G. E. Eperon, T. Leijtens, N. K. Noel, S. D. Stranks, J. T.-w. W. Wang, K. Wojciechowski, and W. Zhang, "Anomalous hysteresis in perovskite solar cells," *Journal of Physical Chemistry Letters*, vol. 5, no. 9, pp. 1511–1515, 5 2014. [Online]. Available: http://pubs.acs.org/doi/abs/10.1021/jz500113x

[150] Y. Zhao and K. Zhu, "Charge Transport and Recombination in Perovskite (CH 3 NH 3)PbI 3 Sensitized TiO 2 Solar Cells," *The Journal of Physical Chemistry Letters*, vol. 4, no. 17, pp. 2880–2884, 9 2013. [Online]. Available: http://pubs.acs.org.ezproxy.lib.purdue.edu/doi/abs/10.1021/jz401527q

[151] J. Hyuck Heo, M. Sang You, M. Hyuk Chang, W. Yin, T. K. Ahn, S.-J. Lee, S.-J. Sung, D. Hwan Kim, and S. Hyuk Im, "Hysteresis-less mesoscopic CH3NH3PbI3 perovskite Hybrid solar cells by introduction of Li-treated TiO2 electrode," *Nano Energy*, vol. 15, pp. 530–539, 2015. [Online]. Available: http://linkinghub.elsevier.com/retrieve/pii/S2211285515002293

[152] O. Malinkiewicz, C. Roldán-Carmona, A. Soriano, E. Bandiello, L. Camacho, M. K. Nazeeruddin, and H. J. Bolink, "Metal-Oxide-Free Methylammonium Lead Iodide Perovskite-Based Solar Cells: the Influence of Organic Charge Transport Layers," *Advanced Energy Materials*, vol. 4, no. 15, p. 1400345, 10 2014. [Online]. Available: http://doi.wiley.com/10.1002/aenm.201400345

[153] M. Gloeckler, A. Fahrenbruch, and J. Sites, "Numerical modeling of CIGS and CdTe solar cells: setting the baseline," in *3rd World Conference onPhotovoltaic Energy Conversion*, vol. 1, 11 2003, pp. 491–494. [Online]. Available: http://ieeexplore.ieee.org/document/1305328/

[154] R. F. Pierret, *Semiconductor Device Fundamentals*. Prentice Hall, 1996.

[155] S. M. Sze and K. K. Ng, *Physics of Semiconductor Devices*, 3rd ed. Wiley-Interscience, 2006.

[156] J. Gray, X. Wang, R. Chavali, X. Sun, K. Abhirit, and J. Wilcox, "ADEPT 2.1," p. John Robert Wilcox, 2015. [Online]. Available: https://nanohub.org/resources/adeptnpt

[157] "Synopsys Sentaurus Semiconductor TCAD Software," East Middlefield Road, Mountain View, CA 94043 USA.

[158] Y. Taur and T. H. Ning, *Fundamentals of Modern VLSI Devices*, 2nd ed. Cambridge University Press, 2009.

[159] T. Song, J. Tyler McGoffin, and J. R. Sites, "Interface-Barrier-Induced JV Distortion of CIGS Cells With Sputtered-Deposited Zn(S,O) Window Layers," *IEEE Journal of Photovoltaics*, vol. 4, no. 3, pp. 942–947, 5 2014. [Online]. Available: http://ieeexplore.ieee.org/lpdocs/epic03/wrapper.htm?arnumber=6740817

[160] P. E. Russell, O. Jamjoum, R. K. Ahrenkiel, L. L. Kazmerski, R. a. Mickelsen, and W. S. Chen, "Properties of the MoCuInSe 2 interface," *Applied Physics Letters*, vol. 40, no. 11, pp. 995–997, 6 1982. [Online]. Available: http://aip.scitation.org/doi/10.1063/1.92955

[161] X. Sun, C. J. Hages, N. J. Carter, J. E. Moore, R. Agrawal, and M. Lundstrom, "Characterization of nanocrystal-ink based CZTSSe and CIGSSe solar cells using voltage-dependent admittance spectroscopy," in *2014 IEEE 40th Photovoltaic Specialist Conference (PVSC)*, vol. 2. IEEE, 6 2014, pp. 2416–2418. [Online]. Available: http://ieeexplore.ieee.org/lpdocs/epic03/wrapper.htm?arnumber=6925415

[162] T. Eisenbarth, T. Unold, R. Caballero, C. a. Kaufmann, and H.-W. Schock, "Interpretation of admittance, capacitance-voltage, and current-voltage signatures in Cu(In,Ga)Se[sub 2] thin film solar cells," *Journal of Applied Physics*, vol. 107, no. 3, p. 034509, 2010. [Online]. Available: http://link.aip.org/link/JAPIAU/v107/i3/p034509/s1&Agg=doi

[163] S. Demtsu and J. Sites, "Effect of back-contact barrier on thin-film CdTe solar cells," *Thin Solid Films*, vol. 510, no. 1-2, pp. 320–324, 7 2006. [Online]. Available: http://www.sciencedirect.com/science/article/pii/S0040609006000472

[164] R. V. K. Chavali, J. R. Wilcox, B. Ray, J. L. Gray, and M. A. Alam, "Correlated Nonideal Effects of Dark and Light IV Characteristics in a-Si/c-Si Heterojunction Solar Cells," *IEEE Journal of Photovoltaics*, vol. 4, no. 3, pp. 763–771, 5 2014. [Online]. Available: http://ieeexplore.ieee.org/document/6777567/

[165] S. S. Hegedus and W. N. Shafarman, "Thin-film solar cells: device measurements and analysis," *Progress in Photovoltaics: Research and Applications*, vol. 12, no. 23, pp. 155–176, 3 2004. [Online]. Available: http://doi.wiley.com/10.1002/pip.518

[166] C. Rincon, S. M. Wasim, G. Marn, and I. Molina, "Temperature dependence of the optical energy band gap in CuIn3Se5 and CuGa3Se5," *Journal of Applied Physics*, vol. 93, no. 1, p. 780, 2003. [Online]. Available: http://scitation.aip.org/content/aip/journal/jap/93/1/10.1063/1.1528305

[167] "Miasole: Datasheet FLEX-02N." [Online]. Available: http://miasole.com/wp-content/uploads/2015/08/FLEX-02N_Datasheet_1.pdf

[168] M. Contreras, J. Tuttle, A. Gabor, A. Tennant, K. Ramanathan, S. Asher, A. Franz, J. Keane, L. Wang, J. Scofield, and R. Noufi, "High efficiency Cu(In,Ga)Se2-based solar cells: processing of novel absorber structures," in *Proceedings of 1994 IEEE 1st World Conference on Photovoltaic Energy Conversion - WCPEC (A Joint Conference of PVSC, PVSEC and PSEC)*, vol. 1. IEEE, pp. 68–75. [Online]. Available: http://ieeexplore.ieee.org/lpdocs/epic03/wrapper.htm?arnumber=519811

[169] M. S. Lundstrom, "ECE 612 Lecture 31: Heterostructure Fundamentals," 2006. [Online]. Available: https://nanohub.org/resources/2082

[170] S. Dongaonkar, X. Sun, M. Lundstrom, and M. A. Alam, "TAG Solar Cell Model (p-i-n thin film)." 2014. [Online]. Available: https://nanohub.org/publications/20

[171] U. Rau, A. Jasenek, H. Schock, F. Engelhardt, and T. Meyer, "Electronic loss mechanisms in chalcopyrite based heterojunction solar cells," *Thin Solid Films*, vol. 361-362, pp. 298–302, 2 2000. [Online]. Available: http://linkinghub.elsevier.com/retrieve/pii/S0040609099007622

[172] T. Walter, R. Herberholz, and H.-W. Schock, "Distribution of Defects in Polycrytalline Chalcopyrite Thin Films," *Solid State Phenomena*, vol. 51-52, pp. 309–316, 1996. [Online]. Available: http://www.scientific.net/SSP.51-52.309

[173] S. Dongaonkar and M. A. Alam, "PV Analyzer," 2014. [Online]. Available: https://nanohub.org/resources/pvanalyzer

[174] B. L. Williams, S. Smit, B. J. Kniknie, K. J. Bakker, W. Keuning, W. M. M. Kessels, R. E. I. Schropp, and M. Creatore, "Identifying parasitic current pathways in CIGS solar cells by modelling dark J-V response," *Progress in Photovoltaics: Research and Applications*, vol. 23, no. 11, pp. 1516–1525, 11 2015. [Online]. Available: http://dx.doi.org/10.1002/pip.1160http://doi.wiley.com/10.1002/pip.2582

[175] B. J. Mueller, C. Zimmermann, V. Haug, F. Hergert, T. Koehler, S. Zweigart, and U. Herr, "Influence of different sulfur to selenium ratios on the structural and electronic properties of Cu(In,Ga)(S,Se)2 thin films and solar cells formed by the stacked elemental layer process," *Journal of Applied Physics*, vol. 116, no. 17, 2014. [Online]. Available: http://dx.doi.org/10.1063/1.4900991

[176] P. M. Salomé, V. Fjällström, P. Szaniawski, J. P. Leitão, A. Hultqvist, P. A. Fernandes, J. P. Teixeira, B. P. Falcão, U. Zimmermann, A. F. da Cunha, and M. Edoff, "A comparison between thin film solar cells made from co-evaporated CuIn 1-x Ga x Se 2 using a one-stage process versus a three-stage process," *Progress in Photovoltaics: Research and Applications*, vol. 23, no. 4, pp. 470–478, 4 2015. [Online]. Available: http://doi.wiley.com/10.1002/pip.2453

[177] K. Ramanathan, M. A. Contreras, C. L. Perkins, S. Asher, F. S. Hasoon, J. Keane, D. Young, M. Romero, W. Metzger, R. Noufi, J. Ward, and A. Duda, "Properties of 19.2% efficiency ZnO/CdS/CuInGaSe2 thin-film solar cells," *Progress in Photovoltaics: Research and Applications*, vol. 11, no. 4, pp. 225–230, 6 2003. [Online]. Available: http://doi.wiley.com/10.1002/pip.494

[178] M. A. Contreras, M. J. Romero, B. To, F. Hasoon, R. Noufi, S. Ward, and K. Ramanathan, "Optimization of CBD CdS process in high-efficiency Cu(In,Ga)Se2-based solar cells," *Thin Solid Films*, vol. 403-404, pp. 204–211, 2 2002. [Online]. Available: http://linkinghub.elsevier.com/retrieve/pii/S0040609001015383

[179] "Matlab2016a," Natick, MA, 2016.

[180] A. Johansson, R. Gottschalg, and D. Infield, "Modelling shading on amorphous silicon single and double junction modules," in *Photovoltaic Energy Conversion, 2003. Proceedings of 3rd World Conference on*, 6 2003, pp. 1934–1937. [Online]. Available: http://www.researchgate.net/publication/224749157_Modelling_shading_on_amorphous_silicon_single_and_double_junction_modules

[181] S. Dongaonkar and M. A. Alam, "End to end modeling for variability and reliability analysis of thin film photovoltaics," in *2012 IEEE International Reliability Physics Symposium (IRPS)*. IEEE, 4 2012, pp. 1–4. [Online]. Available: http://ieeexplore.ieee.org/document/6241828/

[182] S. Puttnins, S. Jander, a. Wehrmann, G. Benndorf, M. Stölzel, a. Müller, H. von Wenckstern, F. Daume, a. Rahm, and M. Grundmann, "Breakdown characteristics of flexible Cu(In,Ga)Se2 solar cells," *Solar Energy Materials and Solar Cells*, vol. 120, pp. 506–511, 1 2014. [Online]. Available: http://linkinghub.elsevier.com/retrieve/pii/S0927024813005096

[183] H. Kufluoglu and M. A. Alam, "A Computational Model of NBTI and Hot Carrier Injection Time-Exponents for MOSFET Reliability," *Journal of Computational Electronics*, vol. 3, no. 3-4, pp. 165–169, 10 2004. [Online]. Available: http://link.springer.com/10.1007/s10825-004-7038-9

[184] H. Bentarzi, *Transport in Metal-Oxide-Semiconductor Structures*, ser. Engineering Materials. Berlin, Heidelberg: Springer Berlin Heidelberg, 2011. [Online]. Available: http://link.springer.com/10.1007/978-3-642-16304-3

[185] W. De Soto, S. Klein, and W. Beckman, "Improvement and validation of a model for photovoltaic array performance," *Solar Energy*, vol. 80, no. 1, pp. 78–88, 1 2006. [Online]. Available: http://linkinghub.elsevier.com/retrieve/pii/S0038092X05002410

[186] A. Gerber, V. Huhn, T. Tran, M. Siegloch, Y. Augarten, B. Pieters, and U. Rau, "Advanced large area characterization of thin-film solar modules by electroluminescence and thermography imaging techniques," *Solar Energy Materials and Solar Cells*, vol. 135, pp. 35–42, 4 2015. [Online]. Available: http://linkinghub.elsevier.com/retrieve/pii/S0927024814005029

[187] S. Lany and A. Zunger, "Light- and bias-induced metastabilities in Cu(In,Ga)Se[sub 2] based solar cells caused by the (V[sub Se]-V[sub Cu]) vacancy complex," *Journal of Applied Physics*, vol. 100, no. 11, p. 113725, 2006. [Online]. Available: http://scitation.aip.org/content/aip/journal/jap/100/11/10.1063/1.2388256

[188] J. Heath, J. Cohen, and W. Shafarman, "Distinguishing metastable changes in bulk CIGS defect densities from interface effects," *Thin Solid Films*, vol. 431-432, no. 03, pp. 426–430, 5 2003. [Online]. Available: http://linkinghub.elsevier.com/retrieve/pii/S0040609003001895

[189] F. Di Giacomo, V. Zardetto, A. D'Epifanio, S. Pescetelli, F. Matteocci, S. Razza, A. Di Carlo, S. Licoccia, W. M. M. Kessels, M. Creatore, and T. M. Brown, "Flexible Perovskite Photovoltaic Modules and Solar Cells Based on Atomic Layer Deposited Compact Layers and UV-Irradiated TiO 2 Scaffolds on Plastic Substrates," *Advanced Energy Materials*, vol. 5, no. 8, pp. n/a–n/a, 4 2015. [Online]. Available: http://doi.wiley.com/10.1002/aenm.201401808

[190] F. Matteocci, L. Cinà, F. D. Giacomo, S. Razza, A. L. Palma, A. Guidobaldi, A. DEpifanio, S. Licoccia, T. M. Brown, A. Reale, and A. D. Carlo, "High efficiency photovoltaic module based on mesoscopic organometal halide perovskite," *Progress in Photovoltaics: Research and Applications*, vol. 20, no. 1, pp. 6–11, 2014. [Online]. Available: http://dx.doi.org/10.1002/pip.1160

[191] T. J. Silverman, M. G. Deceglie, C. Deline, and S. Kurtz, "Partial shade stress test for thin-film photovoltaic modules," N. G. Dhere, J. H. Wohlgemuth, and R. Jones-Albertus, Eds., vol. 9563, no. September, 9 2015, p. 95630F. [Online]. Available: http://proceedings.spiedigitallibrary.org/proceeding.aspx?doi=10.1117/12.2188774

[192] X. Sun, T. J. Silverman, Z. Zhou, M. R. Khan, P. Bermel, and M. A. Alam, "Optics-Based Approach to Thermal Management of Photovoltaics: Selective-Spectral and Radiative Cooling," *IEEE Journal of Photovoltaics*, vol. 7, no. 2, pp. 566–574, 3 2017. [Online]. Available: http://ieeexplore.ieee.org/document/7828043/

[193] C. G. C. Granqvist, A. Hjortsbery, and A. Hjortsberg, "Radiative cooling to low temperatures: General considerations and application to selectively emitting SiO films," *Journal of Applied Physics*, vol. 52, no. 6, p. 4205, 1981. [Online]. Available: http://scitation.aip.org/content/aip/journal/jap/52/6/10.1063/1.329270

[194] D. Faiman, "Assessing the outdoor operating temperature of photovoltaic modules," *Progress in Photovoltaics: Research and Applications*, vol. 16, no. 4, pp. 307–315, 6 2008. [Online]. Available: http://doi.wiley.com/10.1002/pip.813http://dx.doi.org/10.1002/pip.1160

[195] J. R. Barton, A. C. Reiss, and S. W. Silverman, "Glass encapsulation of solar cell arrays to minimize voltage/plasma interaction effects in a space environment," US, 1989.

[196] "COMSOL Multiphysics." [Online]. Available: https://www.comsol.com/comsol-multiphysics

[197] W. Ahn, H. Zhang, T. Shen, C. Christiansen, P. Justison, S. Shin, and M. A. Alam, "A Predictive Model for IC Self-Heating Based on Effective Medium and Image Charge Theories and Its Implications for Interconnect and Transistor Reliability," *IEEE Transactions on Electron Devices*, vol. 64, no. 9, pp. 3555–3562, 9 2017. [Online]. Available: http://ieeexplore.ieee.org/document/7987739/

[198] M. A. Wahab, S. Shin, and M. A. Alam, "Spatio-temporal mapping of device temperature due to self-heating in Sub-22 nm transistors," in *2016 IEEE International Reliability Physics Symposium (IRPS)*. IEEE, 4 2016, pp. 05–1. [Online]. Available: http://ieeexplore.ieee.org/document/7574647/

[199] E. R. Keiter, T. Mei, T. V. Russo, R. L. Schiek, P. E. Sholander, H. K. Thornquist, J. C. Verley, and D. G. Baur, "Xyce Parallel Electronic Simulator Users Guide , Version 6.8," 2017. [Online]. Available: https://xyce.sandia.gov/downloads/_assets/documents/Users_Guide.pdf

[200] L. C. Hirst and N. J. Ekins-Daukes, "Fundamental losses in solar cells," *Progress in Photovoltaics: Research and Applications*, vol. 19, no. 3, pp. 286–293, 5 2011. [Online]. Available: http://doi.wiley.com/10.1002/pip.1024

[201] M. R. Khan and M. A. Alam, "Thermodynamic limit of bifacial double-junction tandem solar cells," *Applied Physics Letters*, vol. 107, no. 22, 2015. [Online]. Available: http://dx.doi.org/10.1063/1.4936341

[202] "The Cary 4000/5000/6000i Series UV-Vis-NIR spectrophotometers." [Online]. Available: https://www.agilent.com/cs/library/brochures/5990-7786EN_Cary-4000-5000-6000i-UV-Vis-NIR_Brochure.pdf

[203] M. A. Steiner, J. F. Geisz, I. Garcia, D. J. Friedman, A. Duda, and S. R. Kurtz, "Optical enhancement of the open-circuit voltage in high quality GaAs solar cells," *Journal of Applied Physics*, vol. 113, no. 12, p. 123109, 2013. [Online]. Available: http://scitation.aip.org/content/aip/journal/jap/113/12/10.1063/1.4798267

[204] D. H. Rose, F. S. Hasoon, R. G. Dhere, D. S. Albin, R. M. Ribelin, X. S. Li, Y. Mahathongdy, T. A. Gessert, and P. Sheldon, "Fabrication procedures and process sensitivities for CdS/CdTe solar cells," *Progress in Photovoltaics: Research and Applications*, vol. 7, no. 5, pp. 331–340, 9 1999. [Online]. Available: http://doi.wiley.com/10.1002/(SICI)1099-159X(199909/10)7:5⟨331::AID-PIP257⟩3.0.CO;2-P

[205] M. R. Vogt, H. Holst, M. Winter, R. Brendel, and P. P. Altermatt, "Numerical Modeling of c-Si PV Modules by Coupling the Semiconductor with the Thermal Conduction, Convection and Radiation Equations," *Energy Procedia*, vol. 77, pp. 215–224, 8 2015. [Online]. Available: http://linkinghub.elsevier.com/retrieve/pii/S1876610215007985

[206] S. John, C. Soukoulis, M. H. Cohen, and E. N. Economou, "Theory of Electron Band Tails and the Urbach Optical-Absorption Edge," *Physical Review Letters*, vol. 57, no. 14, pp. 1777–1780, 10 1986. [Online]. Available: https://link.aps.org/doi/10.1103/PhysRevLett.57.1777

[207] V. Liu and S. Fan, "S4 : A free electromagnetic solver for layered periodic structures," *Computer Physics Communications*, vol. 183, no. 10, pp. 2233–2244, 10 2012. [Online]. Available: http://linkinghub.elsevier.com/retrieve/pii/S0010465512001658

[208] M. Rubin, "Optical properties of soda lime silica glasses," *Solar Energy Materials*, vol. 12, no. 4, pp. 275–288, 9 1985. [Online]. Available: http://linkinghub.elsevier.com/retrieve/pii/0165163385900528

[209] "ATRAN," 1992. [Online]. Available: https://atran.sofia.usra.edu/cgi-bin/atran/atran.cgi

[210] "AGC Solite Glass Datasheet." [Online]. Available: http://www.agc-solar.com/jp/agc-solar-products/patterned-glass/solite.html#uid_2_down

[211] M. D. Bazilian, H. Kamalanathan, and D. Prasad, "Thermographic analysis of a building integrated photovoltaic system," *Renewable Energy*, vol. 26, no. 3, pp. 449–461, 7 2002. [Online]. Available: http://linkinghub.elsevier.com/retrieve/pii/S0960148101001422

[212] "How to choose a bypass diode for a silicon panel junction box," pp. 1–24, 2011. [Online]. Available: http://www.st.com/st-web-ui/static/active/en/resource/technical/document/application_note/DM00034029.pdf

[213] M. Muller, B. Marion, and J. Rodriguez, "Evaluating the IEC 61215 Ed.3 NMOT procedure against the existing NOCT procedure with PV modules in a side-by-side configuration," in *2012 38th IEEE Photovoltaic Specialists Conference*. IEEE, 6 2012, pp. 000 697–000 702. [Online]. Available: http://ieeexplore.ieee.org/lpdocs/epic03/wrapper.htm?arnumber=6317705

[214] S. J. Orfanidis, *Electromagnetic Waves and Antennas*. Piscataway, NJ: Rutgers University, 2008.

[215] W. Holley, S. Agro, J. Galica, L. Thoma, R. Yorgensen, M. Ezrin, P. Klemchuk, and G. Lavigne, "Investigation into the causes of browning in EVA encapsulated flat plate PV modules," in *Proceedings of 1994 IEEE 1st World Conference*

on Photovoltaic Energy Conversion - WCPEC (A Joint Conference of PVSC, PVSEC and PSEC), vol. 1. IEEE, 1994, pp. 893–896. [Online]. Available: http://ieeexplore.ieee.org/lpdocs/epic03/wrapper.htm?arnumber=520105

[216] A. Skoczek, T. Sample, and E. D. Dunlop, "The results of performance measurements of field-aged crystalline silicon photovoltaic modules," *Progress in Photovoltaics: Research and Applications*, vol. 17, no. 4, pp. 227–240, 6 2009. [Online]. Available: http://doi.wiley.com/10.1002/pip.874

[217] P. Bermel, S. V. Boriskina, Z. Yu, and K. Joulain, "Control of radiative processes for energy conversion and harvesting," *Optics Express*, vol. 23, no. 24, p. A1533, 2015. [Online]. Available: http://www.osapublishing.org/viewmedia.cfm?uri=oe-23-24-A1533&seq=0&html=true

[218] T. J. Heb, "Infra-red transmissive mirrors for concentrated photovoltaics," in *2009 34th IEEE Photovoltaic Specialists Conference (PVSC)*. IEEE, 6 2009, pp. 000 984–000 989. [Online]. Available: http://ieeexplore.ieee.org/document/5411188/

[219] J. T. Hebrink, "Durable Polymeric Films for Increasing the Performance of Concentrators," in *Third Generation Photovoltaics*. InTech, 3 2012, no. March, pp. 32–44. [Online]. Available: http://www.intechopen.com/books/third-generation-photovoltaics/durable-polymeric-films-for-increasing-the-performance-of-concentrators-

[220] A. P. Raman, M. A. Anoma, L. Zhu, E. Rephaeli, and S. Fan, "Passive radiative cooling below ambient air temperature under direct sunlight," *Nature*, vol. 515, no. 7528, pp. 540–544, 2014. [Online]. Available: http://www.nature.com/doifinder/10.1038/nature13883

[221] "AVERAGE WIND SPEED IN NEW DELHI." [Online]. Available: https://weather-and-climate.com/average-monthly-Wind-speed,New-Delhi,India

[222] G. M. Kimball, S. Yang, and A. Saproo, "Global acceleration factors for damp heat tests of PV modules," in *2016 IEEE 43rd Photovoltaic Specialists Conference (PVSC)*. IEEE, 6 2016, pp. 0101–0105. [Online]. Available: http://ieeexplore.ieee.org/document/7749557/

[223] M. Armbruster, D. M. Wilt, R. J. Cooper, and R. C. Hoffmann, "Optical and electrical properties of pseudomorphic glass," in *2016 IEEE 43rd Photovoltaic Specialists Conference (PVSC)*. IEEE, 6 2016, pp. 2554–2557. [Online]. Available: http://ieeexplore.ieee.org/document/7750108/

[224] B. P. Rand, J. Genoe, P. Heremans, and J. Poortmans, "Advanced PERC and PERL production cells with 20.3% record efficiency for standard commercial p-type silicon wafers," *Prog. Photovolt: Res. Appl.*, vol. 15, no. February, pp. 659–676, 2007. [Online]. Available: http://dx.doi.org/10.1002/pip.1160

[225] A. Luque, E. Lorenzo, G. Sala, and S. López-Romero, "Diffusing reflectors for bifacial photovoltaic panels," *Solar Cells*, vol. 13, no. 3, pp. 277–292, 1 1985. [Online]. Available: http://linkinghub.elsevier.com/retrieve/pii/0379678785900213

[226] Y. K. Chieng and M. A. Green, "Computer simulation of enhanced output from bifacial photovoltaic modules," *Progress in Photovoltaics: Research and Applications*, vol. 1, no. 4, pp. 293–299, 10 1993. [Online]. Available: http://doi.wiley.com/10.1002/pip.4670010406

[227] U. A. Yusufoglu, T. H. Lee, T. M. Pletzer, A. Halm, L. J. Koduvelikulathu, C. Comparotto, R. Kopecek, and H. Kurz, "Simulation of energy production by bifacial modules with revision of ground reflection," *Energy Procedia*, vol. 55, pp. 389–395, 2014. [Online]. Available: http://dx.doi.org/10.1016/j.egypro.2014.08.111

[228] G. J. Janssen, B. B. Van Aken, A. J. Carr, and A. A. Mewe, "Outdoor Performance of Bifacial Modules by Measurements and Modelling," *Energy Procedia*, vol. 77, pp. 364–373, 8 2015. [Online]. Available: http://linkinghub.elsevier.com/retrieve/pii/S187661021500819X

[229] J. S. Stein, L. Burnham, and M. Lave, "Performance Results for the Prism Solar Installation at the New Mexico Regional Test Center : Field Data from February 15 - August 15 , 2016," Sandia Report (SAND2017-5872), Tech. Rep. June, 2017. [Online]. Available: http://energy.sandia.gov/download/38750/

[230] S. Guo, T. M. Walsh, and M. Peters, "Vertically mounted bifacial photovoltaic modules: A global analysis," *Energy*, vol. 61, pp. 447–454, 2013. [Online]. Available: http://dx.doi.org/10.1016/j.energy.2013.08.040

[231] M. Ito and E. Gerritsen, "Geographical Mapping of The Performance of Vertically Installed Bifacial Modules," in *32nd PVSEC*, 2016, pp. 1603–1609.

[232] N. Bouaouadja, S. Bouzid, M. Hamidouche, C. Bousbaa, and M. Madjoubi, "Effects of sandblasting on the efficiencies of solar panels," *Applied Energy*, vol. 65, no. 1-4, pp. 99–105, 4 2000. [Online]. Available: http://linkinghub.elsevier.com/retrieve/pii/S0306261999000446

[233] H. Lu, L. Lu, and Y. Wang, "Numerical investigation of dust pollution on a solar photovoltaic (PV) system mounted on an isolated building," *Applied Energy*, vol. 180, pp. 27–36, 10 2016. [Online]. Available: http://linkinghub.elsevier.com/retrieve/pii/S0306261916309722

[234] C. S. Lai and M. D. McCulloch, "Levelized cost of electricity for solar photovoltaic and electrical energy storage," *Applied Energy*, vol. 190, pp. 191–203, 3 2017. [Online]. Available: http://linkinghub.elsevier.com/retrieve/pii/S030626191631933X

[235] S. A. Janko, M. R. Arnold, and N. G. Johnson, "Implications of high-penetration renewables for ratepayers and utilities in the residential solar photovoltaic (PV) market," *Applied Energy*, vol. 180, pp. 37–51, 10 2016. [Online]. Available: http://linkinghub.elsevier.com/retrieve/pii/S0306261916309825

[236] X. Sun, M. R. Khan, C. Deline, and M. A. Alam, "Optimization and performance of bifacial solar modules: A global perspective," *Applied Energy*, vol. 212, pp. 1601–1610, 2 2018. [Online]. Available: http://linkinghub.elsevier.com/retrieve/pii/S0306261917317567

[237] I. Reda and A. Andreas, "Solar Position Algorithm for Solar Radiaiton Applications," Tech. Rep., 2008. [Online]. Available: https://www.nrel.gov/docs/fy08osti/34302.pdf

[238] "PV_LIB Toolbox." [Online]. Available: https://pvpmc.sandia.gov/applications/pv_lib-toolbox/

[239] B. Haurwitz, "Insolation in relation to cloudiness and cloud density," *Journal of Meteorology*, vol. 2, no. 3, pp. 154–166, 9 1945. [Online]. Available: http://journals.ametsoc.org/doi/abs/10.1175/1520-0469%281945%29002%3C0154%3AIIRTCA%3E2.0.CO%3B2

[240] ——, "Insolation in relation to cloud type," *Journal of Meteorology*, vol. 3, no. 4, pp. 123–124, 12 1946. [Online]. Available: http://journals.ametsoc.org/doi/abs/10.1175/1520-0469%281946%29003%3C0123%3AIIRTCT%3E2.0.CO%3B2

[241] J. S. Stein, C. W. Hansen, and M. J. Reno, "Global horizontal irradiance clear sky models : implementation and analysis." Sandia National Laboratories (SNL), Albuquerque, NM, and Livermore, CA (United States), Tech. Rep. March, 3 2012. [Online]. Available: http://www.osti.gov/servlets/purl/1039404/

[242] "Surface meteorology and Solar Energy: A renewable energy resource web site (release 6.0)," 2017. [Online]. Available: https://eosweb.larc.nasa.gov/cgi-bin/sse/sse.cgi?

[243] J. Orgill and K. Hollands, "Correlation equation for hourly diffuse radiation on a horizontal surface," *Solar Energy*, vol. 19, no. 4, pp. 357–359, 1977. [Online]. Available: http://linkinghub.elsevier.com/retrieve/pii/0038092X77900068

[244] G. W. Paltridge and C. Platt, *Radiative Processes in Meteorology and Climatology*. Elsevier Science Ltd, 1976.

[245] J. A. Duffie and W. A. Beckman, *Solar Engineering of Thermal Processes*, 4th ed. Wiley, 2013.

[246] E. L. Maxwell, "A quasi-physical model for converting hourly global to direct normal insolation," pp. 35–46, 1987. [Online]. Available: http://rredc.nrel.gov/solar/pubs/PDFs/TR-215-3087.pdf

[247] D. Erbs, S. Klein, and J. Duffie, "Estimation of the diffuse radiation fraction for hourly, daily and monthly-average global radiation," *Solar Energy*, vol. 28, no. 4, pp. 293–302, 1982. [Online]. Available: http://linkinghub.elsevier.com/retrieve/pii/0038092X82903024

[248] D. Reindl, W. Beckman, and J. Duffie, "Diffuse fraction correlations," *Solar Energy*, vol. 45, no. 1, pp. 1–7, 1990. [Online]. Available: http://linkinghub.elsevier.com/retrieve/pii/0038092X9090060P

[249] L. Wong and W. Chow, "Solar radiation model," *Applied Energy*, vol. 69, no. 3, pp. 191–224, 7 2001. [Online]. Available: http://linkinghub.elsevier.com/retrieve/pii/S0306261901000125

[250] R. Perez, R. Seals, P. Ineichen, R. Stewart, and D. Menicucci, "A new simplified version of the perez diffuse irradiance model for tilted surfaces," *Solar Energy*, vol. 39, no. 3, pp. 221–231, 1987. [Online]. Available: http://linkinghub.elsevier.com/retrieve/pii/S0038092X87800312

[251] M. R. Khan, A. Hanna, X. Sun, and M. A. Alam, "Vertical bifacial solar farms: Physics, design, and global optimization," *Applied Energy*, vol. 206, pp. 240–248, 11 2017. [Online]. Available: http://linkinghub.elsevier.com/retrieve/pii/S0306261917310589

[252] N. Martín and J. M. Ruiz, "Annual angular reflection losses in PV modules," *Progress in Photovoltaics: Research and Applications*, vol. 13, no. 1, pp. 75–84, 1 2005. [Online]. Available: http://doi.wiley.com/10.1002/pip.585

[253] N. Martin and J. Ruiz, "Calculation of the PV modules angular losses under field conditions by means of an analytical model," *Solar Energy Materials and Solar Cells*, vol. 70, no. 1, pp. 25–38, 12 2001. [Online]. Available: http://linkinghub.elsevier.com/retrieve/pii/S0927024800004086

[254] "More than half of utility-scale solar photovoltaic systems track the sun through the day." [Online]. Available: https://www.eia.gov/todayinenergy/detail.php?id=30912

[255] "Modelling of Single-axis tracking, applications to HET and IBC modules," Tech. Rep., 2016. [Online]. Available: https://www.helmholtz-berlin.de/media/media/projekte/hercules/hercules-m36-workshop/modelling-of-single-axis-tracking--applications-to-het-and-ibc-modules.pdf

[256] C. Deline, S. MacAlpine, B. Marion, F. Toor, A. Asgharzadeh, and J. S. Stein, "Assessment of Bifacial Photovoltaic Module Power Rating MethodologiesInside and Out," *IEEE Journal of Photovoltaics*, vol. 7, no. 2, pp. 575–580, 3 2017. [Online]. Available: http://ieeexplore.ieee.org/document/7835135/

[257] J. R. Howell, M. P. Menguc, and R. Siegel, *Thermal Radiation Heat Transfer*, 6th ed. CRC Press, 2015.

[258] J. A. Galtiere, "Differential power processing for increased solar array energy harvest," Ph.D. dissertation, University of Illinois at Urbana-Champaign, 2015.

[259] J. Appelbaum, "View Factors to Grounds of Photovoltaic Collectors," *Journal of Solar Energy Engineering*, vol. 138, no. 6, p. 064501, 9 2016. [Online]. Available: http://solarenergyengineering.asmedigitalcollection.asme.org/article.aspx?doi=10.1115/1.4034316

[260] J. A. Coakley, "Reflectance and albedo, surface," Tech. Rep. [Online]. Available: http://curry.eas.gatech.edu/Courses/6140/ency/Chapter9/Ency_Atmos/Reflectance_Albedo_Surface.pdf

[261] J. Appelbaum, "Bifacial photovoltaic panels field," *Renewable Energy*, vol. 85, pp. 338–343, 1 2016. [Online]. Available: http://linkinghub.elsevier.com/retrieve/pii/S0960148115300732

[262] "Prism Solar Bi60 Datasheet." [Online]. Available: https://static1.squarespace.com/static/57a12f5729687f4a21ab938d/t/58cc774837c5819ccd0e5f41/1489794889716/bi60specs.pdf

[263] C. Kuenzer and S. Dech, "Theoretical Background of Thermal Infrared Remote Sensing," 2013, pp. 1–26. [Online]. Available: http://link.springer.com/10.1007/978-94-007-6639-6_1

[264] K. Jaeger, G. Bende, W. Hoffmann, and R. Hezel, "Performance of bifacial MIS-inversion layer solar cells encapsulated in novel albedo collecting modules," in *Conference Record of the Twenty Third IEEE Photovoltaic Specialists Conference - 1993 (Cat. No.93CH3283-9)*. IEEE, pp. 1235–1239. [Online]. Available: http://ieeexplore.ieee.org/document/346945/

[265] B. Soria, E. Gerritsen, P. Lefillastre, and J.-E. Broquin, "A study of the annual performance of bifacial photovoltaic modules in the case of vertical facade integration," *Energy Science & Engineering*, vol. 4, no. 1, pp. 52–68, 1 2016. [Online]. Available: http://doi.wiley.com/10.1002/ese3.103

[266] C. Deline, A. Dobos, S. Janzou, J. Meydbray, and M. Donovan, "A simplified model of uniform shading in large photovoltaic arrays," *Solar Energy*, vol. 96, pp. 274–282, 10 2013. [Online]. Available: http://linkinghub.elsevier.com/retrieve/pii/S0038092X13002739

[267] K. Sugibuchi, N. Ishikawa, and S. Obara, "Bifacial-PV power output gain in the field test using 'EarthON' high bifaciality solar cells," in *Proc. 28th PVSEC*, 2013, pp. 4312–4317.

[268] "Calculating the Additional Energy Yield of Bifacial Solar Modules." [Online]. Available: https://www.solarworld-usa.com/~/media/www/files/white-papers/calculating-additional-energy-yield-through-bifacial-solar-technology-sw9002us.pdf?la=en

[269] J. E. Castillo-Aguilella and P. S. Hauser, "Multi-Variable Bifacial Photovoltaic Module Test Results and Best-Fit Annual Bifacial Energy Yield Model," *IEEE Access*, vol. 4, pp. 498–506, 2016. [Online]. Available: http://ieeexplore.ieee.org/document/7387697/

[270] ——, "Bifacial photovoltaic module best-fit annual energy yield model with azimuthal correction," in *2016 IEEE 43rd Photovoltaic Specialists Conference (PVSC)*. IEEE, 6 2016, pp. 3109–3112. [Online]. Available: http://ieeexplore.ieee.org/document/7750238/

[271] E. W. Peterson and J. P. Hennessey, "On the Use of Power Laws for Estimates of Wind Power Potential," *Journal of Applied Meteorology*, vol. 17, no. 3, pp. 390–394, 3 1978. [Online]. Available: http://journals.ametsoc.org/doi/abs/10.1175/1520-0450%281978%29017%3C0390%3AOTUOPL%3E2.0.CO%3B2

[272] G. TamizhMani, B. King, A. Venkatesan, C. Deline, A. Pavgi, S. Tatapudi, J. Kuitche, A. Chokor, and M. E. Asmar, "Regional soiling stations for PV: Soling loss analysis," in *2016 IEEE 43rd Photovoltaic Specialists Conference (PVSC)*. IEEE, 6 2016, pp. 1741–1746. [Online]. Available: http://ieeexplore.ieee.org/document/7749922/

[273] "PVSYST users manual." [Online]. Available: http://www.pvsyst.com/images/pdf/PVsyst_Tutorials.pdf

[274] M. J. J. Kerr, A. Cuevas, and R. A. A. Sinton, "Generalized analysis of quasi-steady-state and transient decay open circuit voltage measurements," *Journal of Applied Physics*, vol. 91, no. 1, p. 399, 2002. [Online]. Available: http://scitation.aip.org/content/aip/journal/jap/91/1/10.1063/1.1416134

[275] X. Sun, R. V. K. Chavali, and M. A. Alam, "In-Situ Self-Monitoring of Real-Time Photovoltaic Degradation Only Using Maximum Power Point the Suns-Vmp Method," *Progress in Photovoltaics: Research and Applications*, 2018.

[276] K. Lee, "Improving the PV Module Single-Diode Model Accuracy with Temperature Dependence of the Series Resistance," in *IEEE 44th Photovoltaic Specialist Conference (PVSC)*, 2017.

[277] "Siemans Solar Panels Installation Guide." [Online]. Available: http://iodlabs.ucsd.edu/dja/codered/engineering/procedures/solarPower/siemenssolarpanels.pdf

[278] M. Wolf and H. Rauschenbach, "Series resistance effects on solar cell measurements," *Advanced Energy Conversion*, vol. 3, no. 2, pp. 455–479, 4 1963. [Online]. Available: http://linkinghub.elsevier.com/retrieve/pii/0365178963900638

[279] R. V. K. Chavali, J. V. Li, C. Battaglia, S. De Wolf, J. L. Gray, and M. A. Alam, "A Generalized Theory Explains the Anomalous SunsVOC Response of Si Heterojunction Solar Cells," *IEEE Journal of Photovoltaics*, vol. 7, no. 1, pp. 169–176, 1 2017. [Online]. Available: http://ieeexplore.ieee.org/document/7756368/

[280] M. G. G. Deceglie, T. J. J. Silverman, B. Marion, and S. R. R. Kurtz, "Real-Time Series Resistance Monitoring in PV Systems Without the Need for I V Curves," *IEEE Journal of Photovoltaics*, vol. 5, no. 6, pp. 1706–1709, 2015. [Online]. Available: http://ieeexplore.ieee.org/lpdocs/epic03/wrapper.htm?arnumber=7286731

[281] P. Hacke, S. Spataru, S. Johnston, K. Terwilliger, K. VanSant, M. Kempe, J. Wohlgemuth, S. Kurtz, A. Olsson, and M. Propst, "Elucidating PID Degradation Mechanisms and In Situ Dark IV Monitoring for Modeling Degradation Rate in CdTe Thin-Film Modules," *IEEE Journal of Photovoltaics*, vol. 6, no. 6, pp. 1635–1640, 11 2016. [Online]. Available: http://ieeexplore.ieee.org/document/7548311/

[282] "PVDAQ (PV Data Acquisition)." [Online]. Available: http://developer.nrel.gov/docs/solar/pvdaq-v3/

[283] D. C. Jordan and S. Kurtz, "2012 PV degradation risk," in *Technical Report in World Renewable Energy Forum.*

[284] V. Vasudevan and Xuejun Fan, "An acceleration model for lead-free (SAC) solder joint reliability under thermal cycling," in *2008 58th Electronic Components and Technology Conference.* IEEE, 5 2008, pp. 139–145. [Online]. Available: http://ieeexplore.ieee.org/document/4549960/

[285] M. D. Kempe, "Ultraviolet light test and evaluation methods for encapsulants of photovoltaic modules," *Solar Energy Materials and Solar Cells*, vol. 94, no. 2, pp. 246–253, 2 2010. [Online]. Available: http://linkinghub.elsevier.com/retrieve/pii/S0927024809003274

[286] D. Lausch, V. Naumann, O. Breitenstein, J. Bauer, A. Graff, J. Bagdahn, and C. Hagendorf, "Potential-Induced Degradation (PID): Introduction of a Novel Test Approach and Explanation of Increased Depletion Region Recombination," *IEEE Journal of Photovoltaics*, vol. 4, no. 3, pp. 834–840, 5 2014. [Online]. Available: http://ieeexplore.ieee.org/document/6779597/

[287] V. Naumann, D. Lausch, A. Hähnel, J. Bauer, O. Breitenstein, A. Graff, M. Werner, S. Swatek, S. Großer, J. Bagdahn, and C. Hagendorf, "Explanation of potential-induced degradation of the shunting type by Na decoration of stacking faults in Si solar cells," *Solar Energy Materials and Solar Cells*, vol. 120, no. PART A, pp. 383–389, 1 2014. [Online]. Available: http://linkinghub.elsevier.com/retrieve/pii/S0927024813003000

[288] R. Asadpour, R. V. K. V. K. Chavali, and M. A. A. Alam, "Physics-Based computational modeling of moisture ingress in solar modules: Location-specific corrosion and delamination," in *2016 IEEE 43rd Photovoltaic Specialists Conference (PVSC)*. IEEE, 6 2016, pp. 0840–0843. [Online]. Available: http://ieeexplore.ieee.org/document/7749725/

[289] P. Bermel, R. Asadpour, C. Zhou, and M. A. Alam, "A modeling framework for potential induced degradation in PV modules," in *SPIE*, N. G. Dhere, J. H. Wohlgemuth, and R. Jones-Albertus, Eds., 9 2015, p. 95630C. [Online]. Available: http://proceedings.spiedigitallibrary.org/proceeding.aspx?doi=10.1117/12.2188813

[290] B. Zhao, X. Sun, M. A. Alam, and M. R. Khan, "Purdue University Meteorological Tool." [Online]. Available: https://nanohub.org/resources/pumet

[291] S. Pingel, O. Frank, M. Winkler, S. Daryan, T. Geipel, H. Hoehne, and J. Berghold, "Potential Induced Degradation of solar cells and panels," in *2010 35th IEEE Photovoltaic Specialists Conference*. IEEE, 6 2010, pp. 002 817–002 822. [Online]. Available: http://ieeexplore.ieee.org/document/5616823/

[292] K. Trapani and M. Redón Santafé, "A review of floating photovoltaic installations: 2007-2013," *Progress in Photovoltaics: Research and Applications*, vol. 23, no. 4, pp. 524–532, 4 2015. [Online]. Available: http://doi.wiley.com/10.1002/pip.2466

[293] N. Blair, A. P. Dobos, J. Freeman, T. Neises, M. Wagner, T. Ferguson, P. Gilman, and S. Janzou, "System Advisor Model, SAM 2014.1.14: General Description," National Renewable Energy Laboratory, Tech. Rep., 2014. [Online]. Available: https://www.nrel.gov/docs/fy14osti/61019.pdf

[294] W. Luo, Y. S. Khoo, P. Hacke, V. Naumann, D. Lausch, S. P. Harvey, J. P. Singh, J. Chai, Y. Wang, A. G. Aberle, and S. Ramakrishna, "Potential-induced degradation in photovoltaic modules: a critical review," *Energy & Environmental Science*, vol. 10, no. 1, pp. 43–68, 2017. [Online]. Available: http://xlink.rsc.org/?DOI=C6EE02271E

[295] X. Sun, R. Dubey, S. Chattopadhyay, M. R. Khan, R. V. Chavali, T. J. Silverman, A. Kottantharayil, J. Vasi, and M. A. Alam, "A novel approach to thermal design of solar modules: Selective-spectral and radiative cooling," in *2016 IEEE 43rd Photovoltaic Specialists Conference (PVSC)*. IEEE, 6 2016, pp. 3584–3586. [Online]. Available: http://ieeexplore.ieee.org/document/7750340/

[296] NREL, "National Solar Radiation Data Base," 2010. [Online]. Available: http://rredc.nrel.gov/solar/old_data/nsrdb/

[297] M. Alam and S. Mahapatra, "A comprehensive model of PMOS NBTI degradation," *Microelectronics Reliability*, vol. 45, no. 1, pp. 71–81, 1 2005. [Online]. Available: http://linkinghub.elsevier.com/retrieve/pii/S0026271404001751

[298] B. Braisaz, C. Duchayne, M. Van Iseghem, and K. Radouane, "PV Aging Model Applied to Several Meteorological Conditions," in *29th European Photovoltaic Solar Energy Conference (EU PVSEC)*, 2014.

APPENDICES

A. DERIVATION OF PHYSICS-BASED ANALYTICAL MODEL

A.1 Analytical Derivation

Here we will discuss the analytical derivation of the physics-based model. We will illustrate the steps using the example of perovskite solar cells, but the underlying mathematic techniques are also applicable to CIGS solar cells.

A.1.1 Intrinsic Absorber

We will begin with solving the electron and hole continuity equations given in [154]

$$\frac{\partial n}{\partial t} = \frac{1}{q}\frac{\partial J_n}{\partial x} + G(x) - R(x), \tag{A.1}$$

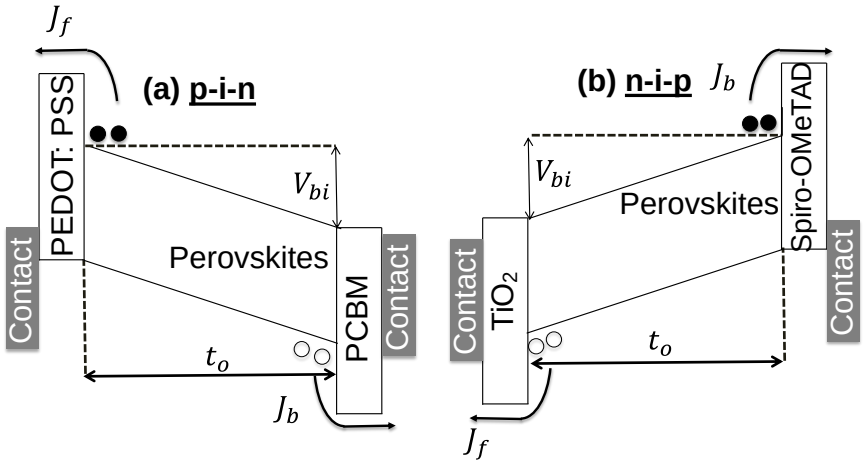

Fig. A.1. (a) The energy diagram of (a) Type 1 (p-i-n) and (b) Type 3 (n-i-p) perovskite

$$\frac{\partial p}{\partial t} = -\frac{1}{q}\frac{\partial J_p}{\partial x} + G(x) - R(x), \tag{A.2}$$

where n and p are the electron and hole concentrations, $G(x)$ and $R(x)$ denote the generation and recombination processes, and J_n and J_p are the electron and hole currents expressed as follows:

$$J_n = q\mu_n nE + qD_n\frac{\partial n}{\partial x}, \tag{A.3}$$

$$J_p = q\mu_p pE - qD_p\frac{\partial p}{\partial x}. \tag{A.4}$$

In Eqns. A.3 and A.4, E is the electric field, μ_n and μ_p are the electron and hole motilities, D_n and D_p are the electron and hole diffusion coefficients, respectively.

Assuming that the bulk recombination is negligible (i.e.,$R(x)$=0) [2], eqns. A.1 to A.4 reduce to,

$$D\frac{\partial^2 n(x)}{\partial^2 x} + \mu E(x)\frac{\partial n(x)}{\partial x} + G(x) - R(x) = 0, \tag{A.5}$$

$$D\frac{\partial^2 p(x)}{\partial^2 x} - \mu E(x)\frac{\partial p(x)}{\partial x} + G(x) - R(x) = 0. \tag{A.6}$$

To solve the equations, we first need to calculate E by solving the Poisson equation, and the generation profile, $G(x)$, by solving the Maxwell equations.

The Poisson equation is written as

$$\frac{\partial^2 \phi}{\partial x^2} = -\frac{\rho}{\varepsilon}. \tag{A.7}$$

Assuming that the absorber is intrinsic (so that ρ=0), therefore, $\phi(x) = ax$. Since the voltage drops primarily across the absorber layer, therefore, $\phi(x = 0) = 0$ and $\phi(x = t_0) = V_{bi} - V$ in the p-i-n structure. Hence, we can express the electric field as $a = \frac{V_{bi}-V}{t_0} = \frac{\partial \phi}{\partial x} = -E$, so that $E = \frac{V-V_{bi}}{t_0}$. Recall that V_{bi} is the built-in potential across the absorber that is mainly determined by the doping of the selective transport

layers as well as the band alignment at the interface, and t_0 is the absorber thickness, see Fig. A.2 (a).

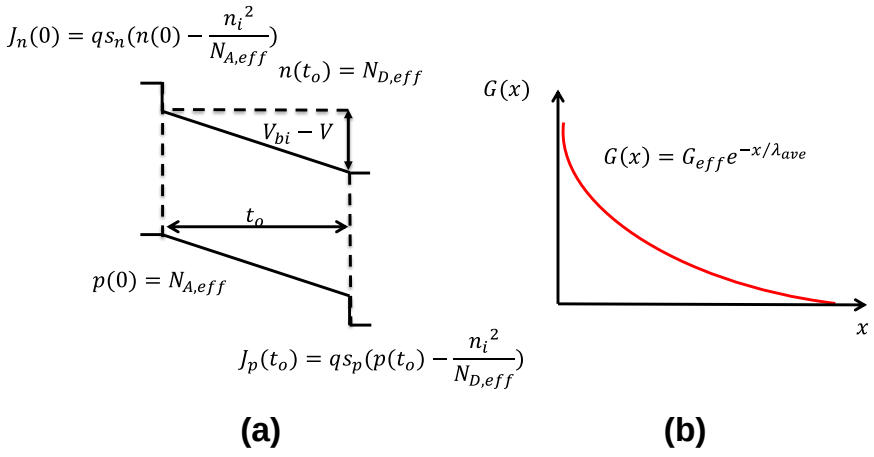

Fig. A.2. (a) The energy diagram of a p-i-n cell with boundary conditions labeled. (b) The approximated generation profile in the absorber

After inserting $E(x)$ and $G(x)$ in Eqns. A.5 and A.6, the general solutions are given by

$$n(x) = A_n e^{-\varepsilon_0 x} + \frac{G_n \lambda_{ave}^2 e^{-\frac{x}{\lambda_{ave}}}}{\varepsilon_0 \lambda_{ave} - 1} + B_n, \tag{A.8}$$

$$p(x) = A_p e^{\varepsilon_0 x} - \frac{G_p \lambda_{ave}^2 e^{-\frac{x}{\lambda_{ave}}}}{\varepsilon_0 \lambda_{ave} + 1} + B_p, . \tag{A.9}$$

where $\varepsilon_0 \equiv qE/kT$ is the normalized electric field, $G_n \equiv G_{eff}/D_n$ and $G_p \equiv G_{eff}/D_p$ represent the normalized generation rates, $A_{n(p)}$ and $B_{n(p)}$ are constants to be determined from the boundary conditions.

In the case of Type 1 (p-i-n), the boundary conditions for eqns. A.8 and A.9 at $x = 0$ and $x = t_0$ are depicted in Fig.A.2, where the effective doping concentration $N_{A,eff}$ and $N_{D,eff}$ are the equilibrium hole and electron concentrations at the ends of the i-layer. The concentrations are determined by the doping and the electron affinities of the transport layers, the built-in potential is $V_{bi} = \frac{kT}{q}\log(\frac{N_{A,eff}N_{D,eff}}{n_i^2})$, and s_n and s_p are the minority carrier surface recombination velocities.

Using the boundary conditions, we solve for B_n and B_p as

$$B_n = \frac{N_{D,eff}e^{\varepsilon_o t_0} - \frac{n_i^2}{N_{A,eff}} + \frac{G_n\lambda_{ave}}{\varepsilon_o t_0 - 1}(\lambda_{ave} - D_n\frac{\varepsilon_o t_0 - 1}{s_n} - \lambda_{ave}e^{\varepsilon_o t - \frac{t_0}{\lambda_{ave}}})}{e^{\varepsilon_o t_0} - 1 + \frac{\varepsilon_o \mu_n}{s_n}\frac{kT}{q}}, \tag{A.10}$$

$$B_p = \frac{N_{A,eff}e^{\varepsilon_o t_0} - \frac{n_i^2}{N_{D,eff}} - \frac{G_p\lambda_{ave}}{\varepsilon_o t_0 + 1}e^{-\frac{t_0}{\lambda_{ave}}}(\lambda_{ave} - D_p\frac{\varepsilon_o t_0 + 1}{s_p} - \lambda_{ave}e^{\varepsilon_o t - \frac{t_0}{\lambda_{ave}}})}{e^{\varepsilon_o t_0} - 1 + \frac{\varepsilon_o \mu_p}{s_p}\frac{kT}{q}}. \tag{A.11}$$

Now utilizing Eqns. A.3 and A.4, the current density $J = J(0) = J_n(0) + J_p(0)$ can be expressed as $J = qE(\mu_n B_n + \mu_p B_p)$. Substituting Eqns. A.10 and A.11, we can find the current divided into two parts, a dark diode J_{dark} (independent of generation), and a voltage-dependent photocurrent J_{photo} so that,

$$J_{dark} = (\frac{J_{f0}}{\frac{e^{V'}-1}{V'} + \beta_f} + \frac{J_{b0}}{\frac{e^{V'}-1}{V'} + \beta_b})(e^{\frac{qV}{kT}} - 1), \tag{A.12}$$

$$J_{photo} = qG_{max}(\frac{\frac{\left(1-e^{V'-m}\right)}{V'-m} - \beta_f}{\frac{e^{V'}-1}{V'} + \beta_f} - \frac{\frac{\left(1-e^{V'+m}\right)}{V'+m} - \beta_b}{\frac{e^{V'}-1}{V'} + \beta_b}e^{-m}), \tag{A.13}$$

$$J_{light} = J_{dark} + J_{photo}. \tag{A.14}$$

Here, $J_{f0(b0)} = q\frac{n_i^2}{N_{A,eff(D,\ eff)}}\frac{D_{n(p)}}{t_0}$ is the diode current for electrons and holes recombining at the front or back contact; $\beta_{f(b)} = \frac{D_{n(p)}}{t_0 s_{n(p)}}$ depends on the diffusion coefficient and surface recombination velocities; $m = \frac{t_0}{\lambda_{ave}}$ is the ratio of the absorber thickness and the average absorption decay length; $G_{max} = G_{eff}\lambda_{avg}$ is the maximum generation ($G_{max} = \int_o^\infty G_{eff}e^{-x/\lambda_{avg}}dx$); V' represents $q(V - V_{bi})/kT$.

Eqns. A.12 to A.14 can be further simplified to

$$\alpha_{f(b)} = 1/(\frac{e^{V'} - 1}{V'} + \beta_{f(b)}), \tag{A.15}$$

$$A = \alpha_f \times (\frac{\left(1 - e^{V'-m}\right)}{V' - m} - \beta_f), \tag{A.16}$$

$$B = \alpha_b \times (\frac{\left(1 - e^{V'+m}\right)}{V' + m} - \beta_b. \tag{A.17}$$

Consequently,

$$J_{dark} = (\alpha_f \times J_{f0} + \alpha_b \times J_{b0})(e^{\frac{qV}{kT}} - 1), \tag{A.18}$$

$$J_{photo} = qG_{max}(A - Be^{-m}). \tag{A.19}$$

Similarly, one can derive the equations **for Type 3 (n-i-p) perovskite** solar cells with different boundary conditions (i.e., $J_p\,(o) = qs_p\left(n_i - \frac{{n_i}^2}{N_{D,eff}}\right)$ and $n(0) = N_{D,eff}$; $J_n(t_o) = qs_n(n_i - \frac{{n_i}^2}{N_{A,eff}})$ and $p(t_o) = N_{A,eff}$).

A.1.2 Doped Absorber

Due to the intrinsic defects, perovskite films might be self-doped. Generally, self-doping is more pronounced in low/medium ($6 \sim 12\%$) efficiency devices. Here, we derive a physics-based compact model for both p-p-n and n-p-p structures following a recipe similar to that of p-i-n/n-i-p structures.

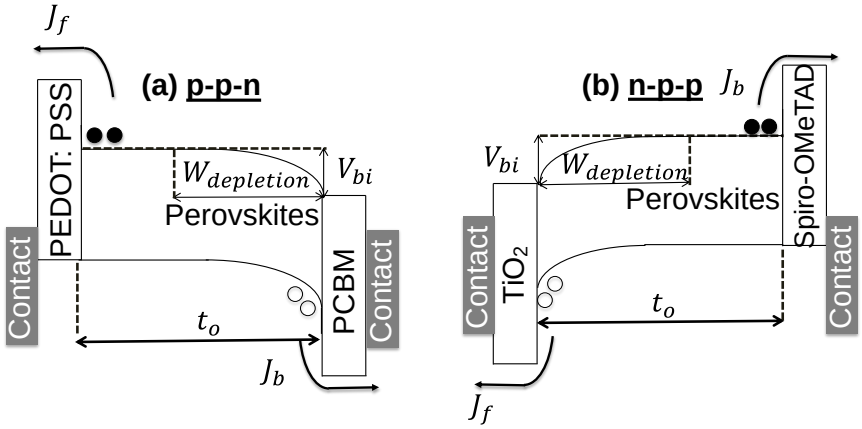

Fig. A.3. (a) The energy diagram of (a) Type 3 (p-p-n) and (b) Type 4 (n-p-p) perovskite cells

The energy diagrams of p-p-n and n-p-p structures are shown in Fig. A.4. The system can be divided into two parts: 1) the depletion region, $W_{depletion}(V) = W_{depletion}(0\ \mathrm{V})\sqrt{\frac{\mathrm{V_{bi}-V}}{\mathrm{V_{bi}}}}(\mathrm{V} < \mathrm{V_{bi}})$; 2) the neutral charge region, $t_0 - W_{depletion}(V)$. Fig. S1.5 shows the corresponding electric field profiles ($V < V_{bi}$), where the field in the neutral charge regions are zero, while that in the depletion region is presumed linear following $|E_{max}(V)| = \frac{2(V_{bi}-V)}{W_{delp}(V)}$.

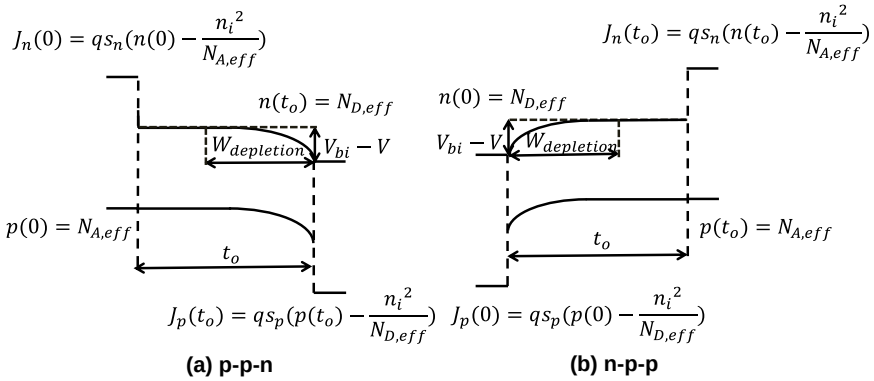

Fig. A.4. The energy diagram of (a) p-p-n and (b) n-p-p perovskite solar cells with boundary conditions labeled.

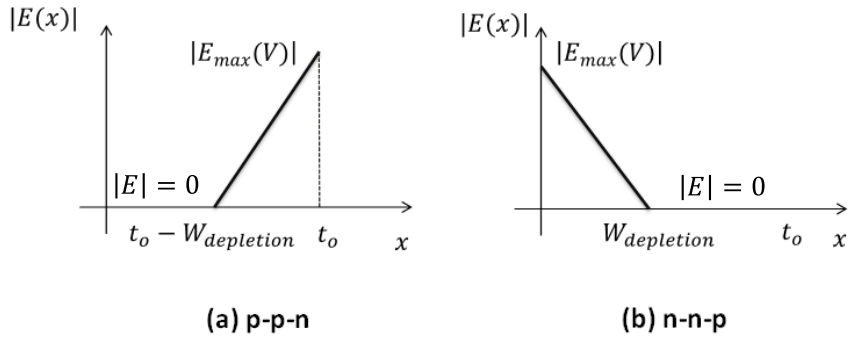

Fig. A.5. Electric field of (a) Type 2 (p-p-n) and (b) Type 4 (n-p-p) perovskite solar cells.

We adopt the same boundary conditions and generation profile as in Section A.1 to solve Eqns. A.5 and A.6. Additionally, the charges and the currents must be con-

tinuous at the boundary between the depletion and neutral regions, i.e., $J_{n(p)}\left(l^{-}\right) = J_{n(p)}\left(l^{+}\right)$ and $n,p\left(l^{-}\right) = n,p\left(l^{+}\right)$, where $l = t_0 - W_{depletion}\left(V\right)$ and $l = W_{depletion}\left(V\right)$ for p-p-n and n-p-p, respectively.

Following the same procedures in Section A.1, we can derive the equations for dark and photo currents ($V < V_{bi}$) following:

Type 2 (p-p-n):

$$\alpha_{f,ppn} = 1/(\Delta + \beta_f), \tag{A.20}$$

$$\alpha_{b,ppn} = 1/(\Delta \times e^{V'} + \beta_b), \tag{A.21}$$

$$A_{ppn} = \alpha_f \times \left(\frac{1}{m}\left(e^{-m\times\Delta} - 1\right) - \beta_f\right), \tag{A.22}$$

$$B_{ppn} = \alpha_b \times \left(\frac{e^{V'}}{m}\left(e^{-m\times(\Delta-1)} - e^{m}\right) - \beta_b\right), \tag{A.23}$$

Type 4 (n-p-p):

$$\alpha_{f,npp} = 1/(\Delta \times e^{V'} + \beta_f), \tag{A.24}$$

$$\alpha_{b,npp} = 1/(\Delta + \beta_b), \tag{A.25}$$

$$A_{npp} = \alpha_f \times \left(\frac{e^{V'}}{m}\left(e^{-m} - e^{m\times(\Delta-1)}\right) - \beta_f\right), \tag{A.26}$$

$$B_{npp} = \alpha_b \times \left(\frac{1}{m}\left(1 - e^{m\times\Delta}\right) - \beta_b\right). \tag{A.27}$$

The new parameter $\Delta = 1 - n\sqrt{(V_{bi} - V)/V_{bi}}$, where $n = W_{depletion}(0\text{ V})/t_0$ is the ratio of the equilibrium depletion width and the absorber thickness.

We assume that the self-doped absorber behaves identically as an intrinsic cell when $V \geq V_{bi}$. Hence we use Eqns. A.15 to A.19 to describe the operation of a

self-doped device at $V \geq V_{bi}$. Please note that Eqns. A.15 to A.19 give the same limit as Eqns. A.20 to A.27 when $V \rightarrow V_{bi}$.

A.2 Assumption Validation - CIGS Solar Cells

Here, we validate the assumptions used to derive the analytical equations for CIGS solar cells based on simulation and experiment data. The simulation was performed using the commercial device simulator, Sentaurus [157]. The discussion is divided into two parts: 1) illumination-independent diode current, and 2) voltage-independent generation-induced bulk recombination current.

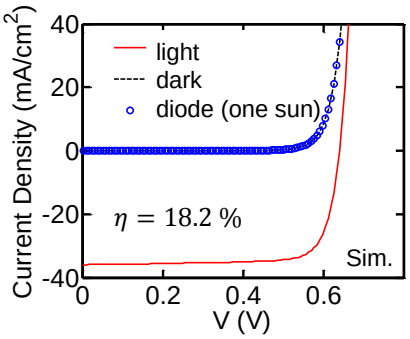

Fig. A.6. The simulated I-V characteristics with 18.2% efficiency, showing that the frozen potential diode (injection) current is the same as dark current

A.2.1 Illumination-Independent Diode Current

We simulate a CIGS solar cell with 18.2% efficiency; see Fig. A.6. The device parameters are summarized in Table A.1. We take the approach discussed in [146] to separate the diode current and photocurrent under illumination, where the illuminated diode (injection) current is obtained by freezing the solution of the potential profile obtained under illumination and solving the frozen potential drift-diffusion equations after setting the photo-generation to zero. As shown in Fig. A.6,

$J_{Diode}\,(one\ sun) = J_{Dark}$ is found for $V < V_{OC}$. We also have experimentally proved that the diode current is illumination-independent by calculating the carrier-collection efficiencies ($\eta\,(V) = (J_{Light}(V) - J_{Dark}(V))/J_{SC}$) for different illumination intensities; see Fig. A.7 (note that it is the same CIGS sample as shown in Fig. 2.6). The argument is that if $J_{Diode} = J_{Dark}$ under different sun intensities, the collection efficiency should not vary with illumination [43]. The results in Fig. A.7 show that the collection efficiencies overlap each other for different illumination intensities (1 sun, 0.8 sun, 0.6 sun, 0.5 sun, 0.4 sun) at various temperatures except for $T = 364$ K, possibly due to high-level injection at high temperature. Therefore, based on the experimental analysis along with the simulation results, it is convincing that the diode current is illumination-independent for high-quality CIGS solar cells.

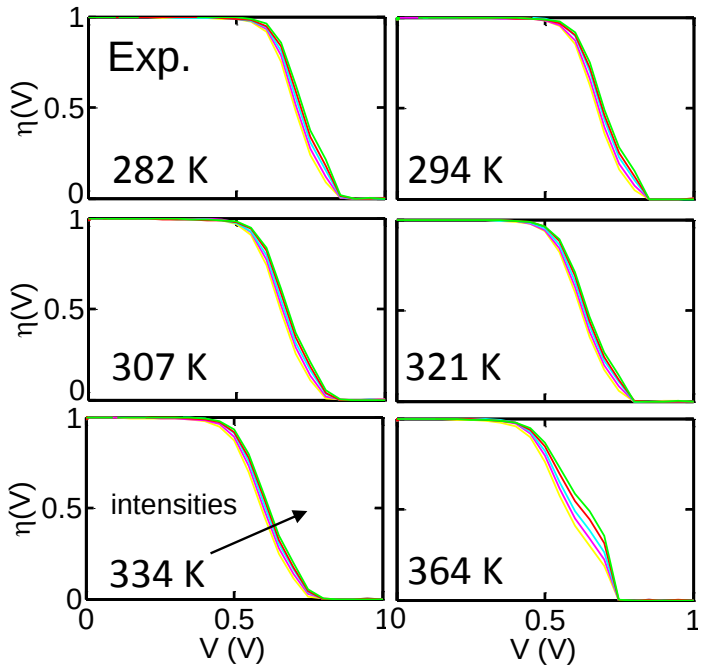

Fig. A.7. The extracted collection efficiency, $\eta(V)$, under varying illumination intensity (1 sun, 0.8 sun, 0.6 sun, 0.5 sun, 0.4 sun) at different temperatures. The plots confirm the assumption of illumination-independent diode current except for 364 K.

A.2.2 Voltage-Independent Generation-Induced Bulk Recombination Current

Here, we try to validate the assumption that the generation-induced bulk recombination current ($J_{Gen-Rec} = \int_o^t (R_{Light}(x) - R_{Dark}(x))dx = \int_o^t R_{Gen}(x)dx$) is voltage-independent up to V_{OC} through simulation. The significance of the voltage-independent generation-induced bulk recombination current is that it allows us to simplify the term $G(x) - R_{Gen}(x)$ in Eq. 2.6 to a normalize generation profile, $G'(x)$, as discussed in Sec. 2.3.1.

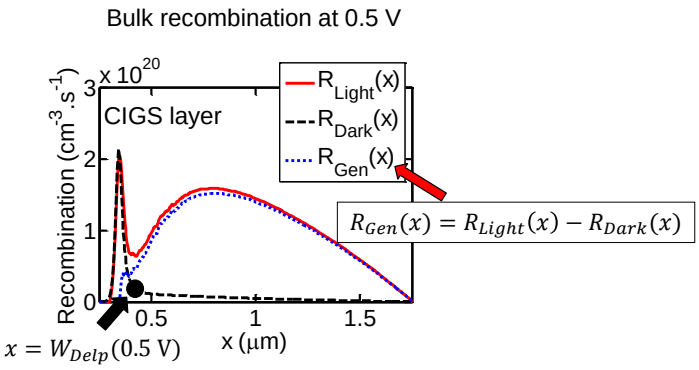

Fig. A.8. The bulk recombination rate as a function of position inside the CIGS layer at 0.5 V. The generation-induced bulk recombination (dots) occurs mostly in the quasi-neutral region.

The bulk recombination rates under dark ($R_{Dark}(x)$) and light ($R_{Light}(x)$) and the generation-induced bulk recombination ($R_{Gen}(x)$) are plotted in Fig. A.8. At $V = 0.5$ V, although there are considerable $R_{Dark}(x)$ and $R_{Light}(x)$ occurring in the depletion region ($x < 0.4$ m), $R_{Gen}(x)$ occurs mostly in the quasi-neutral bulk region. Hence, $R_{Gen}(x)$ is voltage-independent. Consequently, as shown in Fig. A.9(a), the generation-induced bulk recombination current, $J_{Gen-Rec}$, is a small portion of the total generation current and exhibits voltage-independent characteristics up to V_{OC}. Beyond V_{OC}, $J_{Gen-Rec}$ increases with voltage due to high-level injection. In addition, $J_{Gen-Rec}$ remains at 5% of the total generation current, $J_{Tot-Photo}$, for different illumination; see Fig. A.9(b). So the short-circuit current (the maximum photocurrent),

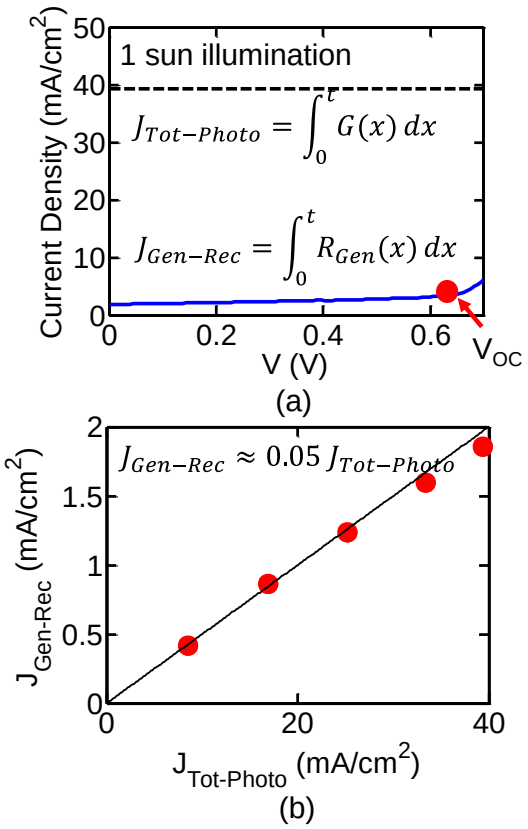

Fig. A.9. (a) Total photocurrent ($J_{Tot-Photo}$) and generation-induced bulk recombination current ($J_{Gen-Rec}$) as a function of bias under one-sun conditions. $J_{Gen-Rec}$ is a small portion of $J_{Gen-Rec}$ and remains almost voltage-independent up to open-circuit voltage. (b) The linear relation between $J_{Gen-Rec}$ and $J_{Tot-Photo}$ for different illumination intensities.

J_{SC}, can be written as $J_{Tot-Photo} - J_{Gen-Rec} = 0.95 \times J_{Tot-Photo}$ and is linear with illumination intensity.

So far, it has been confirmed that the diode current is voltage-independent, and the generation-induced bulk recombination current is voltage-independent under normal operating conditions. With these two assumptions, we can derive Eqns. 2.6–2.11 for photocurrent.

Table A.1.
The simulation parameters used in Sentaurus numerical simulations [153]

Properties		n-layer	n-layer	p-layer
Thickness		200 nm	50 nm	1.5 μm
Doping (cm^3)		1×10^{18}	1×10^{17}	2×10^{16}
Hole mobility (cm^2/Vs))		25	25	25
Electron mobility (cm^2/Vs))		100	100	100
Bandgap (eV)		3.3	2.4	1.15
Electron affinities (eV)		4.4	4.2	4.5
Defect	Type	Donor	Acceptor	Donor
	Defect level (eV)	Midgap	Midgap	Midgap
	Gaussian distribution width (eV)	0.1	0.1	0.1
	Defect density (cm^{-3})	1×10^{17}	1×10^{17}	2×10^{14}
	Hole cross-section (cm^2)	1×10^{-12}	1×10^{-17}	5×10^{-12}
	Electron cross-section (cm^2)	1×10^{-15}	1×10^{-12}	1×10^{-15}
Contact properties		Ohmic contacts ($s_f = 10^7$ cm/s)		

B. COMPREHENSIVE GLOBAL MAPS OF PERFORMANCE AND OPTIMIZATION FOR BIFACIAL SOLAR MODULES

Here we will present four tables of global maps summarizing the optimization and performance (i.e., tilt angle, azimuth angle, annual energy yield, and bifacial gain) for bifacial solar modules with different deployment scenarios (i.e., elevation and albedo).

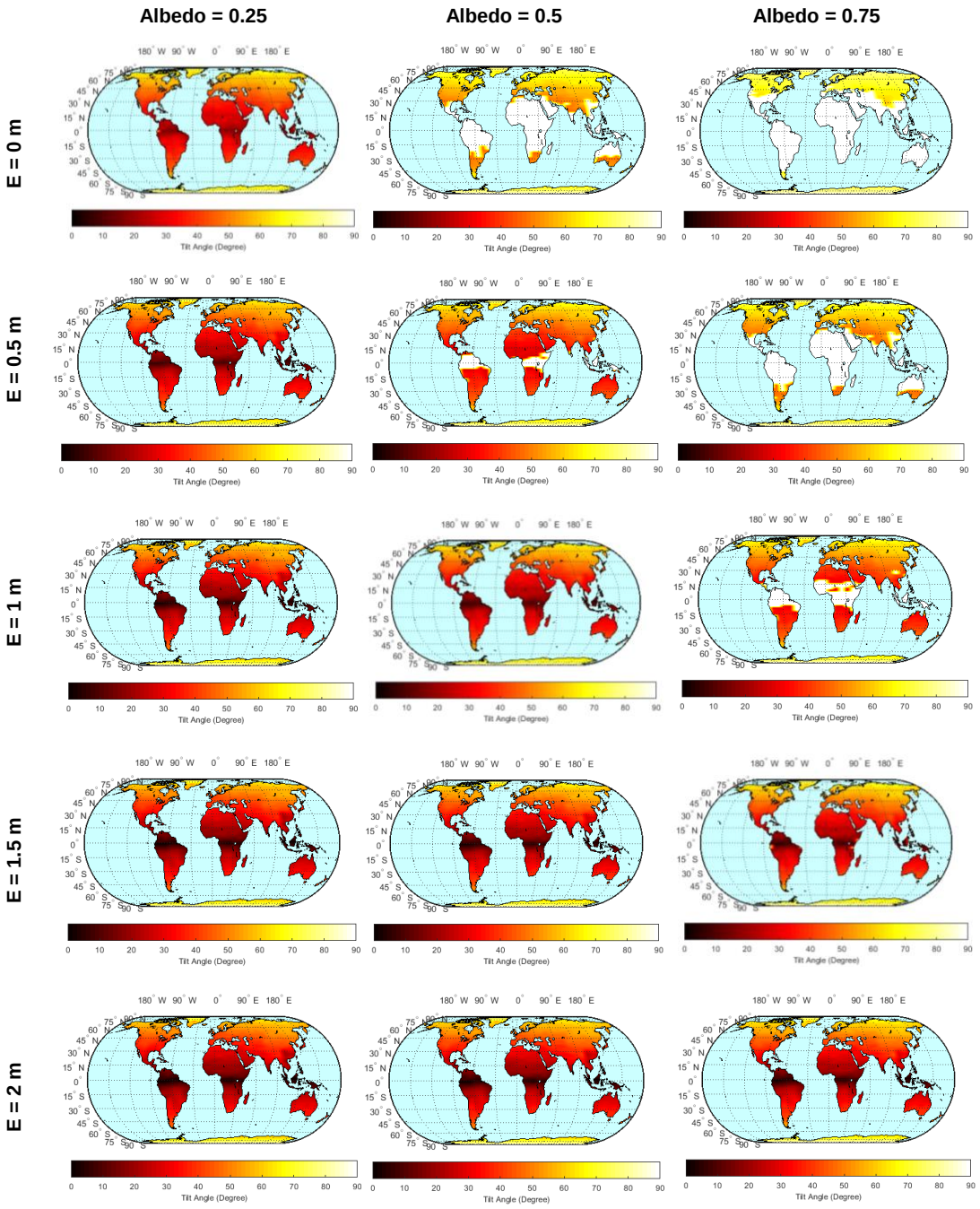

Fig. B.1. Optimal tilt angle of a 1 m high module for different ground albedo and elevations (E).

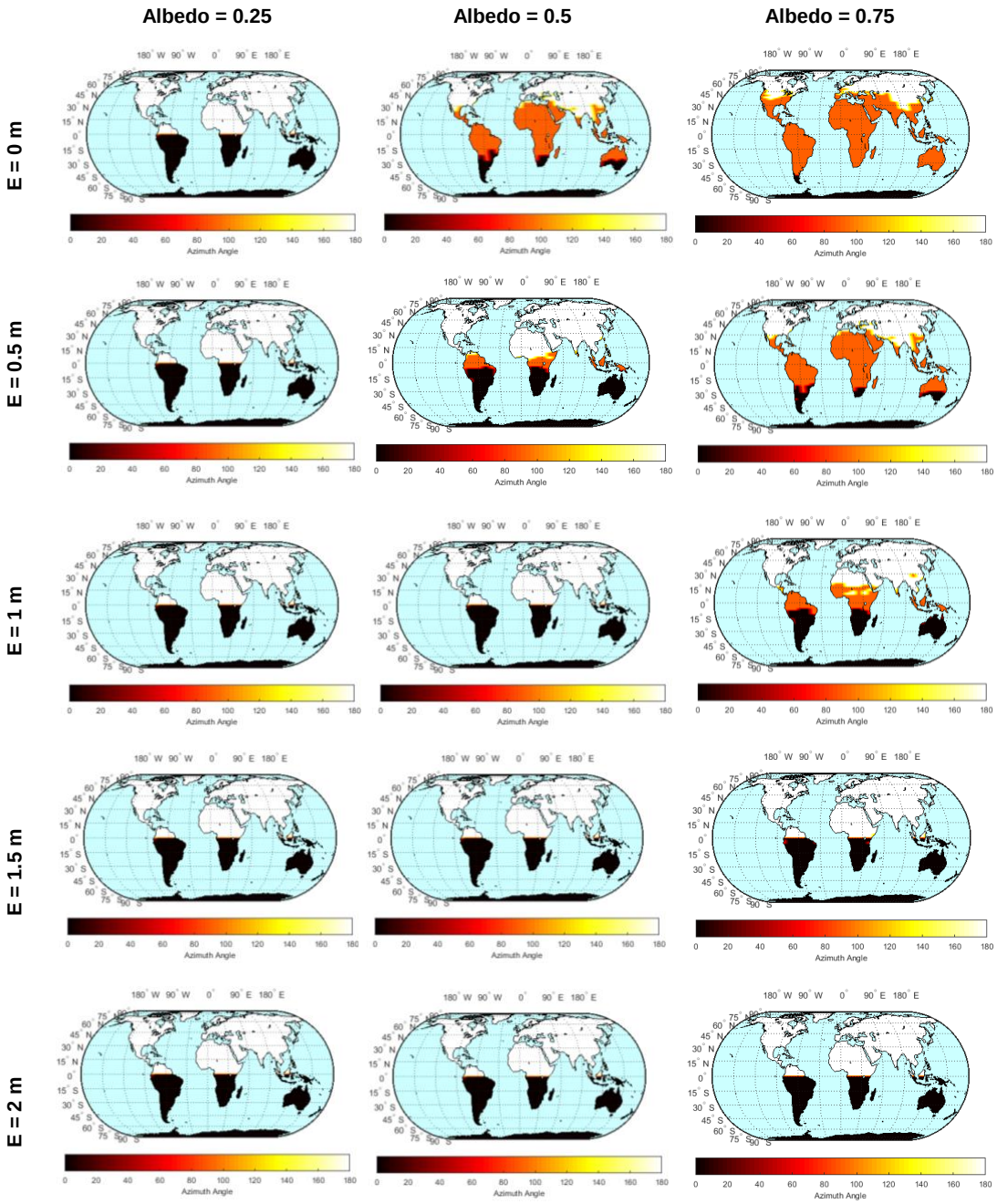

Fig. B.2. Optimal azimuth angle of a 1 m high module for different ground albedo and elevations (E).

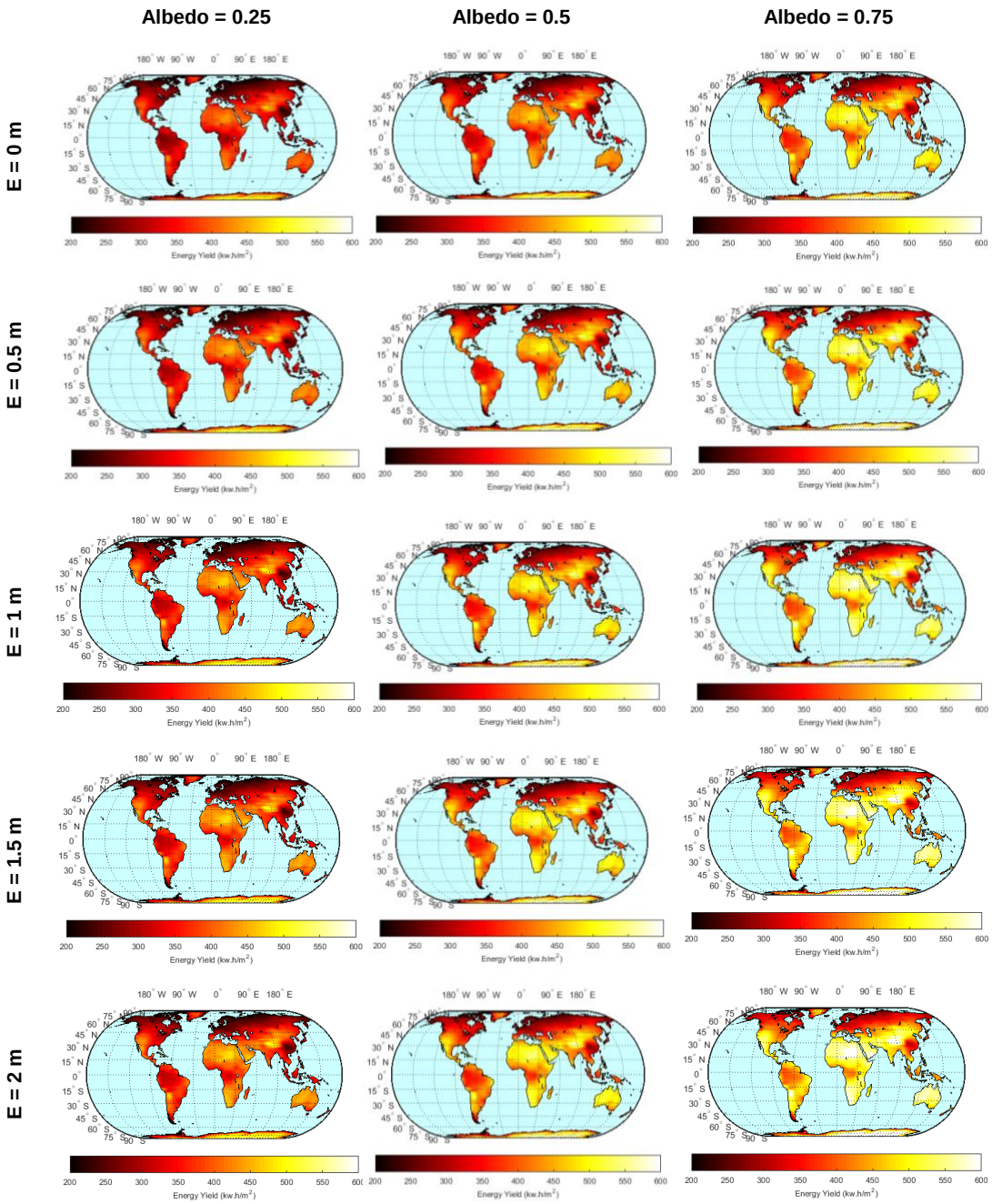

Fig. B.3. Maximum annual electricity yield of a 1 m high module for different ground albedo and elevations (E).

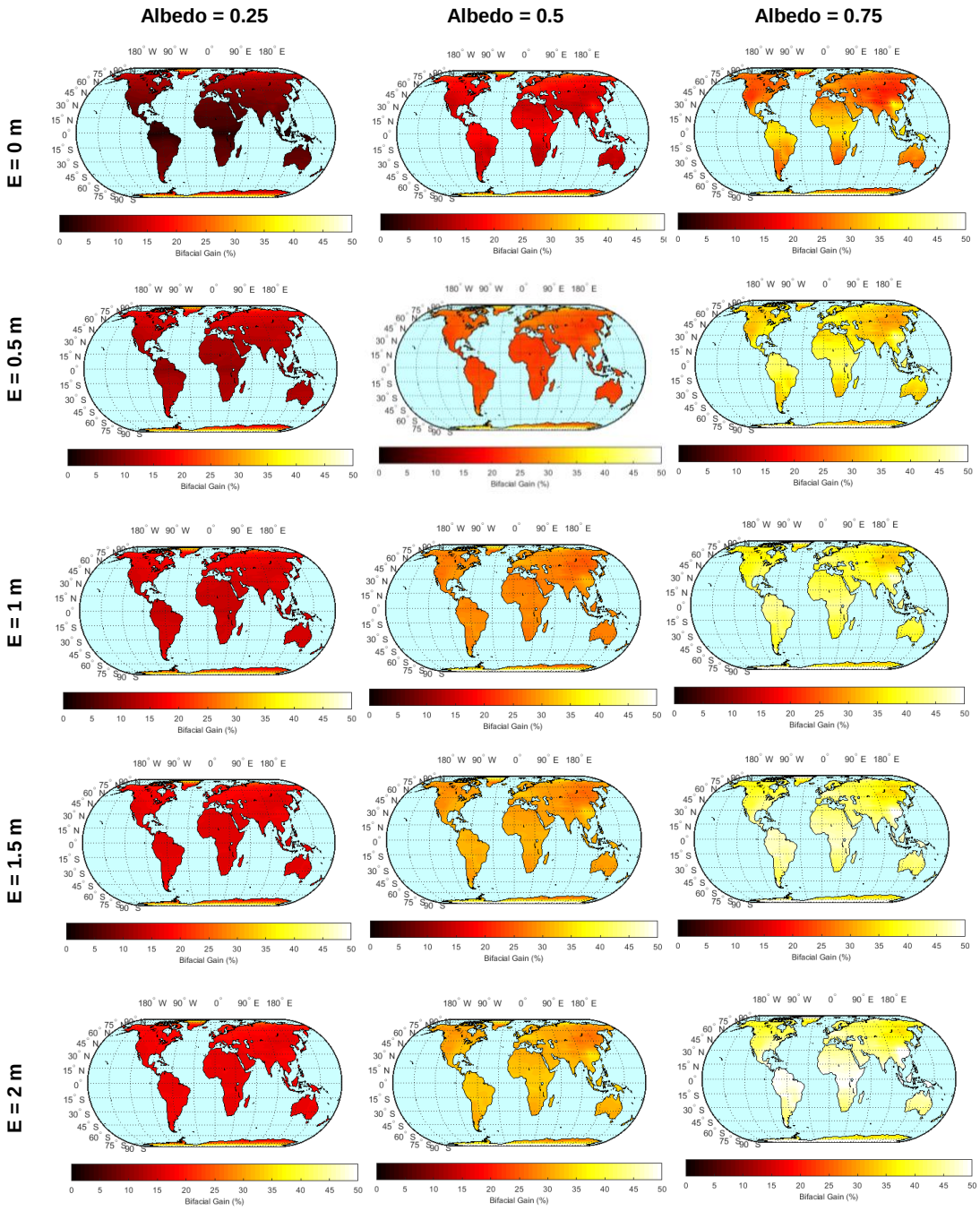

Fig. B.4. Maximum bifacial gain of a 1 m high module for different ground albedo and elevations (E).

C. DETAILED IMPLEMENTATION AND VARIABILITY TEST OF THE SUNS-VMP METHOD

Here we will discuss the specific implementation of data processing and physics-based filtering as well as the analytical equations of the compact model used in the algorithm introduced in Sec. 5.2. In addition, we will examine the susceptibility of the Suns-Vmp method to intra-cell variability and the resulting effects on the parameter extraction.

C.1 Preprocess Environmental Data

The Suns-Vmp method relies on environment data, i.e., cell temperature and irradiance. The weather information is used as inputs to the equivalent circuit to fit the reconstructed MPP IV. The raw data can contain seasonal irradiance variation and temperature correction. Hence, it is important to preprocess the raw data so that the parameters extracted are accurate and robust. Below, we discuss this issue of data preprocessing in detail.

C.1.1 Cell Temperature

Module temperature is typically measured by attaching thermal sensors to the back side of solar modules. The actual cell temperature can be higher than the measured back-side module temperature regardless of convective and radiative heat transfer at the module surfaces. Ref. [**?**] has developed an empirical equation to predict cell temperature (T_C) based on illumination intensity (G_{POA}) and module temperature (T_M), which is used in this algorithm.

C.1.2 Irradiance Data

In addition to thermal information, we also need the illumination data to perform the Suns-Vmp method. The on-site illumination data is typically measured by pyranometers orientated as same as solar modules to collect the plane-of-array irradiance G_{POA}. However, directly applying the raw G_{POA} data to the Suns-Vmp method can cause inaccuracy in extracting short-circuit current because of 1) air mass dependent spectral mismatch between field and standard test condition (STC) and 2) reflection loss of flat-plate solar modules. Thus, one must preprocess G_{POA} data to eliminate the above non-idealities, as discussed below.

C.1.3 Spectral Mismatch

The spectral profile of G_{POA} under which MPP data is generated can differ from the AM1.5G spectrum used in the STC for initial rating. Because the extracted circuits from the Suns-Vmp method are eventually corrected to their STC values, the spectral mismatch between real-time field irradiance and STC can contaminate the fitting results primarily for the short-circuit current. Fortunately, the Sandia PV Array Performance Model (SAPM) has developed a polynomial equation to empirically describe the spectral content of solar irradiance as a function of air mass (AM) [**?**]. In this algorithm, we use the SAPM to correct the real-time G_{POA} to its STC values, where AM is calculated by the Sandia PV modeling library [238] and the Direct Normal Incidence (DNI) is retrieved from [296] at the installation location.

C.1.4 Reflection Loss

Pyranometers can accept irradiance coming from a highly oblique angle of incidence (AOI) thanks to the doom-shaped glass cover, while flat-plane solar modules are susceptible to reflection loss at high AOI. Consequently, one must also adjust G_{POA} measured by pyranometers to account for reflection loss. In this algorithm, we

also utilize the SAPM module [**?**] to correct for reflection loss of the direct normal incidence, given the tilt and azimuth angles of the analyzed solar modules.

Although the metrological information is often available from the on-site weather station, this may not be the always the case. In this case, meteorological databases, such as Ref. [296] can be alternative sources for reproducing illumination and temperature information [194].

C.2 Physics-Based Filtering Algorithm

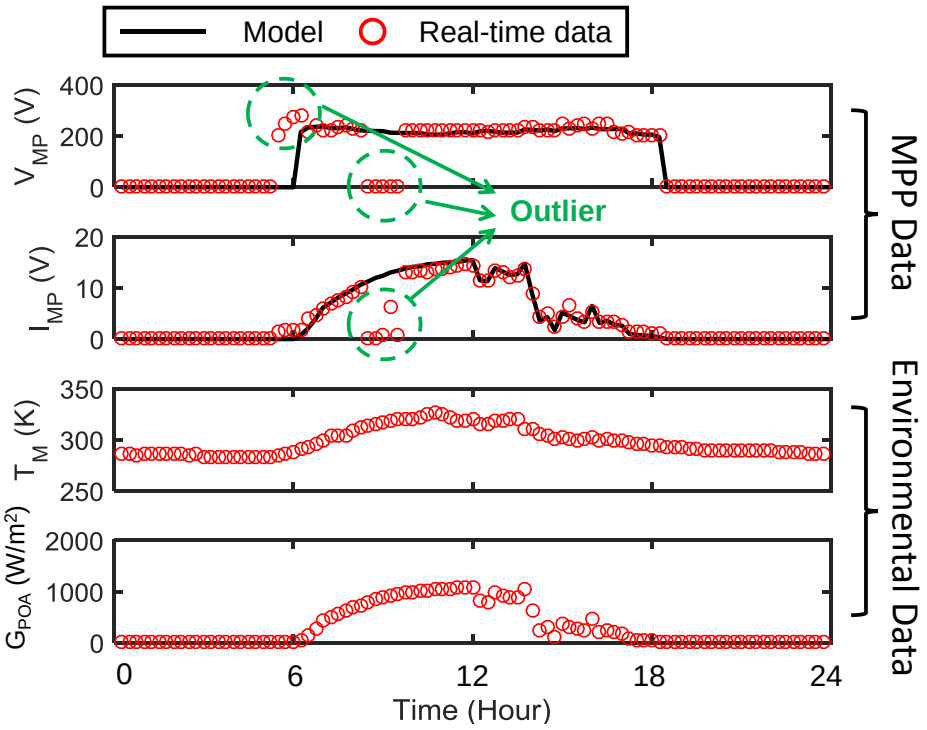

Fig. C.1. Raw MPP data with outliers, filtered MPP data, and the environmental data on 05/16/1994 of the NREL test facility.

Outlier data points due to instrumentation error, inverter clipping, weather condition, etc., can exist in the field data [125]. For example, the Imp data point at around 9 am in Fig. C.1 shows substantial inconsistency with G_{POA}. The inclusion of these outliers in the Suns-Vmp method can induce significant uncertainties in extracting

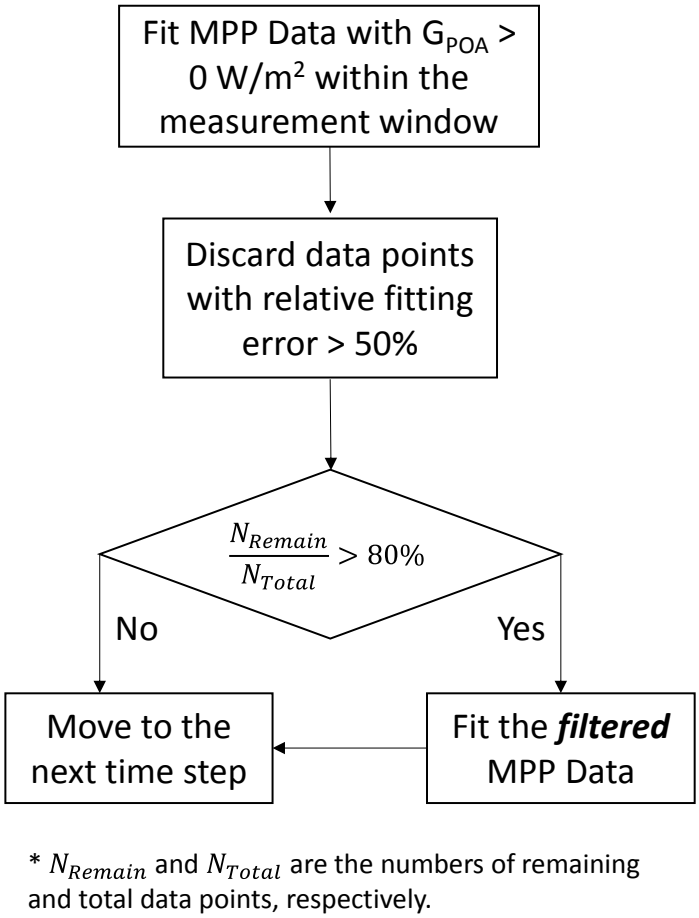

Fig. C.2. Flowchart of our self-filtering algorithm to identify and eliminate outlier data points.

circuit parameters. Therefore, it is necessary to develop a self-consistent scheme to detect and then remove these outliers. Toward this goal, we have created a continuous self-filtering algorithm to eliminate outlier data points, see Fig. C.2. The steps are as follows:

1. Fit the MPP data with non-zero POA irradiance using the equivalent circuit (MPP data with zero irradiance always yields zero current and voltage, thereby irrelevant). Note that this fitting step is confined to the MPP data only within the measurement window at a single time step.

2. Calculate the relative error of fitting each MPP data point. If the error is greater than 50%, the corresponding data point is treated as an outlier and discarded.
3. Examine the number of the remaining data points after step 2. If the remaining still consists of more than 80% of the raw data points, proceed to step 4. Otherwise, the corresponding time step is considered as an outlier as a whole (i.e., remove all the data points at this time step), and will not be analyzed further. Rather, the Suns-Vmp method will directly move to the next time-window. The entire measurement window may consist of corrupted data if temporary instrumentations malfunctions for more than a few days.
4. Fit the filtered MPP data by the equivalent circuit and extract the circuit parameters.
5. Move to next time step.

C.3 Equations of the Five Parameter Model for Si Solar Modules

Table C.1.
The equations of the analytical model

Analytical equations for I-V characteristics	
$J_{D1} = J_0(e^{\frac{qV-J\times R_S}{kT}} - 1)$	
$J_{D2} = J_0(e^{\frac{qV-J\times R_S}{2kT}} - 1)$	
$J_{Shunt} = (V - J \times R_S)/R_{Shunt}$	
$J = J_{Ph} + J_{D1} + J_{D2} + J_{Shunt}$	
Illumination and temperature dependencies of the parameters	
J_{Ph}	$J_{Ph} = \frac{G}{G_{STC}} \times J_{PH,STC} \times (1 + \beta \times (T - T_{STC}))$
J_{01}	$J_{01} = J_{01,STC} \times \left(\frac{T}{T_{STC}}\right)^3 \times \exp(\frac{1}{k}(\frac{E_{G,STC}}{T_{STC}} - \frac{E_G}{T}))$
J_{02}	$J_{02} = J_{02,STC} \times \left(\frac{T}{T_{STC}}\right)^{2.5} \times \exp(\frac{2}{k}(\frac{E_{G,STC}}{T_{STC}} - \frac{E_G}{T}))$
E_G	$E_G = E_{G,STC} + \alpha \times (T - T_{STC})$
R_{Shunt}	$R_{Shunt} = R_{Shunt,STC} \times \frac{G}{G_{STC}}$

Here, we will present the analytical formulation of the five-parameter model [40] used in the Suns-Vmp method (see Fig. 5.2) and the temperature- and illumination-dependency of each parameter in Table C.1. Also, detailed description and initial STC value for Siemens M55 [277] of each parameter is listed in Table C.2. Note that G_{STC} = 1000 W/m^2 and T_{STC} = 25 ^{o}C for standard test condition in for standard test condition in Table C.2.

Table C.2.
Parameter description and their initial STC values for Siemens M55 [277]

$J_{Ph,STC}$	Maximum Photo Current	282 mA/cm^2
$J_{01,STC}$	Diode recombination current with ideality factor of 1	1.3×10^{-8} mA/cm^2
$J_{02,STC}$	Diode recombination current with ideality factor of 2	4.6×10^{-4} mA/cm^2
R_{Shunt}	Shunt resistance	0.12 Ω.cm^2
R_S	Series resistance	1.7×10^{-4} Ω.cm^2
β	Temperature coefficient of short-circuit current	(0.49 %/K)
E_G	Bandgap of Si absorber	(1.12 eV)
α	Temperature coefficient of Si bandgap	(-6×10^{-4} eV/K)

C.4 Variability Test of the Suns-Vmp Method

We have tested the Suns-Vmp method under various scenarios of variability using synthetic weather data in Fig. C.3. Non-uniform degradation of solar cells in the field can occur due to different degradation pathways and have different levels of non-uniformity. Hence, we have emulated four cases of performance variability: 1) 6 out of 36 cells degrades due to contact corrosion (R_S increases tenfold); 2) 6 out of 36 cells have encapsulant delamination (only retain 80% of initial short-circuit current); 3) 6 out of 36 cells suffer from moderate potential-induced degradation (shunt resis-

tance decrease by one order); 4) 6 out of 36 cells suffer from server potential-induced degradation (shunt resistance decrease by two orders). All the tests of performance variability are summarized in Figs. C.4 to C.7.

As shown in Figs. C.4 to C.7, the Suns-Vmp method is still capable of diagnosing the pathology of solar modules with non-uniform degradation. For example, the Suns-Vmp method has attributed efficiency degradation to the increased series resistance in Fig. C.4. This result, however, is not surprising since series resistance can essentially be aggregated into one single resistance in a series-connected circuit in Fig. C.4(a). Remarkably, the Suns-Vmp method is still valid even for non-uniform delamination- and PID-induced degradation where simple superstition of either short-circuit current and shunt resistance of healthy and degraded cells does not hold, see Figs. C.5 and C.6. The Suns-Vmp, however, cannot correctly extract the degraded circuit parameter by only one single equivalent circuit under severe performance variability, see Fig. C.7. Hence, it is recommended to utilize multiple equivalent circuits in the Suns-Vmp method to analyze solar modules with substantial performance variability.

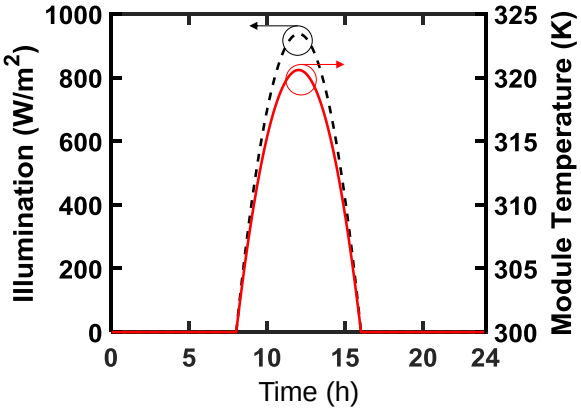

Fig. C.3. Synthetic weather data containing hourly illumination and module temperature is used to test the Suns-Vmp method.

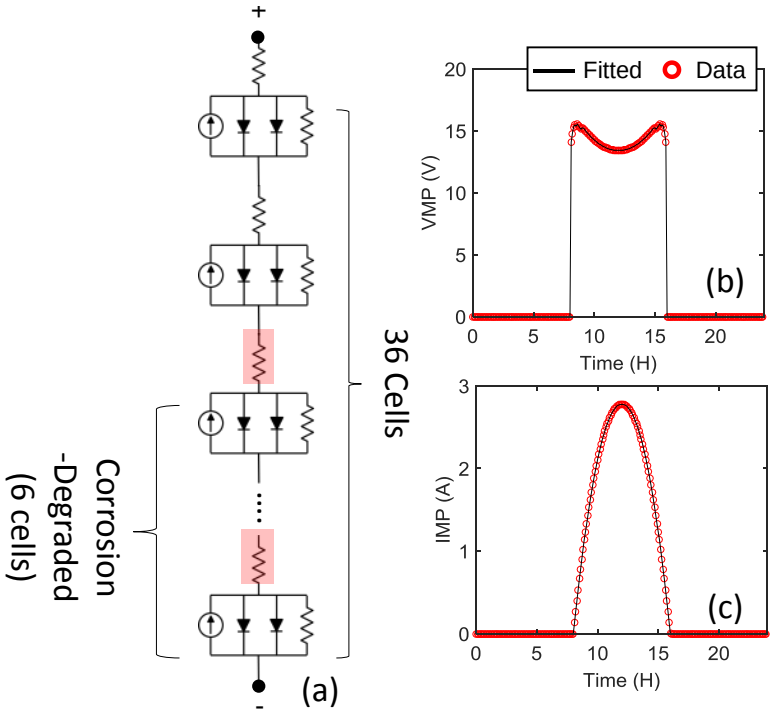

(d) Extracted parameter by the Suns-Vmp method			
	Default (30 cells)	Degraded (6 cells)	Extraction
$J_{PH,STC}$	282 A/m^2	282 A/m^2	282 A/m^2
$J_{01,STC}$	1.3 x 10^{-8} A/m^2	1.3 x 10^{-8} A/m^2	1.3 x 10^{-8} A/m^2
$J_{02,STC}$	4.6 x 10^{-4} A/m^2	4.6 x 10^{-4} A/m^2	4.6 x 10^{-4} A/m^2
$R_{Sh,STC}$	0.12 Ω.m^2	0.12 Ω.m^2	0.12 Ω.m^2
R_S	1.7 x 10^{-4} Ω.m^2	**1.7 x 10^{-3} Ω.m^2**	**4.2 x 10^{-4} Ω.m^2**

Fig. C.4. (a) A schematic of the simulated 36-cell solar module including 6 cells degraded due to contact corrosion. The degraded circuit elements are also highlighted. (b,c) Vmp and Imp of the solar module using the synthetic weather data in Fig. C.3. Circles are simulated data and solid lines are fitting data using the Suns-Vmp method. (d) Table summarizes input parameters (both default and degraded) and extracted parameter set using the Suns-Vmp method (affected parameters are in bold).

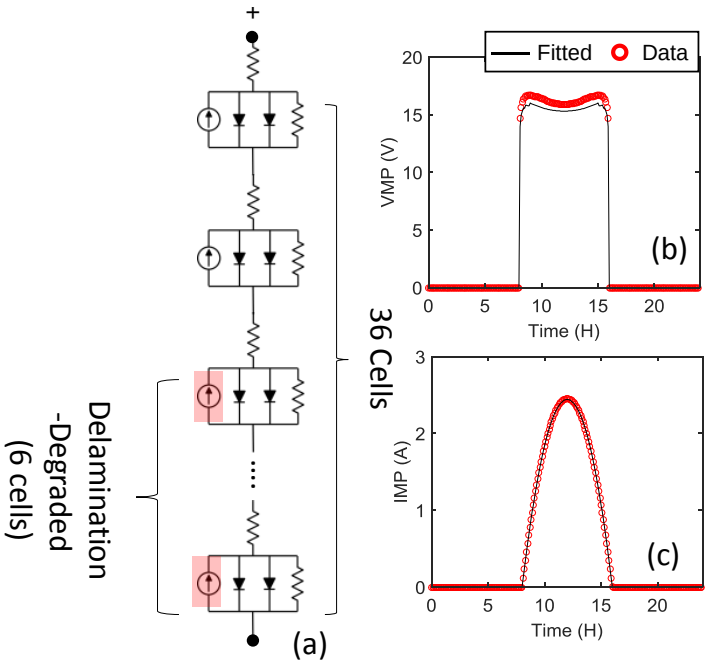

(d) Extracted parameter by the Suns-Vmp method			
	Default (30 cells)	Degraded (6 cells)	Extraction
$J_{PH,STC}$	282 A/m²	**225 A/m²**	**244 A/m²**
$J_{01,STC}$	1.3 x 10^{-8} A/m²	1.3 x 10^{-8} A/m²	1.3 x 10^{-8} A/m²
$J_{02,STC}$	4.6 x 10^{-4} A/m²	4.6 x 10^{-4} A/m²	4.6 x 10^{-4} A/m²
$R_{Sh,STC}$	0.12 Ω.m²	0.12 Ω.m²	0.12 Ω.m²
R_S	1.7 x 10^{-4} Ω.m²	1.7 x 10^{-4} Ω.m²	1.7 x 10^{-4} Ω.m²

Fig. C.5. (a) A schematic of the simulated 36-cell solar module including 6 cells degraded due to delamination. The degraded circuit elements are also highlighted. (b,c) Vmp and Imp of the solar module using the synthetic weather data in Fig. C.3. Circles are simulated data and solid lines are fitting data using the Suns-Vmp method. (d) Table summarizes input parameters (both default and degraded) and extracted parameter set using the Suns-Vmp method (affected parameters are in bold).

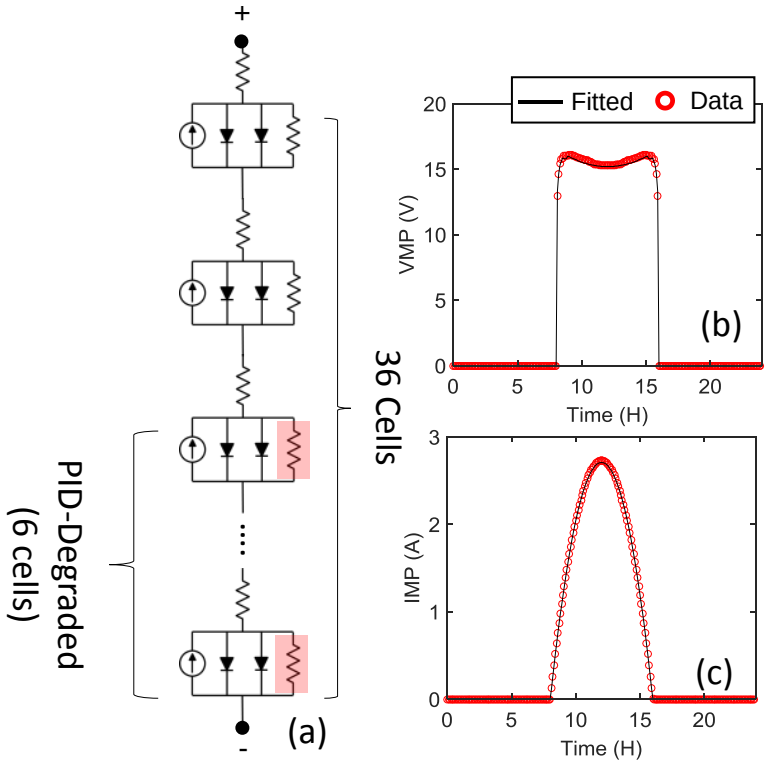

(d) Extracted parameter by the Suns-Vmp method			
	Default (30 cells)	PID- Degraded (6 cells)	Extraction
$J_{PH,STC}$	282 A/m^2	282 A/m^2	282 A/m^2
$J_{01,STC}$	1.3 x 10^{-8} A/m^2	1.3 x 10^{-8} A/m^2	1.3 x 10^{-8} A/m^2
$J_{02,STC}$	4.6 x 10^{-4} A/m^2	4.6 x 10^{-4} A/m^2	4.6 x 10^{-4} A/m^2
$R_{Sh,STC}$	0.12 Ω.m^2	**0.012 Ω.m^2**	**0.026 Ω.m^2**
R_S	1.7 x 10^{-4} Ω.m^2	1.7 x 10^{-4} Ω.m^2	1.7 x 10^{-4} Ω.m^2

Fig. C.6. (a) A schematic of the simulated 36-cell solar module including 6 cells degraded due to moderate potential induced degradation. The degraded circuit elements are also highlighted. (b,c) Vmp and Imp of the solar module using the synthetic weather data in Fig. C.3. Circles are simulated data and solid lines are fitting data using the Suns-Vmp method. (d) Table summarizes input parameters (both default and degraded) and extracted parameter set using the Suns-Vmp method (affected parameters are in bold).

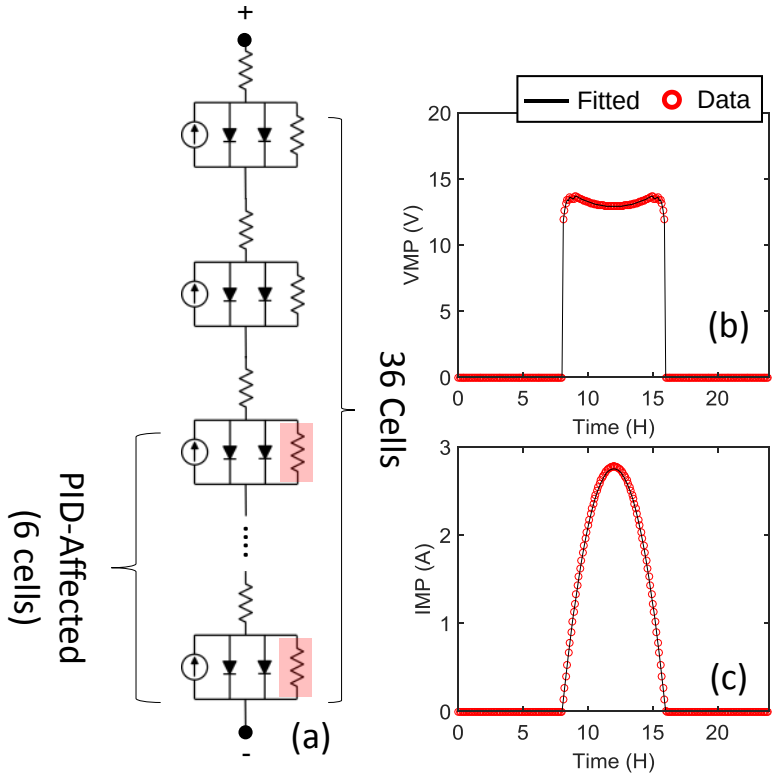

(d) Extracted parameter by the Suns-Vmp method			
	Default (30 cells)	PID- Degraded (6 cells)	Extraction
$J_{PH,STC}$	282 A/m^2	282 A/m^2	282 A/m^2
$J_{01,STC}$	1.3 x 10^{-8} A/m^2	1.3 x 10^{-8} A/m^2	**1.5 x 10^{-7} A/m^2**
$J_{02,STC}$	4.6 x 10^{-4} A/m^2	4.6 x 10^{-4} A/m^2	**2.1 x 10^{-2} A/m^2**
$R_{Sh,STC}$	0.12 Ω.m^2	**0.0012 Ω.m^2**	0.12 Ω.m^2
R_S	1.7 x 10^{-4} Ω.m^2	1.7 x 10^{-4} Ω.m^2	**1.8 x 10^{-4} Ω.m^2**

Fig. C.7. (a) A schematic of the simulated 36-cell solar module including 6 cells degraded due to moderate potential induced degradation. The degraded circuit elements are also highlighted. (b,c) Vmp and Imp of the solar module using the synthetic weather data in Fig. C.3. Circles are simulated data and solid lines are fitting data using the Suns-Vmp method. (d) Table summarizes input parameters (both default and degraded) and extracted parameter set using the Suns-Vmp method (affected parameters are in bold).

D. A SET OF TEMPORAL DEGRADATION MODELS FOR EVA YELLOWING, POTENTIAL-INDUCED DEGRADATION, METAL CORROSION

Here we will briefly discuss the physics of three important degradation mechanisms, i.e., EVA yellowing, potential-induced degradation (PID), and metal corrosion, as well as the temporal models used to simulate their processes and impacts on PV performance. These models have been validated against a set of accelerated tests.

D.1 EVA Yellowing

Physics of EVA Yellowing. In commercial solar modules, a polymer layer ethylene-vinyl acetate (EVA) is applied to encapsulate the solar cells for mechanical stability (a buffer between rigid glasses and solar cells), and it can also impeding moisture diffusion. The EVA layer must be transparent in the solar spectrum to pass the useful photons into solar cells for energy conversion. EVA itself is essentially a copolymer of ethylene (C_2H_4) and vinyl acetate ($C_4H_6O_2$), consists of a variety of chemical bonds (e.g., C-C, C-H, C-O) to form a polymer chain. Unfortunately, the bonding energies of these bonds (e.g., C-C = 3.6 to 3.7 eV) are lower than the UV photon energy; therefore, they (R) can be broken by photoexcitation under UV exposure described as below

$$\mathrm{R} + h\nu \xrightarrow{\mathrm{k_2}} \mathrm{Y}.$$

The broken bonds become defects and produce light-absorbing yellow chromophores (Y), which increase the yellowing index. Consequentially, they reduce the optical transmission of the EVA encapsulants. The entire process is known as EVA yellowing.

UV Absorber for Protection. To combat EVA yellowing, people have added UV-protective chemical into EVA to strengthen the yellowing-resistance [94]. This

chemical additive behaves as a UV absorber; namely, it absorbs the detrimental UV photons, which otherwise will be absorbed by EVA itself. Hence, it can significantly reduce UV-induced bond breaking and inhibit EVA yellowing. This process, referred as photo-bleaching, is carried out by an independent photo-induced reaction as

$$\mathrm{A} + h\nu \xrightarrow{\mathrm{k}_1} \mathrm{B}.$$

Here, A is the nascent UV absorber, and B is the photo-bleached UV absorber. Because photo-bleaching will gradually deplete the UV absorber, it is not a permanent cure for yellowing; instead, can only delay the yellowing process temporarily, see Fig. D.1.

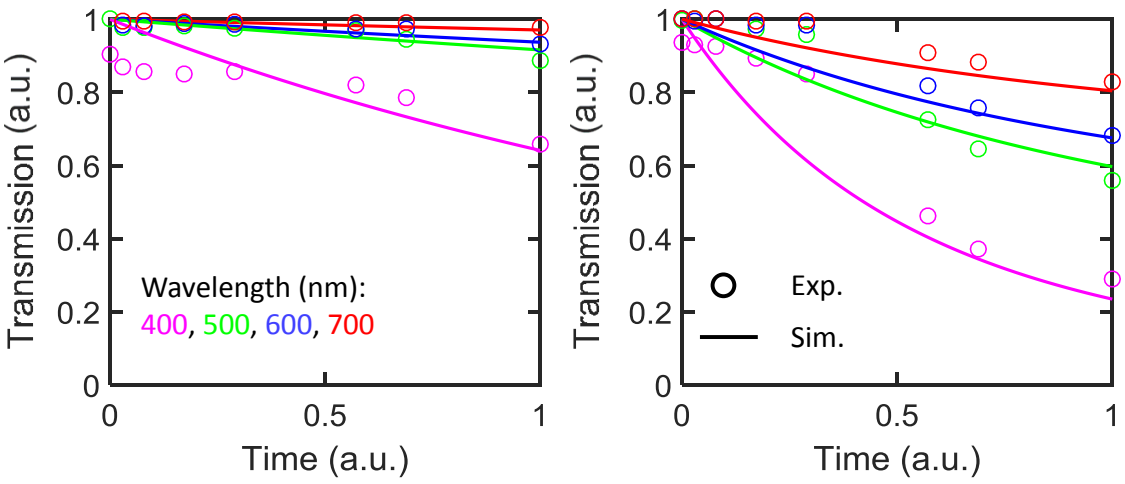

Fig. D.1. Test results as a function of exposure time in accelerated UV tests at 50 °C (left) and 110 °C (right). The wavelength ranges from 400 to 700 nm. The data is obtained from [94].

Model the reactions. Now we know that EVA yellowing is the result of two independent yet concurrent photo-induced reactions, where 1) the protective UV absorber is being consumed and 2) EVA is being broken into yellow chromophores. These two processes must be taken into account simultaneously to properly model the yellowing degradation. We apply the kinetic equations (see Table D.1) to describe the reaction rates herein, which are calculated by the pre-factors ($k_1(t)$ and $k_2(t)$) and the reagent

concentrations ($A(t)$ and $R(t)$). This approach has successfully simulated physical processes akin to yellowing (e.g., defect generation in MOSFETs [297]). These two prefactors are proportional to the total number of absorbed UV photons by the UV absorber and the EVA, respectively. In the beginning, we assume that the EVA does not absorb any UV photons (i.e., $k_2(0) = b \times (A(0) - A(0)) \times N_{UV} = 0$), thereby extricated from yellowing. Later, as a result of the UV absorber depletion, the rate for the EVA-breaking reaction accelerates. Also, since the prefactors are thermally activated (exponentially depend on temperature), yellowing develops much faster with elevated temperature, see Fig. D.1.

Model optical loss. Once obtaining the concentration of the yellow chromophore, one can estimate the resulting optical loss by applying the Beer-Lambert law. If one assumes no reflection loss, the light transmission (T) can be calculated by the Beer-Lambert law following

$$T = 1 - \exp(\alpha \times thickness_{EVA}), \tag{D.1}$$

where α denotes the absorption coefficient which depends on the photon wavelength. McIntosh *et al.* have experimentally demonstrated weak wavelength dependence above 400 nm [**?**]. Therefore, we can approximate the light absorption using a single effective absorption coefficient α_{eff} across the spectrum. Since the Beer-Lambert also indicates that the absorption coefficient is proportional to the concentration of light-attenuating species (the yellow chromophore in this case), we assume that α_{eff} increments linearly with the concentration of the yellow chromophore, which is simulated in the photo-induced reaction mentioned above, see Table D.1. Lastly, we can calculate the evolving transmission loss caused by EVA yellowing and reduce the maximum photocurrent available for solar modules accordingly.

Model validation. Up to now, we have successfully developed a physics-based model for EVA yellowing that, starts with simulating two involving photo-induced reactions inside EVA, and then translate the amount of the produced yellow chromophore to the optical loss via the Beer-Lambert law. We have validated the model

Table D.1.
The Temporal Degradation Model for EVA Yellowing

Encapsulant Photo-Thermal Kinetics Modeling	
Photo-Induced Reactions	Time-Dependent Equations
A + hv $\xrightarrow{k_1}$ B	$\frac{dA(t)}{dt} = -k_1(t) \times A(t)$
	$k_1(t) = a \times N_{UV}$
R + hv $\xrightarrow{k_2}$ Y	$\frac{dY(t)}{dt} = k_2(t) \times R(t)$
	$k_2(t) = b \times (A(0) - A(t)) \times N_{UV}$
Optical Performance Modeling	
Physical Outputs	Analytical Equations
Effective Absorption Coefficient for the Useful Solar Spectrum	$\alpha_{eff}(t) = \alpha_{eff}(0) + c \times Y(t)$
Optical Transmission of the EVA Layer	$T(t) = 1 - \exp(\alpha_{eff}(t) \times thickness_{EVA})$

against accelerated UV test [94] for different wavelengths (400, 500, 600, 700 nm) at different temperatures (50 and 100 °C) as shown in Fig. D.1. Remarkably, an excellent agreement has been attained.

D.2 Potential-Induced Degradation

Physics of Potential-Induced Degradation. Potential-Induced degradation (PID) has long been recognized to be one of the most detrimental degradation pathways for solar modules [291]. Revealed by its name, PID ensues from high electrical potential drop between the grounded metal framework and solar cells which consequentially drives sodium ions toward to solar cells. This displacement of charged sodium ion creates what is known as leakage current, an indicator for PID. Then, sodium ions get neutralized by the electrodes and pile up. Next, they diffuse through the SiN anti-reflection coating and eventually shorted the semiconductor junctions

[287], which reflects as a reduced shunt resistance in the circuit model. Other studies also have illustrated that PID can increase the carrier recombination current by introducing mid-gap recombination defects in silicon, sodium ions [286].

Model Potential-Induced Degradation. Undeniably, PID is a complex process that involves drift-diffusion of ions and defect generation in semiconductors, where external factors such as temperature and applied voltage must be accounted for. Here, we introduce the semi-empirical model developed by Braisaz *et al.* to simulate PID analytically [298], see Table D.2. *First*, the model calculates the degradation factor of the shunt resistance based on a set of inputs. Note that ion drift is proportional to the electrical field induced by the applied voltage, and the mobility of ions is also a thermally activated process. Hence, the degradation factor for PID is proportional to the applied voltage (V) while being exponentially dependent on temperature characterized by an activation energy E_A. Moreover, Hoffmann and Koehl have manifested a humidity threshold beyond which an electrically conductive layer starts to form on the glass by the condensed moisture and greatly exacerbates PID [105]. Therefore, a sigmoidal function is used to model the dependence of PID on relative humidity (RH). *Second*, to account for the incremental deterioration by PID over time, we estimate the decreasing shunt resistance as a function of time by integrating the degradation factor, see Table D.2. Finally, we validate the model by showing that the simulated PID-impacted shunt resistance coincides greatly with the experimental data from accelerated test [298], see Fig. D.2.

Table D.2.
The Temporal Degradation Model for Potential Induced Degradation

Out Parameters	Temporal Equations
Degradation Factor of Shunt Resistance	$R_D(t) = A \times V \times \exp(-\frac{E_A}{kT}) \times \frac{1}{1+\exp(B-C\times RH)}$
Shunt Resistance	$R_{SH}(t) = \frac{R_{SH}(0)}{1+\int_0^t R_D(u)du}$

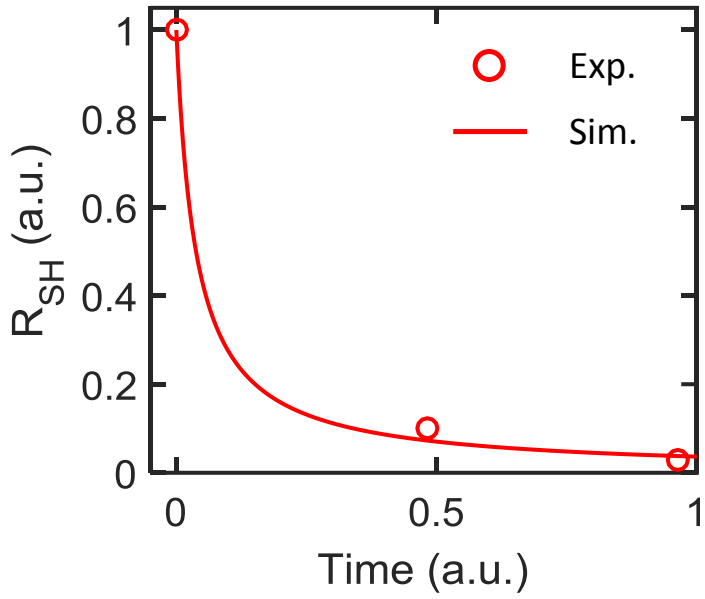

Fig. D.2. Temporal Evolution of R_{SH} at with T = 60 °C and RH = 85% under a -1000V voltage stress [298].

D.3 Metal Corrosion

Physics of Metal Corrosion. Moisture can intrude solar module in many ways, e.g., through glass microcrack, sealing plugs for electrical wiring, degraded backsheet. Sequentially, moisture diffuses through EVA encapsulants and attack the metallic contact. Moisture ingress can thin the metal grid by corrosion and also dissolve the silver paste adhering metals to solar cells, both of which in turn increase the series resistance in the equivalent circuit. Metal corrosion is particularly detrimental in a hot and humid environment where there exist abundant moistures in the ambient to quickly diffuse (a thermally activated process) into solar modules.

Model for Metal Corrosion. In this section, we introduce a modified Peck model presented in [298] to simulate metal corrosion, see Table D.3. In this model, a power law for humidity stress and an exponential Arrhenius law for temperature stress are applied to calculate the degradation factor. The final series resistance is simulated by integrating the calculated degradation factor over time. The model is

also validated against experimental data under different humidity and temperature stressors, see Fig. D.3.

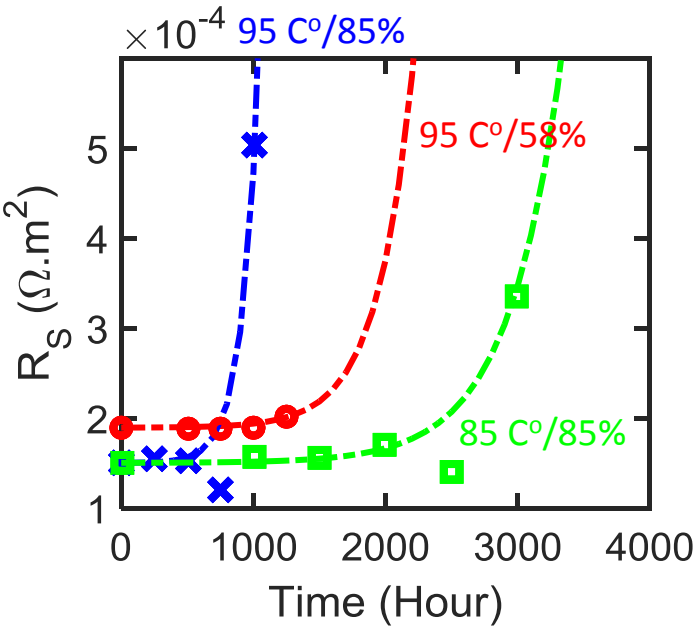

Fig. D.3. Temporal evolution of series resistance in the accelerated tests with temperature/relative humidity of 95 °C/85%, 95 °C/58%, and 85 °C/85%. Symbols and dashed lines are experimental and simulation data, respectively.

Table D.3.
The Temporal Degradation Model for Metal Corrosion

Output Parameters	Temporal Equations
Degradation Factor of Series Resistance	$R_D(t) = A \times (RH)^n \times exp(-\frac{E_A}{kT})$
Series Resistance	$R_S(t) = R_S(0) + \int_0^t R_S(u)du$

VITA

VITA

Xingshu Sun was born in Hangzhou, Zhejiang, China. He received his B.S. degree in the School of Electrical and Computer Engineering with distinction in 2012 from Purdue University, West Lafayette, IN, USA, where he has been working toward his Ph.D. degree in the same department since then. During graduate school, he also interned at IBM Research where he contributed to reducing the tunneling leakage current of the 7/10 nm FinFETs. His research interests include characterization and simulation of nanoscale transistors as well as system-level performance and reliability of photovoltaics. He also received Best in Session Award at TECHCON in 2015, and two Best Poster Awards at the 2017 IEEE Photovoltaic Specialists Conference.